Chip-Scale Atomic Magnetometer

Savino Piccolomo

A thesis presented for the degree of
Doctor of Philosophy

Department of Physics
University of Strathclyde
2016

‘This thesis is the result of the author’s original research. It has been composed by the author and has not been previously submitted for examination which has led to the award of a degree.’

Signed: Date:

September 26, 2016

Abstract

This thesis describes the physics and technology adopted to implement a Bell-Bloom type atomic magnetometer [1] at Strathclyde University. We show that the device is a functional experimental prototype, useful as the primary reference for future chip-scale miniaturization.

The sensor head and core of the device is a small (approximatively 20 mm^3) cubic cell derived from a silicon wafer structure and filled with a caesium azide (CsN_3) compound.

When the wafer is exposed to UV light, the azide is dissociated in its components; in this way the cells are filled with caesium atoms in the vapour form, which constitute the magnetically sensitive elements of the device, and nitrogen gas, used to optimize the performances of the sensor head.

We are able to characterize a whole wafer in a relatively short period of time, in terms of caesium vapour and nitrogen gas pressures, and for this purpose, we developed a data analysis tool based on caesium spectroscopy.

In the Bell-Bloom scheme the magnetic resonance is not excited by RF coils but by optical modulation of the input laser light: the laser could be modulated in frequency, amplitude (i.e. intensity) or polarization [2] but we adopted the amplitude modulation scheme because it requires the use of only one beam and an overall simpler set-up; it also allows the possibility of directly detecting Larmor oscillations.

In the basic experimental set-up, a light beam from a diode laser, tuned to the D_1 line of the caesium spectrum, is elliptically polarized and amplitude modulated; the light is then focused in and out the cell, through its opposite glass apertures, and the transmitted light is detected.

The sensor head is enclosed inside a magnetic shield where the desired (low-noise and spatially uniform) magnetic field is generated by two orthogonal pairs of Helmholtz coils. The cell is heated to reach the desired caesium vapour density with a non-magnetic resistor: its current is switched *on* and *off* and the signal is detected only during the *off* part to avoid undesired magnetic noise.

The laser intensity is cycled from a short and intense impulse, called “pump”, to a longer and weaker beam, named “probe”. The first is used to align the spins of the caesium atoms, so that the macroscopic magnetization precess around the magnetic field, while the second detects this so-called Larmor precession. The two orthogonal polarization components of this oscillation are found to be almost out of phase which justifies the use of a polarimeter to separately analyse their properties and investigate the possibility of signal subtraction to improve the signal-to-noise ratio.

In order to describe and optimize the experiment, the main experimental pa-

rameters (polarization, pump and probe intensities, sensor head temperature, laser frequency, magnetic field intensity and direction) have been analysed extensively in their effect on the oscillating signals.

We observed that the Larmor oscillations are damped and a pseudo magnetic field is generated by the laser, and that both are proportional to the probe intensity.

This research also presents a model that successfully explains the main experimental observations and extends the common representation in current literature [3,4,5] by further predicting the best laser frequency and input polarization and the out of phase phenomena previously described. The model uses the multi-pole expansion of the density matrix, truncated to its first order, and gives a satisfactory vectorial representation of the relationships between the main experimental parameters.

Finally, we have reached a complete noise characterization of the apparatus in the frequency domain. A data analysis tool is able to fully describe the performances of the magnetometer in terms of its sensitivity relatively quickly. A sensitivity lower then 5 $\mathrm{pT}/\sqrt{\mathrm{Hz}}$ at 850 Hz has been achieved which, if reproduced on a miniaturised level, will allow the device to compete with the current chip-scale atomic magnetometers.

Acknowledgements

First and foremost, I sincerely thank my academic supervisor **Erling Riis** for allowing me to be part of this scientific adventure; none of this work would have been possible without him. He has been a great teacher, the best boss and very supportive during tough times.

I also sincerely thank my industrial supervisor **Terry Dyer**; I enjoyed working with him and I appreciated his patience and supportive attitude. He is the ideal colleague and supervisor.

I would also like to acknowledge **TI** not only for sponsoring, but also believing in the work and effort required to create the magnetometer object of this thesis. Particularly I thank all the TI group for the patience in assisting and contributing to our weekly meetings and, most importantly, for their invaluable contribution to the project.

I would like to acknowledge all the colleagues in the *Experimental Quantum Optics and Photonics* group for their scientific support and for making the Ph.D also a fun experience.

A special thanks goes to the staff at the electronic workshop for their patient technical support.

I would like to thank Lynne for all the wonderful weekends and finally my family for allowing me to follow this path.

Contents

List of Figures

List of Tables

Acronyms

AOM Acusto-Opto-Modulator. 54, 60, 95

CPT Coherent Population Trapping. 4, 5

CRB Cramér-Rao lower bound. 64, 67

CSAM Chip-Scale Atomic Magnetometer. 1–4

DFT Discrete Fourier Transform. 70, 71, 79

FID Free Induction Decay. 54

FSR Free Spectral Range. 40, 42

FWHM Full Width at Half Maximum. 35

GNSS Global Navigation Satellites System. 3

ITO indium-tin-oxide. 2, 4

MEMS Mictoelectromechanical Systems. 1, 4

NDE Non-Destructive Evaluation. 3

NIST National Institute of Standards and Technology. 3, 4

PBS Polarizing Beam Splitter. 3, 54

RF Radio Frequency. 5, 56, 151

SERF Spin-Exchange Relaxation Free. 5

SVEA Slowly-Varying Envelope Approximation. 170

TI Texas Instruments. 1, 11, 47, 144

UV Ultra Violet. 10, 13, 15, 18, 50–52, 144

VCSEL Vertical-cavity surface-emitting laser. 2, 3

Physical Constants

Symbol	**Quantity**	**Value**	**Unit**	**Source**
k_b	Boltzmann Constant	$1.380\,648\,52 \times 10^{-23}$	$\mathrm{m^2 \cdot kg \cdot s^{-2} \cdot K^{-1}}$	[6]
a.m.u.	Atomic Mass Unit	$1.660\,539\,040 \times 10^{-27}$	g	[6]
$\hbar$	Reduced Planck Constant	$1.054\,571\,800 \times 10^{-34}$	J·s	[6]
ϵ_0	Vacuum Permittivity	$8.854\,187\,817 \times 10^{-12}$	$\mathrm{F \cdot m^{-1}}$	[6]
c	Speed of Light	$2.997\,924\,58 \times 10^{8}$	m/s	[6]
μ_B	Bohr Magneton	$9.274\,008\,99 \times 10^{-24}$	J/T	[7]

Table 1: Fondamental Physical Constants.

Symbol	**Quantity**	**Value**	**Unit**	**Source**
m_{Cs}	Caesium Atomic Mass	132.9 054 519	a.m.u.	[8]
γ	D_1 Decay Rate	4.561 2	MHz	[7]
ν_{D_1}	D_1 Central Frequency	335.1 160 488 07	THz	[7]
g_I	Nuclear Spin Landé g-factor	0.000 398 853 95		[9]
g_S	Electron Spin Landé g-factor	2.002 319 304 373		[6]
g_J	Electron Orbital Landé g-factor	2.002 540 32		[9]
g_F	Hyperfine Landé g-factor	0.250 318		[7]
γ_ν	Gyromagnetic Ratio	3.503 51	GHz/T	eq. 6.19
ω_e	D_1 Excited States Frequency Difference	1.167 680	GHz	[7]
ω_g	D_1 Ground States Frequency Difference	9.192 631 770	GHz	[7]
d_0 (eq. 3.10)	D_1 Transition Dipole Matrix Element	$2.698\,024 \times 10^{-29}$	C·m	[7]

Table 2: Caesium Physical Contants.

Chapter 1

The Project

1.1 Introduction

Highly sensitive magnetometers capable of measuring magnetic fields below 1 pT have an impact on a number of applications ranging from geophysical surveying to the detection of unexploded ordinance and the health care [10].
In the last years, it has been shown that laboratory optical magnetometers, based on the precession of the spins of alkali atoms in the vapour phase, could achieve sensitivities in the femtotesla range, comparable or even exceeding those of superconducting quantum interference devices [10, 11]. Despite the progress in improving the sensitivity of these instruments in a laboratory setting, they remain complex, expensive and difficult to assemble and operate. On the other hand, many applications would benefit greatly if the size, power consumption and cost of these devices could be reduced [11, 12].
Recently a great impulse in this direction was given by the so called miniaturization based on microelectromechanical systems (MEMS), which in addition to small size, offers other advantages like low power consumption, improved power dissipation, high-volume, wafer-based production and highly reduced production costs. The increasing use of this technology for magnetometers miniaturization had lead to new emerging devices called **chip-scale atomic magnetometers** (CSAM) [11, 13, 14, 15, 16].
This new growing market captured the attention of Texas Instruments (TI), a company with already a strong background in MEMS technology.
Following this impulse, a collaboration was established from the end of 2011 between the *Experimental Quantum Optics and Photonics* group at Strathclyde University and Texas Instruments to build a CSAM. The project aimed at delivering a small and highly sensitive device with low power consumption and integrated components for wafer-based production.

The first established milestone was the realization of a functional experimental prototype on a laboratory setting, which would work as a primary reference for future miniaturization. The present thesis describes the physics and technology used to achieve this first primary goal.
This introductory chapter gives an overview of the project, starting with the general outcome and the main technological background; the chapter also introduces the physics of the device, and presents possible applications.

1.2 Envisioned Magnetometer

The aim of the project is the realization of a CSAM able to give a real time measure of the external magnetic field with the following points of strength:

- **chip-scale** dimensions (less then 1 cm^3);
- **wafer-based production** for cost reduction, easy production and integration with other components;
- **low power consumption**: <200 mW;
- **high bandwidth**: the bandwidth of a magnetometer measures how fast it can track changes in the magnetic field. For many applications, such as medical health, a bandwidth of 1 kHz is needed [17, 18, 19].
- **highly sensitive**: 10-20 pT/$\sqrt{\text{Hz}}$; the sensitivity measures the accuracy of the magnetometer in measuring magnetic fields.
  In the most basic example, the measures of a constant external magnetic field are affected by white noise. This form of noise can be easily reduced by averaging, i.e. time integration; since this operation also reduces the magnetometer bandwidth, the ratio between the noise and (radical) bandwidth, and not the noise alone, is used as a more meaningful way of measuring the magnetometer performance. Chapter 4 gives a more complete description of the sensitivity.

The final structure of the CSAM will most likely be described by the following parts:

- a vertical-cavity surface emitting laser (**VCSEL**) is mounted on a base plate;
- above the VCSEL a **micro-optics** package is mounted which attenuates the light power, changes the beam polarization and collimates the beam;

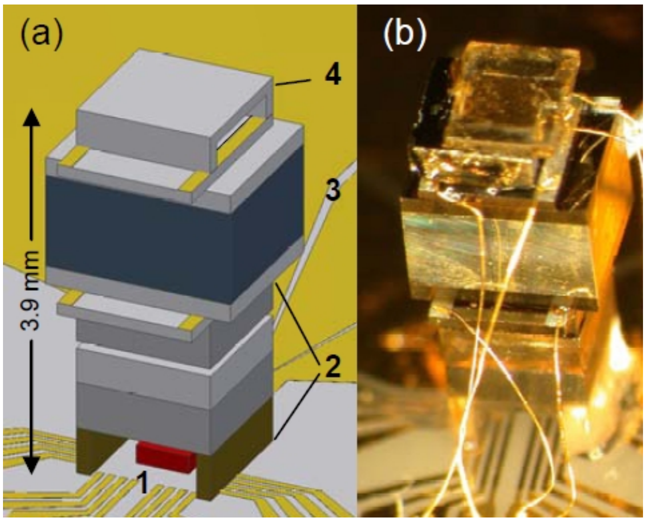

Figure 1.1: Schematic (a) and photograph (b) of the CSAM realized at NIST [14]. The components are: 1 - VCSEL, 2 - micro-optics, 3 - caesium vapour cell, 4 - photodiode.

- a micro-fabricated **caesium vapour cell** is mounted with a transparent indium-tin-oxide (ITO) heater or a deposited resistor wire, placed above and below it; this component increases the cell temperature and creates enough atomic density to absorb a significant fraction of the light.
- a polarizing beam splitter (PBS) is mounted above the cell to separate the desired output light polarization and a **photo-diode** monitor the light transmission through the atomic vapour.

Figure 1.1 shows the CSAM schematic realized at the *National Institute of Standards and Technology* (NIST) in Colorado [10, 12, 13, 14, 16, 20], which well represents the guideline for the final magnetometer.

Possible Applications Some examples of possible CSAM applications are:

- non destructive evaluation (NDE), remote sensing of the position of a moving metallic component [11, 13];
- detection of bio-magnetic signals for health care such as magneto-cardiography and magneto-encephalography [10, 11, 13, 14, 20, 21];
- geophysical surveying, such as navigation GNSS devices (Global Navigation Satellites System) [10, 12, 21, 22, 23];

- detection of magnetic anomalies produced by metallic objects, such as unexploded ordinance [10, 11, 20];
- navigation [10];
- mineral and oil exploration [14, 20];
- space science [11, 21];
- commercial communication system, such as modern cellular telephone networks [12, 23].

1.3 Project Outcome

As previously mentioned, the the outcome of this project, is the realization of the atomic magnetometer in a laboratory setting that would serve as a prototype for the corresponding CSAM.

For this purpose, we made considerable effort to meet the requirements necessary for the future envisioned CSAM; in particular we have achieved wafer based production of the sensor head (the caesium vapour cell), and we have met the sensitivity target previously outlined.

1.4 Background

The main inspiration for our project has been the work done by NIST.

Using a combination of optical spectroscopy, atomic physics and MEMS techniques, they have build a small low-power magnetic sensor based on alkali atoms [11, 12, 13, 15, 16, 20].

We present here the main CSAM designs and technology developed at NIST:

- **Coherent population trapping** (CPT) based magnetometer. For alkali atoms, a CPT signal is detected when two resonant optical fields interacts with the atoms so that their frequency difference matches the energy difference between the two hyperfine atomic ground states; in this situation the atoms are excited in a “dark state”, resulting from a quantum superposition of two ground states, which cannot be probed by both optical fields; the atoms are effectively “trapped” and never excited into the excited state. The two optical fields are generated by modulating the injection current of a diode laser [13]. The cell is heated with a pair of resistive heaters implemented as films of ITO on a glass surface and the magnetic field is measured only when the heater current is off. The magnetic sensor has a size of 12 mm^3 and dissipates 195 mW of power. The sensitivity reached is about 40 pT/$\sqrt{\text{Hz}}$ at 10 Hz [10, 13, 16].

- In an $\mathbf{M}_z$ **magnetometer**, the atomic sample is optically pumped in the direction of a static magnetic field, while in the $\mathbf{M}_x$ **magnetometer** in the transverse direction (at an angle of about 45°). A coherent precession about the magnetic field is then excited with an applied radio frequency (RF) field. The design is similar to the CPT magnetometer previously described, except for the addition of two coils in the stack that enable the drive field to be applied to the atoms. The M_z scheme is more accurate but slower: it's speed is limited by the longitudinal (along the magnetic field) relaxation rate of the magnetization. The M_x scheme is faster and simpler, but not as accurate. The best sensitivity reached fot these configuration is as low as 6 pT/$\sqrt{\text{Hz}}$ from 1 Hz to 1 kHz. [15, 24, 25, 26].

- **Bell Bloom scheme** magnetometer: In the Bell-Bloom scheme the magnetic resonance is not excited by RF coils but by optically modulating the input laser light in frequency, amplitude (i.e. intensity) or polarization [2] and the same light is used for pumping and probing the atoms [1, 20, 26]. As we will fully explain in chapter 4, this is the scheme adopted as the main inspiration for our experiment because it requires the use of only one beam and an overall simpler set-up; it also allows the possibility of directly detecting Larmor oscillations.

- Magnetometer based on **frequency modulated non-linear magneto-optical rotation** [14]. Here, linearly polarized light propagates along the direction of the magnetic field, and the optical frequency of this light is modulated at twice the Larmor frequency moving the optical resonance *on* and *off*. The laser frequency is scanned by modulating the injection current of the laser. The measured magnetic sensitivity in the unlocked mode is around 0.15 pT/$\sqrt{\text{Hz}}$ at 1 Hz.

- **SERF magnetometers**. The sensitivity of most atomic magnetometers is limited ultimately by alkali-alkali collisions. At low alkali density the signal from the atoms is proportional to the number of atoms; however at higher densities alkali-alkali spin-exchange or spin-destruction collisions begin to broaden the magnetic resonance. When the density is very high (i.e. high temperatures) and at weak magnetic field, the alkali spin relaxation precess is much weaker resulting in sensitivities up to one hundred times better [11, 27]. This type of magnetometer is known as spin-exchange relaxation free (SERF). A zero field magnetic resonance is measured resulting in a 10-70 $\mathrm{fT}/\sqrt{\mathrm{Hz}}$ above 125 Hz [11, 13, 28].

1.5 Physical Principle

The aim of the project is the realization of a magnetometer in the **Bell-Bloom scheme** [1, 20, 26]; here an amplitude modulated light is used both to pump and probe the atoms by cycling the laser intensity from a short and intense impulse (the pump), to a longer and weaker beam (the probe).
The basic physics of the experiment can be described by a three-step process:

- **Pumping**. the high intensity pump creates a macroscopic polarization in the direction of the beam; the polarized beam creates a population imbalance in the Zeeman sub-levels of the ground state which results in a optically pumped dark state [29] and in an overall macroscopic polarization [3, 5];

- **Precession**. The polarization precesses around the magnetic field at the so called **Larmor** (angular) **frequency** ω_l, proportional to the magnetic field amplitude B itself [3, 4, 5, 30, 31]. The proportionality is easily written as:
$$\omega_l = \gamma B, \tag{1.1}$$
where γ is the gyromagnetic ratio which for caesium atoms is around 3.5 Hz/nT;

- **Probing**. The magnetization oscillations are detected by the weak probe and its frequency is used to measure the corresponding magnetic field using equation 1.1 [2, 32].

1.6 Thesis Structure

The thesis is structured as follows:

- The first part of the thesis describes the cell properties and spectroscopic characterization. In particular, chapter 2 describes the core of the device, the sensor head, in terms of its fabrication, properties and gives a preliminary analysis of the (gas and vapour) pressures. Chapter 3 describes the sensor head characterization in terms of its spectroscopic properties.

- In the second part of the thesis we describe the magnetometer and report the main experimental findings. In chapter 4 we describe the experiment used to measure the magnetic field and introduce the main tools used to characterize its performance. Chapter 5 characterizes the oscillating signal in terms of the main experimental parameters and the device in term of its sensitivity and spectral characteristics.

- In the third and last part of the thesis, we develop a model that describes the main observations. In particular, in chapter 6 we use a first order multipole approximation of the density matrix to describe the evolution of the quantum-mechanical system in 8 relatively simple vectorial equations. In chapter 7 we describe the interaction of the laser with the sensor head based on the Maxwell equations, and connect the results to the description developed in the previous chapter to successfully explains the main experimental observations.

Part I

Sensor Head Characterization

Chapter 2

The Sensor Head

The sensor head is the core of our magnetometer, as well as of most CSAMs [12,13,14,15], being the element sensitive to external magnetic fields. In our case, it is a cell filled with caesium atoms in the vapour form.

This chapter describes the cell fabrication, how the vapour is obtained from dissociation of a caesium compound and the pressures and diffusion mechanism inside the cell. The next chapter will be focused on the characterization of the sensor head in term of its spectroscopic properties.

2.1 Why Caesium

For most atomic magnetometers, the element used is in the vapour form in order to allow all the atoms to undergo the same (almost exactly) energy transitions, which won't be possible with solid or liquid elements.

The atoms usually chosen are alkali atoms (the ones on the left-hand side of the periodic table) because they have a fairly simple electronic structure: a single electron in addition to a filled shell. Caesium is chosen over other alkali atoms because:

- at reasonable temperatures, caesium has a high vapour pressure [7], making resonance effects relatively easy to observe;
- as opposed for example to rubidium, caesium has just one stable natural isotope which doesn't give rise to multiple spectroscopic lines, and, most importantly, caesium doesn't require isotopic separation [7,33];
- caesium is widely used in atomic clocks because it is the element used for the definition of the second [34,35]; since most atomic magnetometers and frequency standards share the same basic technology [12], caesium is widely used in many CSAMs as well.

The main disadvantage of using caesium is that it has a big collisional cross section, which means that at high density (i.e. high temperature) collisions between atoms lead to undesired effects [36].

2.2 Fabrication

The cells, derived from a silicon wafer structure, were designed and fabricated at TI, and delivered to Strathclyde University already filled with a caesium compound.

The fabrication method could be summarized as follows: the cell cavities are created by etching of the silicon wafer, and its bottom side is anodically bonded to a glass surface, so that the etched holes can be filled with a caesium azide water-based solution; after the water part of the compound is evaporated under vacuum, a final stage of anodic bonding seals the top face of the wafer with a second glass surface. Finally, the wafer is UV exposed to dissociate the azide into its constituents, so that the cells, now filled with nitrogen and caesium atoms in the vapour form, are ready to be singulated and tested: in the following sections we detail this process.

2.2.1 The Wafer

The wafer is a 1 mm thick silicon disk, ~20 cm in diameter. After the cell holes are etched, the disk is sealed on both sided by two, 1 mm thick, glass layers. An example of the final product is is shown in figure 2.1.

Etching is a common technique of chemically remove layers from the surface of a wafer during manufacturing. Usually every wafer undergoes many etching steps before it is complete.

During the etching process, part of the wafer is protected from the etchant by a masking material which resists etching. In some cases, the masking material is a photo-resist which has been patterned using photo-lithography, other situations require a more durable mask, such as silicon nitride [37,38,39,40]. For our wafers, a liquid-phase (*wet*) etchant based on potassium hydroxide (KOH) was used, which etches the crystalline materials at very different rates depending upon which crystal face is exposed: or silicon wafers, this effect can allow very high anisotropy [37].

Anodic Bonding is a method of hermetically and permanently joining glass to silicon without the use of adhesives.

The silicon-glass layers are subjected to a force of 500 N and a high voltage

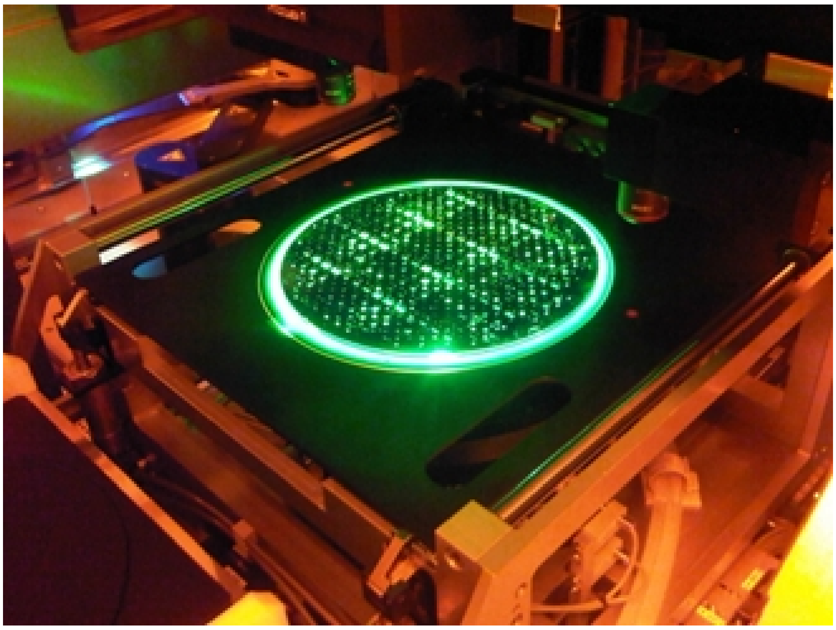

Figure 2.1: An example of the wafer designed and fabricated at TI

gradient. The temperature reaches typically 300°C which causes the sodium ions in the glass to become mobile and the alkali cations to migrate from the interface resulting in a depletion layer. As the depletion is formed, the anodic bonding current shows a clear decrease after which the bonding is considered complete [38, 39, 40, 41, 42, 43].
This result in a permanent chemical bond between the glass and the silicon.

2.2.2 The Cell

The sensor head cavities (cells), obtained by photo-lithography of silicon, have mainly all rectangular or square shape, like the one shown in figure 2.2.

Dimensions The cell is 1 (or 1.5) mm deep with a side length varying from 1 to 8 mm (usually 4).
The vertical sides are tiled by 35.2° with respect to the vertical direction; this is due to the anisotropic etching process which follows a particular silicon crystal plane. The results is a cell with a rectangular trapezoidal shape (see figure 2.3). Assuming 1 mm thick cells, the volume (in mm^3) is:

$$V = lw - t(l + w) + \frac{4}{3}t^2$$

where l is the length, w is the width and $t = \tan 35.3°$.

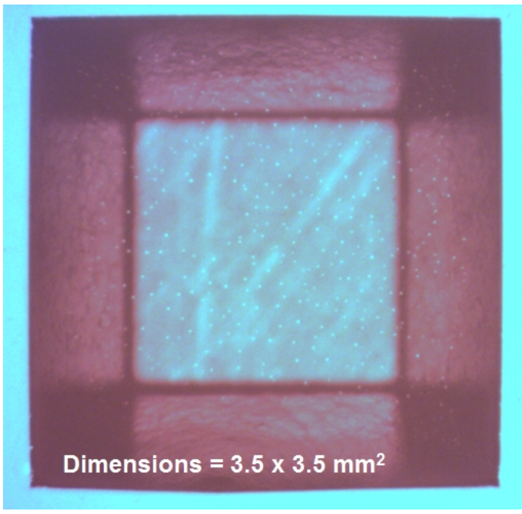

Figure 2.2: A typical square cell seen from the upper glass aperture; the lower glass aperture and the silicon walls are visible.

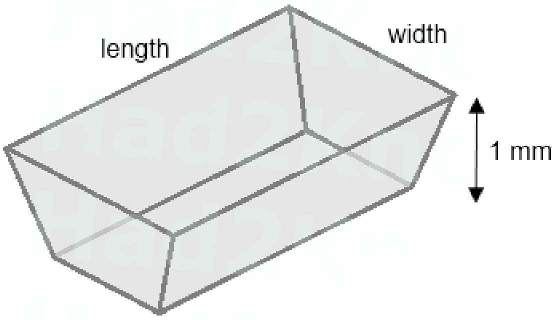

Figure 2.3: Cell shape: rectangular trapezoid.

2.2.3 Azide Dispense

The cells were dispensed with caesium azide (CsN_3) in water solution, before anodically sealing the last glass surface.

Since the azide is highly toxic, a fume cupboard is used so that the air flow is controlled and no toxic particle is inhaled [38].

The solution is dispensed manually using a micro-pipette within the cells [40], which is able to dispense a controllable amount of liquid in a reliable way. A future possibility is the use of a robotic dispense method to automatize the process.

Optionally, the last upper glass surface could be anodically sealed in the presence of a variable amount of nitrogen pressure in order to fill the cells with an additional amount of buffer gas, before the azide dissociation process.

2.2.4 Azide Dissociation

We use a method suggested in literature [43, 44] to decompose the azide in its constituents, nitrogen as a gas and caesium in the metallic form with its corresponding vapour. The method suggests to expose the cells with UV light for the photolysis of the azide [43].

We use a UV system which is able to expose an entire wafer in few hours. The total energy required to photo-decompose the azide is approximately 5 J/mm^2 [43]; the lamp has a power of 87 $\mu J/mm^2$ at 254 nm, which results in a total exposure time of the order of 15 h.

When caesium atoms are liberated from the azide, they float in the cells in the vapour form; as the UV process continues the vapour saturates the cell and the condensation process starts. As expected, after few hours of UV exposure, we observe silver droplets of metallic caesium condensing on the glass walls of the cells. Figure 2.4 shows the presence of caesium droplets on the upper glass surface. Crystallize azide residual is still visible usually close to the borders of the lower glass surface.

Attempts were made to use very low amounts of azide, but no caesium was spectroscopically detected after UV exposure. This is explained as a wall effect in the sense that the internal surfaces of the cell capture an initial amount of caesium.

Figure 2.5 shows the caesium droplets at different exposure times, for 3 different sensor heads. Caesium droplets are visible in the uppermost surface of each cell and the quantity of droplets increases with time.

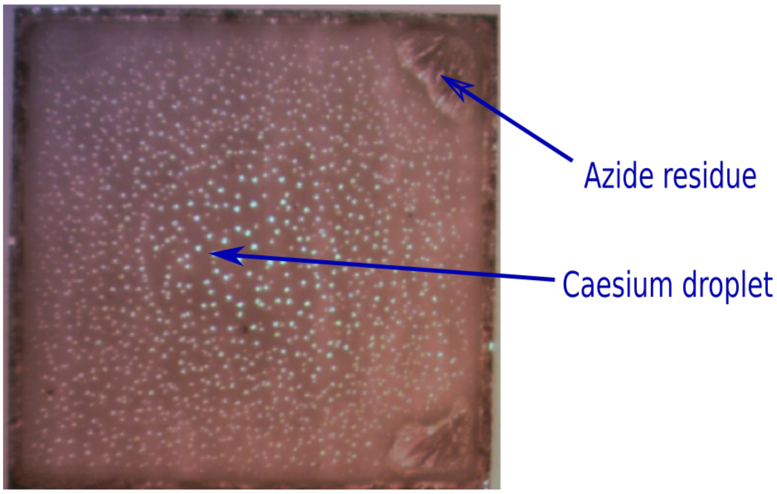

Figure 2.4: Caesium droplets visible in the upper surface of the cell.

2.2.5 Dissociation Products

As said the dissociation process liberates caesium and nitrogen. The following paragraphs describe their characteristics.

Caesium is a silvery-white alkali metal that is very soft and ductile. It has the second lowest melting point of all metallic elements and is liquid near room temperature. It is a very reactive metal: it combines quickly with oxygen in the air [45] and reacts violently with water; combined with water forms caesium hydroxide (CsOH), which is the strongest base available and can attack glass. In the reaction with water, hydrogen gas is released. Hydrogen gas ignites immediately as a result of the heat given off by the reaction.

Nitrogen is liberated in the cell as a gas and its presence is essential for the correct functioning of the sensor head. The reasons why nitrogen is considered a *buffer gas* are:

- nitrogen drastically increase the time caesium atoms can be detected by the laser by changing its diffusion properties [46, 47] (see section 2.4);
- caesium atoms hold information about the magnetic field in their quantum state coherences and populations and when they collide between each other the information is lost (spin de-coherence). The presence of

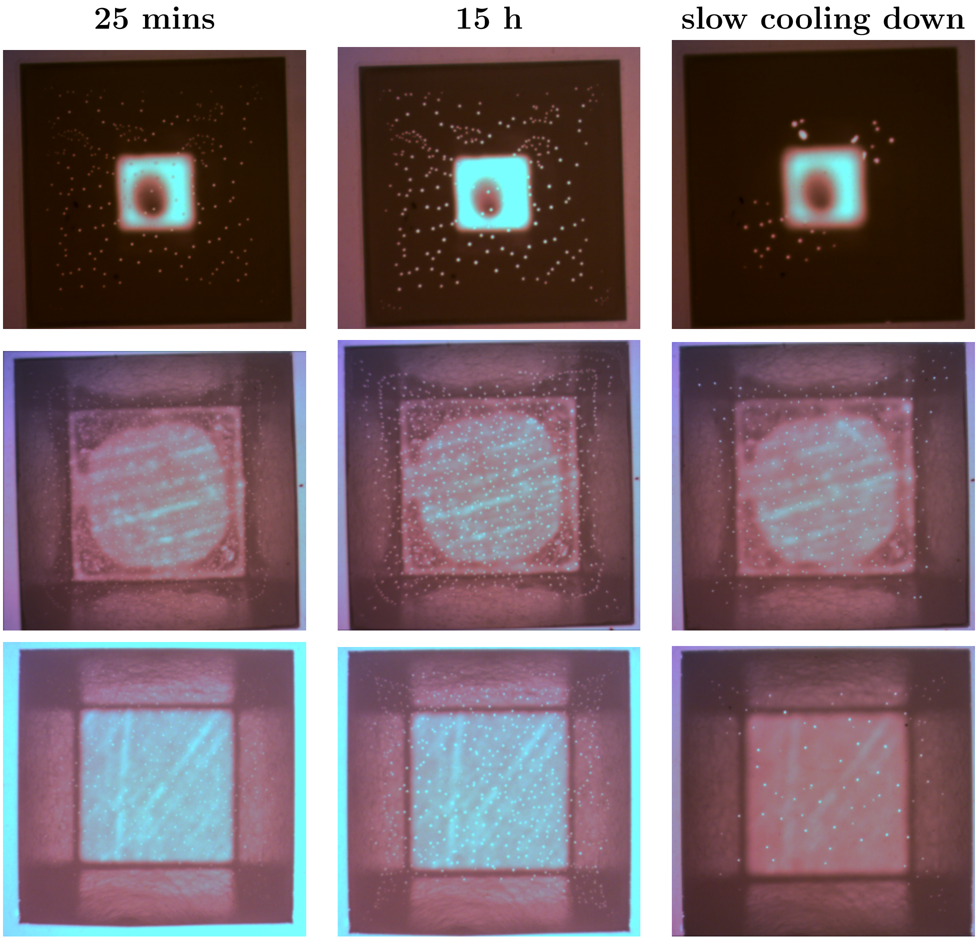

Figure 2.5: Figure showing the UV dissociation process at different times (columns) for 3 different cells (rows): caesium droplets are visible in the uppermost surface of each cell. The last column shows the effect of the final cooling down process. The bottom side of the cells in the center of each picture is whiter then the rest. Azide residues are visible in the first cell (upper row) by a darker spot in the middle of the bottom face; for the second cell (middle row) the residues are visible on the sides of the bottom face.

nitrogen gas reduces this probability by reducing the caesium collisional cross section [48, 49];

- with a similar mechanism nitrogen decreases the rate of caesium atoms hitting the walls which would cause information loss;
- nitrogen causes the ground-excited state coherences to decay much faster [50]. This makes the sensor head spectrum broader if compared with the spectrum of caesium alone, which results in a increased transmitted light. This phenomena, known as pressure broadening is addressed in section 3.3.
- nitrogen causes the excited states coherences to decay very fast and it quenches the excited stated populations. This causes a decreased spontaneous re-emission of light which could destroy the spin polarization of caesium [51, 52].

2.3 Pressures

We analyse the pressure of both caesium vapour and nitrogen gas in the sensor head due to the dissosiation process.

2.3.1 Caesium

Caesium is a metal that remains solid until $T_l = 28.44°\text{C}$. When it liberates from the azide, it fills the cell volume as a vapour, while condensing on the walls as liquid or solid, depending on the temperature.
The vapour pressure of caesium is a function of the temperature that can be modelled by these two functions, depending on which state the corresponding condensed caesium is in (solid or liquid) [53]:
solid phase ($T \leq T_l$):

$$\begin{aligned}\log p_v = \; & -219.482\,00 + \tfrac{1088.676}{T} - 0.083\,361\,85\,T + \\ & +94.887\,52 \log_{10} T,\end{aligned} \tag{2.1}$$

liquid phase ($T > T_l$):

$$\begin{aligned}\log p_v = \; & 8.221\,27 - \tfrac{4006.048}{T} - 0.000\,601\,94\,T + \\ & -0.196\,23 \log_{10} T,\end{aligned} \tag{2.2}$$

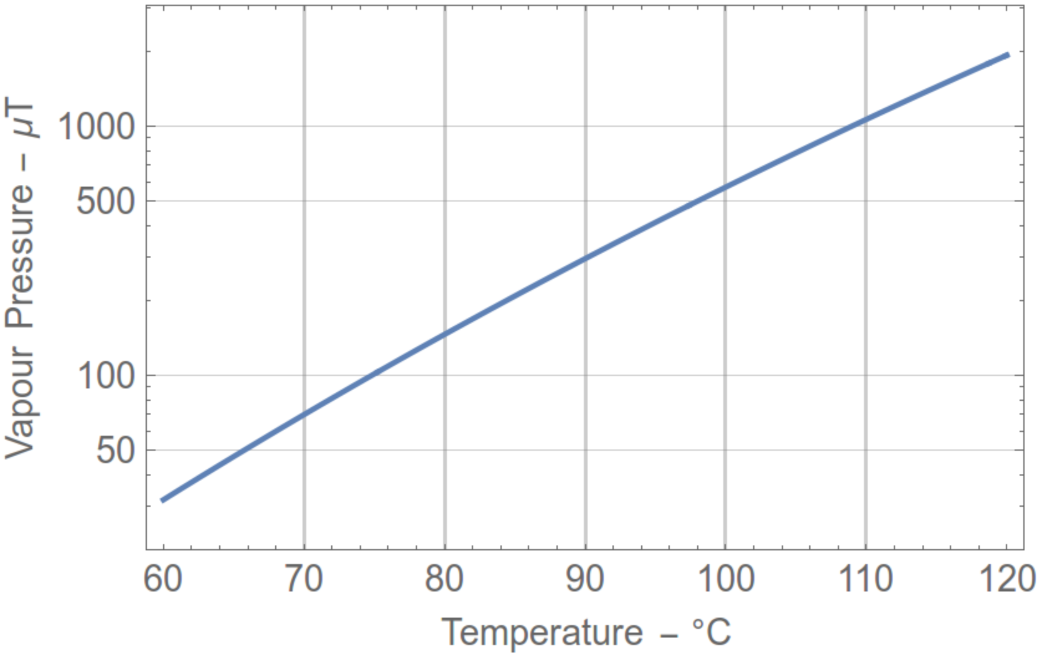

Figure 2.6: Vapour pressure of caesium from the model of equation 2.2.

where p_v is the caesium vapour pressure expressed in Torr and T the temperature expressed in Kelvin. Figure 2.6 shows the corresponding logarithmic plot for the temperature range of interest: as it can be seen the pressure follows a highly exponential trend.

As a first approximation we can use the ideal gas law to calculate the corresponding caesium number density n, defined as the number of atoms per unit volume:

$$n = \frac{p_v}{k_b T}, \tag{2.3}$$

where k_b is the Boltzmann constant.

The number of caesium atoms N^v_{Cs} in the vapour state, in a typical 20 mm^3 cell, as a function of the sensor head temperature is plotted in figure 2.7. As it can be seen it tends to double at temperature steps of 10°C. The number of caesium atoms in the vapour form in a typical cell (20 mm^3) at 110°C is:

$$N^v_{\mathrm{Cs}} \cong 5.4 \times 10^{11}. \tag{2.4}$$

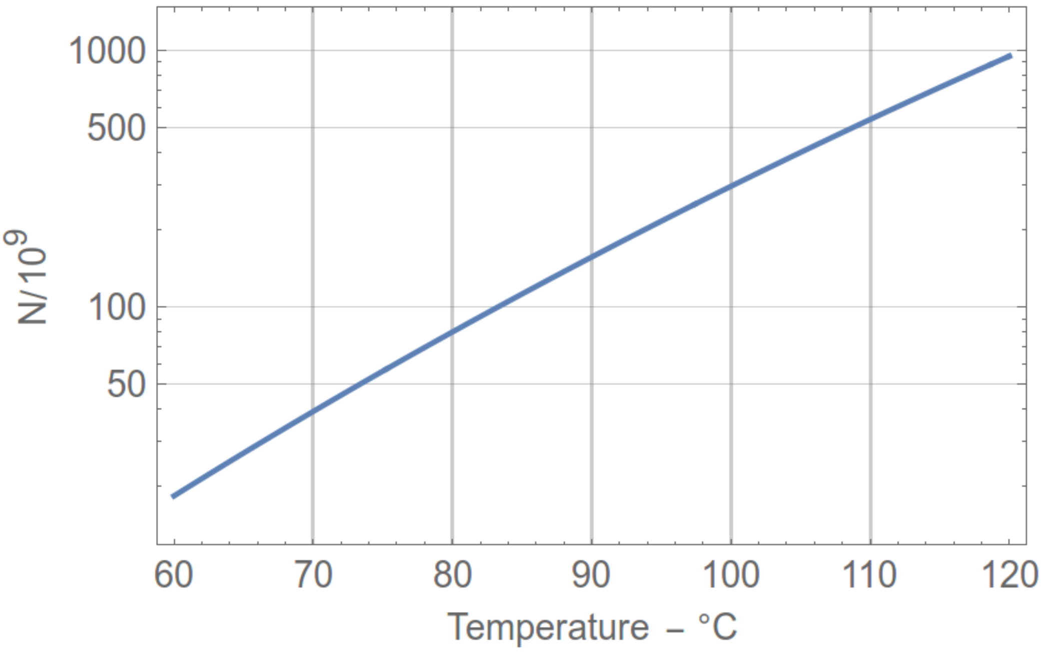

Figure 2.7: Number of caesium atoms N^v_{Cs} in the vapour form in a typical 20 mm^3 cell as a function of the operating temperatures (see equation 2.3).

2.3.2 Nitrogen

The total number N of caesium azide ($\mathrm{CsN_3}$) molecules is given by:

$$N = \frac{M}{m},$$

where M is the total mass of the azide and m the mass of one of its molecule. More specifically:

$$m = (A_{\mathrm{Cs}} + 3A_N) = (A_{\mathrm{Cs}} + \frac{3}{2}A_{N_2}) \text{ a.m.u.},$$

here A_{Cs}, A_N and A_{N_2} are the atomic numbers of caesium and the nitrogen atom and molecule respectively, and a.m.u is the atomic mass unit.
If the UV process dissociates a fraction α of them (at best 1), the number of caesium atoms in the cell is:

$$N_{\mathrm{Cs}} = \alpha N = \frac{\alpha M}{m}. \tag{2.5}$$

Calculating this number[1] we incidentally discover that the number of total caesium atoms is ≈2×10^5 higher than the number of caesium atoms in the

---

[1] Assuming M = 80μg, $\alpha = 0.3$ and T = 110°C then $N_{\mathrm{Cs}} = 9.3\times10^{16}$.

vapour state alone (see formula 2.4), which suggests that that the big majority of caesium is condensate in the cell walls.
The number of nitrogen molecules can be calculated analogously as:

$$N_{N_2} = \frac{3}{2}\alpha N = \frac{3\alpha M}{2m}.$$

Since nitrogen is in the gaseous state, we can use the ideal gas law to find its pressure:

$$p_{N_2} = \frac{N_{N_2} T k_b}{v} = \frac{3dMTk_b}{2mv},$$

where v is the cell volume. This expression can be re-written in a more practical form if we use reference values for the azide mass, the temperature and the volume, respectively M_r, T_r and v_r; we can write:

$$p_{N_2} = p_0\,\alpha\,\left(\frac{M}{M_r}\right)\left(\frac{T}{T_r}\right)\left(\frac{v}{v_r}\right)^{-1}, \tag{2.6}$$

where we have defined the reference pressure p_0 as:

$$p_0 = \frac{3dk_bT_rM_r}{2mv_r}.$$

If we set the references to reasonable values like $T_r = 380$ K $\approx 110°$C, $M_r = 20\ \mu$g and $v_r = 20$ mm^3, then the reference pressure is:

$$p_0 = 203.2 \text{ Torr}.$$

The real values of mass, temperature and volume will not deviate too much from their corresponding reference values so that, in equation 2.6, the expressions in parenthesis are not too far from one in most cases. We can therefore say that αp_0 gives a good first guess estimate of the nitrogen pressure in our sensor head. Assuming $\alpha \approx 0.3$, the pressure inside the cell p_{N_2} should be around:

$$p_{N_2} \approx 68 \text{ Torr}.$$

As already mentioned in section 2.2.3, in some cases, the upper and last layer of glass is anodically bonded on the silicon disk under a further nitrogen pressure p_b, called bonding pressure, usually ranging from 0 to 1000 Torr, at temperature T_b ($\approx$ 600 K); in this case equation 2.6 can be expanded to:

$$p_{N_2} = p_0\,d\,\left(\frac{M}{M_r}\right)\left(\frac{T}{T_r}\right)\left(\frac{v}{v_r}\right)^{-1} + p_b\frac{T}{T_b}.$$

As it can be seen from figure 2.6, in all cases the caesium pressure in the cell is way lower than the nitrogen one.

2.4 Diffusion

As already introduced in section 1.5, the laser beam cyclically pumps and probe the caesium atoms. Only the atoms that cross the optical path of the laser are pumped while the other remain un-polarized. This, on the other hand, determines a polarization gradient in the sensor head which causes a diffusion process. Since the atoms are probed in the same region they have been previously pumped, it is important to consider the diffusive properties of caesium and how nitrogen affects them.

We present here a classical way of approaching this issue. In the first part we consider the classical phenomena of one gas diffusing, in the second part the results are extended to two gases diffusing into each other; finally we will outline some numerical considerations relevant for our experiments.

2.4.1 One Gas

If a gas has a spatial concentration given by the function $\phi(x, y, z)$, the diffusion mechanism is described by the Fick's law[2] [54]:

$$\frac{\partial \phi}{\partial t} = D\nabla^2\phi. \tag{2.7}$$

In a gas (of atoms or molecules) the diffusion constant can be written as [55]:

$$D = \frac{1}{3}lv,$$

where each gas particle is considered moving, from one collision to the next, in a straight trajectory with a mean thermal velocity v_{th} and a mean free path l.

Mean Thermal Velocity Using the well known Maxwell-Boltzmann velocity distribution for particles in three dimensions, we can define the mean thermal velocity v_{th} as [55]:

$$v_{\text{th}} = \sqrt{\frac{8k_bT}{\pi m}}, \tag{2.8}$$

where m is the particle mass.

---

[2] This law can be easilly obtained from the following continuity equation:

$$\frac{\partial \phi}{\partial t} = D\vec{\nabla} \cdot \vec{F},$$

connecting the concentration derivative $\frac{\partial \phi}{\partial t}$ to the diffusion flus $\vec{F} = D\vec{\nabla}\phi$; equation 2.7 results remembering that $\nabla^2 = \nabla \cdot \nabla$.

Mean Free Path The mean free path l of a particle is defined as the average distance travelled by a particle from one collision to the next. To arrive at its explicit formula, we note that this quantity can be alternatively defined as the distance d travelled by the molecule, in a arbitrary time t, divided by the number of collisions N occurred in the same time:

$$l = \frac{d}{N}.$$

Since the molecule mean velocity is v_{th}, the distance d is obviously $d = v_{\mathrm{th}}t$. During its trajectory of time t, the particle will sweep out an interaction volume V, so that the total number of collisions occurring in the same time is:

$$N = Vn,$$

where n is the gas number density, i.e. the number of particles per unit volume. The volume of interaction is the product of the particle cross section and the distance d' travelled by the particle relative to the the other particles:

$$V = \sigma d'.$$

Note that d' is not the exactly the same as d since the relative velocity v_r between the particle and the targets has to be taken into account. We can still write:

$$d' = v_r t.$$

So that the mean free path of a particle can be written as:

$$l = \left(\frac{v_r}{v}\sigma n\right)^{-1}. \tag{2.9}$$

It is easy to prove that the the relative velocity of any two particles travelling at velocities v_1 and v_2 is:

$$v_{\mathrm{r}} = \sqrt{v_1^2 + v_2^2}.$$

In our case $v_r = v_2 = v_{\mathrm{th}}$ so that $v_r = \sqrt{2}v_{\mathrm{th}}$, which implies:

$$l = \left(\sqrt{2}\sigma n\right)^{-1}. \tag{2.10}$$

Molecular Cross Section Using Serway's approach [56], the collision of two particles of diameter d can be modelled by one circle of diameter $2d$ interacting with a target modelled by a point. The collisional cross section σ is the area of the circle:

$$\sigma = \pi d^2,$$

which can be used in equation 2.10 to give an expression for the mean free path of a particle, in a gas composed by the same type of particles:

$$l = (\sqrt{2}\pi d^2 n)^{-1}. \tag{2.11}$$

Diffusion Velocity If we consider the diffusion mechanism, we can see that a molecule starts in a determined point and then it spreads, so that its position is undetermined and can be described by a Gaussian profile in space and time, like the following [55]:

$$P(r,t) = \frac{1}{\sqrt{4\pi Dt}} e^{-\frac{r}{4Dt}},$$

where r is the distance of the molecule from its starting position, and t is the time from the starting moment. The Gaussian width is time dependent and given by:

$$\sigma(t) = \sqrt{2Dt}.$$

If we consider its time derivative

$$\sigma'(t) = \sqrt{\frac{D}{2t}}$$

one can see that the "diffusion velocity" goes from infinite at $t = 0$ to 0 at $t \to \infty$. Following this reasoning we will define the time to reach a certain position r by diffusion with the expression:

$$t(r) = \frac{r^2}{2D}.$$

2.4.2 Two Gases

Here we present a simple way of modelling the diffusion process of one gas into another by extending the results outlined in the previous section. In particular the collisional cross section of two particles (one for each gas) is approximated by the sum of the particles circles area, with each circle diameter given by the particles dimension. Obviously this is only a first approximation and its limit will be clarified later.

Let's consider two gasses labelled a and b, with number densities n_a and n_a respectively. Fallowing the same reasoning used in the previous section, we can write the total number of interactions of one molecule of gas a with both gasses as:

$$N_a = V_a n_a,$$

where the volume of interactions of the particle in gas a with gas a and b is:

$$V_a = \sigma_{aa} d_{aa} + \sigma_{ab} d_{ab}. \tag{2.12}$$

In this formula d_{aa} and d_{ab} are the distances travelled by the particle in gas a relative to gas a and b respectively, which can be written as:

$$
\begin{aligned}
d_{aa} &= v_{aa}t = \sqrt{2}v_a t, \\
d_{ab} &= v_{ab}t = \sqrt{v_a^2 + v_b^2}\,t,
\end{aligned}
$$

where v_{aa} and v_{ab} are the relative velocity of the molecule in gas a relative to gas a and b respectively.

In formula 2.12 also, σ_{aa} and σ_{ab} are the collisional cross section of the molecule in gas a with gas a and b respectively which, following the same approach outlined in the previous section, can be written as:

$$\sigma_{aa} = \pi d_a^2, \tag{2.13}$$

$$\sigma_{ab} = \pi \left(\frac{d_a + d_b}{2} \right)^2 . \tag{2.14}$$

It is almost certain that the correct expression for σ_{ab} would contain an interaction contribution, which we are ignoring in order to give a first order approximation of the mean free path. In our case (caesium diffusing in nitrogen) we find that the value of σ_{ab} predicted by equation 2.14 is ≈ 0.64 times the experimental value found in [57]; for this reason we will use the theoretical expression of σ_{ab} in the equation. Putting everything together we can extend formula 2.11 to obtain the mean free path of molecule in gas a in both gasses:

$$l = \left(\sqrt{2}\pi d_a^2 n_a + \sqrt{1 + \frac{m_a}{m_b}}\,\pi \left(\frac{d_a + d_b}{2} \right)^2 n_b \right)^{-1},$$

where we have used:

$$\frac{v_b^2}{v_a^2} = \frac{m_a}{m_b},$$

which comes from equation 2.8.

2.4.3 Numerical Conclusions

We applied the conclusions outlined in the previous sections in 3 cases: caesium vapour alone, nitrogen gas alone and caesium vapour in nitrogen gas, assuming that the temperature of the sample and the nitrogen pressure are respectively 110°C and 100 Torr; we also assume that the diameter of a caesium atom and a nitrogen molecule is respectively $d_{\mathrm{Cs}} = 2 \times 265$ pm and $d_{N_2} = 370$ pm [58]. The results are expressed in the following table:

	Cs	N_2	Cs in N_2	unit
Pressure	0.001	100	0.001	Torr
Thermal Velocity	247	538	247	mm/ms
Free-Path	$3\cdot 10^4$	6.2	0.5	μm
Time of Flight	$1.2\cdot 10^5$	11.5	2	ns
Diffusion C.	$2.5 \cdot 10^3$	1.11	0.04	mm^2/ms
Time for 1 mm	$2 \cdot 10^{-4}$	0.5	**12**	ms

The effect of 100 Torr of nitrogen is evident from the last row of the table; the time to diffuse caesium in 1 mm goes from 202 ns, without buffer gas, to ∼12 ms with nitrogen, $\sim 6 \cdot 10^4$ longer. This result clearly demonstrates the utility of using nitrogen as a buffer gas.

The presence of buffer gas reduces the rate of spin de-coherence due to caesium atoms colliding with each other and with the cells walls; at a certain buffer gas pressure the spin de-coherence due to caesium atoms colliding with the buffer gas itself will start to prevail [59]. This implies the existence of a optimum buffer gas pressure at which the overall de-coherence phenomena is minimized.

Chapter 3

Caesium Spectroscopy

We use the spectroscopic properties of the sensor head to measure the amount of caesium and nitrogen in the cell volume and obtain precise information on the azide dissociation process.

The following chapter gives an introduction on the caesium spectroscopy and shows how it applies first in the simpler case of a reference cell filled only with caesium, and then in the sensor head where we extend the analysis to include the effects of the buffer gas. In the chapter we detail also the procedures followed to give a complete spectroscopic analysis of the sensor head.

3.1 Initial Definitions

As a laser radiation passes through a medium (usually in the vapour form), it is absorbed[1] to an extent depending on the medium thickness and the laser-matter interaction level. This is usually modelled defining the **absorbance** A as:

$$A = \alpha L, \tag{3.1}$$

where α is the **absorption coefficient** of the medium, and L the optical path of the laser[2].

Since the absorption is proportional to the medium number density n (i.e. the number of molecules per unit volume of the medium), we can write:

$$\alpha = \sigma n, \tag{3.2}$$

---

[1] More precisely the light is absorbed and then scattered through spontaneous emission.

[2] The absorbance is a dimensionless quantity while the absorption, measuring the absorbance per unit length, is measured in m^{-1}.

where σ is called **cross section** which measures the laser-matter interaction level[3].

Beer-Lamber law The total cross section (and so the total absorption coefficient and absorbance) is not directly observable. What is usually observed is the intensity of the laser at the end of the cell. The relationship between the two quantities can be determined using the so called Beer-Lamber law[4] which describes the intensity of the beam inside the cell:

$$\frac{d}{dx}I(x) = -\alpha I(x). \tag{3.3}$$

If α is independent on the intensity (or is very weakly dependent on it), the equation can be easily integrated and the intensity at the end of the cell, called **transmitted intensity**, is given by:

$$I_T = I_L = I_0 e^{-\alpha L} = I_0 e^{-A},$$

where $I_0 = I(0)$ and $I_L = I(L)$ are respectively the intensity at the beginning and the end of the laser optical path in the medium. It is often useful to use its normalized value, called **transmission**, given by:

$$T_n = \frac{I_L}{I_0} = e^{-A}. \tag{3.4}$$

In the same way one can define the **absorbed intensity** as:

$$I_a = I_0 - I_L = I_0(1 - e^{-A}),$$

and its normalized value called **absorption**[5] given by:

$$A_b = \frac{I_a}{I_0} = 1 - e^{-A}.$$

From this equation it follows that, if the absorbance is very low, it is practically equal to the absorption: $A_b \approx A$ and the corresponding transmission in this case is $T_n \approx 1 - A$.

---

[3] In laser physics, transition cross sections, usually dependent on the laser frequency, are used to quantify the likelihood of optically induced transition events, e.g. of absorption or stimulated emission. Typically, such transitions involve resonances, which can lead to strongly peaked cross-section spectra.

[4] We will provide a theoretical demonstration of the Beer-Lamber law in chapter 7.

[5] The absorption A_b has not to be confused with the absorption coefficient α.

3.2 Caesium D Line

We are exciting the outer most electron of the caesium structure, from a state of orbital angular momentum $L = 0$ to a state of orbital angular momentum $L = 1$ (D line).

Fine Structure The coupling between the orbital angular momentum $\vec{L}$ with the spin $\vec{S}$ of the electron determines the fine structure doublet [7]. The total electron angular momentum is then given by $\vec{J} = \vec{L} + \vec{S}$ and the corresponding quantum number J must lie in the range:

$$|L - S| \leq J \leq L + S.$$

For the ground state, where $L = 0$ and $S = 1/2$, the only allowed value of J is 1/2; for the excited state, where $L = 1$, there are two possible values of J, 1/2 and 3/2. The energy of any particular level is shifted according to the value of J, so that the D line is split into two components, the D_1 line ($6^2S_{1/2} \rightarrow 6^2P_{1/2}$) and the D_2 line ($6^2S_{1/2} \rightarrow 6^2P_{3/2}$)[6].

HyperFine Structure The hyperfine structure is the result of the coupling of the total angular momentum J with the nuclear angular momentum I [7]. The interaction is similar to that of two magnets, that of the nucleus and that of the electron; based on whether the nuclear and electron spins are parallel or anti-parallel, the interaction gives rise to two very closely spaced electronic energy levels[7].
The total atomic angular momentum F is then given by $F = J + I$. As before, the magnitude of F can take the values:

$$|J - I| \leq F \leq J + I.$$

For the caesium ground state, $J = 1/2$ and $I = 7/2$, so $F = 3$ or $F = 4$.
For the D_1 excited state ($6^2P_{1/2}$) as well, F is either 3 or 4, while for the D_2 line ($6^2P_{3/2}$), F can take any of the values 2, 3, 4, or 5, and the atomic

---

[6] The meaning of the energy level labels is as follows: the first number is the principal quantum number of the outer electron, the superscript is $2S+1$, the letter refers to L (i.e., $S \leftrightarrow L = 0$, $P \leftrightarrow L = 1$), and the subscript gives the value of the total electron angular momentum J.

[7] It is this pair of precise and closely spaced energy levels that makes possible the caesium clock mechanism. The splitting is tiny, about 10^{-5} the ionization energy and even 10^{-3} smaller then the thermal kinetic energy of the atom. But the exceptional precision of that tiny energy splitting allows to measure time with a precision of 1 part in 10^{17} (equivalent to 1 second in 1.8 billion years) [60].

energy levels are shifted according to the value of F.
We use the D_1 line cause it has a simpler hyperfine structure: only 4 levels for the D_1 versus 6 levels for the D_2 line.

3.2.1 D_1 Transitions

The hyperfine atomic structure of the caesium D_1 line is shown in figure 3.1. The 4 allowed transitions, labelled using the ground to excited total angular momentum ($F_g \to F_e$) are [7]:

i	$F_g \to F_e$	ν	Frequency (GHz)
1	$4 \to 3$	ν_1	0
2	$4 \to 4$	ν_2	1.167 680
3	$3 \to 3$	ν_3	9.192 631 770
4	$3 \to 4$	$\nu_4 = \nu_3 + \nu_2$	10.36 031 177

The transitions are ordered from lower to higher energy using the transition number i going from 1 to 4. The corresponding frequencies are shown.

3.2.2 D_1 Cross Sections

A laser, tuned close to the caesium D_1 line, when passing trough a cell filled with caesium vapour alone, stimulates in general all the four transitions in different measure. Formally the total absorption coefficient α is the sum of different contributions α_i corresponding to the 4 transitions of the D_1 line. We can then write:

$$\alpha = \sum_i^4 \alpha_i$$

The absorption coefficient can be obtained from the imaginary part of the (dimensionless) susceptibility χ as [32]:

$$\alpha_i = k\mathrm{Im}(\chi_i), \tag{3.5}$$

where $k = 2\pi/\lambda$ is the laser wave number and λ the laser wavelength. It can be shown that the imaginary part of the susceptibility χ_i is [32]:

$$\mathrm{Im}(\chi_i) = \frac{S_i}{2(2I+1)} \frac{n}{\hbar\epsilon_0} f_i(\nu), \tag{3.6}$$

where $\hbar$ is the reduced Planck's constant, ϵ_0 is the vacuum permittivity, I the caesium nuclear spin (7/2), $f_i(\nu)$ is the line-shape of the i-th transition[8]

---

[8] The dimension of $f_i(\nu)$ is second while $\frac{d_0^2 n}{\hbar\epsilon_0}$ has dimensions of Hz so that $\mathrm{Im}(\chi_i)$ is dimensionless.

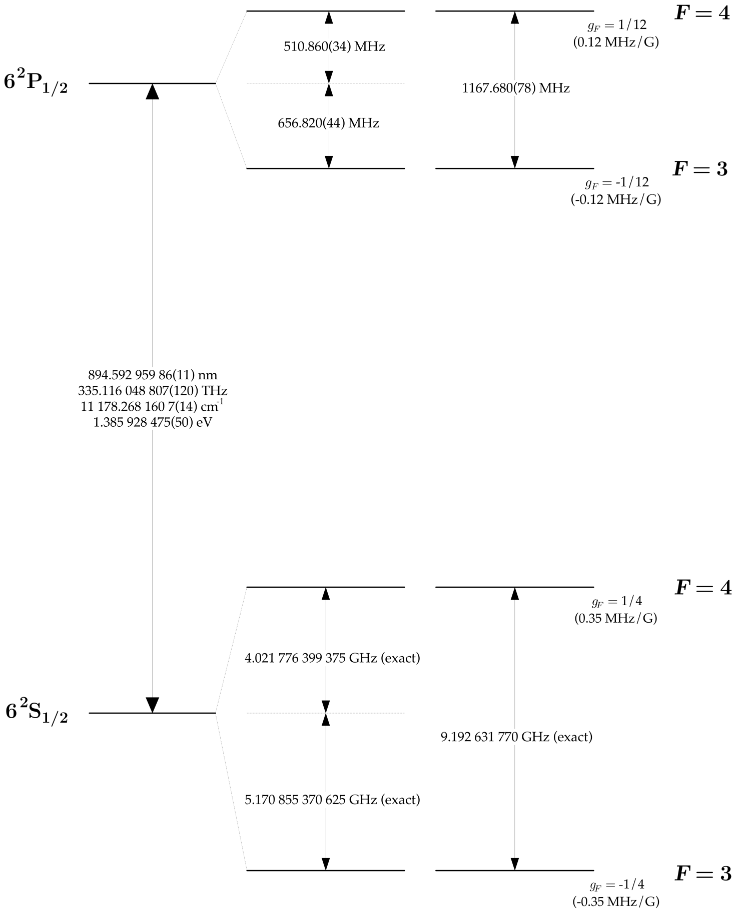

Figure 3.1: Caesium D_1 hyperfine structure [7].

and S_i is the strength of the i-th transition $F_g \to F_e$ defined as:

$$S_i = \sum_{m_g} |\langle F_g m_g | d_q | F_e m_e \rangle|^2$$

where $|\langle F_g m_g | d_q | F_e m_e \rangle|^2$ represents the strength of the transition $|F_g m_g\rangle \to |F_e m_e\rangle$, d_q is the component q of the dipole operator $\vec{d}$ in the spherical basis (see appendix C.3) and q represents the light input polarization (linear for $q = 0$ and circular for $q = \pm 1$). The sum is done only over m_g because for fixed polarization $m_e = m_g + q$, however in the next section we show that the line strengths S_i are independent on q.

Transitions Strength Using the Wigner-Eckart theorem [7, 61] we can write:

$$\langle F_g m_g | d_q | F_e m_e \rangle = \langle F_g | \vec{d} | F_e \rangle \, (-1)^{F_e + m_g - 1} \begin{pmatrix} F_e & 1 & F_g \\ m_g & -q & -m_g \end{pmatrix}. \tag{3.7}$$

This expression can be further expanded using the relationship between $\langle F_g | \vec{d} | F_e \rangle$ and $\langle J_g | \vec{d} | J_e \rangle$ [62]:

$$\langle F_g | \vec{d} | F_e \rangle = \langle J_g | \vec{d} | J_e \rangle \, (-1)^{F_e + J_g + I + 1} \sqrt{(2F_e + 1)(2J_g + 1)} \begin{Bmatrix} J_g & J_e & 1 \\ F_e & F_g & I \end{Bmatrix}. \tag{3.8}$$

and the analogous relationship between $\langle J_g | \vec{d} | J_e \rangle$ and $\langle L_g | \vec{d} | L_e \rangle$ [61]:

$$\langle J_g | \vec{d} | J_e \rangle = \langle L_g | \vec{d} | L_e \rangle \, (-1)^{J_e + L_g + S + 1} \sqrt{(2J_e + 1)(2L_g + 1)} \begin{Bmatrix} L_g & L_e & 1 \\ J_e & J_g & S \end{Bmatrix}. \tag{3.9}$$

The terms in between the rounded and curled brackets are known as the Wigner 3j and 6j symbols respectively. In our case (where $L_g = 0, L_e = 1, J_g = J_e = 1/2, S = 1/2$), 3.9 results in:

$$\langle J_g | \vec{d} | J_e \rangle = \frac{d_0}{\sqrt{3}},$$

where the matrix element of the dipole operator $\vec{d}$ is defined as:

$$d_0 := \langle L_g | \vec{d} | L_e \rangle \, . \tag{3.10}$$

Using equations 3.7, 3.8 and 3.9, it is possible to factor the element d_0 out of the transition strength S_i, and write:

$$S_i = \sum_{m_g} |\langle F_g m_g | d_q | F_e m_e \rangle|^2 = s_i |\langle L_g | \vec{d} | L_e \rangle|^2 = s_i d_0^2, \tag{3.11}$$

where s_i depends on F_g and F_e; one usually refers to s_i as the **line strength** of the i-the transition $F_g \to F_e$. The values of s_i, corresponding to the 4 transitions of the caesium D_1 line are independent on q, and are reported in the following table:

i	$F_g \to F_e$	$s(F_g, F_e)$
1	4→3	7/12
2	4→4	5/12
3	3→3	7/36
4	3→4	7/12

Alternative Line Strengths Note that the sum over q of the transition components $\langle F_g m_g | d_q | F_e m_e = m_g + q \rangle$ (labelled $\bar{s}(F_g, F_e)$) is independent on the the particular magnetic sub-level m_g chosen; in fact:

$$\bar{s}(F_g, F_e) = \sum_q |\langle F_g m_g | d_q | F_e m_e = m_g + q \rangle|^2 = (2F_e{+}1)(2J_g{+}1) \begin{Bmatrix} J_g & J_e & 1 \\ F_e & F_g & I \end{Bmatrix}^2 .$$

that's why some sources (see for example [7, 57]) use this expression as an alternative definition for the line strengths. Furthermore this numbers obey the following sum rule [7]:

$$\sum_{F_e} \bar{s}(F_g, F_e) = 1.$$

Even tough we won't use this definition, we report the alternative line strengths $\bar{s}(F_g, F_e)$ in the following table:

i	$F_g \to F_e$	$\bar{s}(F_g, F_e)$
1	4→3	7/12
2	4→4	5/12
3	3→3	1/4
4	3→4	3/4

Decay rate We can find a more convenient expression for d_0 using the expression for the lifetime of the transition [63]:

$$\Gamma = \frac{k^3}{3\pi\epsilon_0\hbar} \frac{2J_g + 1}{2J_e + 1} |\langle J_g | \vec{d} | J_e \rangle|^2, \tag{3.12}$$

the matrix element $\langle J_g | \vec{d} | J_e \rangle$ is connected to the dipole element d_0 by equation 3.9; so one can write:

$$\Gamma = \frac{k^3 d_0^2}{9\pi\epsilon_0\hbar}.$$

Cross Section Using equation 3.5 and 3.6 with the results in equation 3.11, the cross section of the i-th transition can be written as:

$$\sigma_i = \frac{\alpha_i}{n} = \frac{k\mathrm{Im}(\chi_i)}{n} = \frac{s_i}{2(2I+1)}\frac{d_0^2 k}{\hbar\epsilon_0} f_i(\nu). \tag{3.13}$$

We can use the expression previously found for the transition lifetime (equation 3.12) to write a more convenient expression for the cross section of the i-th transition:

$$\sigma_i = s_i \sigma_0 \Gamma f_i(\nu).$$

where we have defined:

$$\sigma_0 = \frac{9\pi}{2(2I+1)k^2} = \frac{9\pi}{16k^2},$$

As for the absorption coefficient, using equation 3.2, we can express the total cross section σ as the sum of different contributions σ_i coming from the 4 transitions of the D_1 line:

$$\sigma = \sum_i^4 \sigma_i = \sigma_0 \Gamma \sum_i^4 s_i f_i(\nu), \tag{3.14}$$

The formula can be extended to the absorption coefficient as:

$$\alpha = \alpha_0 \Gamma \sum_i^4 s_i f_i(\nu),$$

defining $\alpha_0 = n\sigma_0$; in the same way the absorbance can be written as:

$$A = A_0 \Gamma \sum_i^4 s_i f_i(\nu), \tag{3.15}$$

where we have defined $A_0 = \alpha_0 L = n\sigma_0 L$ which is a measure of the total absorbance integrated over all frequencies, since each function $f_i(\nu)$ is already normalized. The value of A_0 is highly temperature dependent, cause of the strong dependency of the vapour pressure n on the temperature (see section 2.3.1).

Line Shape The line shape f_i of each transition is described by a Voigt profile [32], which is a convolution of a Gaussian profile of width σ_g with a Lorentzian profile of width σ_l (see appendix A.1). Formally we can write:

$$f_i(\nu) = \mathrm{Voigt}(\nu, \nu_i, \sigma_g, \sigma_l),$$

where ν_i is the centre frequency of each transition and σ_g and σ_l are respectively its Gaussian and Lorentzian width[9].
If the medium is composed of caesium vapour alone, the width σ_l is simply given by the **natural decay rate** $\gamma = \Gamma/2\pi$ of the D_1 transition [7].
The Gaussian width σ_g is due to thermal Doppler broadening and given by [64]:

$$\sigma_g = \nu_{D_1}\sqrt{\frac{k_b T}{m_{\mathrm{Cs}} c^2}}, \tag{3.16}$$

where T is the temperature of the caesium vapour, k_b is the Boltzmann constant, m_{Cs} is the mass of the caesium atom, c is the speed of light and ν_{D_1} is the D_1 central frequency. Each of the four hyperfine lines share the same Doppler and Lorentzian width σ_g and σ_l.

Caesium Spectrum An example of the corresponding transmission spectrum of pure caesium at room temperature can be seen in figure 3.2, where the four transitions have been outlined. The function used to model the transmission is obtained from equations 3.4 and 3.15:

$$I_T = I_0 \exp\left(-A_0 \Gamma \sum_i^4 s_i f_i(\nu)\right) \tag{3.17}$$

3.3 Buffer Gas Effects

If the cell contains caesium vapour with a buffer gas[10] the absorbance shape 3.15 is modified by two phenomena:

- **Shift**: the centre frequencies ν_i of the four lines are shifted by the same amount s proportional to the pressure p of the buffer gas [64, 65, 66, 67, 68, 69]:

  $$s = \delta p, \tag{3.18}$$

  where δ is a constant dependent on the particular buffer gas and slightly dependent on the temperature. For nitrogen gas this dependence is [66, 68]:

  $$\delta(T) = \delta(T_r)\left(\frac{T_r}{T}\right)^{0.82}, \tag{3.19}$$

---

[9] Note that, as explained in the appendix, while the Lorentzian width is the half width at half maximum, the Doppler one is the standard half width at $1/\sqrt{e}$ maximum.

[10] Possible buffer gasses, other then nitrogen (N_2), are hydrogen (H_2), Hydrogen deuteride (HD) and Methane (CH_4).

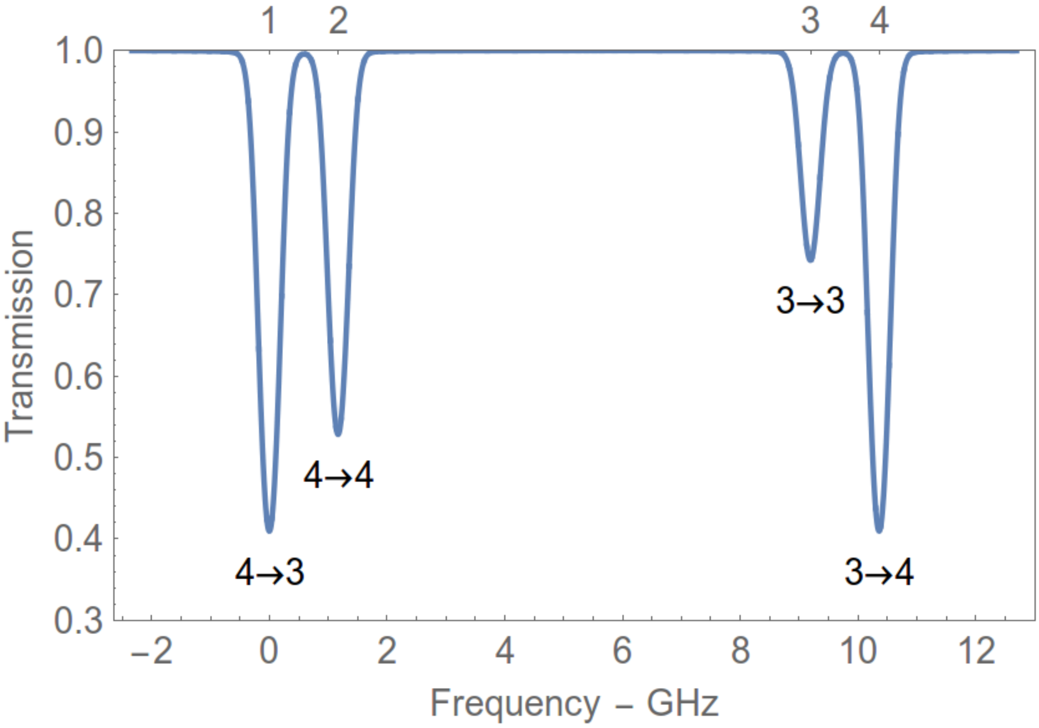

Figure 3.2: Example of the transmission spectrum for the caesium D_1 line. The data is obtained from the model in equation 3.17, assuming a temperature of 25°C.

γ_p(MHz/Torr)	T_r(K)	Source	γ_p at 318 K
15.82± 0.05	318	[64]	15.23
16.36± 0.02	323	[64]	15.87
15.66± 0.08	333	[64]	15.43
19.51± 0.06	294	[70]	18.06
30.93± 295	5.71	[71]	28.69
14.73± 294	0.69	[72]	15.73
δ(MHz/Torr)	T_r(K)	Source	δ at 318 K
-7.69± 0.01	318	[64]	-7.22
-7.71± 0.01	323	[64]	-7.34
-7.41± 0.01	333	[64]	-7.23
-8.23± 0.02	294	[70]	-7.25
-7.38± 0.11	295	[71]	-6.52
-8.90± 0.69	393	[72]	-9.95

Table 3.1: Measured broadening and shift rates for the D_1 transition of caesium due to nitrogen gas. The last column shows the reference values at 318 K.

where T_r is a reference temperature.

- **Broadening**: the Gaussian width is not affected by the presence of the gas while the Lorentzian broadening σ_l is a linear function of the buffer gas pressure [64, 65, 69, 70]:

  $$\sigma_l(p) = \gamma_p p + \Gamma, \tag{3.20}$$

  where γ_p is a constant dependent on the particular buffer gas. This phenomena is known as **pressure broadening** and it is also shown to be dependent on the temperature [64]; in fact, for nitrogen gas, the coefficient γ_p can be written as:

  $$\gamma_p(T) = \gamma_p(T_r)\left(\frac{T_r}{T}\right)^{\frac{1}{2}}. \tag{3.21}$$

Nitrogen As already mentioned, nitrogen is the buffer gas in our sensor head. Table 3.1 shows the values[11] for both $\gamma_p(T_r)$ and $\delta(T_r)$ for nitrogen at the temperature of measurement. Reference values are extracted at a common temperature (318 K) using respectively equations 3.19 and 3.21. The weighted averaged value of γ_p at 100°C is 15.31 MHz/Torr. The weighted

---

[11] The table shows the pressure broadening as the full width at half maximum (FWHM).

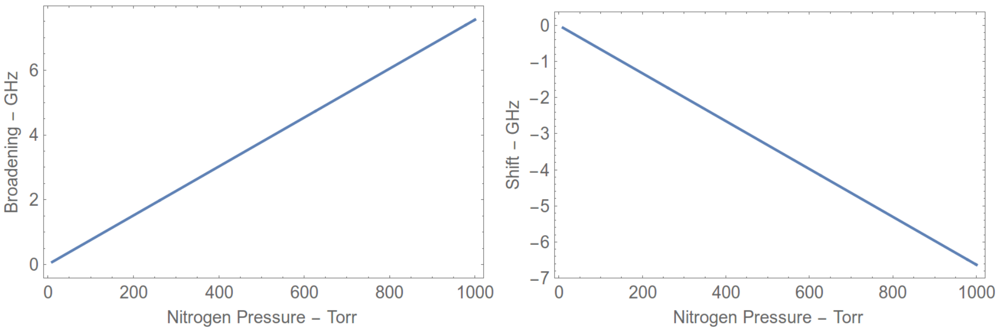

Figure 3.3: Expected broadening (on the left) and shift (on the right) as a function of nitrogen pressure for fixed temperature (100°C).

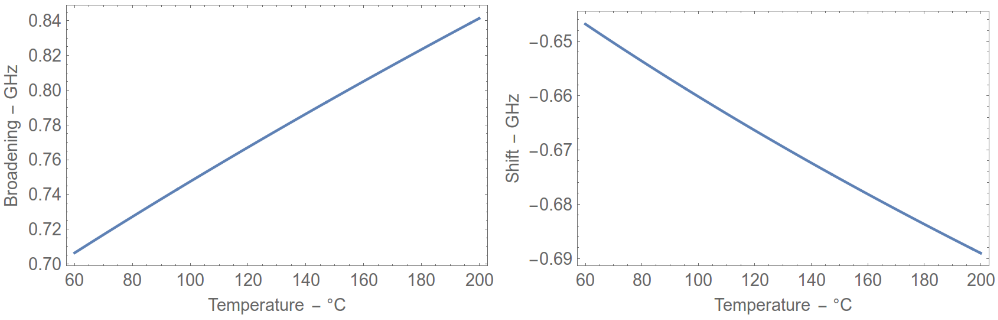

Figure 3.4: Expected broadening (on the left) and shift (on the right) of the D_1 caesium spectrum as a function of temperature for fixed nitrogen pressure (100 Torr).

averaged value of δ at the same temperature is -6.78 MHz/Torr.

It is worth noticing that the ratio between the broadening and the shift is very slightly dependent on temperature and can be viewed as a fingerprint of the buffer gas. For nitrogen gas this value is -2.3 (around 110°C).

The plots in figure 3.3 show the expected broadening and shift of the D_1 caesium spectrum as a function of the nitrogen pressure, while the plots in figure 3.4 show the expected broadening and shift as a function of temperature for constant nitrogen pressure (100 Torr)[12]. As it can be seen from the plots, the broadening and (absolute) shift both increase with nitrogen pressure and temperature.

---

[12] When considering the temperature dependency of the broadening and the shift, one has to take into account that the pressure grows linearly with the temperature as well (as a consequence of the ideal gas law); so the formula $p/T = k$, where k is a constant, has been included.

Caesium Spectrum with Buffer Gas We modeled the expected spectrum of the sensor head filled with caesium and nitrogen gas using the same model, in equation 3.17, used for a reference cell filled with caesium alone, where the line shapes f_i of the 4 transitions are now described by:

$$f_i(\nu, T, p) = \text{Voigt}(\nu_i - s, \sigma_g(T), \sigma_l(p)), \tag{3.22}$$

where the effect of the shift and the broadening has been included by the factors s and $\sigma_l(p)$ respectively.

Figure 3.5 plots the expected cell transmission at different nitrogen pressures: the shift and broadening of the lines is evident. As it can be seen, when the nitrogen pressure is less than ≈100 Torr the spectrum shows 4 normal peaks slightly shifted and broadened. For higher pressure values the transitions $4 \rightarrow 3$ and $4 \rightarrow 3$, as well as the transitions $3 \rightarrow 3$ and $3 \rightarrow 3$ cannot be resolved due to pressure broadening; at this point the spectrum shows 2 peaks. Above ≈800 Torr no transition can be resolved and the spectrum shows a very broadened and shifted single peak.

3.4 Sensor Head Spectroscopy

We present here the set-up, the software and the procedure used to obtain a complete spectroscopic characterization of the sensor head.

3.4.1 Set-up

The experimental set-up implemented to obtain a full spectroscopic characterization of the sensor head is described in figure 3.6. As it can be seen the linearly polarized laser beam is directed trough the sensor head, to detect its spectroscopic properties. The beam intensity is lower than the saturation intensity of caesium (≈ 2.5 mW/cm^2 $= 25$ μW/mm^2 [7]) to avoid power broadening. The beam is divided several times using a 90-10 fiber coupler and 2 un-polarizing beam splitters.

As it will be fully described in section 3.4.2 part of the beam is used to compensate the laser background; a second beam is directed though a Fabry-Perot etalon to compensate the non-linearity in the laser frequency scan; a third beam, directed through a 10 cm long cell, containing caesium vapour alone, is used as a spectroscopic reference.

3.4.2 Reference Signals

We used a Toptica diode laser to investigate the spectroscopic properties of the sensor head. As we explained in section 3.3, the buffer gas in the

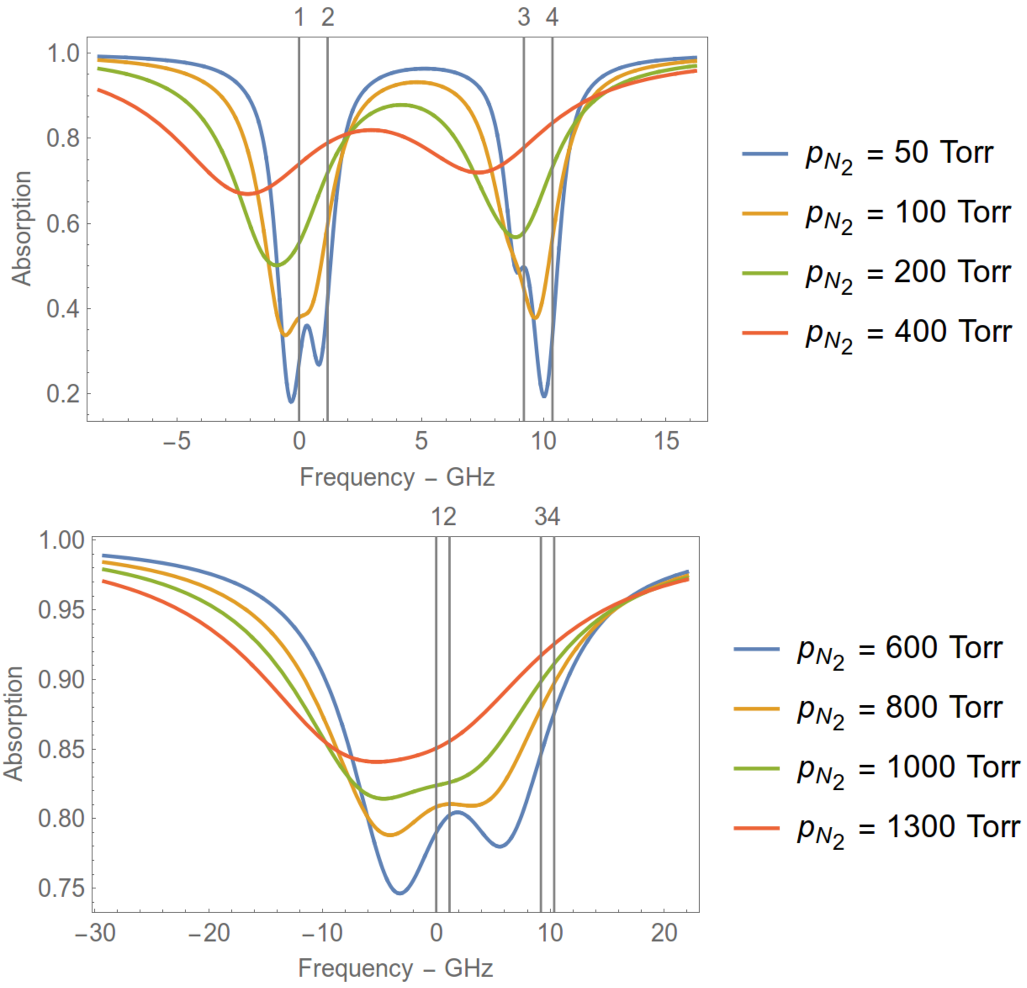

Figure 3.5: Example of the theoretical predicted caesium absorption spectrum broadened by the presence of nitrogen gas at different pressures and fixed temperature (100°C). The four vertical lines corresponds to the 4 transitions of the caesium D_1 line. Note that the scale in the lower plot is expanded. The shifts and broadening parameters are determined empirically from [64, 70, 71, 72]

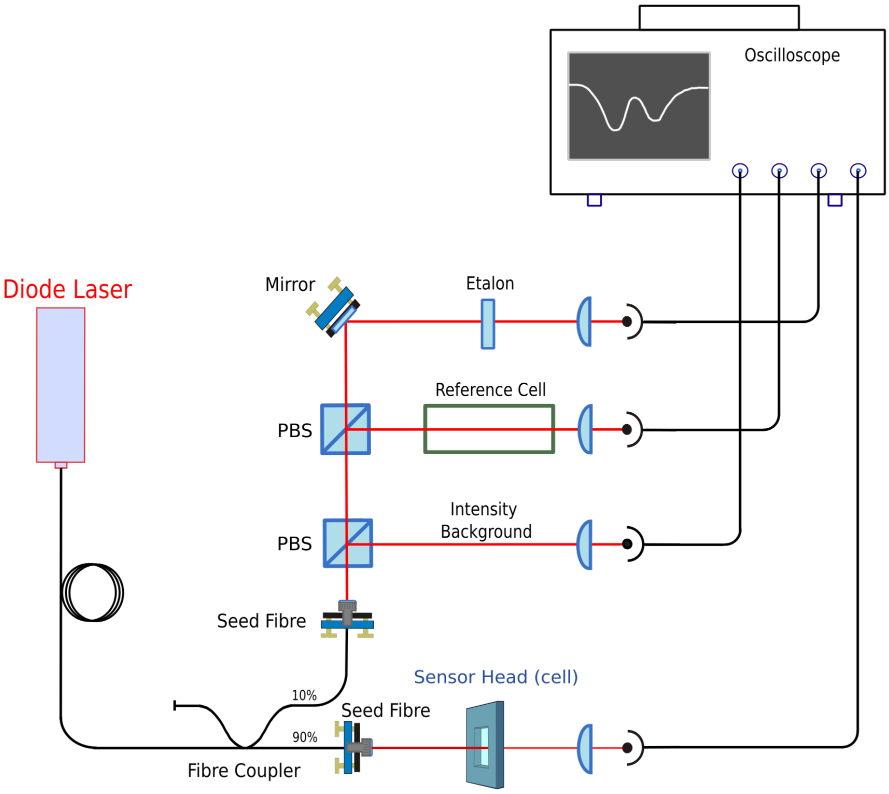

Figure 3.6: Experimental set-up implemented to study the spectroscopy of the sensor head.

cell substantially changes the detected spectrum compared to a cell with no buffer gas. To quantify this perturbation we use a reference system (called *black box*) which provides 3 signals:

- **intensity normalization**: the laser light frequency is scanned with an amplitude of about 30 GHz (at a rate of 13 Hz), around the central frequency ν_{D_1} of the caesium D_1 line. The scanning process produces an undesired and almost linear background, which affects all other signals deteced; by capturing a fraction of the input laser light the signal are re-normalised with a proper signal division.
- **Etalon Fringes**: the scanning process is non-linear in frequency; we use the signal coming from a Fabry Perot (etalon) system to map and compensate this non-linearity (see section 3.4.2).
- **Caesium D_1 lines**: the transmitted signal from a cell filled with caesium alone provides the reference caesium D_1 spectrum.

Etalon Fringes

A Fabry Perot etalon consists of a transparent plate with two reflecting surfaces. The transmitted signal is caused by the interference between the multiple reflections of light between the two surfaces. Constructive interference occurs if the transmitted beams are in phase, which corresponds to a high-transmission peaks; destructive interference occurs if the beams are out-of-phase, which corresponds to a transmission minimum. Whether the beams are in phase or not depends on the wavelength ($\lambda = c/\nu$) of the light (in vacuum), the angle the light travels through the etalon (θ), the thickness of the etalon (l) and the refractive index n of the material between the reflecting surfaces [73]. The phase difference δ between each successive transmitted pair of beams is given by:

$$\delta = \frac{2\pi}{\lambda} 2nl\cos(\theta). \tag{3.23}$$

The etalon free spectral range (FSR) $\mathscr{F}$ is defined as the spacing, in optical frequency, between two successive reflected beams and it can be re-written as:

$$\mathscr{F} = \frac{c}{2nl\cos(\theta)},$$

and be used to re-write equation 3.23 as:

$$\delta = \frac{2\pi}{\mathscr{F}}\nu,$$

where $\nu = \frac{c}{\lambda}$ is the laser frequency. If both surfaces have a reflectance R, the transmission (defined in section 3.1) of the etalon is given by:

$$T_n = \frac{1}{1 + F\sin^2(\frac{\delta}{2})}, \tag{3.24}$$

where:

$$F = \frac{4R}{(1-R)^2}.$$

The reflection R is connected to the etalon refractive index n by:

$$R = \frac{n-1^2}{n+1}.$$

Since the etalon is made by glass ($n \approx 1.5$), the reflectance index is very small ($R \approx 4\%$), and in this case the transmission function can be approximated to:

$$T_n \simeq 1 - \frac{F}{2}\left(1 - \cos\left(\frac{2\pi}{\mathscr{F}}\nu\right)\right), \tag{3.25}$$

which is a sinusoidal function of the laser frequency ν.

Non-linear Scanning Spectroscopic signals are a sequence of discrete numbers S_i where S represents usually a transmitted intensity, and i the discrete sequential numerical label identifying the data point. Since the laser is scanned, i is a measure of the laser frequency ν; in the simplest case the relationship between the two is just linear, and given by:

$$\nu_i = c_1(i - i_0),$$

where c_1 is the proportionality factor and i_0 is the measure point in which the frequency is set conventionally[13] to 0.

In reality the laser scanning process is non-linear; in other words the previous formula has so been extended to include higher order components. In most cases a second order approximation is sufficient. We can then write:

$$\nu_i = c_1(i - i_0) + c_2(i - i_0)^2, \tag{3.26}$$

where c_2 represents the second order factor.

The non-linearity can be mapped and compensated using the transmitted signal from the etalon (like the one in equation 3.25). Figure 3.7 shows the observed etalon signal and its fitted sinusoid using both linear and non linear functions. As it is evident, a non-linear mapping of the frequency is necessary.

---

[13] This usually corresponds to the first absorption peak of the caesium reference spectrum.

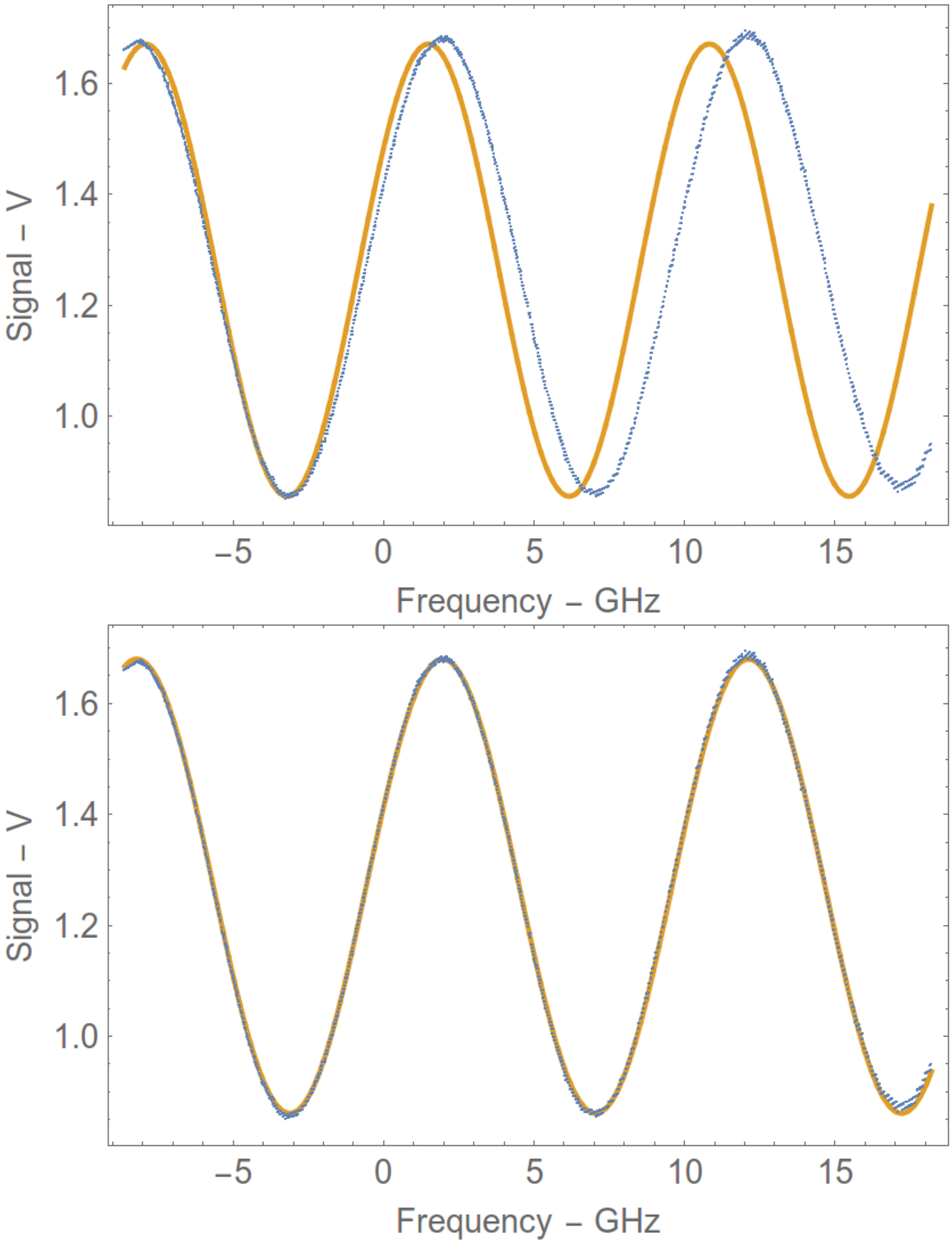

Figure 3.7: Etalon signal fitted both with a linear (at the left) and non-linear (at the right) frequency map. The non-linear model fits the data much more accurately. The etalon FSR is ≈ 10.2 GHz.

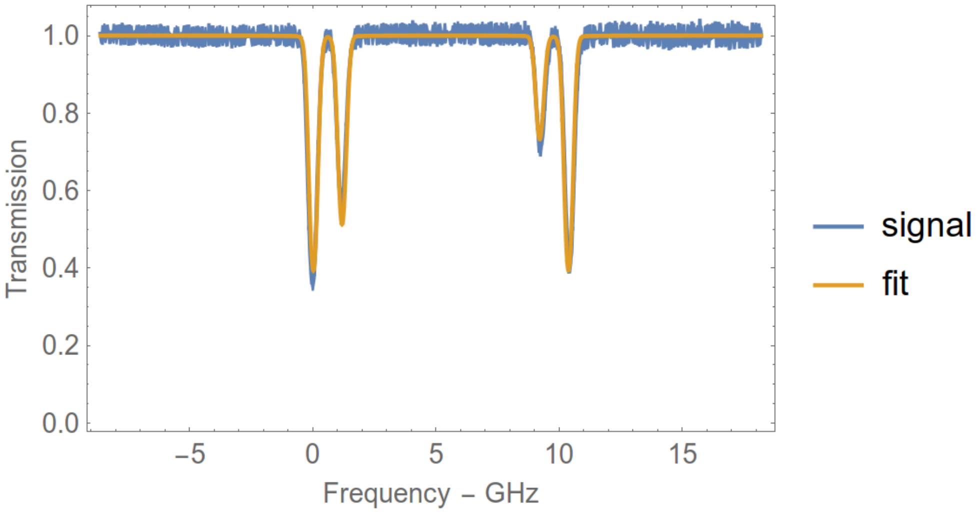

Figure 3.8: The data shows the reference D_1 line spectrum (blue) and the corresponding fit (orange). The reference cell contains caesium alone with no buffer gas and so no pressure broadening is observed.

Caesium Reference Spectrum

As said, we use a reference cell filled with caesium alone to provide a reference spectrum for the D_1 line. Figure 3.8 shows a real example of a reference D_1 line spectrum signal. We fit the data expanding the model in equation 3.17 to:

$$I_T = I_0(\nu)\exp\left(-A_0\Gamma\sum_i^4 s_i f_i(\nu)\right) + p, \tag{3.27}$$

where we have assumed a non-constant laser background, which is due to etalon fringes caused by the opposite glass aperture of reference cell, and an offset, called *pedestal*, due to non-resonant frequency components in the laser spectrum. As said each function f_i is given by a Voigt profile; as is it fully explained in appendix A.1, this function is computationally very demanding, that's why a numerical approximation has been used for fitting purposes.

3.4.3 Sensor Head Signal

Figure 3.9 shows an example of the spectroscopic signal recorded from the sensor head. We fit the data using the model in equation 3.17, with the Voigt functions in equation 3.22; the process allows to provide an estimate of the shift and broadening of the 4 lines, which is combined to give an estimate of the nitrogen pressure inside the sensor head ($\approx$ 174 Torr in this case).

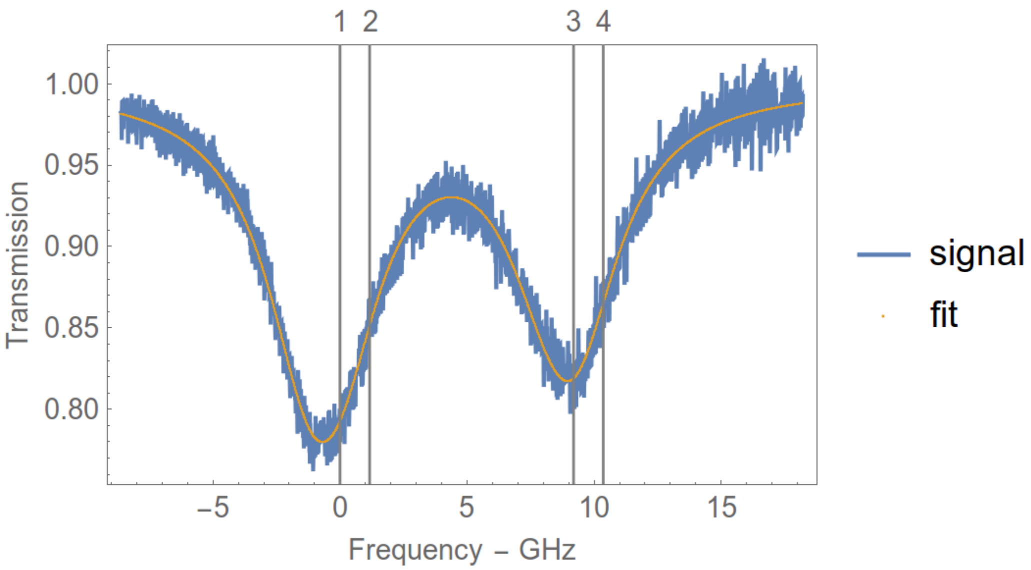

Figure 3.9: Spectroscopic signal from the sensor head cell (blue) and corresponding fit (orange). The measured nitrogen gas pressure, from broadening and shift, is ≈ 174 Torr.

3.4.4 Spectrum Analysis Software

We have created a data analysis tool using Wolfram Mathematica® to rapidly extract the main spectroscopic properties of the sensor head directly from our computerized oscilloscope. The software interface is shown in figure 3.10. Its main sections are here described:

- **mask**: these button opens an input windows in which the main properties of the sensor head can be stored; these range from cell id, experimental parameters, azide content, total UV exposure time and cell side lengths. From the azide content and cell volume the program extracts the expected nitrogen pressure, using equation 2.6, useful to obtain an initial guess of the shift and broadening for the fitting process. In this context, the user can chose the polynomial order to use to model the sensor head signal background.

- With no laser light, the detectors still record small constant offsets that need to be subtracted from the real spectroscopic signals. The **offset** section is used to locate these files.

- The section **simulate** allows for a full data simulation, which has been

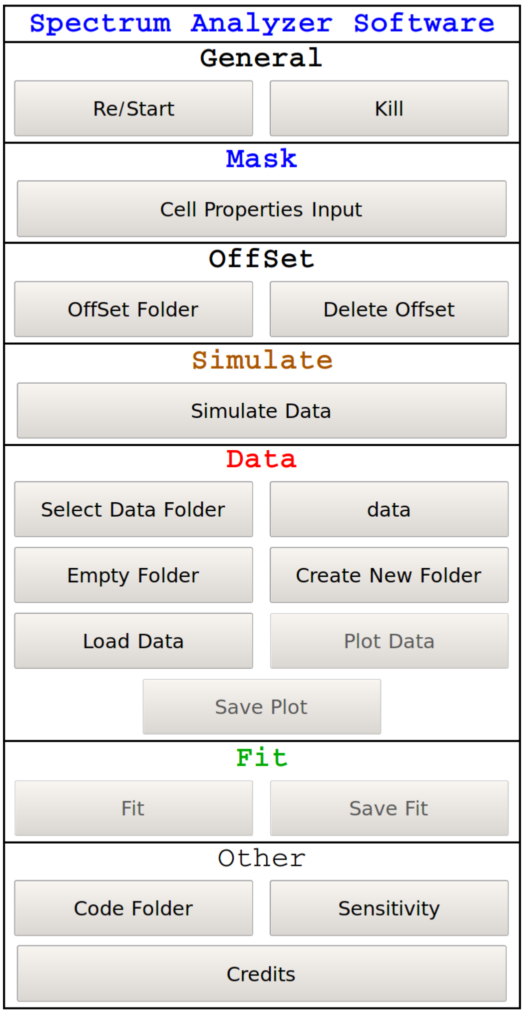

Figure 3.10: *Spectrum Analysis Software* interface.

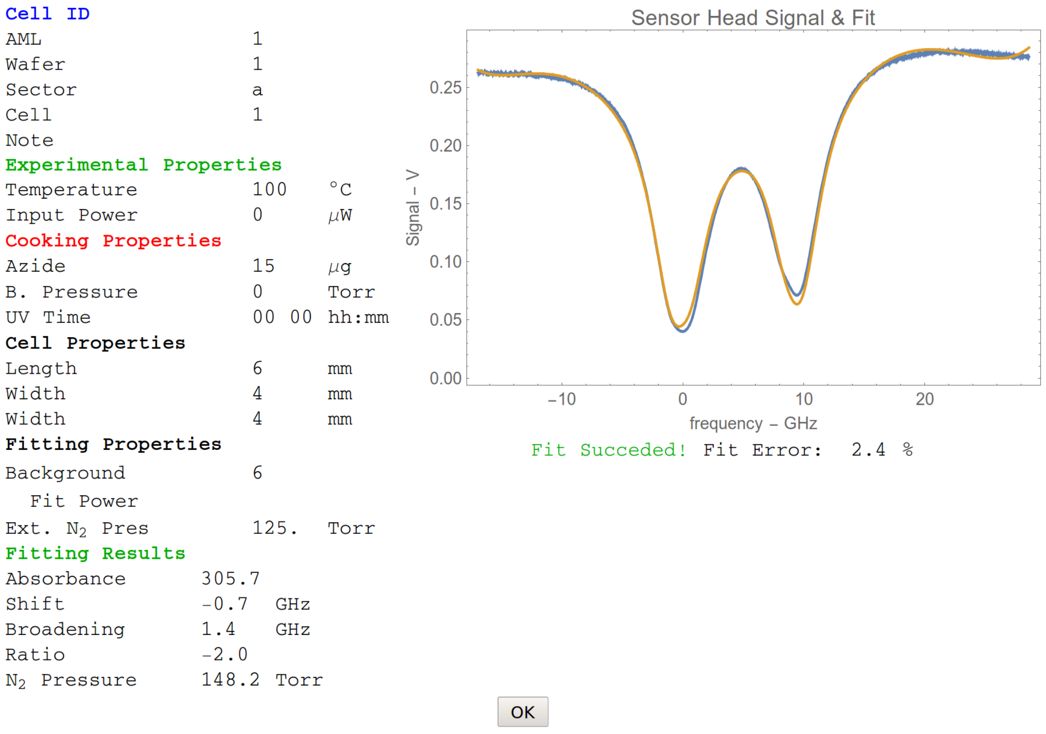

```
Cell ID
AML                    1
Wafer                  1
Sector                 a
Cell                   1
Note
Experimental Properties
Temperature            100    °C
Input Power            0      μW
Cooking Properties
Azide                  15     μg
B. Pressure            0      Torr
UV Time                00 00  hh:mm
Cell Properties
Length                 6      mm
Width                  4      mm
Width                  4      mm
Fitting Properties
Background             6
  Fit Power
Ext. N2 Pres           125.   Torr
Fitting Results
Absorbance         305.7
Shift              -0.7   GHz
Broadening         1.4    GHz
Ratio              -2.0
N2 Pressure        148.2  Torr
```

```
Fit Succeded!  Fit Error:   2.4  %
```

Figure 3.11: An example of the fitting result outputted by the software.

useful to verify the internal consistency and accuracy of the fitting process.

- The section **data** allows to locate the folder containing the real spectroscopic signals and to plot them before fitting.

- Finally the data can be **fitted** using the corresponding button. An example of the result outputted by the program is shown in figure 3.11. The window show the sensor head main parameters and the numerical results obtained from the fit; these are the absorption, broadening and shift, the extracted nitrogen pressure and the broadening to shift ratio. On the right side a plot of the original sensor head signal is shown with the corresponding fit.

As said in section 3.4.2, in order to proper fit the spectroscopic signal from the sensor head we record 3 more signals: the intensity background, the etalon fringes, and a reference caesium spectrum. The algorithm used to manipulate these signals is:

- Data normalization: the intensity background signal is fitted with a third order polynomial and all the other signals are divided by its corresponding fit.
- The 4 peaks of the reference caesium spectrum are extracted and used to give an initial guess of the frequency to data point parametrization (see equation 3.26), which results in an estimate of the parameters i_0, c_0 and c_1.
- The etalon signal is fitted using equation 3.25 together with 3.26 to perfect the estimate of c_1 and c_2.
- The reference caesium signal is fitted using equation 3.17 to ameliorate the estimate of i_0. The Lorentzian broadening is fixed to the natural line-width (γ) while the Gaussian width to the thermal broadening in equation 3.16.
- The sensor head spectrum is fitted using formula 3.17 with the Voigt function in equation 3.22. The fit returns the caesium absorption, and the shift and pressure broadening caused by the nitrogen.
- The nitrogen pressure in the sensor head is obtained combining the measures of the shift and broadening obtained from the fit.

Spectroscopy Automation TI has successfully implemented a robotic system which allows for the automatic characterization of an entire wafer in a relatively short period of time. The system set-up is conceptually identically to the one in figure 3.6 with the addition of a robotic system which sequentially move the wafer at regular steps: in this way the laser automatically intersects each cell in the wafer to detect a proper spectroscopic signal. The data is then sent to a computerized system which, using a software similar to the one in figure 3.10, automatically records the spectroscopic properties of each cell. This system would be especially useful for possible mass production of the sensor heads.

3.5 Spectrum and Temperature

We analysed the properties of the sensor head spectrum as a function of its temperature. Figure 3.12 shows the different spectra taken at different temperatures. From each fit we extracted the absorbance, the broadening and the shift.

Figure 3.13 shows the extracted absorbance A_0 which, as it can be seen, tends

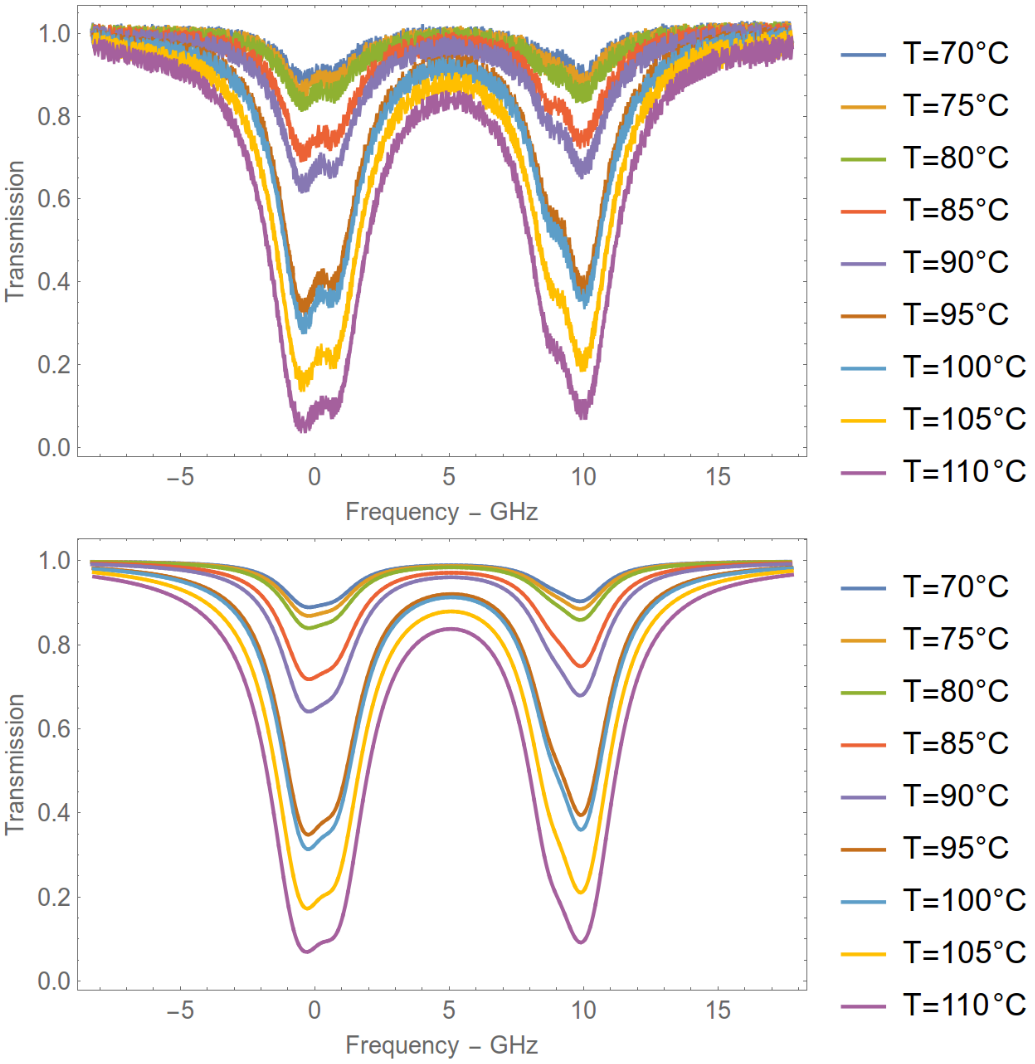

Figure 3.12: Sensor head spectra at different temperatures. The top plots refers to the normalised transmission data at different temperatures, while the lower plots to the their corresponding fits.

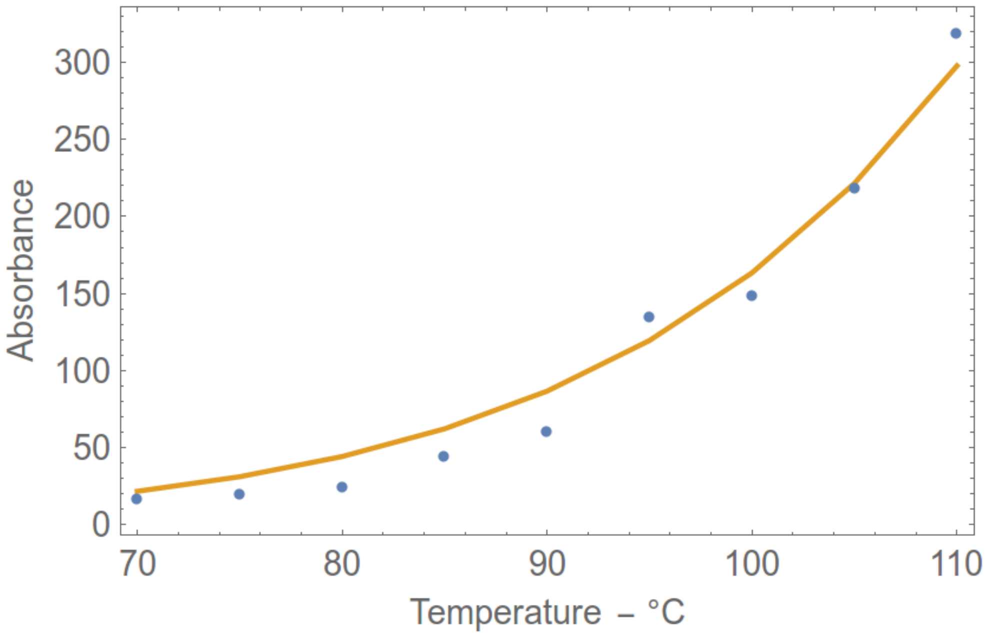

Figure 3.13: The absorption (obtained from the fit of each spectra) plotted against the sensor head temperature. The exponential behaviour has been fitted with equation 3.28.

to increase exponentially with the temperature. As described in section 3.2.2 (see formula 3.15), A_0 has been defined by:

$$A_0(T) = n(T)L\sigma_0, \tag{3.28}$$

where $L = 1$ mm is the depth of the sensor head corresponding to the optical length of the laser. This function is highly dependent on the temperature and has been used for fitting the absorbance curve; as it can be seen from the plot in figure 3.13 the function 3.28 well describes the data.

Figure 3.14 plots the corresponding extracted pressure broadening which, contrary to expectations (see figure 3.4), shows a decreasing behaviour as a function of temperature; this results may be explained by the presence of other buffer gasses in the sensor head, possibly liberated during the UV exposure.

3.6 Spectrum and UV Exposure

We have analysed the azide dissociation process using the spectroscopic data collected at subsequent UV exposure times of the same sensor head cell.

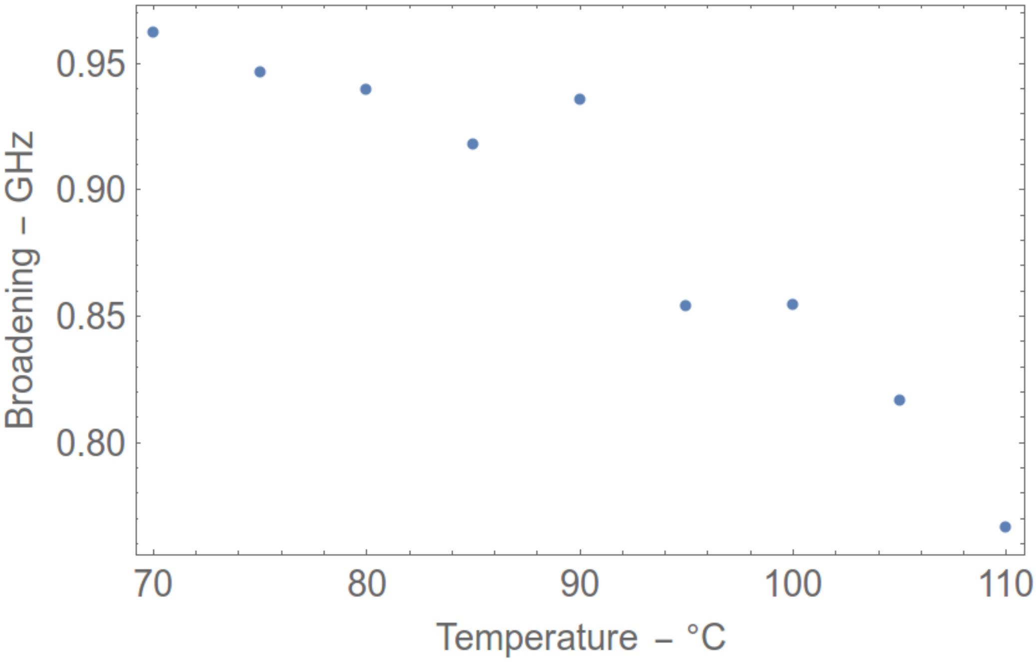

Figure 3.14: The pressure broadening (obtained from the fit of each spectra) plotted against the sensor head temperature. The plot shows a decreasing trend which is not predicted by equation 3.20.

From each spectrum the absorbance and the pressure broadening have been extracted; the first is used to give a relative measure of the caesium pressure, while the latter to extract the nitrogen pressure inside the sensor head.
Figure 3.15 shows the cell spectra taken at subsequent exposure times; the extracted absorbance is plotted in fig 3.16, while the extracted nitrogen pressure (from pressure broadening) is plotted in figure 3.17. As it can be seen, initially (in the first hour) no spectrum is detected because the caesium liberated by the UV exposure process firstly condenses on the cell internal walls; the rapidity of the saturation in the absorbance plot is explained by the very low pressure required to fill the cell volume at a given temperature; the rest of the caesium atoms will condensate on the cells walls as caesium droplets. The nitrogen pressure shows an incomplete saturation behaviour which suggests that the UV dissociation process is still not totally completed after 29 hours; the data can still be described by a saturation curve but with a much bigger time scale. The dissociation process is still not finished after 29 hours or other gasses are liberated interfering with the analysis.

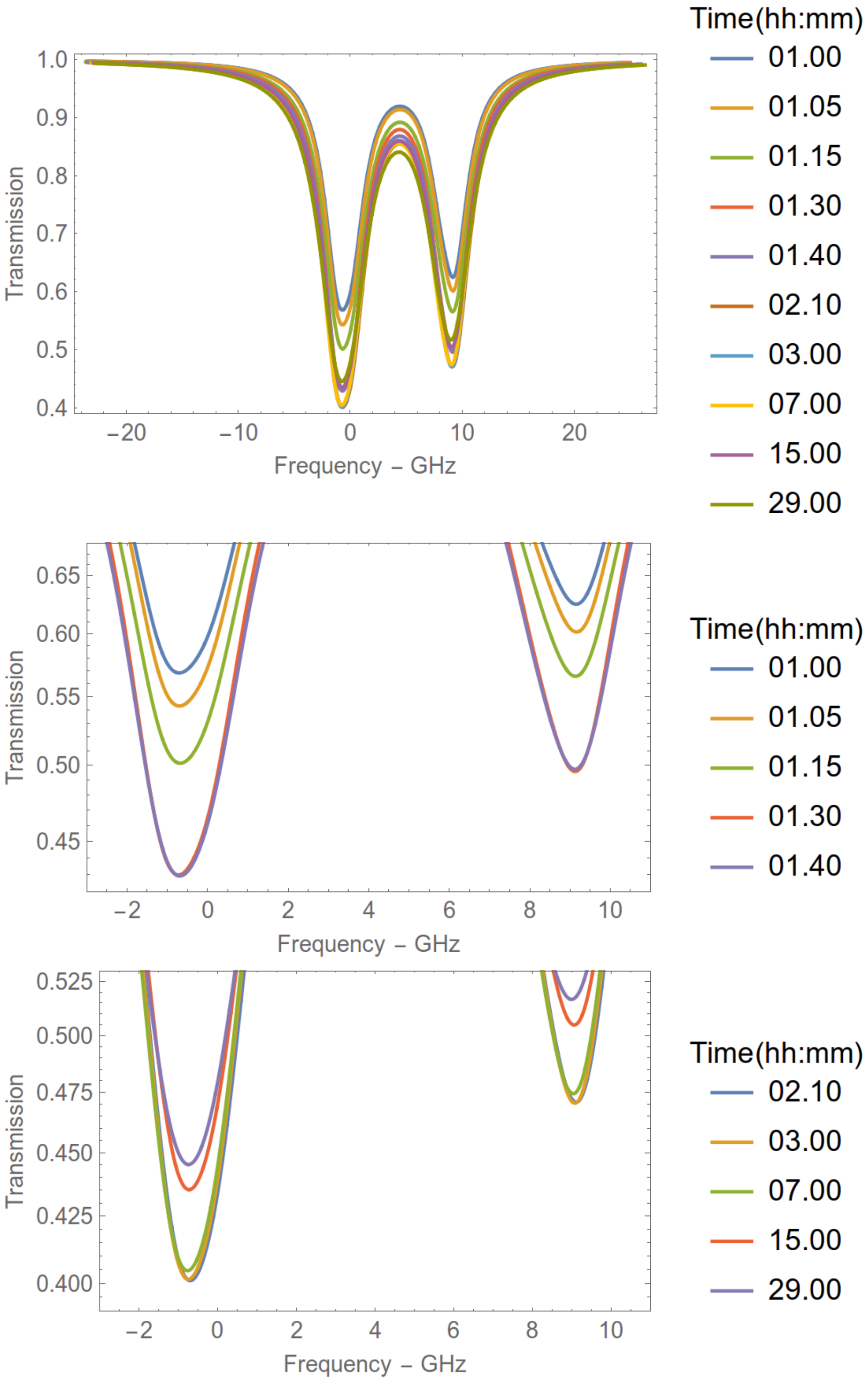

Figure 3.15: Sensor head transmission spectra at subsequent UV exposure times (upper plot); the fitted and normalized values are shown for a comparison otherwise not possible with real data. The lower plots show the same spectra where both transmission and frequency scales have been adjusted to improve visual comparison.

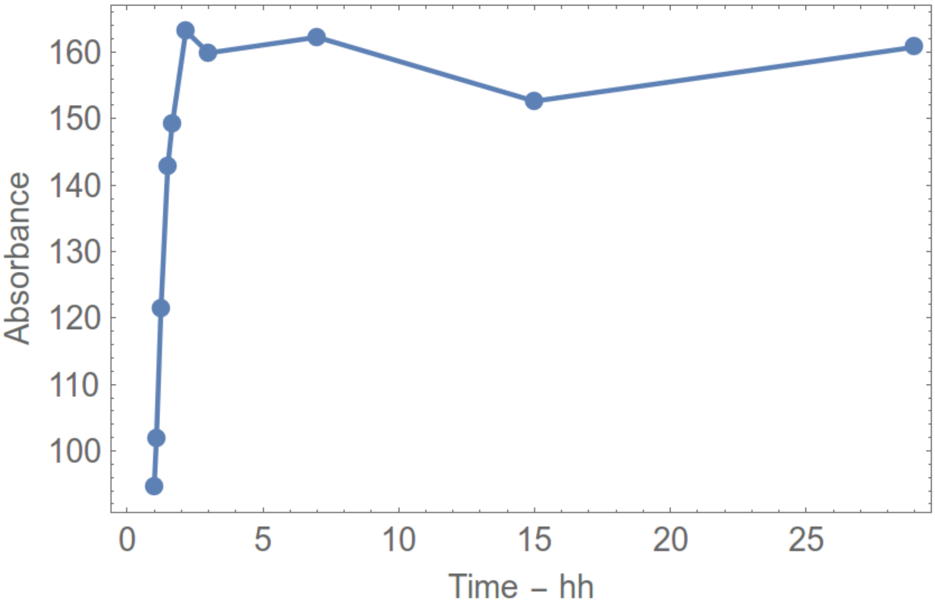

Figure 3.16: Extracted absorbance as a function of the UV exposure time.

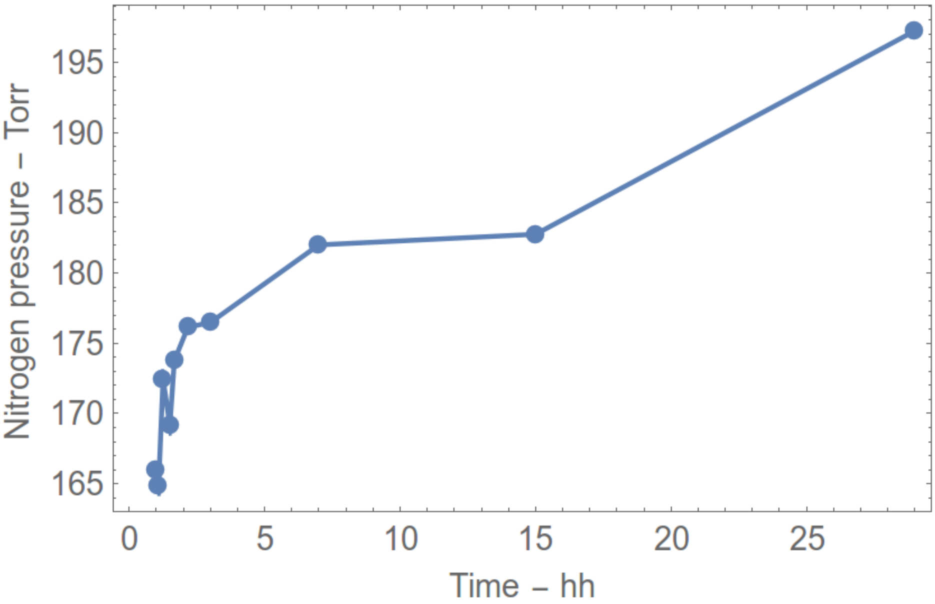

Figure 3.17: Extracted nitrogen pressure (from broadening) as a function of the UV exposure time.

Part II

The Magnetometer

Chapter 4

The Experiment

In the following chapter we describe the experimental set-up of the magnetometer on the optical table, the physical principle behind it and how a magnetic signal is extracted from an oscillating optical signal. We then present a way to measure the level of noise on the measured magnetic field[1], and introduce the concept of sensitivity used as the standard way of measuring the performances of a magnetometer.

4.1 Set-up

We build a magnetometer mainly following the amplitude modulated [2, 21, 74] Bell-Bloom [1, 75] scheme[2]. The experimental set-up is shown in figure 3.6. The diode laser frequency is tuned to the 3 → 3 transition of the D_1 caesium spectrum; its intensity is varied using a combination of a $\lambda/2$ wave-plate with a polarizing beam splitter (PBS): the laser intensity is adjusted by rotating the wave-plate optic axes.
The light is focused in an acusto-optic-modulator (AOM); this devices consists of a piezoelectric transducer which creates sounds waves in a material made of quartz. By properly tilting the AOM, the input light is deflected from the flat sound waves into several orders, the higher the order the higher the diffraction angle[3]. With a good alignment, almost all light can be deflected into the first order beam, so that the AOM can be considerer as an optic gate[4]. The light intensity is modulated by electronically driving the

---

[1] The magnetic field is measured in Tesla (T) or Gauss (G): $1\text{T} = 10^4$ G or $1\text{G} = 100\ \mu\text{T}$.

[2] The main difference is that we don't modulate the light at the larmor frequency but we detect instead the FID

[3] The direction of the zero order beam coincides with that of the incident light.

[4] The AOM efficiency (defined as the first to zero order power ratio) achieved is around 88%.

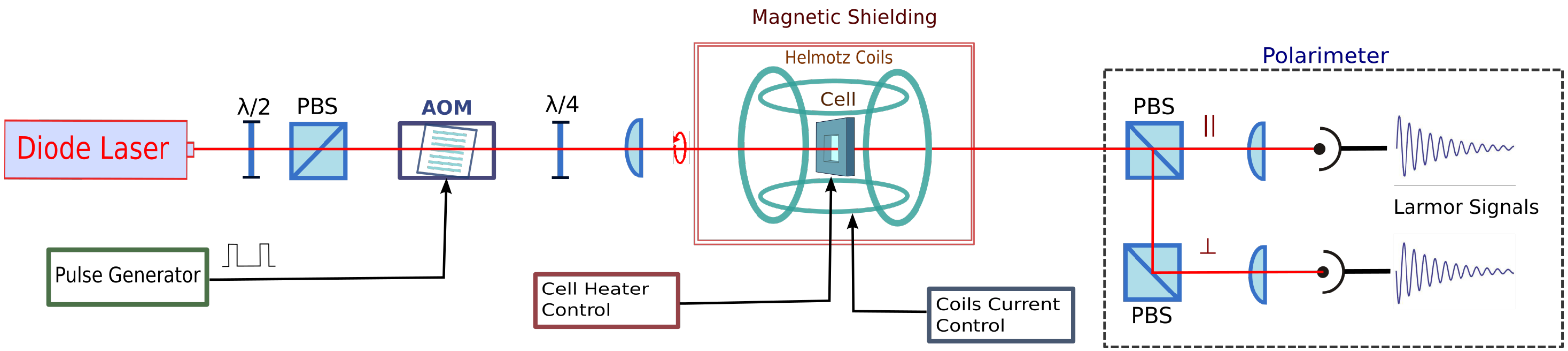

Figure 4.1: Experimental set-up of our Bell-Bloom type magnetometer.

AOM with a RF pulse generator.

To activate, the AOM needs a sinusoidal input signal at 80 MHz with a power of 30 dBm (=1 W); before being supplied to the AOM, this signal is multiplied with a RF square function generated by a pulse generator, so that the first-order laser light intensity is modulated synchronously with the RF pulse; the result is that a short impulse, which works as the pump, is followed by a longer and weaker beam, called the probe.

The modulated light is elliptically polarized using a $\lambda/4$ wave-plate before being focused in and out of the sensor head. The laser beam size is adjusted with a set of telescopic lenses and the position of the main lens is mapped against the beam size in correspondence of the sensor head.

Two pairs of Helmholtz coils surround the cell and generate two independent (low noise) magnetic fields, one in the direction of the beam and the other perpendicular to the laser direction and parallel to the earth magnetic field[5]. The coils driver schematic is shown in appendix B.1.1: the circuit can drive two independent magnetic fields (one parallel and one perpendicular to the laser light) with intensity up to 100 mG.

The cell is heated with a pair of circular resistive coils positioned close to its opposite glass surfaces. The heater current is chopped *on* and *off* and the signal is analysed only in the *off* stage, to avoid undesired magnetic noise. The circuit schematic of the heater driver is presented in appendix B.1.2; the driver transforms a RF periodic voltage signal (from a pulse generator) in the corresponding current signal, necessary to drive the heater. The magnetic shield[6] protects from external magnetic influences both the cell and the coils.

All the wires reaching the cell inside the magnetic shield, particularly the coils and heater wires, are made of copper and double twisted to avoid undesired magnetic fields.

Finally, the transmitted light from the cell is split into into its two linear polarization components: *parallel* ($\|$) and *perpendicular* ($\perp$); the term *parallel* refers to the linear component of the laser which is transmitted by a PBS, while the term *perpendicular* refers to the component that is reflected. The two polarization components of the Larmor oscillations are found almost out of phase; this suggests the use of the polarimeter for signal subtraction; for this reason the polarimeter returns also the difference of the two signals (labelled *difference*).

---

[5] We label these two magnetic fields with the terms parallel and perpendicular whether their direction is respectively parallel or perpendicular to the laser beam.

[6] The level of shielding is around 200.

The Coils Our sensor is located in the middle point of two orthogonal pairs of Helmholtz coils. It is commonly known that, in this point, the magnetic field, produced by each pair of coils, is quite uniform.
The magnetic field is calculated formally in literature only in the centre of the coils, or at best, along its axis (the one perpendicular to the coils plane, and passing through the coils centres). Since our sensor is mostly spread along the perpendicular axis, we calculated the magnetic field produced in a generic point in space to give an exact estimate of the magnetic uniformity.
To reach this goal we first calculate the magnetic field of a single coil in a generic point in space, then we generalize these results to the Helmholtz coils and give an analytical and numerical expression for the magnetic uniformity for our experimental case.
As fully explained in the appendix B.2, an expansion of the uniformity up to order 4 was necessary. The uniformity in the centre of the double Helmholtz coil structure is less than one part over 1000; since the coils deliver a magnetic field intensity up to 100 mG, the maximum noise due to the coils is 0.1 mG = 10 nT.

4.2 Physical Principle

The physics of the experiment can be modelled by a four-step process:

1. When a magnetic field is present, the ground and excited Zeeman sub-levels of the D_1 caesium spectrum are non-degenerate: a level with total angular quantum number F splits into $2F+1$ magnetic sub-levels. This allows the pump to transfer population in one of the two ground state sub-levels with highest absolute magnetic quantum number ($m_F = \pm F$) by **optical pumping**. If the input laser polarization is σ^+, the population will be transferred to the $m_F = F$ ground-state sub-level, otherwise if the input polarization is σ^-, the population is transferred to the $m_F = -F$ sub-level. An example of optical pumping with σ^+ light on a simplified two level system, can be seen in figure 4.2. As it will explained in chapter 6, this imbalance results in a macroscopic magnetization $\vec{m}$ build in the direction of the laser beam.

2. After a macroscopic magnetization is created by optical pumping, the high intensity pump is followed by the low intensity probe beam. In this way the magnetization vector $\vec{m}$ can precess around the magnetic field vector $\vec{B}$ at the so called **Larmor frequency** (ν_l), proportional to the field amplitude itself ($B = |\vec{B}|$) [29, 30, 76, 77]:
$$\omega_l = 2\pi\nu_l = \gamma B = 2\pi\gamma_\nu B, \tag{4.1}$$

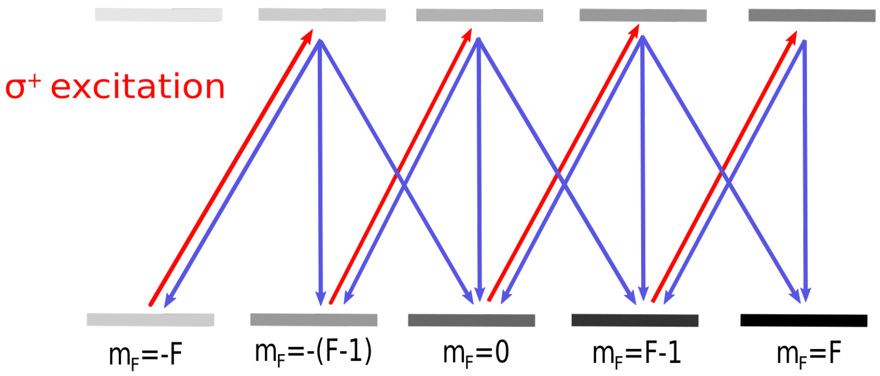

Figure 4.2: An illustrative example of optical pumping for $F = 2$. The red arrows represent transitions caused by the σ^+ excitation which transfer population from a ground state sub-level to an excited state sub-level with $\Delta m + 1$. The blue arrows represent decay transitions from the excited to the ground state, that respect the selection rule $\Delta m_F = 0, \pm 1$. State with higher population are represented with a darker bar, to show that population is eventually build into the $m_F = F$ ground state.

The factor of proportionality γ_ν in the equation is called *gyromagnetic ratio*, which for caesium atoms is[7] around 3.5 Hz/nT (see equation 6.19 in chapter 6).

3. We can visualize a caesium atom with its corresponding magnetization vector oscillating at the Larmor frequency. The frequency information held the by atom is lost when it collides with another caesium atom or with the cell walls. This phenomena, known as de-coherence, causes a **damping** of the oscillations and can be minimized either with wall coating or by filling the sensor head with a buffer gas. In the latter case, an inert gas is used as a buffer to minimize the caesium collisions, and so increase its mean free path. As already described in chapter 2, the buffer gas used in our experiment is nitrogen.

   Even so, the damping phenomena cannot be totally cancelled[8]: this

---

[7] The caesium gyromagnetic ratio can be alternativelly written as 350 Hz/mG or 3.5 kHz/μT.

[8] An exception is represented by the spin-exchange relaxation-free (SERF) magnetometer where the spin orientation scramble is avoided using a high density of potassium atoms

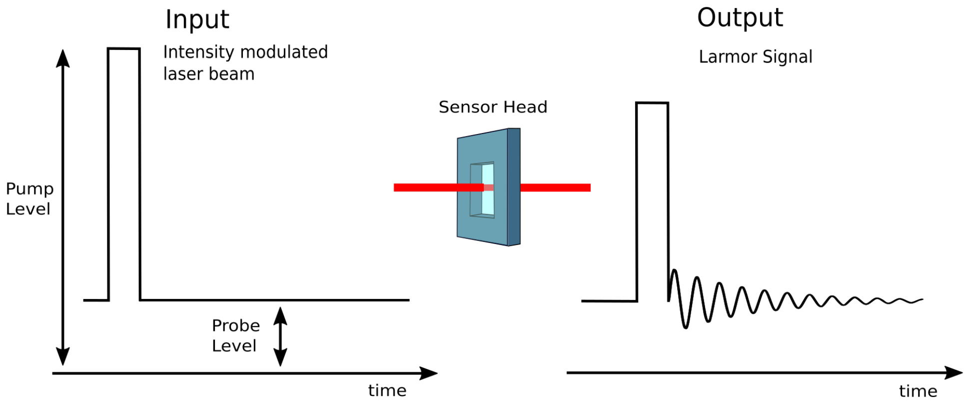

Figure 4.3: An illustrative example of the input intensity modulated light (on the left) and the output transmitted light displaying a typical Larmor signal on the probe part of the beam.

makes the Larmor oscillations detectable only in a finite time window, typically few hundreds of μs.

4. The damped oscillations are detected by the probe beam and its Larmor frequency ν_l can be easily used to measure the corresponding magnetic field amplitude B trough equation 4.1:

$$B = \frac{\nu_l}{\gamma_\nu}$$

Experimentally the process is illustrated in figure 4.3; the input intensity modulated laser light traverses the sensor head cell and the transmitted output light displays a dumped oscillating signal (the Larmor signal) on the probe part of the beam, which is separated and analysed.
At this point the atomic magnetization vectors need realignment and re-pumping through another pump impulse, that's why the process is automatically repeated to collect an appropriate numbers of consecutive damped (Larmor) oscillating signals.
The experiment is conceptually represented in the animated figure 4.4.

---

and a very low magnetic field [78].

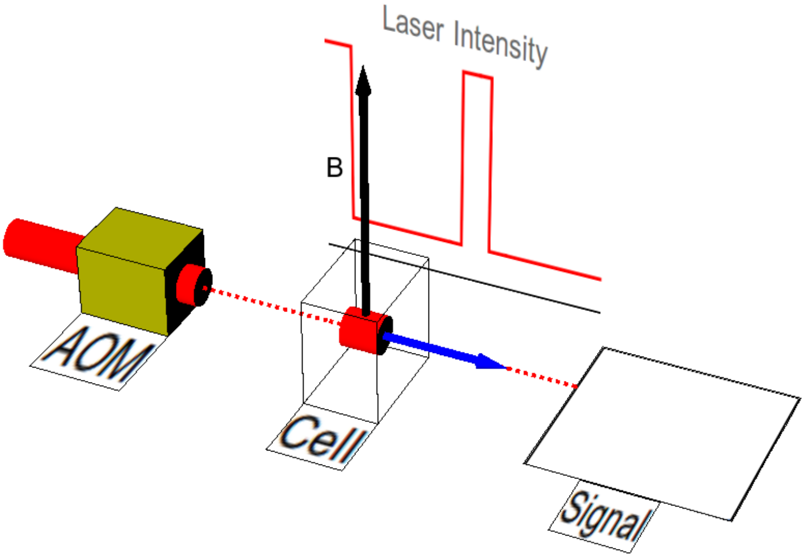

Figure 4.4: Conceptual representation of the experiment: the animated figure can be seen in the electronic version of this document and it can be reached by the following external link. The laser light (the red cylinder on the left side) is amplitude modulated by the AOM (the yellow box), so that short and intense pulses of light (the moving red cylinders) polarize the caesium ensemble in the cell. The resulting macroscopic magnetization (the blue arrow) precess around the external magnetic field (the black arrow), and the weak probe beam (the dotted red line) detects the corresponding Larmor precession (on the right side). As it can be seen, the oscillations are damped by the spin de-coherence phenomena inside the cell and the process is repeated to collect a sufficient amount of Larmor signals.

4.3 Larmor Damped Oscillations

We can imagine the magnetization vector $\vec{m}$ oscillating in the plane perpendicular to the magnetic field direction. As it will be explained in chapter 7, both of the signals detected by the polarimeter (*parallel* and *perpendicular* signals) are proportional to the magnetization projection m_z along the beam direction (z axis) m_z. This oscillation can be analytically modelled in time by the function [3, 29, 75]:

$$m_z(t) = m_0 \sin(\omega_l t + \phi) e^{-f_d t},$$

where m_0 is the initial magnetization obtained through optical pumping (stage one in section 4.2), $\omega_l = 2\pi\nu_l$ is the Larmor angular frequency (ν_l the corresponding frequency), ϕ an initial phase, and f_d the decay rate due to the damping phenomena. This function is plotted in figure 4.5.

4.4 Signal Sampling

We introduce here some useful definitions concerning sampled signals which will be useful in the next sections. Let's consider a signal of time duration T sampled by N data points: the **sample interval** is defined as $T_i = T/N$, while the **sampling rate** S_r is:

$$S_r = \frac{N}{T} = \frac{1}{T_i}.$$

The **bandwidth** is the interval of frequencies that can be detected with a given sample rate. The highest frequency component of a signal can be detected only if it is lower than half the sample rate (Nyquist-Shannon sampling theorem). From this consideration we will define the bandwidth as:

$$b_w = \frac{N}{2T} = \frac{S_r}{2}.$$

In other words the **Nyquist frequency** is the highest possible frequency detectable and it coincides with the bandwidth upper limit.

The bandwidth lower limit will be called **bin resolution**, which is the lowest frequency measurable and it is defined as:

$$b_r = \frac{1}{T}.$$

For the rest of the discussion the term bandwidth will refer only to its upper limit. When detecting a train of repeating signals (see section 4.7) each of time duration T, it is useful to introduce the **driving frequency**, which determines the rate at which each signal is extracted; it is defined as $f = 1/T$ and coincide with the single signal bin resolution.

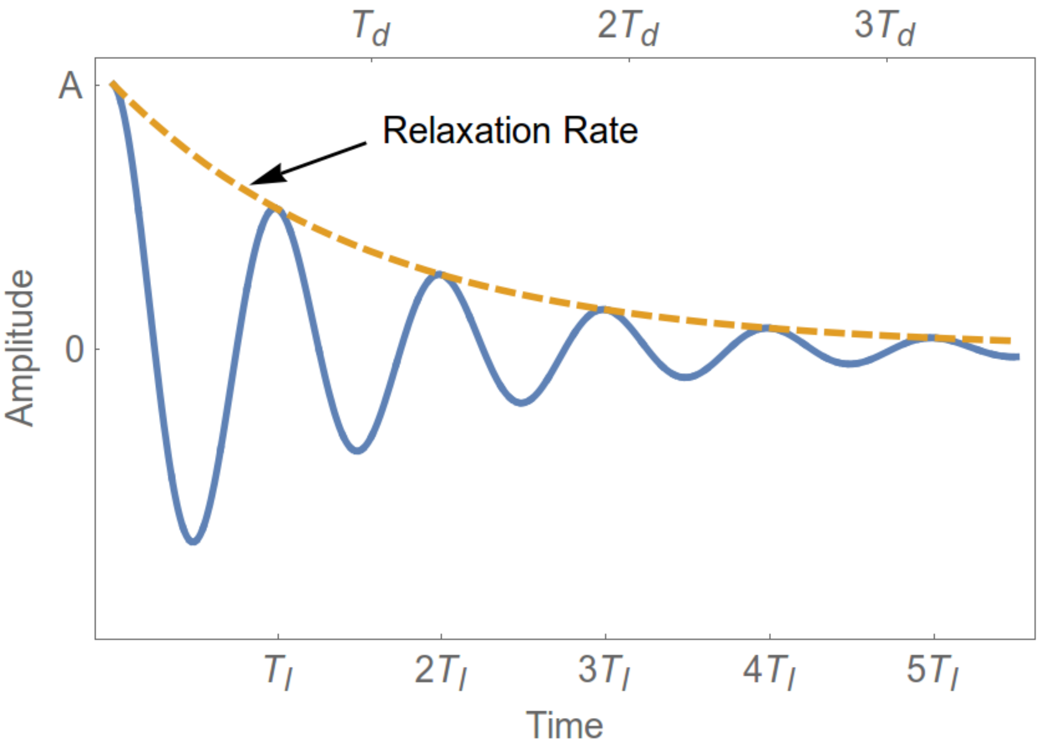

Figure 4.5: A conceptual representation of the magnetization component $m_z(t)$ along the laser direction z showing the Larmor precession caused by the magnetic field and the damping caused by the de-coherence phenomena. The lower horizontal scale unit is the Larmor period $T_l = 1/f_l$, while the upper scale unit is the decay time $T_d = 1/f_d$.

4.5 Larmor Signal

The signal corresponding to the magnetization oscillations $S(t) \propto m_z(t)$ can therefore be written as:

$$S(t) = A \sin(\omega_l t + \phi) e^{-f_d t}, \tag{4.2}$$

where $A \propto m_0$ is the signal (maximum) amplitude. The corresponding discrete signal S_m, sampled by N points for a period T, can be represented by:

$$S_n = A \sin(\bar{\omega}_l n + \phi) e^{-\bar{f}_d n} + \nu_n, \tag{4.3}$$

where n represents the data point, $\bar{\omega}_l = 2\pi \bar{f}_l$ is the signal Larmor angular frequency (expressed as sample points per second) and $\bar{f}_d$ is the signal decay rate (expressed as sample points per second).

Representations The two representations (time and data points) are connected by the sample rate $S_r = N/T$ (see section 4.4); more precisely:

$$\omega_l = S_r \bar{\omega}_l, \tag{4.4}$$

$$f_d = S_r \bar{f}_d. \tag{4.5}$$

It is often useful to deal with quantities independent on the type of representation used. Therefore we can define the *frequency* and *decay number* l and d respectively, as follows:

$$l = \bar{f}_l N = f_l T, \tag{4.6}$$

$$d = \bar{f}_d N = f_d T, \tag{4.7}$$

which represent respectively the number of Larmor oscillations and decay periods in one signal; these numbers are independent on the representation used.

4.5.1 Signal Noise

The signal in equation 4.3 is embedded in a noise of standard deviation σ_ν. The noise component is usually different at different frequencies and it is therefore better described by its power spectral density ρ_ν^2:

$$\rho_\nu^2 = \frac{\sigma_\nu^2}{b_w},$$

which describes the distribution of the noise in the frequency domain. The variance of the noise, captured by the sampling process, is therefore limited by the signal bandwidth b_w:

$$\sigma_\nu^2 = \int_0^{b_w} \rho_\nu^2 d\nu,$$

which, as defined in section 4.4, is proportional to the sampling rate ($b_w = S_r/2$).

A very common way of describing the quality of a signal is to use the **signal-to-noise ratio** R_{SN}, which we define in this case as:

$$R_{SN} := \frac{A}{\sigma_\nu}. \tag{4.8}$$

Note that the signal-to-noise ratio is independent on the damping rate and a function of the system bandwidth and so of the sampling rate.

In order to give an estimate of the signal-to-noise ratio for a given discrete signal we created an estimator of the signal noise σ_ν which is presented in appendix B.3.

4.5.2 Real Signal Examples

Figures 4.6 and 4.7 shows some Larmor oscillations detected by the polarimeter[9] for increasing (perpendicular) magnetic field amplitude. Both the signal (blue) and the correspondent fit (orange) is visible; from the fit the main information about the signal are extracted and printed on the right side of the correspondent plot. As it can be seen the magnetic field amplitude is increasing and at the same time the signal amplitude (and so the signal-to-noise ratio) is decreasing while the decay rate is increasing. The highest magnetic field detected is around 100 mG.

4.6 Data Processing Noise

The signal noise σ_ν could have different origin: it could be traced to the laser, the detectors or the sensor head or it could come from external magnetic noise or the data processing noise.

Whatever the source, the noise σ_ν will affect the quality of the magnetic measure obtained from the Larmor frequency (extracted from the signal fit) extracted out of the signal. The following sections formalize this connection.

4.6.1 Frequency Noise (Data Processing)

The information extracted from the discrete signal 4.3 (i.e. amplitude, angular frequency, phase and decay rate) with any fitting procedure, will invariably be affected by the signal noise σ_ν; in other words the measures will be affected by some errors; the Cramér-Rao lower bound conditions (CRB) [79] establishes their lowest possible values.

As fully explained in appendix B.4, the CRB condition for the angular frequency, extracted from an un-damped signal[10], is:

$$\sigma^2_{\bar{\omega}_l} \geqslant \frac{24}{R^2_{SN} M^3},$$

where $\sigma^2_{\bar{\omega}_l}$ is the noise of the angular frequency $\bar{\omega}_l$ and the right-hand side represents its CRB level.

In the general case of a *damped* signal, the noise is increased by the corrective factor $C_2(d)$. The CRB condition in this case is:

$$\sigma^2_{\bar{\omega}_l} \geqslant \frac{24}{R^2_{SN} M^3} C_2(d), \tag{4.9}$$

---

[9] In this example we show the *difference* signals, because it has a higher signal to noise.

[10] In the limit of high sampling points M.

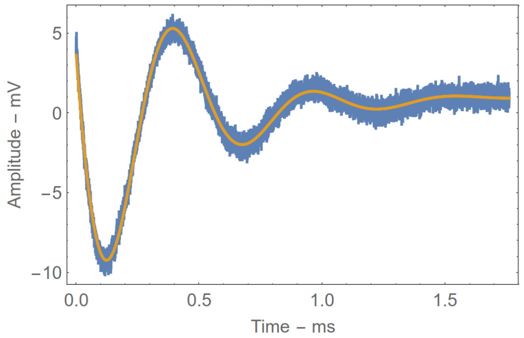

Amplitude	16.4	mV
Signal Noise	0.2	mV
Signal–to–noise	78	
Larmor Frequency	1.8	kHz
Larmor Period	0.6	ms
Magnetic Field	0.51	μT
	5.1	mG
Decay Rate	2.9	kHz
Decay Period	0.3	ms

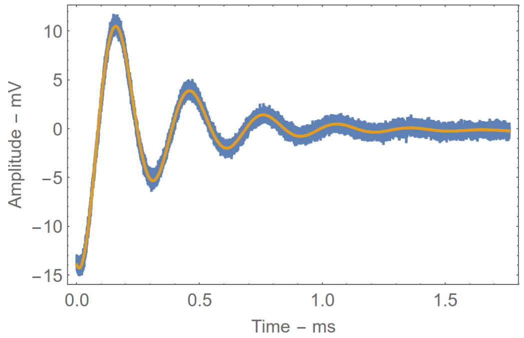

Amplitude	16.5	mV
Signal Noise	0.2	mV
Signal–to–noise	90	
Larmor Frequency	3.3	kHz
Larmor Period	0.3	ms
Magnetic Field	0.95	μT
	9.5	mG
Decay Rate	3.3	kHz
Decay Period	0.3	ms

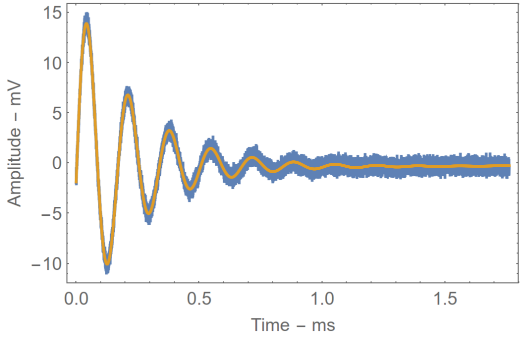

Amplitude	16.9	mV
Signal Noise	0.2	mV
Signal–to–noise	78	
Larmor Frequency	5.9	kHz
Larmor Period	0.2	ms
Magnetic Field	1.69	μT
	16.9	mG
Decay Rate	4.2	kHz
Decay Period	0.2	ms

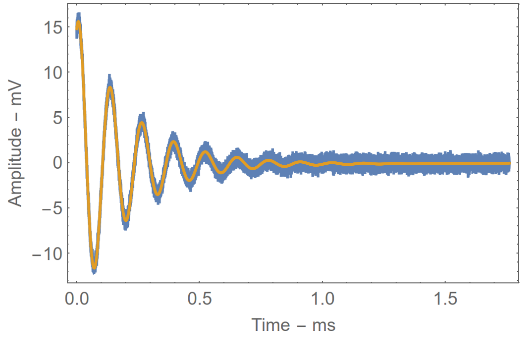

Amplitude	16.3	mV
Signal Noise	0.2	mV
Signal–to–noise	74	
Larmor Frequency	7.8	kHz
Larmor Period	0.1	ms
Magnetic Field	2.21	μT
	22.1	mG
Decay Rate	4.8	kHz
Decay Period	0.2	ms

Figure 4.6: Some example of Larmor oscillations detected (blue) and corresponding fit (orange).

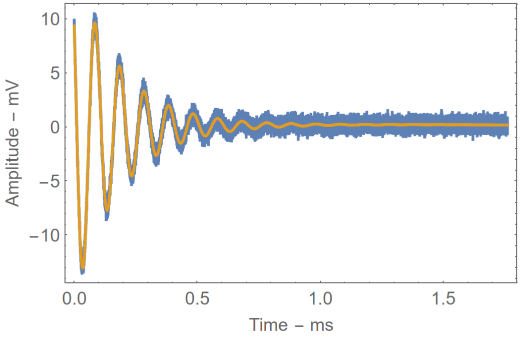

Amplitude	15.5	mV
Signal Noise	0.2	mV
Signal–to–noise	70	
Larmor Frequency	10	kHz
Larmor Period	0.1	ms
Magnetic Field	2.86	μT
	28.6	mG
Decay Rate	5.4	kHz
Decay Period	0.2	ms

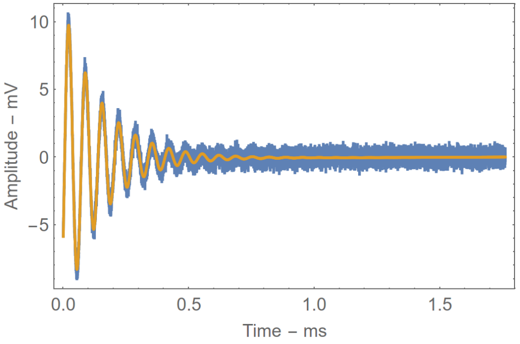

Amplitude	11.6	mV
Signal Noise	0.2	mV
Signal–to–noise	53	
Larmor Frequency	15	kHz
Larmor Period	0.1	ms
Magnetic Field	4.29	μT
	42.9	mG
Decay Rate	6.7	kHz
Decay Period	0.2	ms

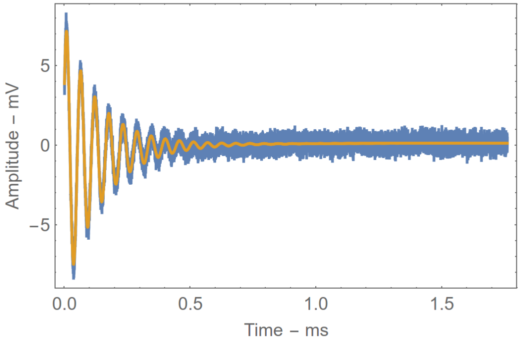

Amplitude	8.6	mV
Signal Noise	0.2	mV
Signal–to–noise	40	
Larmor Frequency	17.8	kHz
Larmor Period	0.1	ms
Magnetic Field	5.09	μT
	50.9	mG
Decay Rate	7	kHz
Decay Period	0.1	ms

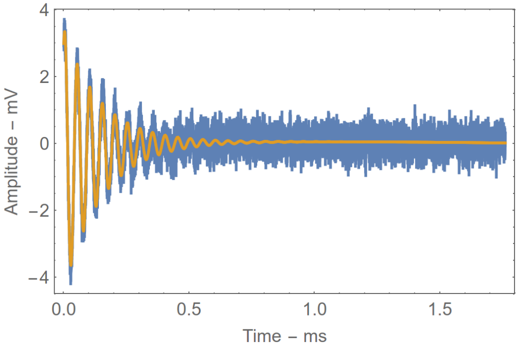

Amplitude	3.9	mV
Signal Noise	0.2	mV
Signal–to–noise	20	
Larmor Frequency	20	kHz
Larmor Period	0.1	ms
Magnetic Field	5.7	μT
	57	mG
Decay Rate	6.7	kHz
Decay Period	0.1	ms

Figure 4.7: Some example of Larmor oscillations detected (blue) and corresponding fit (orange).

where the function $C_2(d)$ (reported in the appendix) is such that $C_2(0) = 1$.

Fit Quality The real frequency error $\sigma^2_{\bar{\omega_l}}$ on the angular frequency $\bar{\omega_l}$ extracted would be at best equal to its CRB limit and in general higher. We can therefore define a fitting quality factor q as:

$$q := \frac{\sigma^2_{\bar{\omega_l}}}{CRB(\bar{\omega_l})}, \tag{4.10}$$

which measures the quality of the fitting process. Its best value is obviously 1 but it is generally slightly bigger depending on the quality of the fit. The fitting process used has a fit quality parameter q almost consistently around $\cong 1.3$, that's why it is useful to include it in equation 4.9 and write:

$$\sigma^2_{\bar{\omega_l}} = \frac{24q}{R^2_{SN} N^3} C_2(d). \tag{4.11}$$

which measures the level of noise on the angular frequency $\bar{\omega_l}$ extracted, assuming a constant quality factor q.

4.6.2 Magnetic Noise (Data Processing)

The magnetic field is measured from the Larmor frequency extracted using equation 4.1; this equation can be updated using equation 4.4:

$$B = \frac{\omega_l}{\gamma} = \frac{S_r}{\gamma}\bar{\omega_l}, \tag{4.12}$$

which combined with equation 4.11 can be used to evaluate the magnetic noise due to the fitting process σ_{FP} as:

$$\sigma^2_{\mathrm{FP}} = \frac{S_r^2}{\gamma^2}\sigma^2_{\bar{\omega_l}} = \frac{24q}{\gamma^2 R^2_{SN} N T^2} C_2(d). \tag{4.13}$$

4.6.3 Optimum Measurement

In this paragraph we answer one question: for a given number of sampling point N, what is the optimal time window T, that gives the lowest expected noise in the measured magnetic field extracted from the signal 4.3?
To answer this question we write $T = d/f_d$ (see equation 4.7) and use it in equation 4.13 to find the minimum of the function:

$$\mathrm{CRB}_B \propto \frac{C_2(d)}{d^2}.$$

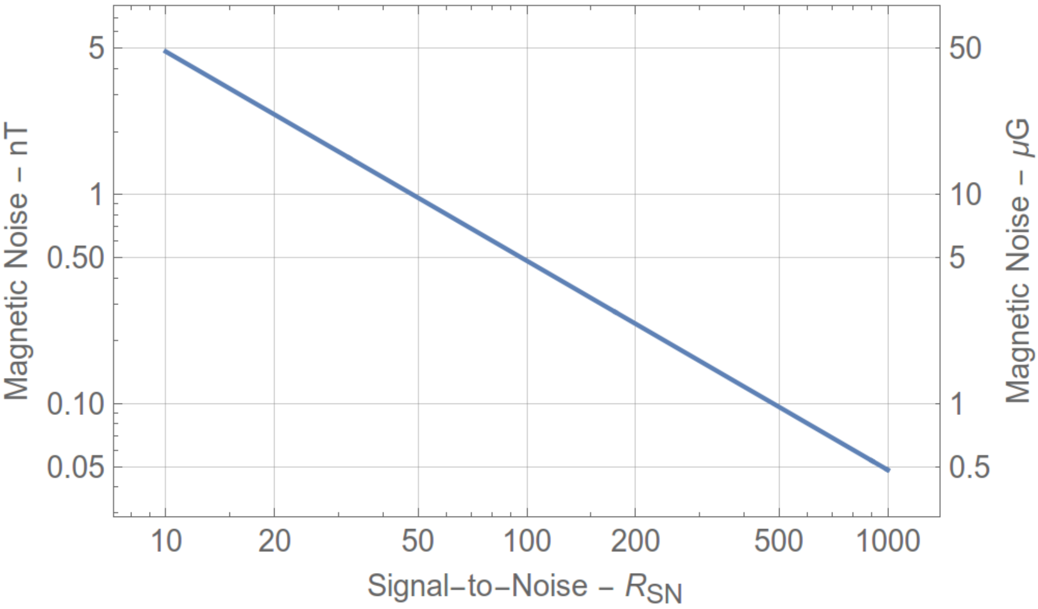

Figure 4.8: The expected magnetic noise (due to the fitting process) as a function of the signal-to-noise ratio, assuming $N = 500$, f_d =3 kHz and $q = 1.3$ (see equation 4.15). The plot is in bi-logarithmic scale.

It can be numerically shown that the best value of the decay number d_{opt} is around 2:

$$d_{\mathrm{opt}} \cong 2,$$

and so the best time window that minimize the noise level on the magnetic field is $T \cong 2/f_d$, and the optimum driving frequency f_{opt} is:

$$f_{\mathrm{opt}} \cong f_d/2. \tag{4.14}$$

In this condition $C_2(2) \cong 8$ and the best value for the magnetic noise due to the fitting process is:

$$\sigma^2_{\mathrm{FP}_{\mathrm{opt}}} \cong \frac{48q}{\gamma^2 R^2_{SN}} \frac{f_d^2}{M}. \tag{4.15}$$

Figure 4.8 shows the expected magnetic noise, in the optimum condition, as a function of the signal-to-noise ratio. As it can be seen, a noise lower than 1 nT is expected when $R_{\mathrm{SN}} \gtrsim 50$.

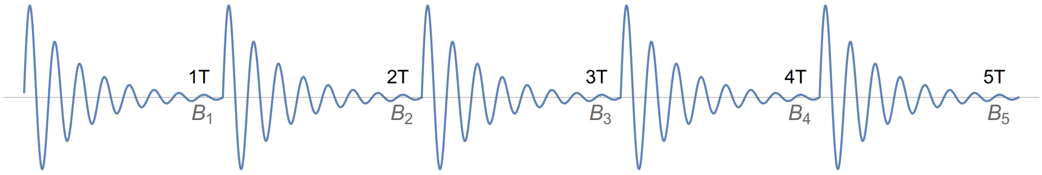

Figure 4.9: An illustrative example of a train of damped sinusoidal signals each of time duration T. A magnetic measure B_i is extracted with a time interval T.

4.6.4 Magnetic Range

The magnetic range is defined as the interval of Larmor frequencies ν_l detectable (and so of magnetic field intensities detectable), which coincides with the single signal bin resolution, and bandwidth respectably:

$$\nu_l \in [f = 1/T, S_r/2]. \tag{4.16}$$

As explained in section 4.6.3, the best driving frequency f is around half the decay rate $f \cong f_d/2 \cong 1.5$ kHz. Furthermore, as already mentioned in section 4.5.2, we experimentally observe that the highest magnetic amplitude detectable is around 100 mG, which coincide to a Larmor frequency upper limit of $f_l^{\text{lim}} \cong 35$ kHz; from formula 4.16, it follows that there is no need to use a sample rate superior to 75 kHz and the magnetic range can be written as:

$$r_m \cong \left[\frac{f_d}{2}, f_l^{\text{lim}}\right] \cong [1.5, 35] \text{ kHz} \equiv [4.3, 100]\text{mG} \equiv [0.43, 10]\mu T. \tag{4.17}$$

This range is very important to characterize the magnetometer and can be expanded by reducing the decay rate, which on the other hand will also reduce the data processing noise (see equation 4.15).

4.7 Magnetic Noise

To measure the external magnetic field in real time it is not enough to detect just one Larmor signal; in fact we generally deal with a train of R (typically from 50 up to 10,000) damped sinusoidal signals; an example is shown in figure 4.9.

Let's imagine we want to measure the amplitude of a constant external magnetic field B_c in the vicinity of the sensor head; we can extract a magnetic measure from each component of a the train of R damped Larmor signals and obtain the sequence B_i of measured magnetic fields (with i going from 1 to R). The magnetic field values B_i of the real magnetic field B_c would be corrupted by the fitting process used to obtain the measure and by the magnetometer response to the magnetic field. In the case of no external magnetic noise the sequence B_i can be written as:

$$B_i = B_c + \nu_i^{\mathrm{FP}} + \nu_i^I, \tag{4.18}$$

where $1 \leq i \leq R$. The sequence ν_i^{FP} (of variance σ^2_{FP}) measures the noise due to the fitting process (see equation 4.13) while ν_i^I (of variance σ_I^2) measures the noise due to the internal response of the magnetometer to the external magnetic field. Therefore the variance σ_B^2 of the sequence B_i can be written as the sum:

$$\sigma_B^2 = \sigma^2_{\mathrm{FP}} + \sigma_I^2. \tag{4.19}$$

Note that while the data processing noise σ^2_{FP} is white one cannot say the same for the internal noise σ_I^2 of the magnetometer. Equation 4.19 suggests that in order to study the magnetometer response, the fitting noise σ^2_{FP} has to be lower than the internal noise σ_I^2.

Where also an external magnetic noise ν_i^E (of variance σ_E^2) is present, one can extend equation 4.18 to:

$$B_i = B_c + \nu_i^{\mathrm{FP}} + \nu_i^I + \nu_i^E. \tag{4.20}$$

In the same way, equation 4.19 can be extended to:

$$\sigma_B^2 = \sigma^2_{\mathrm{FP}} + \sigma_I^2 + \sigma_E^2,$$

which suggests that in order to detect external magnetic noise σ_E^2, this has to be bigger that the sum of the fitting process noise σ^2_{FP} and the internal noise of the magnetometer σ_I^2.

The conclusion is that one Larmor signal is enough only to evaluate the fitting process noise through equation 4.13 (provided that a good guess of the fitting quality factor is given), while to evaluate the internal and external noise it is necessary to use a train of Larmor signals. Another reason to use multiple signals is to provide a description of the noise in the frequency domain; we address this problem in the next secion.

4.7.1 Noise Power Spectrum

In this section we illustrate the utility of the discrete Fourier transform (DFT) to provide a full description of a signal noise in the frequency domain.

Let's suppose we measure a signal sequence B_i like:

$$B_i = B_c + \nu_i,$$

with $1 \leq i \leq R$ and the time distance between each measure is T; we assume that the noise ν_i has standard deviation σ and for now we don't focus on the particular nature of the noise (fitting process, internal or external); just for illustrative purposes we assume instead that it comes from a sinusoidal function at a particular frequency f_ν:

$$\nu_i = A \sin\left(2\pi f_\nu i\right).$$

In order for ν_i to have standard deviation σ, the amplitude A has to fulfil the equation $A = \sqrt{2}\sigma$.
Applying the concepts of bin resolution and bandwidth, outlined in section 4.4, we can say that $f_\nu \in [1/(RT), 1/(2T)]$. It is more convenient to express the frequency in term of the corresponding frequency number[11] $l_\nu := RTf_\nu$ (see definition in equation 4.6); in this way the frequency range can be more easily written as $l_\nu \in [1, R/2]$. We can then write:

$$\nu_i = \sqrt{2}\sigma \sin\left(\frac{2\pi}{R} l_\nu i\right). \tag{4.21}$$

In order to describe the properties of the signal B_i in the frequency domain we consider the corresponding DFT sequence F_l defined as:

$$F_l = \frac{1}{\sqrt{R}} \sum_{r=1}^{R} B_r e^{i \frac{2\pi}{R} lr}, \tag{4.22}$$

where the index l, ranging from 1 to $R/2$, actually refers to a frequency number; in fact for our particular signal it can be easily demonstrated[12] that:

$$F_l = 0 \text{ for } l \neq l_\nu, \tag{4.23}$$

$$|F_{l_\nu}|^2 = \frac{R}{2}\sigma^2. \tag{4.24}$$

This result, illustrated in figure 4.10, can be easily extended to the general case of noise components at different frequencies. Let's generalize the previous result and write the noise ν_i as:

$$\nu_i = \sqrt{2} \sum_{l=1}^{R/2} \sigma_l \sin\left(\frac{2\pi}{R} li\right),$$

---

[11] The definition of frequency number is given in equation 4.7.

[12] The demonstration is easy computationally but very demanding analytically.

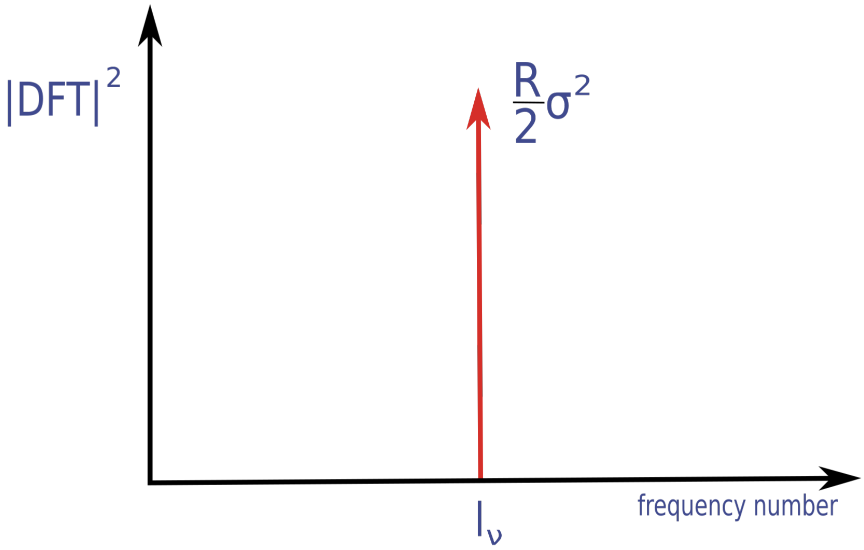

Figure 4.10: Absolute squared DFT plot of noisy signal showing a single peak at the noise single frequency; the peak hight is proportional to the noise variance.

where σ_l is the noise level at the frequency number l and obviously:

$$\sigma^2 = \sum_{r=1}^{R/2} \sigma_l^2. \tag{4.25}$$

In this case equations 4.23 and 4.24 can be extended to the single equation:

$$|F_l|^2 = \frac{R}{2}\sigma_l^2. \tag{4.26}$$

valid this time for all $l_\nu \in [1, R/2]$.
This example illustrated that the DFT measures the noise component at each frequency number.

4.7.2 White Noise Example

If the frequency components of the noise ν_i are the same for all frequency numbers l, then from the identity 4.25 one can write:

$$\sigma_l^2 = \frac{2}{R}\sigma^2,$$

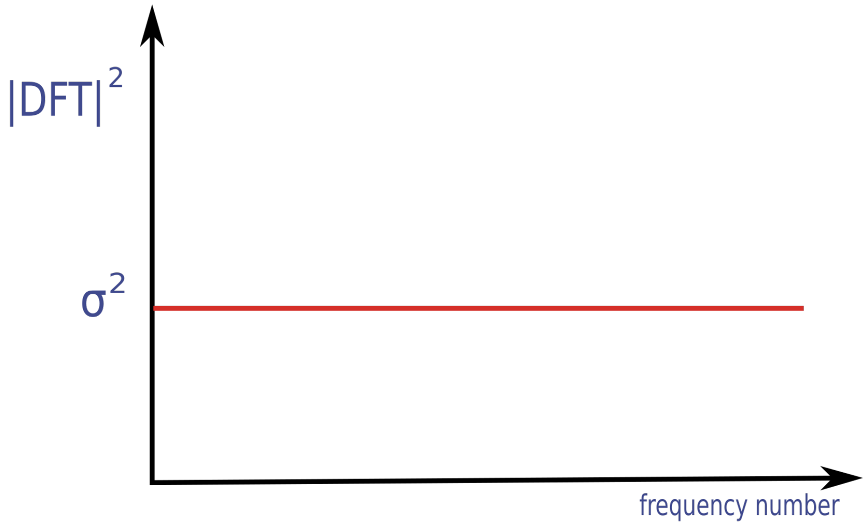

Figure 4.11: Absolute squared DFT plot of a signal embedded in white noise: the flat level hight is proportional to the noise variance.

so that equation 4.26 becomes:

$$|F_l|^2 = \sigma^2.$$

This is the most basic example of white noise and it is illustrated in figure 4.11: a signal with flat (i.e. constant) DFT; a general white noise will not have a perfectly flat DFT plot, nevertheless the DFT average value coincides with the noise variance, i.e for white noise it is verified that:

$$< |F_l|^2 >= \sigma^2, \tag{4.27}$$

where the symbol <> denotes the average value.
A computationally simulated example is illustrated in figure 4.12 where a constant (simulated) magnetic field is embedded in white noise (top plot); the (absolute square) DFT plot (on the bottom) shows a flat spectrum with average equal to the noise variance.
A general signal is not perfectly white and will display trends and/or peaks in the DFT plot. We can generally expect that the DFT of a magnetic signal wil display these three features:

- a **flat component**: this is typically coming from the fitting process noise σ^2_{FP};

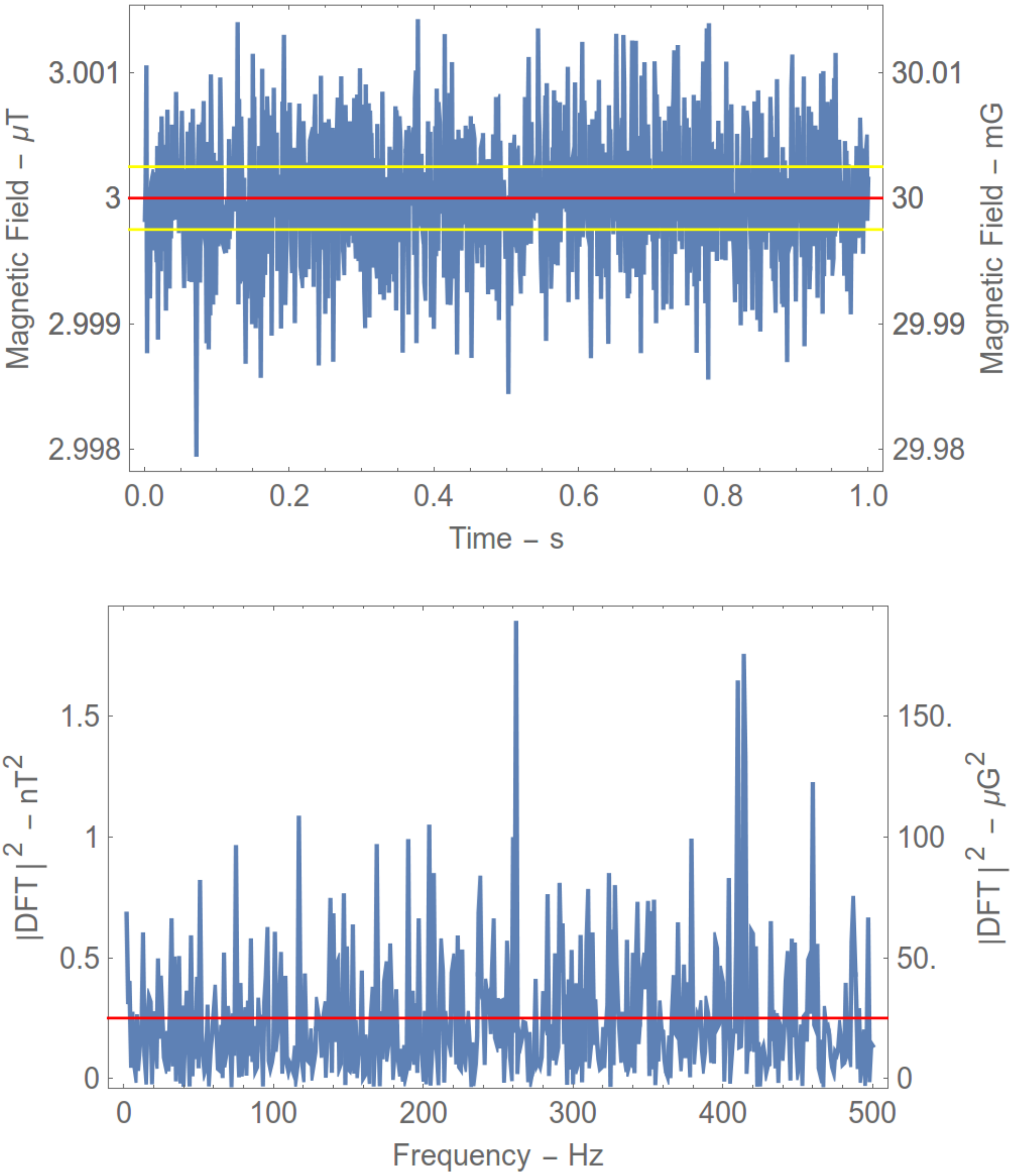

Figure 4.12: The figure on the top plots a (simulated) magnetic field: it's mean (red line) is 30 mG and the standard deviation (equal to the distance between the yellow lines) is 5 μG. The plot on the bottom shows the (squared absolute) DFT of the magnetic signal. The red line shows its average value which coincides with the magnetic field noise variance (25 $\mu\mathrm{G}^2$).

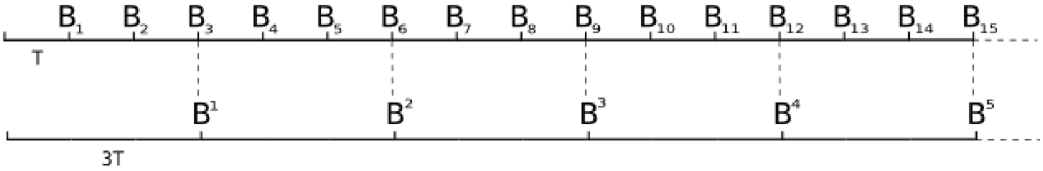

Figure 4.13: From the original discrete sequence B_i the sequence B^j is obtained by averaging over 3 realizations.

- **continuous trends** which could be ascribed to the internal response of the magnetometer σ_I^2;
- **peaks** most likely coming from external noise σ_E^2.

4.7.3 Magnetic Spectral Range

We define the magnetic spectral range as the interval of frequencies within which the DFT is defined. When the DFT is plotted the frequency number l in equation 4.22 is converted in the corresponding frequency $f_l = l/(RT)$. Since $l_\nu \in [1, R/2]$, it follows that:

$$f_\nu \in \left[\frac{1}{RT}, \frac{1}{2T}\right] = \left[\frac{f}{R}, \frac{f}{2}\right] \cong [\frac{1.5}{R}, 0.75] \text{ kHz}, \tag{4.28}$$

Where we have used $f = 1/T \cong f_d/2 \cong 1.5$ kHz.

The magnetic spectral range is also the interval of magnetic field *variations* (and so Larmor frequency variations) detectable. It coincides with the magnetic signal bin resolution and bandwidth respectively.

The term **magnetometer bandwidth** (b_m) usually refers to the magnetic spectral range upper limit, which in our case is around 1.5 kHz, and it measures how fast the magnetometer can track variations in the magnetic signal; it coincide with half the driving frequency and in the optimum case to a quarter of the Larmor signal decay rate.

4.8 Integrated Magnetic Signal

A measure of the magnetic field is delivered at a rate equal to $f = f_d/2 \cong$ 1.5 kHz which, for some applications, may be too fast resulting in too much noise. To overcome this issue a group of magnetic signals could be integrated (i.e. averaged) in a larger period of time.

In the common scenario we dispose of a series R of magnetic signal realizations B_i distanced in time by T (see figure 4.5). We can divide this list in R/n sub groups each containing n elementary magnetic measures so that the averaged value B^j is delivered every nT. An example is depicted in figure 4.13.
Since each of the n measures share the same noise variance σ_B^2, the noise of their average is reduced by a factor n:

$$\sigma_B^2 \longrightarrow \sigma_B^2/n. \tag{4.29}$$

The bandwidth of the integrated signal follows a similar behaviour:

$$b_m = \frac{f}{2} = \frac{1}{2T} \longrightarrow b_i = \frac{1}{2nT} = \frac{b}{n}.$$

In other words it is possible to decrease the magnetic noise at the expense of the magnetometer bandwidth i.e. by reducing the highest variation detectable in a magnetic signal. Since the bandwidth can vary depending on the particular application, a better way of measuring the magnetometer performance in terms of noise would be σ^2/b_m, since this ratio is independent on the integration time. This leads to the definition of sensitivity presented in the next section.

4.8.1 Sensitivity

The sensitivity of the magnetometer is defined by the **root spectral density**[13] ρ_B as:

$$\rho_B^2 = \frac{\sigma_B^2}{b_m}, \tag{4.30}$$

where $b_m = f/2$ is the magnetometer bandwidth (see definition in section 4.7.3); the sensitivity is measured in $\mathrm{T}/\sqrt{\mathrm{Hz}}$.
Let's consider here the contribution to the noise coming from the fitting process in the *optimum* case (see equation 4.15); in this case $f \cong f_d/2$ (see equation 4.14) and so:

$$b_m \cong \frac{f_d}{4},$$

this result, together with equation 4.15, can be used in equation 4.30 to evaluate the contribution to the sensitivity coming from the fitting process (in the *optimum* case) as:

$$\boxed{\rho_{\mathrm{FP}}^2 = \frac{194q}{\gamma^2 R_{SN}^2}\frac{f_d}{N}.} \tag{4.31}$$

---

[13] The quantity ρ^2 is called *power spectral density.*

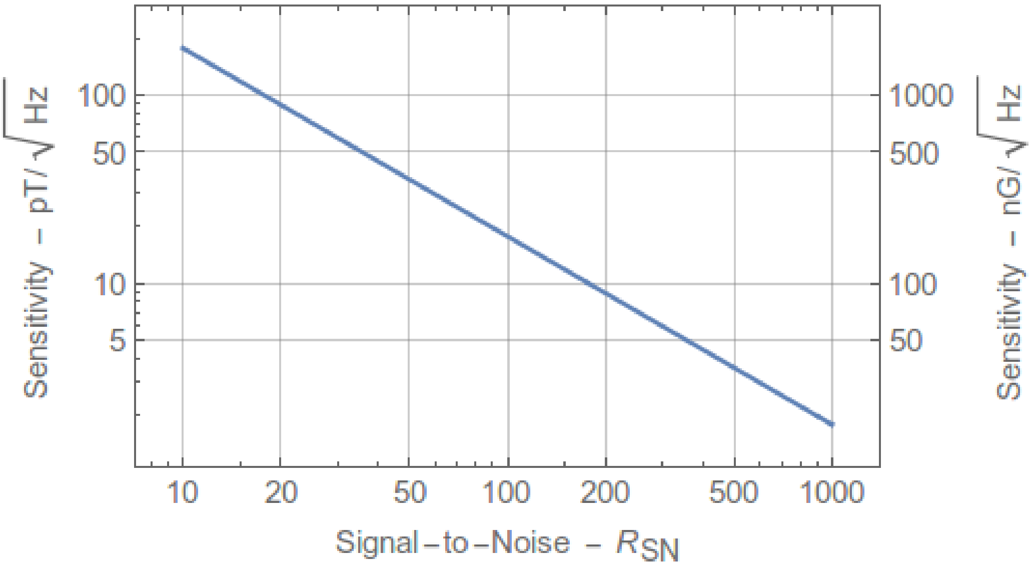

Figure 4.14: Expected sensitivity (due to the fitting process) as a function of the signal-to-noise R_{SN} in bi-logarithmic scale. A decay rate of 3 kHz, a quality factor of around 1.3 and $N = 500$ have been assumed (see equation 4.10).

As it can be seen, the fitting noise part of the sensitivity is linearly proportional to the decay rate f_d, which means that any improvement (i.e. any decrease) in the decay rate will positively affect the sensitivity. Incidentally it will also extend the magnetic range (see equation 4.17). Figure 4.14 shows the expected sensitivity as a function of the signal-to-noise R_{SN}; as it can be seen, a sensitivity lower than 10 pT/$\sqrt{\text{Hz}}$ can be reached when $R_{\text{SN}} \gtrsim 200$.

4.8.2 Spectral Density Plot

The DFT plot of a generic magnetic signal B_i helps understanding the noise level at different frequencies. As seen in section 4.8.1, the sensitivity is a better way of measuring the noise performances of the magnetometer but, as defined in 4.30, it is only a single number; a plot of the sensitivity over the frequency range would be more useful.

For this purpose, We define the power spectral density sequence ρ_l^2 of the

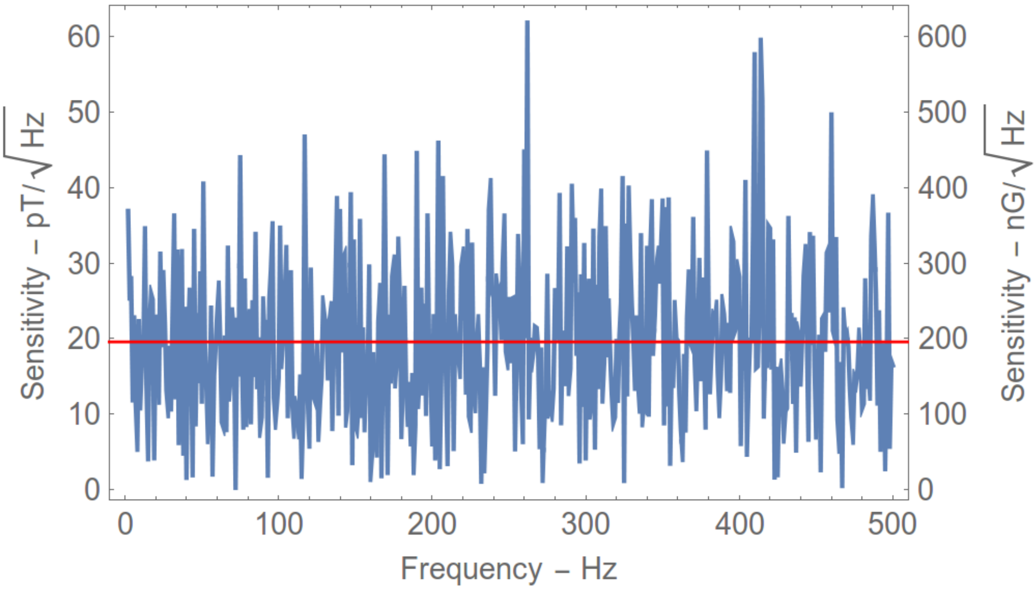

Figure 4.15: The figure plots the sensitivity plot of the (simulated) magnetic signal in figure 4.12;

magnetic signal B_i $(1 \leq i \leq R)$ as:

$$\rho_l^2 = \frac{|F_l|^2}{b_m},$$

where F_l is the Fourier transform F_l $(1 \leq l \leq R/2)$ of the magnetic signal. In fact, from equation 4.27, if the magnetic signal is embedded in white noise of variance σ_B only, then the average value of the sequence ρ_l^2 is:

$$< \rho_l^2 >= \frac{< |F_l|^2 >}{b_m} = \frac{\sigma^2}{b_m} = \rho_B^2$$

which coincides with the single number defined in equation 4.30. This results proves the internal coherence in the definition of the sensitivity sequence ρ_l. Figure 4.15 shows the sensitivity plot, i.e. the root spectral density of the (simulated) magnetic signal in figure 4.12; as it can be seen the plot displays a flat noise trend due to the white noise; in this example σ_B=500 pT=5 nG, the magnetometer bandwidth (i.e. the upper frequency limit of the DFT plot) is 500 Hz and the sensitivity is 22.4 pT/$\sqrt{\text{Hz}}$=224 nG/$\sqrt{\text{Hz}}$.

4.8.3 Minimum Signal Detectable

Let's suppose a constant magnetic field is embedded in two forms of noise: a white noise background and a "peaked noise" i.e. a noise characterized by a single frequency; the first could be due, for example, to the fitting process while the latter to external magnetic influences, like a 50 Hz noise. We can write:

$$B_i = B_c + \nu_i^W + \nu_i^E.$$

where ν_i^W is the white noise with standard deviation σ_W and ν_i^E is the external noise of standard deviation σ_E; we can imagine to heuristically write ν_i^E as in equation 4.21:

$$\nu_i^E = \sqrt{2}\sigma_E \sin\left(\frac{2\pi}{R} l_E i\right),$$

where l_E is the frequency number of the external noise. From the results in equations 4.23 and 4.24, we know that this signal will contribute the the DFT plot only at the frequency number l_E with a peak $(R/2)\sigma_E^2$ high. The rest of the DFT plot would be constant with a level given by the white noise variance σ_W^2; the situation is illustrated in figure 4.16

We can imagine that the minimum external noise detectable, of standard deviation $\bar{\sigma}_E$, has to display a peak at least as high as the flat background in order to be distinguished from the white noise. Following this observation we can define σ_E from:

$$\frac{R}{2}\bar{\sigma}_E^2 = \sigma_W^2 \Rightarrow \bar{\sigma}_E^2 = \frac{2}{R}\sigma_W^2.$$

Since the magnetometer bandwidth is $b_m = f/2$ and the bin resolution $b_r = f/R$, we can express R as:

$$R = \frac{2b_m}{b_r},$$

which can be used to rewrite the minimum amplitude detectable as:

$$\bar{\sigma}_E^2 = \frac{b_r}{b_m}\sigma_W^2.$$

If we now use the definition of sensitivity from equation 4.30 we can conclude that:

$$\boxed{\bar{\sigma}_E^2 = \rho_B^2 b_r = \frac{\rho_W^2}{T_{\text{tot}}},} \tag{4.32}$$

where the sensitivity correspondent to the white noise σ_W is ρ_W and we have used $b_r = 1/(TR) = 1/T_{\text{tot}}$. Equation 4.32 shows that the minimum external

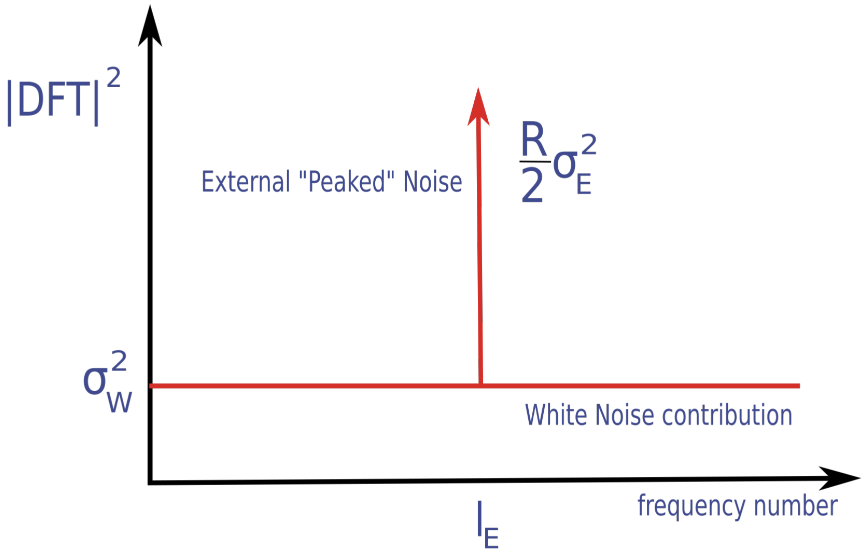

Figure 4.16: Plot of the absolute squared Fourier DFT of a signal embedded in both white noise and an external noise peaked at a given frequency.

noise detectable out of a white noise is proportional to the the sensitivity and the magnetic bin resolution or, alternatively, inversely proportional to the total signal time.
The sensitivity characterizing a magnetometer refers usually to the flat background in the DFT plot ρ_W, which is the standard way of measuring the noise performance of the magnetometer: the result helps translating the sensitivity into a more physically meaningful quantity: the smallest magnetic signal detectable.

4.9 Polarimeter Signals

The polarimeter detects the two orthogonal linear polarization components ($\|$ and $\perp$) of the laser light and it is used because we find the two components of the Larmor oscillations out of phase, which suggests the use of their difference to reach higher sensitivity. In this section we measure the quality of the *difference* signal as a replacement of two original signals, in order to justify or not its use.

Let's label the two signals with numbers 1 and 2 and their difference (signal 1 minus signal 2) with the letter d. The amplitude, signal error variance, signal-to-noise ratio, decay rate and sensitivity of the general signal i is labelled with the symbols A_i, σ_i^2, R_i, f_i, ρ_i respectively (with i being 1,2 or d). We introduce these experimental parameters:

$$\begin{aligned}
q_A &= \frac{A_d}{A_1 + A_2}, \\
q_\sigma &= \frac{\sigma_d}{\sigma_1 + \sigma_2}, \\
q_f &= \frac{f_d}{f_1 + f_2}, \\
q_R &= \frac{R_d}{R_1 + R_2}, \\
q_\rho &= \rho_d / \min(\rho_1, \rho_2),
\end{aligned}$$

where their meaning is as follows: q_A measures the degree of phase opposition of signal 1 to signal 2; with perfect phase opposition $A_d = A_1 + A_2$ and $q_A = 1$ while with no phase opposition $A_d = |A_1 - A_2|$ and a reaches it lowest value; q_σ measures the degree of noise cancellation between the two signals: it is 1 for no noise cancellation and 0 for perfect noise cancellation; q_R measures the gain in signal to noise, q_F the gain in decay rate and finally q_s the gain in sensitivity.

Experimentally we find:

- $q_A \cong 1$, i.e. nearly perfect phase opposition;
- $q_\sigma \cong 1$, which means almost no noise cancellation; this must mean that almost all noise comes from the detectors;
- $q_R \cong 0.6$, i.e. the signal-to-noise R_d is just above the average value of R_1 and R_2;
- $q_f \cong 0.5$, i.e the decay rate of the difference signal is almost the average of the decay rate of signal 1 and 2.
- $q_s \cong 1.3$, i.e. the sensitivity of signal d is 1.3 higher that the minimum sensitivity of the signals 1 and 2.

A typical example of the signals captured by the polarimeter is shown in figure 4.17. The results are summarized in this table:

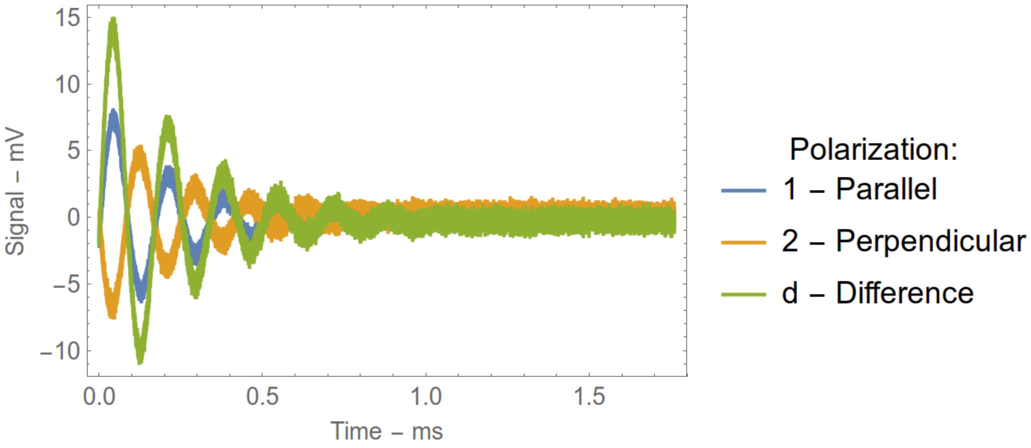

Figure 4.17: An example of the two signals detected by the polarimeter. As it can be seen the oscillations are out of phase.

	1	2	d	q
A (mV)	9.1	7.97	16.95	0.99
σ^2 (mV^2)	0.01	0.04	0.05	1
R	86.01	42.2	78.36	0.61
f_d (kHz)	4.34	4.12	4.22	0.5
ρ (pT/$\sqrt{\text{Hz}}$)	37.02	73.45	40.05	1.08

As it can be seen the phase opposition alone is not enough to justify the use of signal *d* as a replacement of signal 1 and 2; this results doesn't make the polarimeter useless because without it we would detect a signal roughly proportional to the sum of signal 1 and 2, i.e. a very poor signal; the result suggests the use of only one of the two linear components of the Larmor oscillations depending on which of the two signals is higher.
As it will be seen in the next chapter, in our experimental case the best signal is the *parallel* one (signal 1).

4.10 Sensitivity Analysis Software

We have created a data analysis tool using Wolfram Mathematica® to rapidly extract the all the main properties from a train of consecutive Larmor signals. The software interface is shown in figure 4.18. Its main sections are here described:

- **mask**: the button opens an input windows in which the main properties

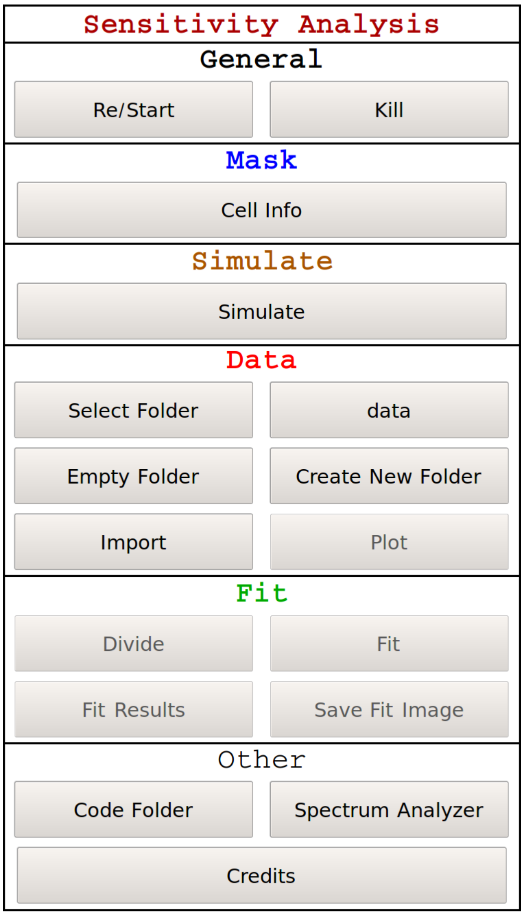

Figure 4.18: *Sensitivity Analysis Software* interface.

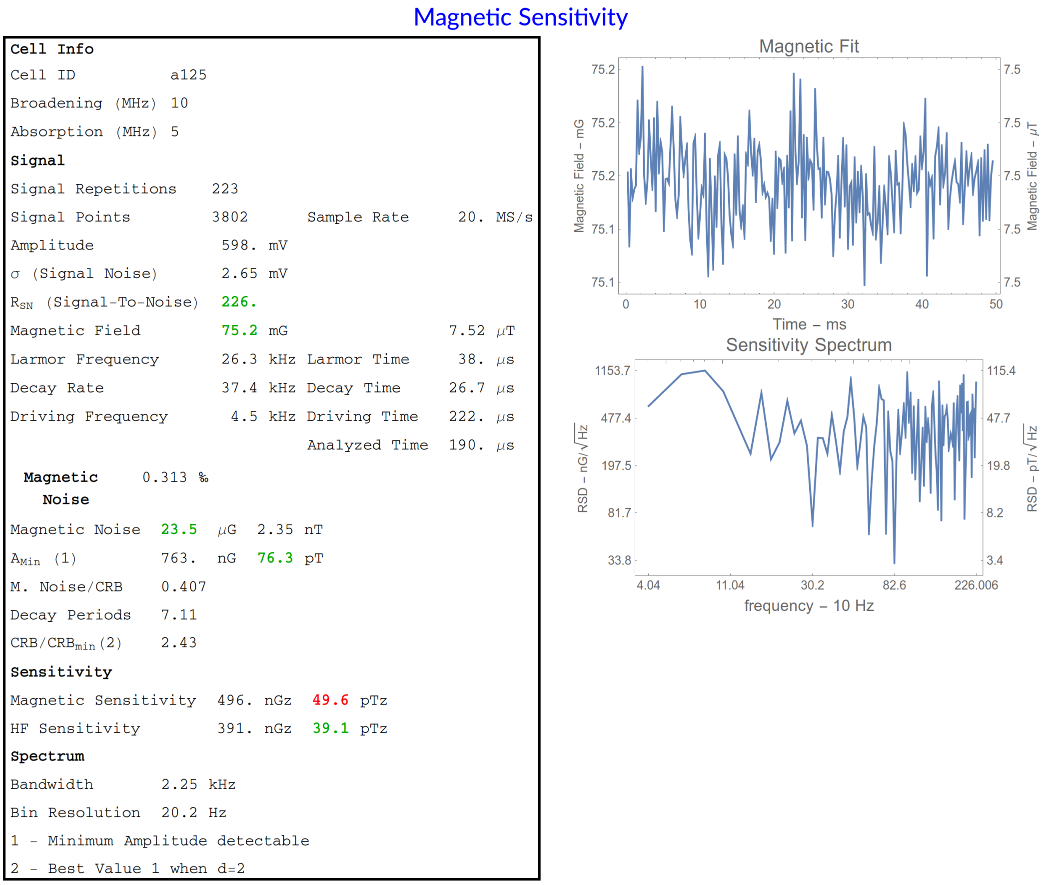

Magnetic Sensitivity

```
Cell Info
Cell ID          a125
Broadening (MHz)  10
Absorption (MHz)  5
Signal
Signal Repetitions    223
Signal Points         3802      Sample Rate      20. MS/s
Amplitude              598. mV
σ (Signal Noise)       2.65 mV
RSN (Signal-To-Noise)  226.
Magnetic Field         75.2 mG                   7.52 μT
Larmor Frequency       26.3 kHz Larmor Time      38. μs
Decay Rate             37.4 kHz Decay Time      26.7 μs
Driving Frequency       4.5 kHz Driving Time    222. μs
                                Analyzed Time   190. μs

  Magnetic     0.313 %
    Noise
Magnetic Noise  23.5  μG  2.35 nT
AMin (1)        763.  nG  76.3 pT
M. Noise/CRB    0.407
Decay Periods   7.11
CRB/CRBmin(2)   2.43
Sensitivity
Magnetic Sensitivity  496. nGz  49.6 pTz
HF Sensitivity        391. nGz  39.1 pTz
Spectrum
Bandwidth       2.25 kHz
Bin Resolution  20.2 Hz
1 - Minimum Amplitude detectable
2 - Best Value 1 when d=2
```

Figure 4.19: An example of the result outputted by the software: here the unit z stands for $\mathrm{Hz}^{-0.5}$.

of the sensor head can be stored;

- The section **simulate** allows for a full data simulation, which has been useful to verify the internal consistency and accuracy of the fitting process.
- in the **data** section, the button *divide* allows to properly extract the meaningful Larmor oscillation out of each Larmor signal; the other buttons allow to locate and import the data correspondent to the train of Larmor signals; the first signal can be plotted, before a complete analysis, with the button *plot*.
- in the **fit** section, the data can be finally analysed and the result outputted. An example of the final result is shown in figure 4.19.

Chapter 5

Results

Introduction

In the following experiments we have studied in detail how the Larmor signals properties (i.e. its amplitude, Larmor frequency, phase and decay rate) depends on the main experimental variables. The analysis covers both signals measured by the polarimeter (*parallel* and *perpendicular* polarizations) and their difference.
The experimental parameters that have been studied, in their effect on the signals, are:

- laser frequency (see section 5.1),
- temperature (section 5.2),
- laser input polarization (section 7.1.2),
- pump intensity (section 5.4.1),
- probe intensity (section 5.4.2),
- magnetic fields (section 5.5).

Main Results The main results found can be summarized as follows:

- the Larmor signals show a typical relaxation rate; its best value is around 3 kHz (see decay rate plot in figure 5.8);
- the sensor head best temperature (in terms of sensitivity) is close to 125°C (see figure 5.4);

- the best laser frequency is close to the 3→3 transition of the D_1 caesium spectrum (see plot in figure 5.2).
- the two orthogonal linear polarization components of the output signal, as seen by the polarimeter, are nearly out of phase (see phase difference plot in figures 5.3, 5.5, 5.7 and 5.8);
- the best laser polarization is elliptical (see plot in figure 5.5);
- The best signal (in term of sensitivity) is the *parallel* one, because it is favoured by the input laser elliptical polarization (see sensitivity plot in figures 5.2, 5.4, 5.13 and 5.16);
- the relaxation rate is proportional to the laser probe intensity (see decay rate plot in figure 5.8);
- the best pump intensity is the highest available (see plot in figure 5.7);
- the best probe intensity is around 1.1 $\mathrm{mW/mm^2}$ (see plot in figure 5.8);
- the magnetic range is $\approx [4, 100]$ mG (see plot in figures 5.12 and 5.15);
- the best angle of detection (magnetic field to direction of laser) is between 0 and 90° or, nominally, 45°;
- we reached a sensitivity as low as 4.3 $\mathrm{pT}/\sqrt{\mathrm{Hz}}$ (see sensitivity plot in figure 5.18);
- the magnetometer bandwidth is $\approx$ 850 Hz (see x-axis of the sensitivity plot in figure 5.18).

In the following sections we presents the main experimental findings in details which will prove the main results already outlined.

Experimental Conditions In the following experiments the input power is measured through a glass plate positioned just before the cell, which reflects nearly 4% of the laser light, enough to be measured and used for power measurements; the intensity considered is the average one given by $I = P/\sigma$, where P is the total laser power before the cell and σ is the laser beam size in correspondence of the cell (at $1/e^2$ of peak value). The beam diameter in correspondence of the cell is fixed for all the following experiments to roughly 1.4 mm.

We will refer to the parallel and perpendicular linear polarizations of the output Larmor signal and their difference simply with the terms *parallel*,

perpendicular and *difference.*
In the following experiments, we recorded how each Larmor signals (*parallel, perpendicular* and *difference*) changes when the experimental parameter selected is varied; the results show the signals properties (in terms of amplitude, Larmor frequency, phase and decay rate) as a function of the selected experimental parameter. Note that, in all results, with the term *phase difference* we mean the difference between the phase of the *parallel* and *perpendicular* signal and not the phase of the *difference* signal.
Each data point is obtained from the fitting of the corresponding Larmor signal.
Except when they are varied, the laser light input polarization and frequency are optimized to their best values, as described respectively in section 5.1 and 7.1.2.

5.1 Laser Frequency

In this experiment the Larmor signals have been analysed as a function of the laser frequency (measured directly with a wave meter), leaving all other parameters constants: the probe intensity is around 837 μW/mm^2, the temperature is ~118°C and the input polarization is set to its best elliptical value (see section 7.1.2).
The results are shown in figure 5.1, where the signal properties are plotted as a function of the laser frequency; the four vertical lines correspond to the 4 lines of the caesium D$_1$ spectrum (see section 3.2.1) and serve as a frequency reference.
As it can be seen, the input elliptical polarization makes the output *parallel* signal usually higher than the *perpendicular* one. The best decay rate value is reached around the third line of the D_1 caesium spectrum (transition 3→3), while the best amplitude is reached at a frequency 1 GHz lower; the amplitude and decay rate peak is approximately 10 GHz broad. A secondary maximum in amplitude is visible at a frequency 16 GHz lower than the peak one, i.e. at a frequency 7 GHz lower than the first line (transition 4→3).
The same conclusions are confirmed by observing the predicted sensitivity in figure 5.2 for all the three signals. The plot, obtained from equation 4.31, encapsulates in one picture the combined behaviour of both amplitude and decay rate and it is the one to use to find the best predicted performance (see section 4.8.1).
As shown in figure 5.1, the frequency is much more stable and reliable in the vicinity of the third peak where the signal-to-noise ratio is much higher.
The phase difference plot shows a rapid phase change around the two peaks

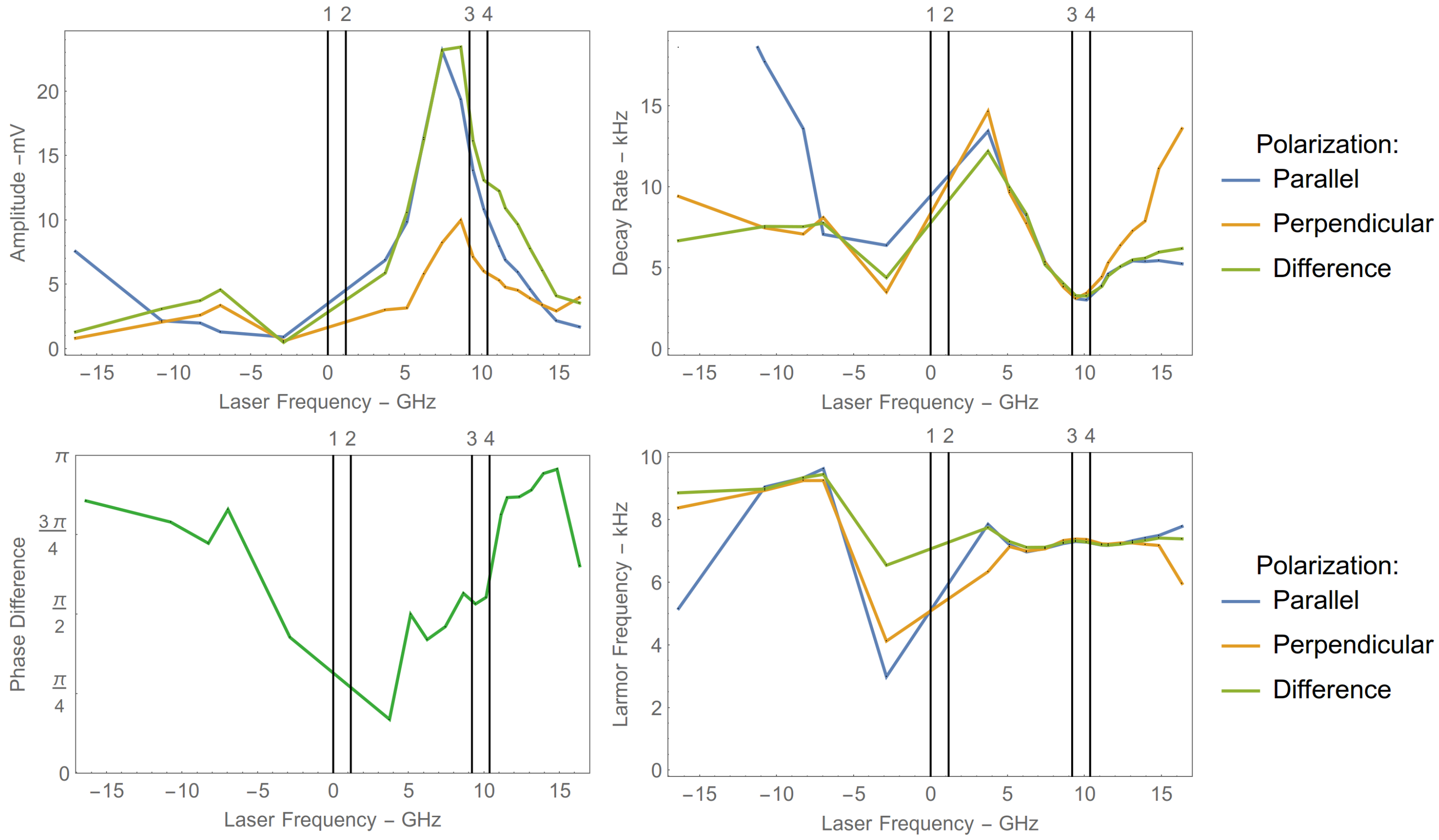

Figure 5.1: Larmor signals properties as a function of the laser frequency.

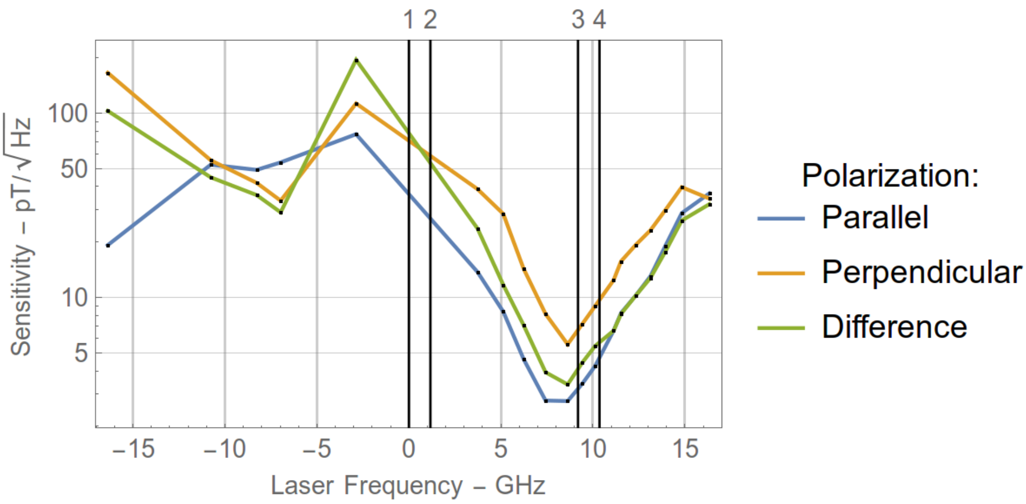

Figure 5.2: Predicted sensitivity as a function of the laser frequency.

in amplitude; the phase difference around the main peak is nearly $\pi/2$ and changes rapidly around the peak: for higher frequencies it goes closer to phase opposition while for lower frequencies it goes close to phase match where the polarimeter is less useful for signal subtraction. This explains why the *difference* signal doesn't provide a gain in sensitivity around the main peak.

Since the phase difference is very sensitive to the laser frequency (especially around the third line), we were able to reach nearly perfect phase opposition by adjusting the experimental parameters and remain very close to the sensitivity peak.

The model we developed in chapter 7 predicts the Lorentzian line shape of the signal amplitude and the rapid phase shift close to resonance (see respectively equation 7.32 and 7.34 in section 7.2.1).

5.2 Sensor Head Temperature

The following experiment describes the Larmor signals properties as a function of the sensor head temperature, all other parameters are constants: the probe intensity is around 806 μW/mm^2.

The results are shown in figure 5.3. As it can be seen, the amplitude of all signals reach a peak around 125°C and the peak relative to the perpendicularly polarized signal is reached at slighter higher temperature. The decay rate is peaked at a different temperature, around 100°C, and the combined

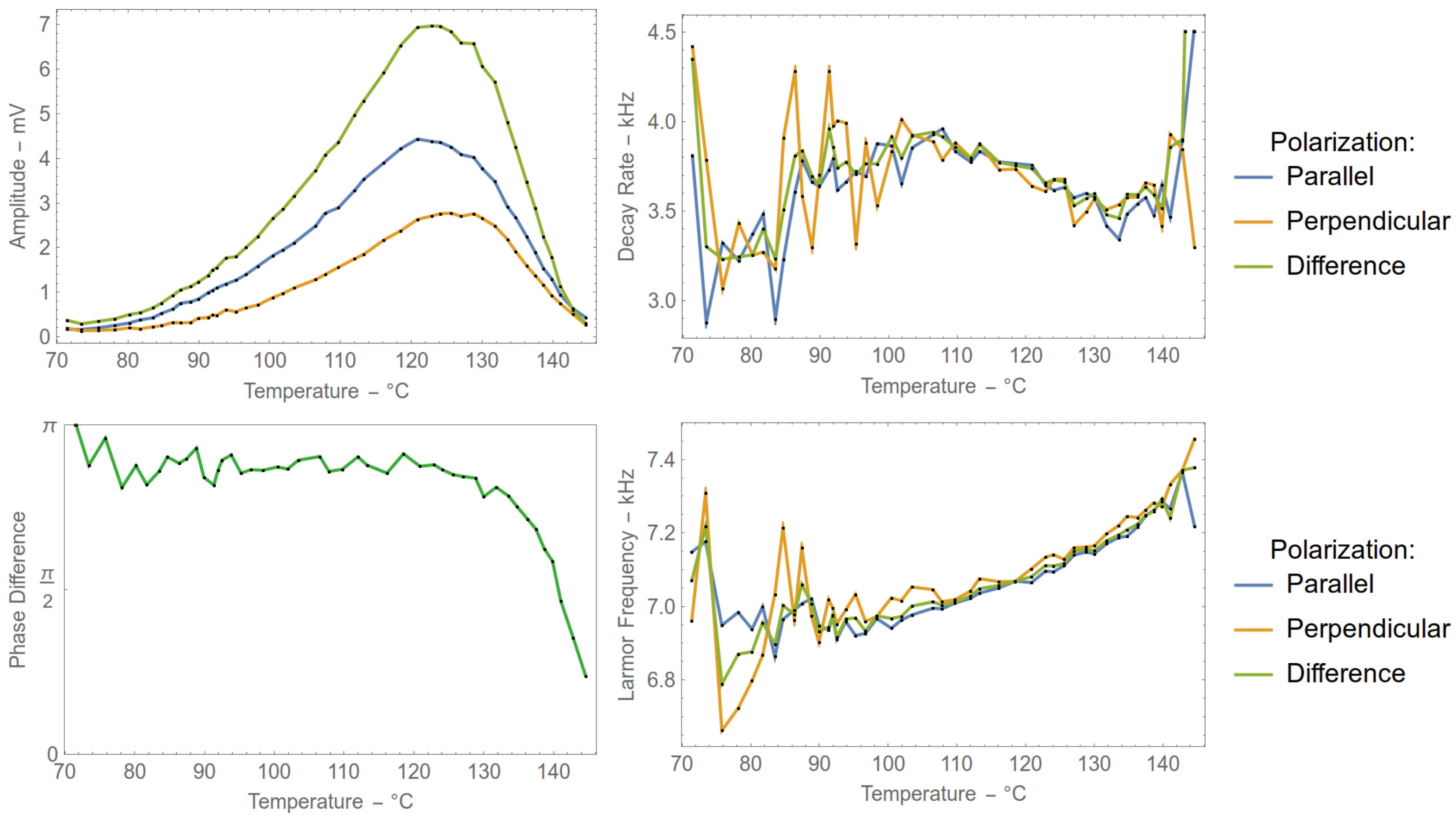

Figure 5.3: Larmor signals properties as a function of the sensor head temperature.

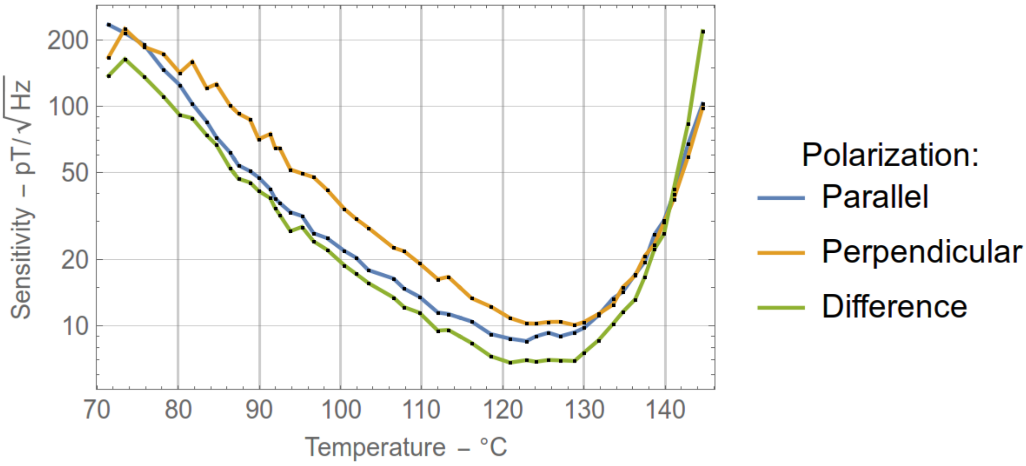

Figure 5.4: Predicted sensitivity as a function of the sensor head temperature.

(amplitude and decay rate) behaviour is shown in figure 5.4, which shows the predicted sensitivity plotted against the sensor head temperature; as it can be seen, the minimum (i.e. the best sensitivity) is reached around 125-130°C.

The behaviour described by the plot is simply explained by an initial increase in vapour density $n(T)$, which makes the caesium more visible, and a subsequent increase in caesium spin de-coherence, which causes a decreased visibility of the Larmor oscillations for temperatures higher than 125°C.

Furthermore the *parallel* and *perpendicular* signals are mostly in phase opposition but for temperatures higher than ∼135°C the phase difference tends to zero.

In a first instance, one can think that the crescent trend of the Larmor frequency is most likely due to the thermal expansion/contraction of the Helmholtz coils caused by the sensor head heater, which is reflected in an increase in the coils magnetic field in correspondence of the sensor head. Remembering the equation of the magnetic field B generated by a pair of Helmholtz coils of radius R in its centre point (see equation B.1), we can write:

$$B \propto \frac{1}{R} \Rightarrow dB \propto -\frac{1}{R^2}dR \propto -\frac{B}{R}dR \Rightarrow \frac{dB}{B} = -\frac{dR}{R},$$

where dB is the magnetic field variation generated by the radius variation dR; on the other end from equation 4.1:

$$\frac{d\nu_l}{\nu_l} = \frac{dB}{B},$$

where ν_l and $d\nu_l$ are respectively the Larmor frequency and its variation generated by the radius variation dR. Combining the two equations above we can write:

$$\frac{d\nu_l}{\nu_l} = -\frac{dR}{R}.$$

This identity suggests that the frequency variation observed (around 0.4 kHz over 7 kHz) should correspond to a radius variation of about -1.3 mm (i.e a contraction)[1].

This result is not physically possible for two reasons: the thermal expansion of the coils structure (plastic) is too low to justify such a variation in size and, most importantly, the material should expand not contract. As seen in section 3.5, we already suspect the presence of other buffer gasses in the cell which may cause undesired effects; for this reason, the increasing Larmor frequency, at increasing sensor head temperature, needs further careful investigation.

5.3 Laser Polarization

The following experiment analyse the Larmor signals as a function of the laser input polarization[2]; all other parameters are constants: the probe intensity is around 775 μW/mm^2 and the temperature around 124°C.

The polarization is changed using a $\lambda/4$ wave-plate positioned before the sensor head and it is measured through its angle of rotation: at 0 or 90° the input polarization is linear[3], at 45° is circular, and for all other angles is elliptical with a degree of ellipticity measured by the angle itself.

The results are synthesized in figure 5.5.

As it can be seen, the amplitude highest value is reached at $\frac{\pi}{8}$ and $\frac{3\pi}{8}$, where the polarization is elliptical. The Larmor frequency and decay rate are roughly stationary; the phase difference is also constant with a value slightly below phase-opposition for angles lower than 45° and slightly higher otherwise.

The light input polarization is rotated when interacting with the atoms in the sensor head. The output polarization can be measured easily by the polarimeter comparing the signals offsets of the *parallel* and *perpendicular*

---

[1] We are considering the Helmholtz coils, generating the perpendicular magnetic field, of radius R=2.35 cm.

[2] Here the term polarization shouldn't be confused with the same term used for the linear orthogonal components of the transmitted light out of the sensor head.

[3] More precisely the linear polarization is *parallel*; in other words it is fully transmitted by a PBS.

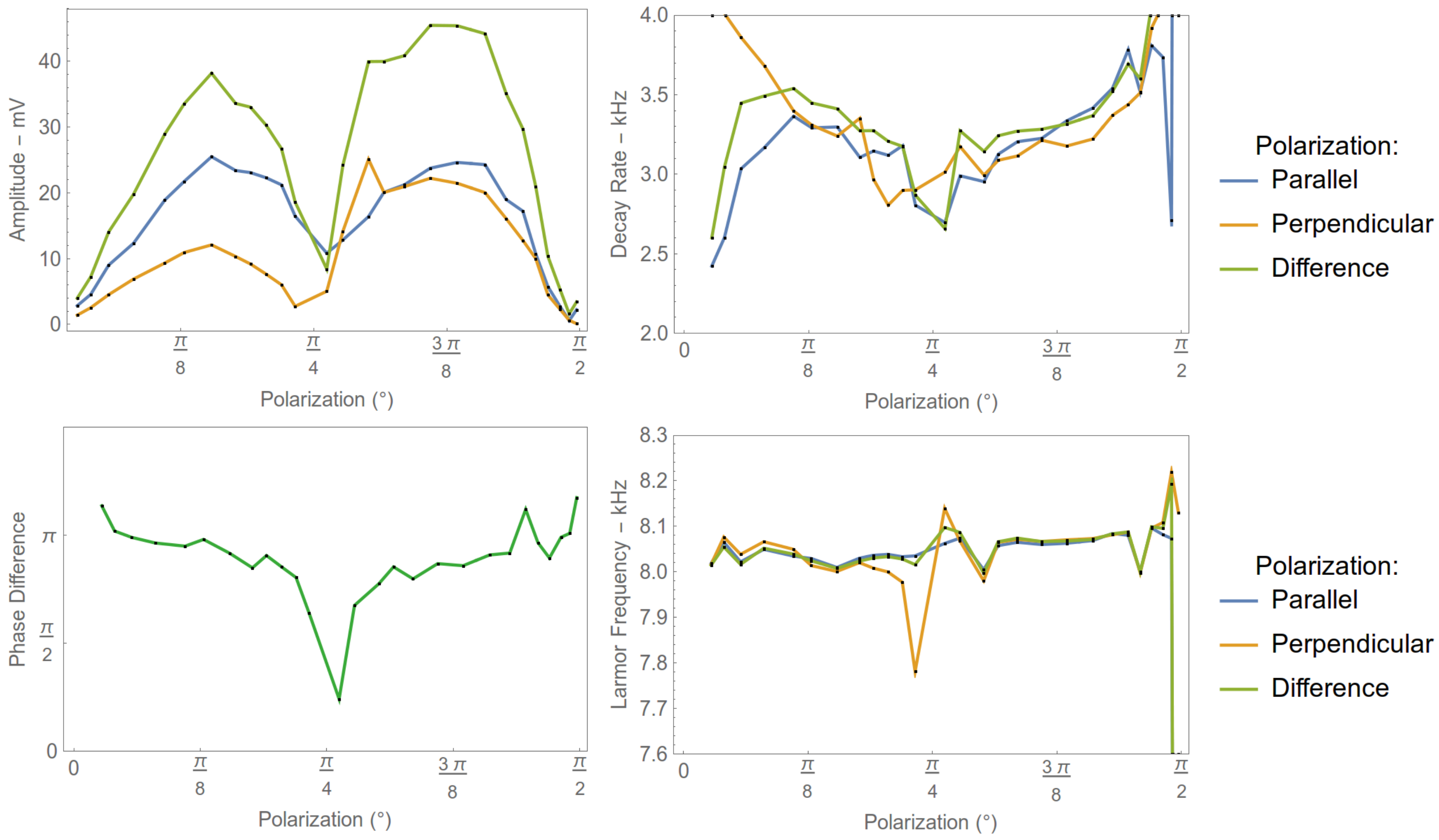

Figure 5.5: Larmor signal properties as a function of the light input polarization.

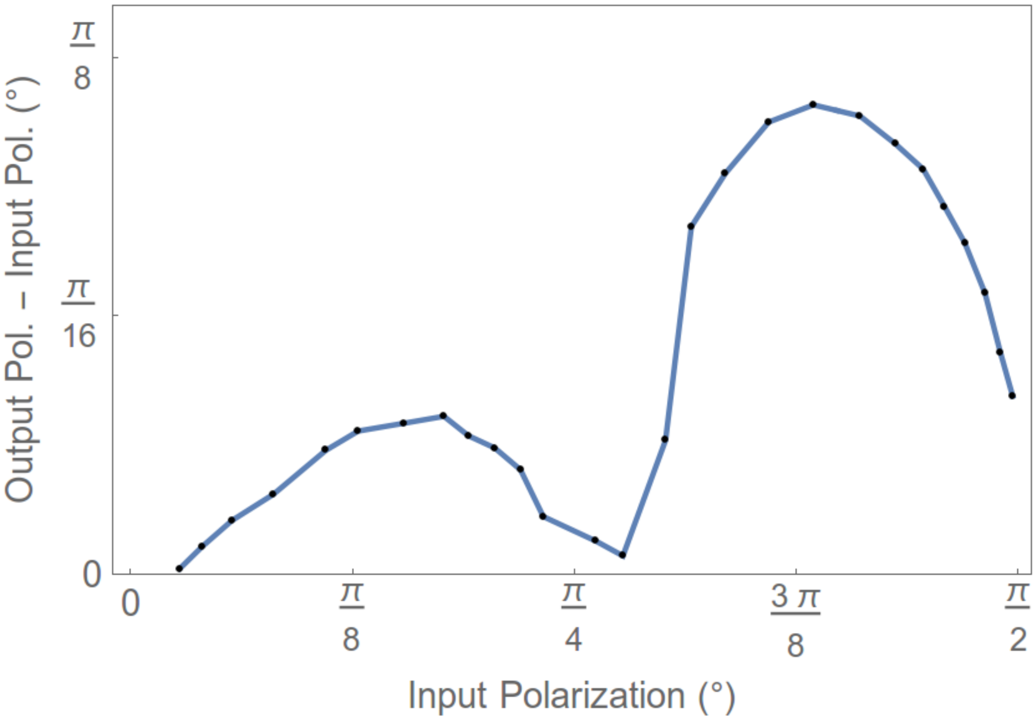

Figure 5.6: Polarization rotation as a function of input polarization.

signals (i.e. the output probe level). The plot in figure 5.6 depicts the output polarization rotation, i.e the difference between the output and input laser polarization as a function of the input laser polarization.
As it can be seen, the rotation peaks are very close to the amplitude ones, which proves that the best signal is reached when the atoms are having their highest interaction with the laser.

5.4 Laser Intensity

In this experiments we investigate the effect of the laser intensities on the signals. As already explained in section 4.1, the laser is amplitude modulated so that a short and highly intensive beam, called pump, is cyclically followed by a longer and weaker beam, called probe; this is represented in figure 4.3. We analyse the effects of both pump and probe intensities on the Larmor signals. In both cases, no parallel magnetic field is applied while the perpendicular magnetic field is fixed to 22.4 mG (i.e. a Larmor frequency of ∼7.9 kHz).

5.4.1 Pump Intensity

In this experiment the signals have been recorded varying the pump intensity while maintaining the probe intensity fixed (∼1 mW/mm^2, see section 5.4.2), and the temperature to 124 °C. The pump level is changed electronically by varying the driving frequency that controls the AOM out of the default 80 MHz.

The results are synthesized in figure 5.7. As expected, the amplitude follows a saturation curve, while the Larmor frequency, decay rate and phase difference are basically constant.

The experiment suggests the use of the highest available pump intensity to obtain the best macroscopic magnetization vector in the direction of the beam[4], because its high value doesn't influence the other signals properties: the phase difference, decay rate and most importantly the Larmor frequency.

5.4.2 Probe Intensity

In this experiment the signals have been analysed as a function of the probe intensity; the pump intensity is fixed to its highest value (∼ 3 mW/mm^2), and the temperature to ∼120 °C. The probe power is controlled by electronically changing the AOM efficiency, which in turns changes the power of its zero order beam (the one used in the experiment). The results are plotted, for both polarizations (and their difference), in figure 5.8.

Let's analyse the results separately:

- The **amplitude** reaches a peak at an intensity ∼44 times the saturation level[5] (1.1 mW/mm^2). For higher intensities the amplitude drops due to a drop of the pump level relative to the probe one and, secondary, because the undesired optical pumping phenomena, caused by the probe beam, interferes destructively with the Larmor precession.
  As it can be seen, the *perpendicular* signal drops more rapidly then the *parallel* one at intensities higher that 1.1 mW/mm^2.
- The **phase difference** between the two polarizations is almost stationary with a slight increasing behaviour around almost phase opposition.
- The Larmor **frequency** for all signals shows an initial stationary behaviour followed by an increase linearly proportional to probe intensity (the slope is roughly 360 Hz every 1 mW/mm^2); at intensities higher

---

[4] The amplitude of the magnetization vector is proportional to the Larmor signal amplitude (see section 4.5).

[5] The saturation intensity for the D$_1$ caesium line is 25 μW/mm^2=2.5 mW/cm^2.

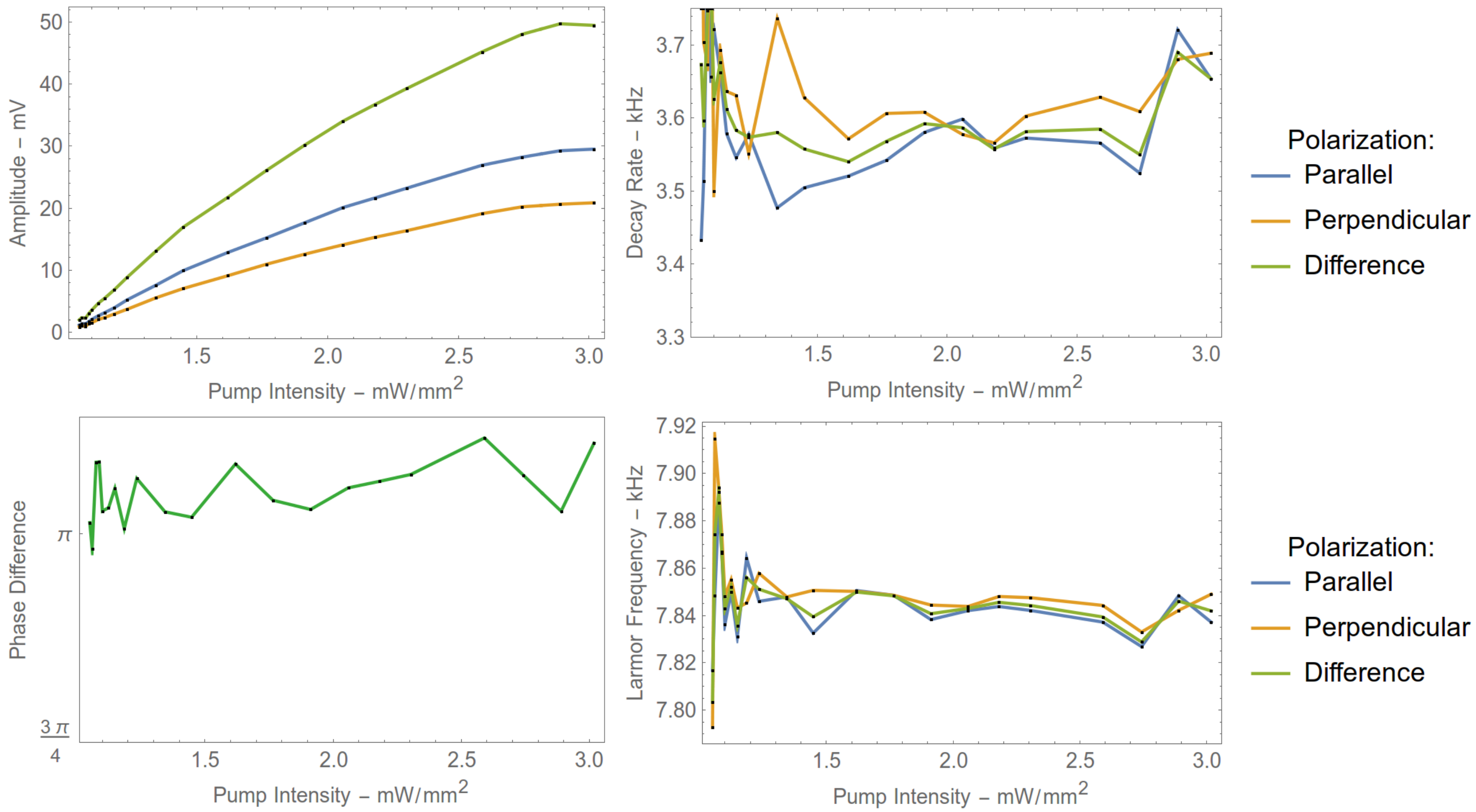

Figure 5.7: Larmor signals properties as a function of pump intensity.

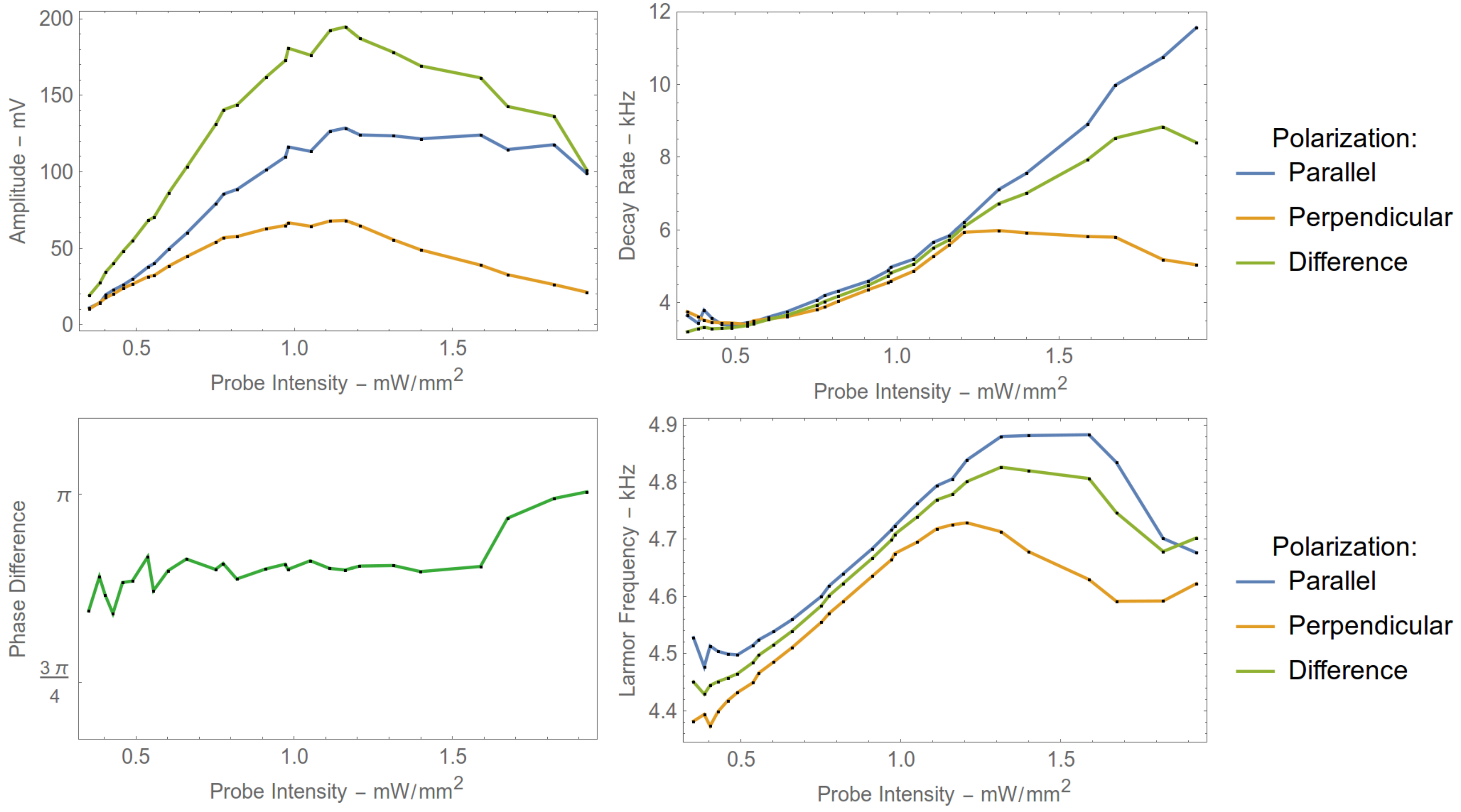

Figure 5.8: Larmor signals properties as a function of the probe intensity.

than ~1.2 mW/mm^2 the frequency strats to drop and the drop is more clear for the *parallel* signal. In part III, we will present a model, based on a first order multipole approximation of the density matrix, that explains how the laser generates a pseudo-magnetic field in the direction of the light (in this case 103 nT every 1 mW/mm^2) resulting in higher Larmor frequency for higher probe intensities. The model doesn't explain, however, the second phenomena (the decreasing frequency for higher intensities), which we can imagine related to a second order multi-pole contribution: at that point, the optical pumping is so high that slows down the Larmor oscillations.
The frequency extracted from the *parallel* and *perpendicular* signals are slightly different; the slight frequency gap can be justified by an initial polarization in favour of the parallel polarization, which results in a bigger pseudo-magnetic field for that component. Figure 5.9 shows

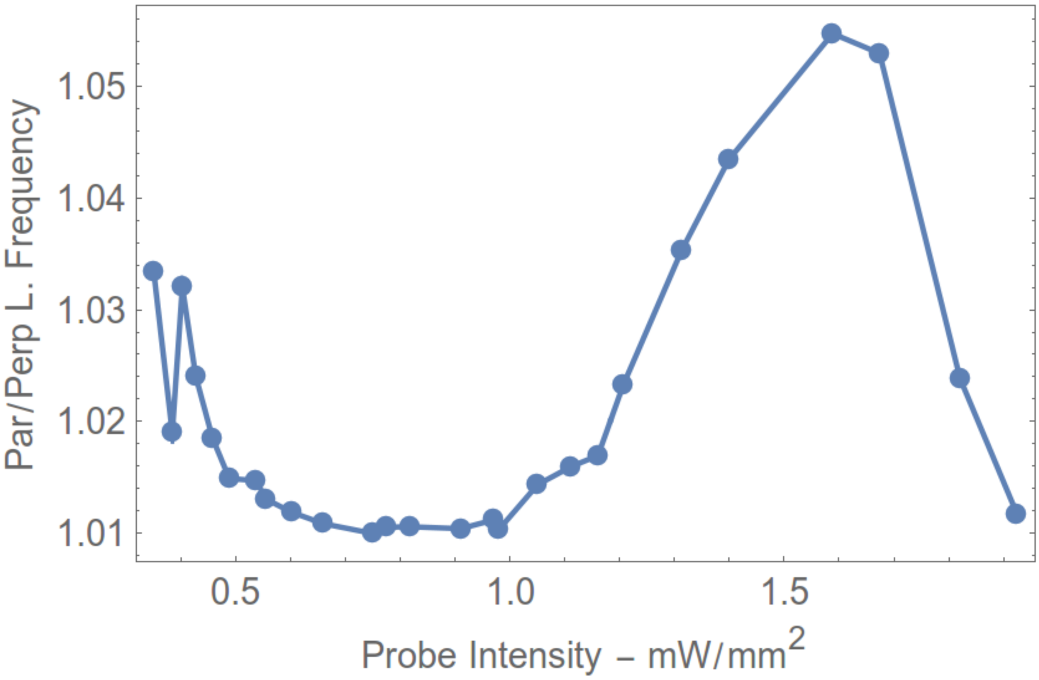

Figure 5.9: Parallel to perpendicular Larmor frequency ratio as a function of the probe intensity.

the parallel to perpendicular frequency ratio as a function of the probe intensity, which suggest the best intensity range of detection in the interval 500-1200 μW/mm^2; around the amplitude peak, the parallel and perpendicular Larmor frequencies have still roughly the same value.

- The **decay rate** shows a stationary initial behaviour for lower intensities, followed by a (slightly parabolic) increase and a subsequent slight decrease of the *perpendicular* component for intensities higher than ~1.2 mW/mm^2. The model we developed predicts the initial increasing trend; it doesn't however predicts the slight parabolic trend; we can ascribe this and the following slightly decreasing trend of the *perpendicular* component to a second order optical pumping phenomena.

5.5 Magnetic Field

In this experiments the Larmor signals have been explored as function of the magnetic fields, leaving all other parameters constant (probe intensity around 1.1 mW/mm^2, pump at its highest value value, temperature near 130°C). We used two pair of Helmholtz coils to generate two independent and orthogonal components of the magnetic field in correspondence of the sensor head: one parallel and the other perpendicular to the laser beam direction. The effect that these two components have on the signals have been explored in two independent experiments; in the first one the perpendicular magnetic field is varied and the parallel one is set to zero, in the second the parallel magnetic field is changed leaving the perpendicular one constant[6].
We measure the magnetic field amplitude in correspondence of the sensor head by applying formula 4.1 to the extracted Larmor frequency.
We have preventively verified that we are measuring a real magnetic field by conducting an experiment in which the magnetic field obtained from the Larmor frequency is compared to the magneic field measured from the current flowing in the Helmholtz coils applying formula B.1; the result is plotted in fig 5.10. As it can be seen the slope is almost one and the offset is due to the fact that formula B.1 applies in the ideal case of perfect Helmholtz coils, and measure performed exactly in its centre point.
In the following sections we analyse the effects of the perpendicular and parallel magnetic fields on the Larmor signals.

5.5.1 Perpendicular Magnetic Field

When varying the perpendicular magnetic field, the Larmor frequency extracted from the *parallel* and *perpendicular* signals are consistent to one another (see plot in figure 5.11), so we have used the frequency extracted from the *difference* signal to measure the magnetic field, using equation 4.1.

---

[6] As we will clarify, the perpendicular magnetic field must have a non zero initial value for a signal to be observed.

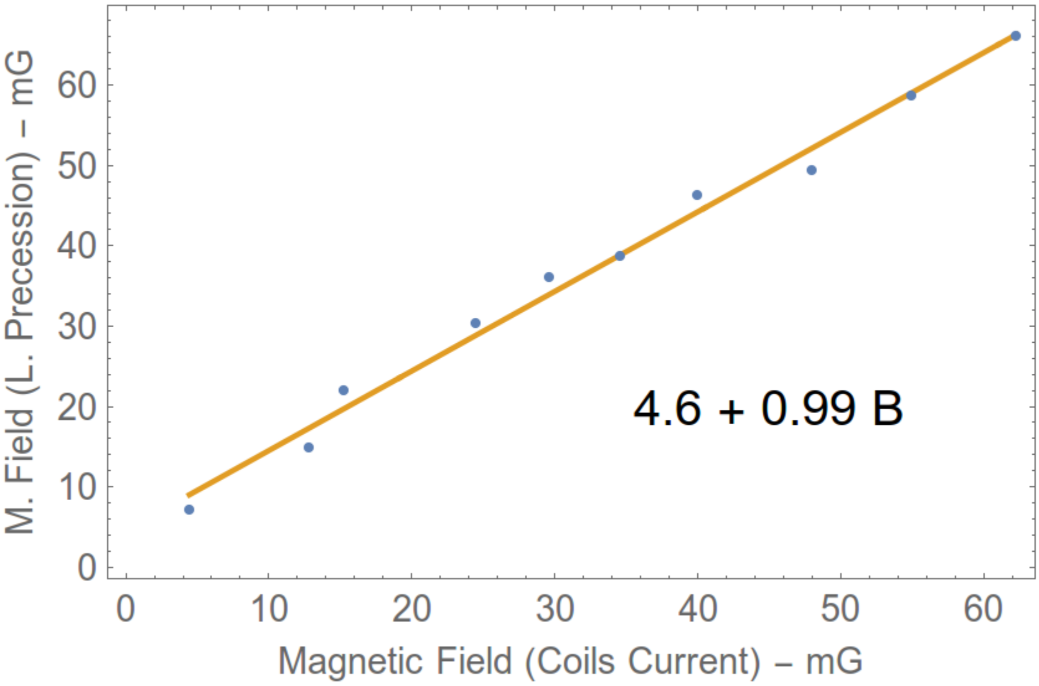

Figure 5.10: The plot shows the magnetic field extracted from the signals Larmor frequency against the magnetic field extracted from the measured coils current.

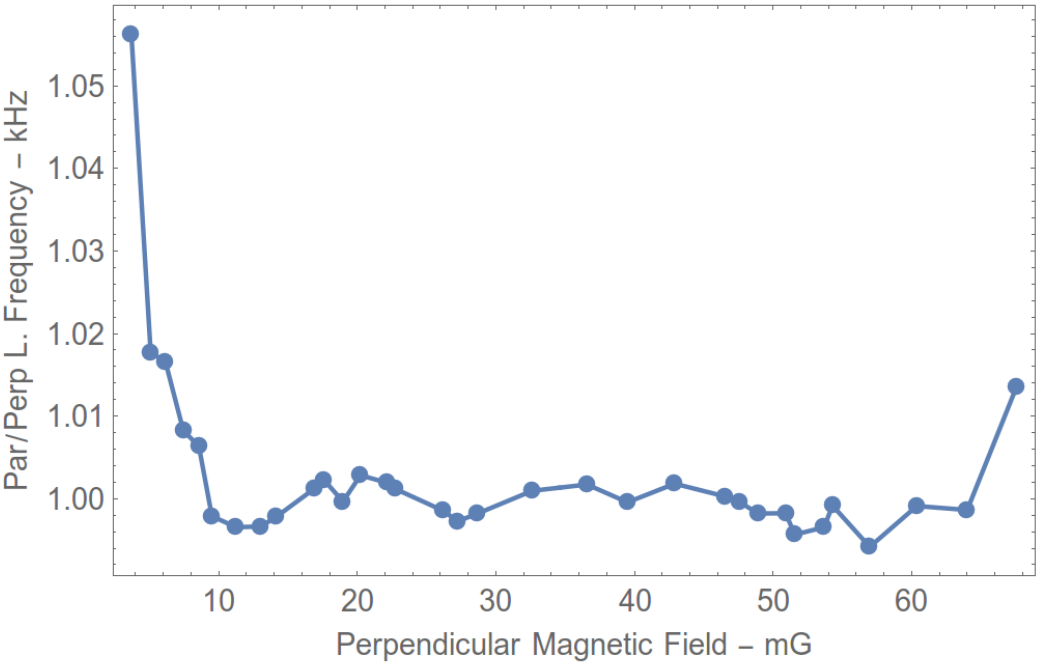

Figure 5.11: The ratio between the frequency extracted from the *parallel* and *perpendicular* signals is plotted against the magnetic field extracted from the *difference* signal. The plot simply shows that the two measures are consistent with one another.

The general results are plotted in figure 5.12, where, as said, the x axis corresponds to the magnetic field sequence extracted from the *difference* signal. As it can be seen, the amplitude of the three signals is almost constant until 40 mG where it starts to rapidly drop, while the decay rate grows linearly with the magnetic field. Those two behaviour are predicted by our model, as explained in chapter 7. The phase difference shows a slight decreasing trend around phase opposition.
Figure 5.13 plots the predicted sensitivity as a function of the perpendicular magnetic field amplitude; the highest magnetic field measurable is ≈100 mG, as already mentioned in section 4.6.4.

5.5.2 Parallel Magnetic Field

As in the previous case, the Larmor frequency extracted from the *parallel* and *perpendicular* signals are consistent with one another (see plot in fig-

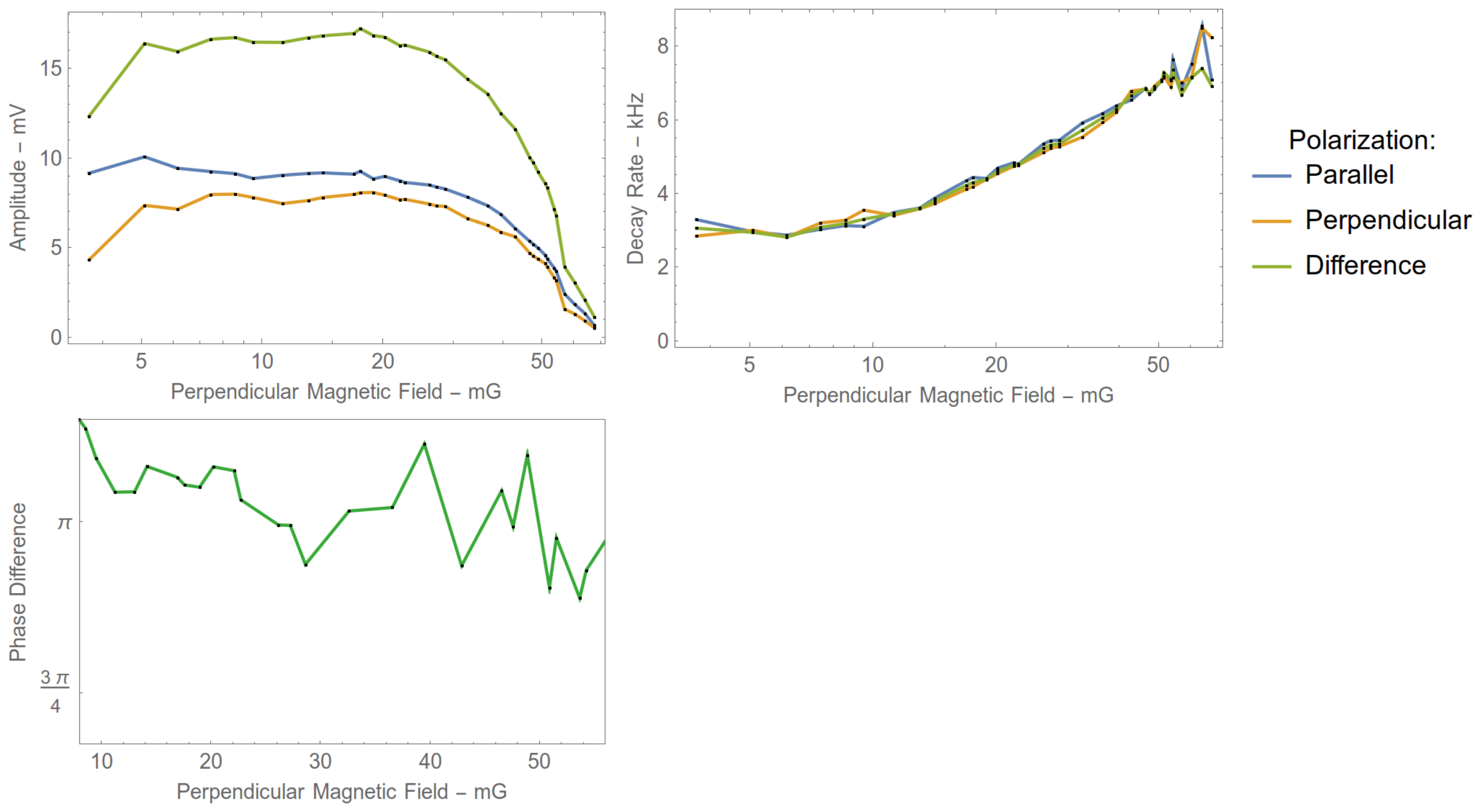

Figure 5.12: Larmor signal as a function of perpendicular magnetic field amplitude. The x axis of the amplitude and decay rate plots is in logarithmic scale.

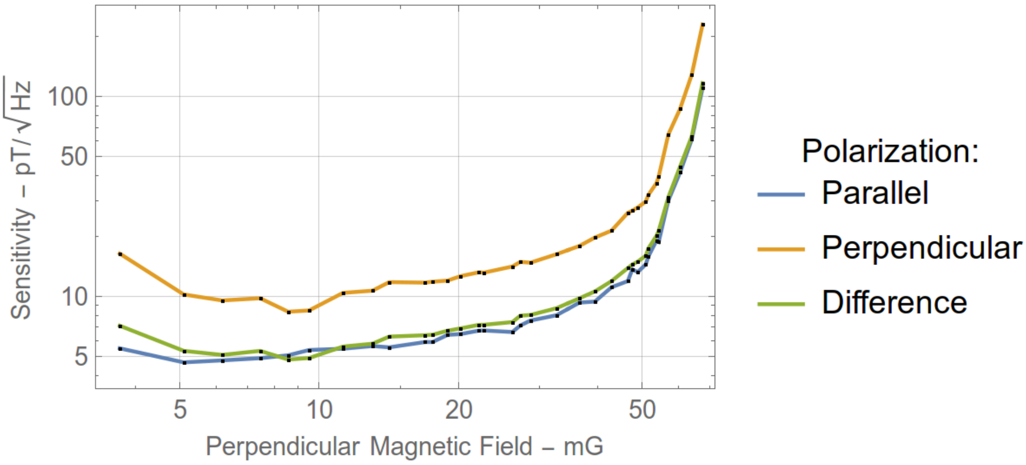

Figure 5.13: Expected sensitivity as a function of the perpendicular magnetic field amplitude. The x axis is in logarithmic scale.

ure 5.14), and we have used the frequency extracted from their difference to measure the magnetic field.

We find experimentally that we don't detect a signal when only the parallel magnetic field is applied; in fact the magnetization generated by the pump in the direction of the laser beam cannot precess when only a parallel magnetic field is present.

In this experiment the perpendicular magnetic field is fixed to 9 mG and the parallel one is varied. As it can be seen in the results in figure 5.15, the amplitude reaches a peak around 11 mG; we find that this value is not fixed and it is resonant with the pump time duration.

The best amplitudes reached in this case is more than double the best amplitudes reached with only a perpendicular magnetic field (see amplitude plot in figure 5.12); this, together with the observation that no signal is detected with only a parallel magnetic field, suggests the detection of an external magnetic field at an angle between 0 and 90° to the laser direction, or as is typically done [15, 26], fixed at 45°.

The decay rate plot shows a minimum around the resonant magnetic field, followed by a linear trend: its slope is lower (and around half) the slope found in the previous experiment (for the perpendicular magnetic field).

Figure 5.16 shows the expected sensitivity plotted against the parallel magnetic field amplitude. As it can be seen, the expected sensitivity reaches a minimum lower than the minimum reached by the sensitivity of the perpendicular magnetic field alone (see plot in figure 5.13); this suggests an increased

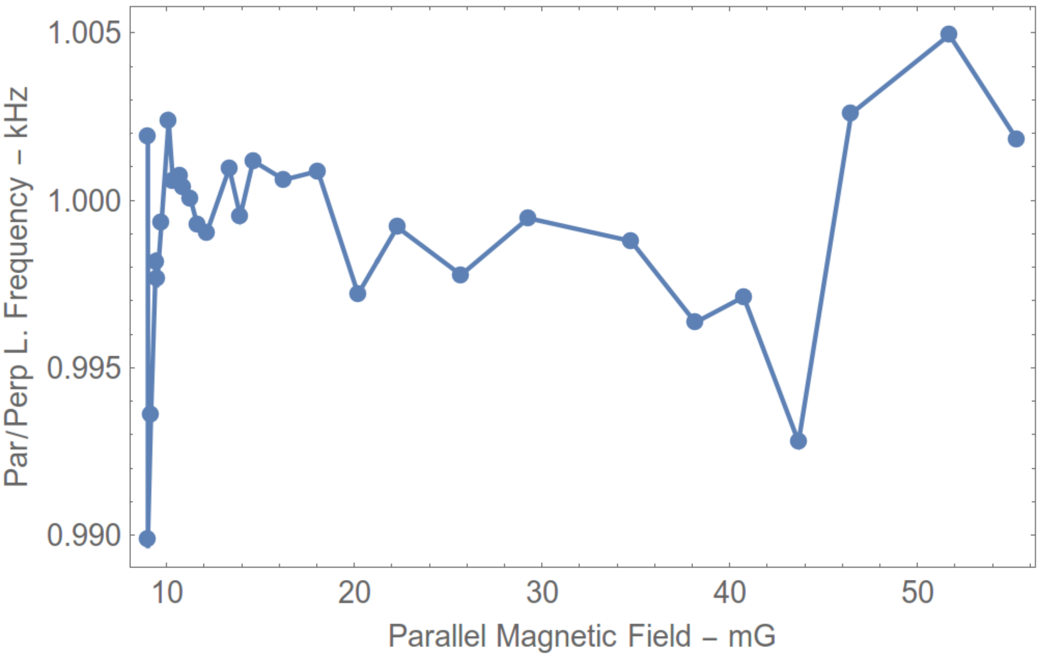

Figure 5.14: The ratio between the frequency extracted from the *parallel* and *perpendicular* signal is plotted against the magnetic field extracted from the *difference* signal. The plot shows that the two measures are consistent to one another.

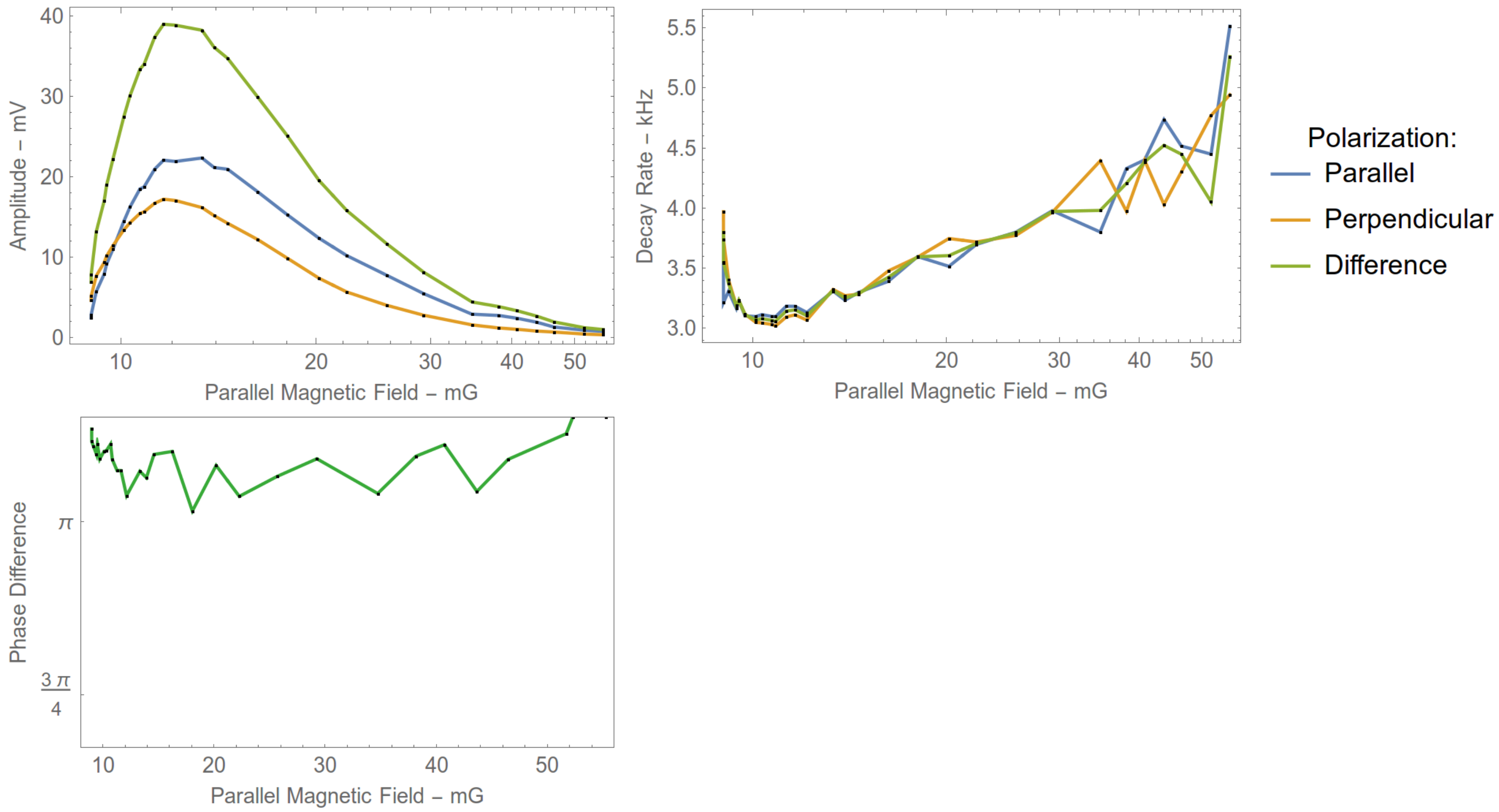

Figure 5.15: Larmor signals properties as a function of the parallel magnetic field amplitude. The x axis of the amplitude and decay rate plots is in logarithmic scale.

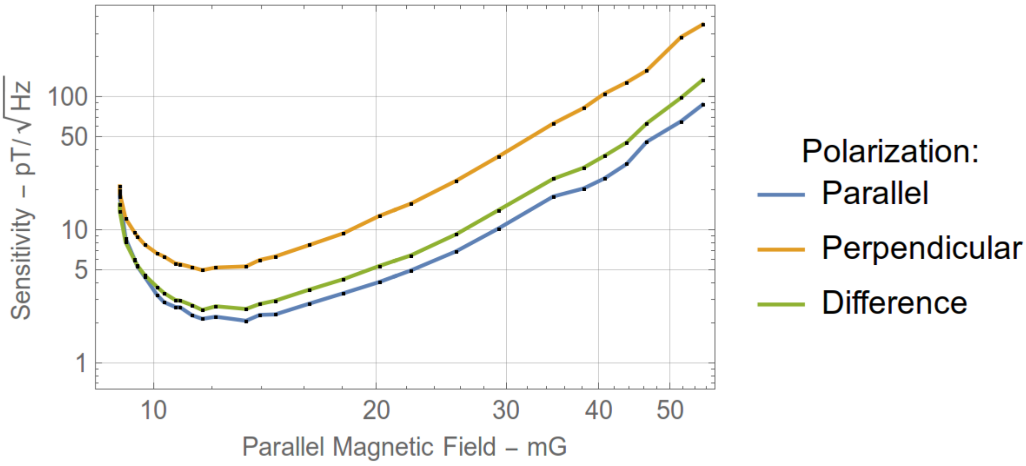

Figure 5.16: Expected sensitivity as a function of the parallel magnetic field amplitude. The x axis is in logarithmic scale.

performance when detecting both a parallel and perpendicular component of the magnetic field.

5.6 Sensitivity

The previous results focus on the properties of a single Larmor signal (one for each polarization component); as discussed in section 4.7, to give a complete characterization of the apparatus sensitivity in the frequency domain it is necessary to record a train of Larmor signals[7].
An example of a measured magnetic field sequence is shown in figure 5.17; each measure is extracted from a train of 339 Larmor signals, each lasting 588 μs; the total signal time is therefore 200 ms. The external perpendicular magnetic field (generated by a pair of Helmholtz coils) is around 25.3 mG (red line).
The plot in figure 5.18 shows, in logarithmic scale, the corresponding sensitivity plot in the frequency domain. The magnetometer bandwidth[8] of ∼ 850 Hz defines the highest frequency in the plot.
In the magnetic plot (figure 5.17), a periodic magnetic noise is visible; this is confirmed by the peak in the sensitivity plot at around 200 Hz (figure

---

[7] In the following experiment we capture only the *parallel* signal cause it gives slightly better results in terms of sensitivity then both the *perpendicular* and *difference* signal.

[8] As seen in section 4.7.3, the magnetometer bandwidth is defined as $f/2$, where $f = 1/T$ is the magnetic sequence driving frequecy and T the duration of each signal.

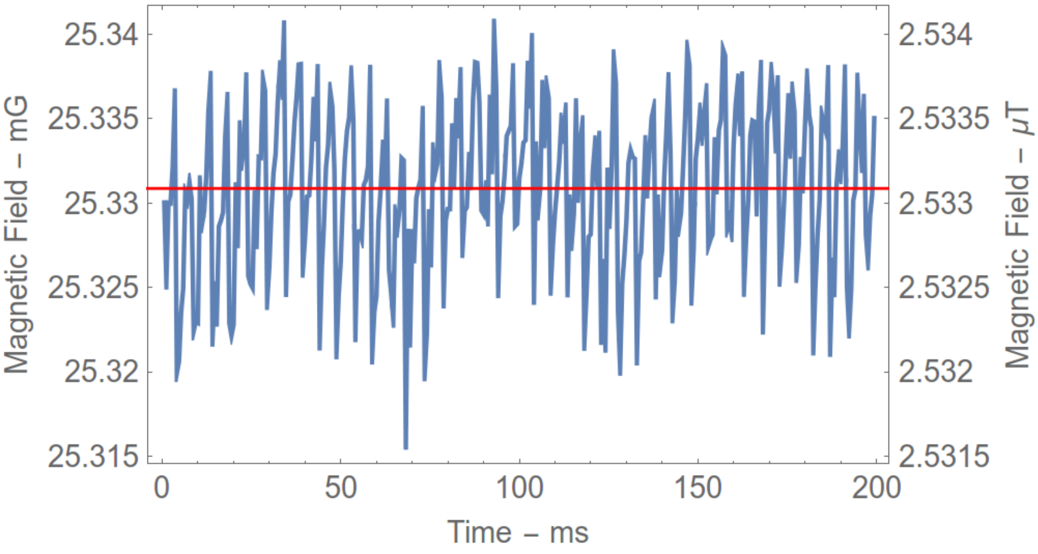

Figure 5.17: The sequence of magnetic field measures (extracted from a train of Larmor signals) is plotted as a function of time. The red line indicates the magnetic field averaged value $\sim$ 25.3 mG (2.05 μT).

5.18). The peak value is much higher then the average one, which causes the sensitivity mean value to increase; in order to give a measure of the sensitivity white background, we used the geometric mean (green line) which is less affected by rare values, which are mostly caused by external magnetic noise. As it can be seen we are able to reach a sensitivity as low as 8.3 pT/$\sqrt{\text{Hz}}$ (the flat level in the sensitivity plot); this level is due mostly to the fitting noise and any other source of white magnetic noise, while the peak at 200 Hz can be ascribed to external magnetic noise. No trend is visible in the sensitivity plot which means that the noise due to the magnetometer response is either white or lower than the flat background.
Another example of magnetic signal detected, with corresponding sensitivity plot, is reported in figure 5.19; in this case we reached a sensitivity as low as 4.3 pT/$\sqrt{\text{Hz}}$ with the same magnetometer bandwidth.

5.6.1 Magnetic Field Artificial Modulation

We tested the apparatus by artificially modulating the magnetic field with a square wave with an amplitude of 0.2 mG and a frequency of 100 Hz. Figure 5.20 shows on the upper plot the corresponding magnetic signal measured,

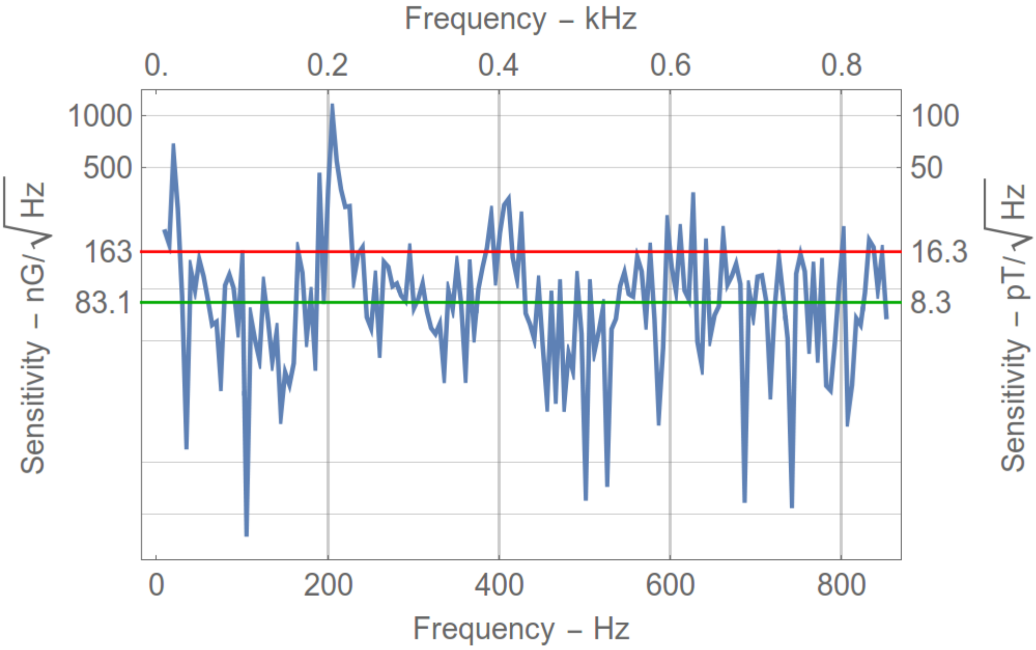

Figure 5.18: Sensitivity plot corresponding to the magnetic signal in figure 5.17. The red line represents the sensitivity average (16.3 pT/$\sqrt{\text{Hz}}$), while the green line indicates the sensitivity geometric mean (8.3 pT/$\sqrt{\text{Hz}}$) which is less affected by peaked values.

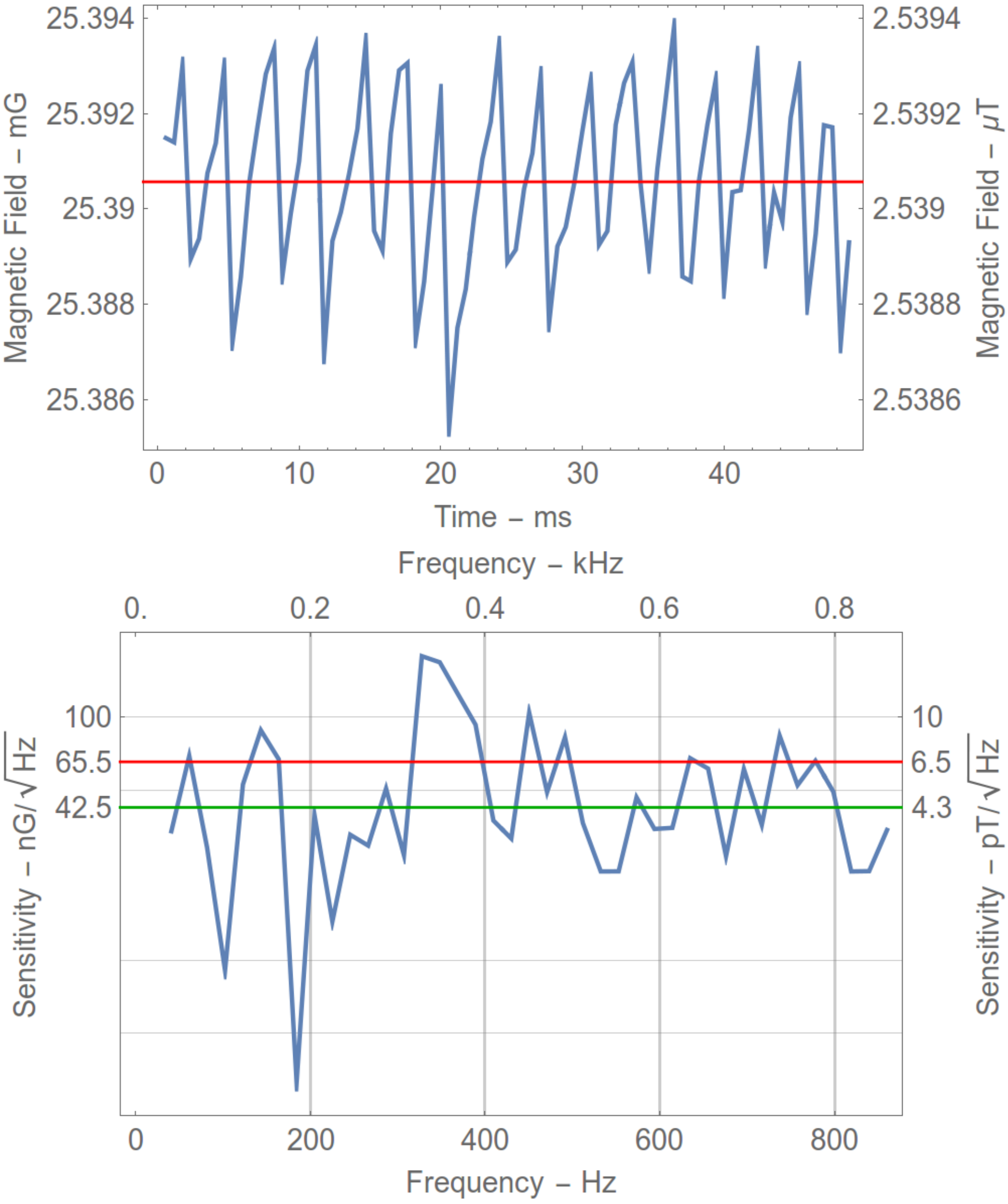

Figure 5.19: Another example of magnetic signal (top) and corresponding sensitivity plot (bottom). The sensitivity geometric mean (green line) is 4.3 pT/$\sqrt{\text{Hz}}$. An external noise peaked at ≈ 350 Hz is detected.

in which the external modulation is reflected in the plot. The selectivity plot on the bottom side of the figure shows, as expected, a high peak at the modulation frequency.
Using formula 4.32 with T_{tot}=50 ms we find that the sensitivity correspondent to 0.2 mG is 4 nT/$\sqrt{\mathrm{Hz}}$, which corresponds to the sensitivity peaked value at 100 Hz. From the averaged sensitivity value (176 pT/$\sqrt{\mathrm{Hz}}$) we find that the actual minimum signal detectable in this case is $\approx$ 8 pT=80 nG.

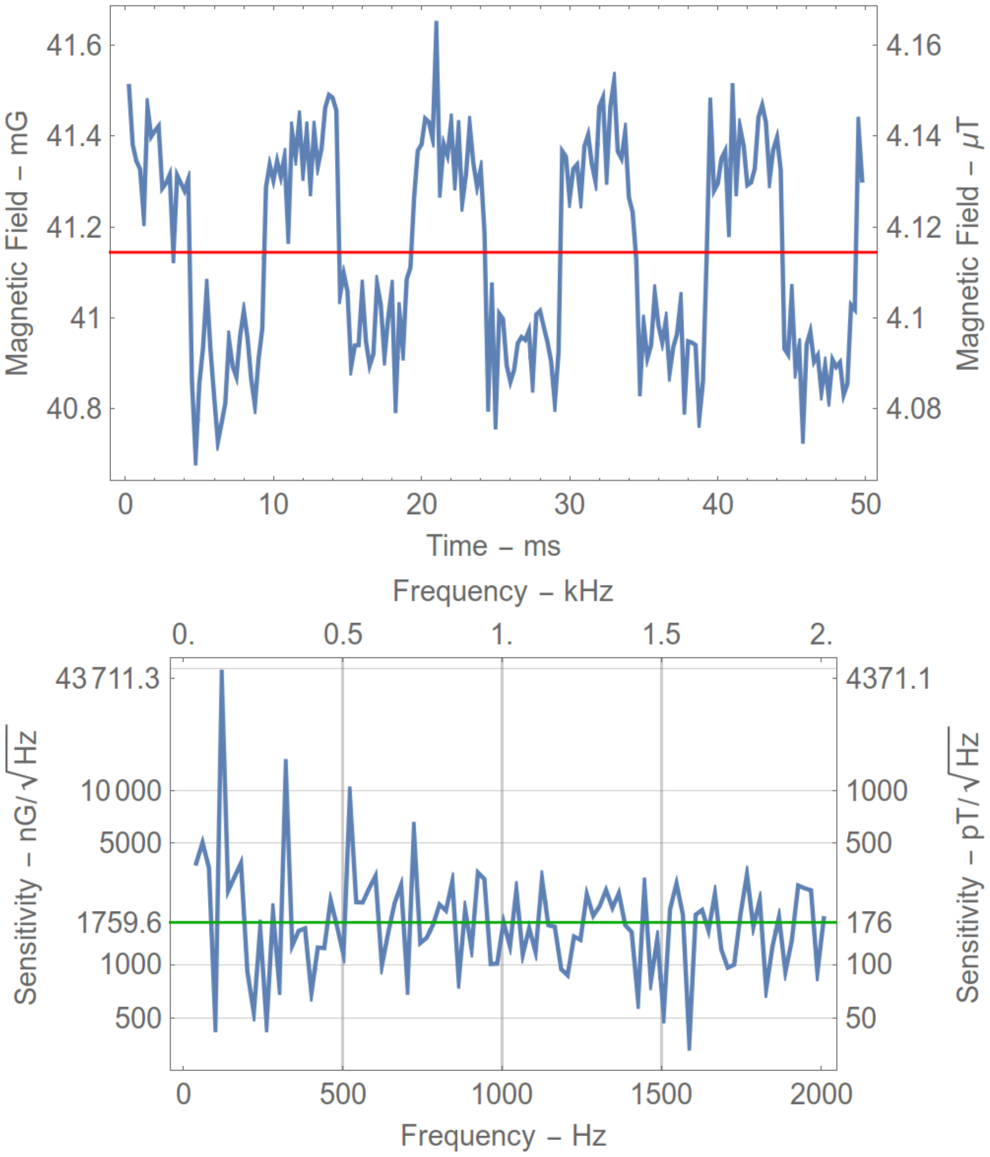

Figure 5.20: The upper plot shows the magnetic field obtained from the artificial modulation of the external magnetic field with a square wave. The lower plot shows the corresponding sensitivity.

Part III

Theory

Chapter 6

Density Matrix Formalism

The goal of this chapter is to develop a first order multipole model, under the density matrix formalism, that describes the optical pumping phenomena inside the sensor head cell. In this chapter we provide the technical formalism used to support the main conclusions outlined in the next and last chapter.

6.1 System Definition

We label the ground and excited states of the D_1 line with the letters g and e respectively. The hyperfine structure produces a double splitting of the ground and excited states; each sub-level will be denoted with the numbers *1* and *2* respectively. Their total atomic angular momentum is $F_1 = 3$ and $F_2 = 4$ for both ground and excited states. The energy structure and labelling is depicted in figure 6.1. As it can be seen, in the presence of a magnetic field $\vec{B}$, each hyperfine level (F) splits in $2F + 1$ magnetic sub-levels, which otherwise are degenerate.

6.1.1 System Simplification

The system presented, composed of four levels, each spit in magnetic sub-levels, is too complicated to be solved analytically but, as we will show, we are able to analytically solve a two levels system, composed of a ground and excited state with Zeeman sub-levels, under a first order approximation. The results are enough to draw the main qualitative conclusions about the experiment, but the model can also be extended to the general case of two ground and excited states.

In the following we will analytically describe only one of the four possible $g \rightarrow e$.

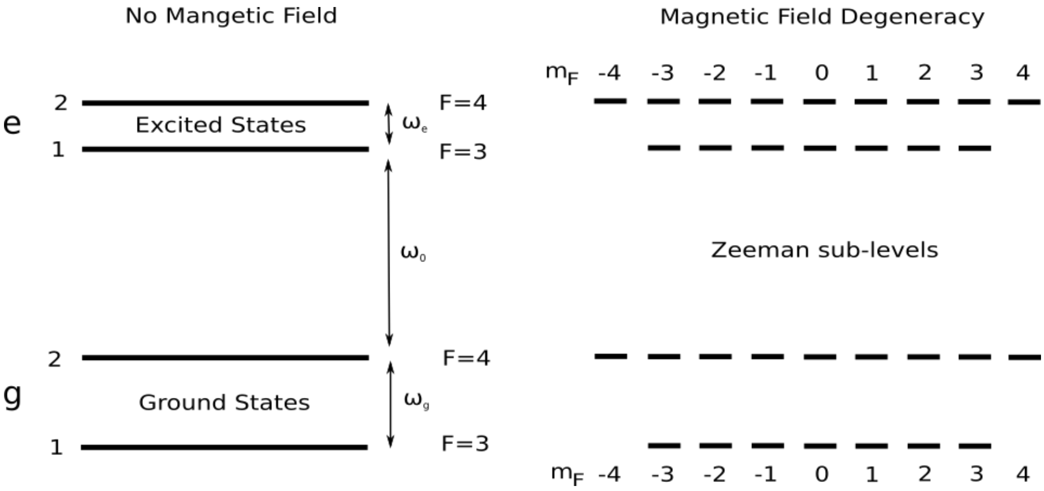

Figure 6.1: The plot on the left shows the energy structure of the D_1 caesium spectrum, without magnetic degeneracy; the values of ω_0, ω_g and ω_e are reported in table 2. When a magnetic field is present each hyperfine level (F) is split into $2F+1$ magnetic Zeeman sub-levels (see plot on the right).

6.1.2 Quantum States

The system is described by the state $|\psi\rangle$ given by a superposition of the eigenvectors $|l, m_l >$, labelled using the Dirac notation: l stands for the level label (g or e) and m_l refers to the Zeeman sub-level. The general state $|\psi\rangle$ can be written as:

$$|\psi >= \sum_{l=g}^{e} \sum_{m_l=-F_l}^{F_l} c(l, m_l) \, |l, m_l\rangle \, ,$$

where the population[1] of the state $|l, m_l\rangle$ is given by:

$$|c(l, m_l)|^2 = | \, \langle l, m_l | l, m_l \rangle \, |^2,$$

while all other terms $\langle l_1, m_{l_1} | l_2, m_{l_2}\rangle$ represents the system coherences.

6.1.3 Density Matrix

The density matrix operator is defined by:

$$\rho = |\psi\rangle \langle\psi| = \sum_{l_1, m_{l_1}} \sum_{m_2, m_{l_2}} \langle l_1, m_{l_1} | l_2, m_{l_2}\rangle \, |l_1, m_{l_1}\rangle \, \langle l_2, m_{l_2}| \, . \tag{6.1}$$

---

[1] The term *population* refers to the probability of the system to be in that particular state.

The **average value** $\underline{\mathrm{A}}$ of a generic operator A (which could be also vectorial) is given by:

$$\underline{\mathrm{A}} := |A\rho|, \tag{6.2}$$

where $|\cdot|$ is the trace operator.

6.1.4 Projection Operators

The ground and excited states projection operators P_g and P_e[2] are respectively defines by:

$$\begin{aligned} P_g &= \sum_{m_g} |g, m_g\rangle \langle g, m_g| \,, \\ P_e &= \sum_{m_e} |e, m_e\rangle \langle e, m_e| \,. \end{aligned} \tag{6.3}$$

The effect of these operators on the general state $|\psi\rangle$ is to collapse the system onto the ground or the excited states respectively, hence the name projection operators. It is easy to prove that:

$$P_g + P_e = 1. \tag{6.4}$$

The ground and excited state overall populations p_g and p_e are respectively:

$$\begin{aligned} p_g &= \underline{\mathrm{P}}_g = |P_g\rho|, \\ p_e &= \underline{\mathrm{P}}_e = |P_e\rho|. \end{aligned}$$

6.1.5 Master Equation

The density matrix ρ is used to write the **Shrödinger-von Neumann equation**, given by:

$$\partial_t\rho = -\frac{i}{\hbar}[H, \rho] + V_D. \tag{6.5}$$

In this equation H is the system Hamiltonian which describes the dynamics of the system; in particular H is a sum of the free atomic Hamiltonian H_A, which describes the basic system dynamics, the atom-field interaction Hamiltonian H_{AF}, which describes the interaction between the light and the

---

[2] We use the symbol P for both the polarization vector $\vec{P}$ and the projection operators P_g and P_e; the symbols are easily distinguishable cause the first is used as a vector while the second always with subscripts g or e; furthermore in this context the polarization vector is not used.

caesium vapour, and the magnetic Hamiltonian H_B, describing the effect of the magnetic field $\vec{B}$. Therefore we can formally write:

$$H = H_A + H_{\mathrm{AF}} + H_B. \tag{6.6}$$

The term V_D in equation 6.5 is the decay operator which describes the natural quenching of the excited states populations, due to spontaneous emission, and the rapid decay of the coherences.
We define the time **derivative** (averaged value) $\underline{\dot{\mathrm{A}}}$ of a generic operator A as:

$$\underline{\dot{\mathrm{A}}} := |\dot{\rho}A| = \frac{1}{i\hbar}|[H,\rho]A| + |V_D A| = \frac{1}{i\hbar}|\rho[A,H]| + |V_D A|, \tag{6.7}$$

where, in the last step, we have used the identity $|[H,\rho]A| = |\rho[A,H]|$. Equation 6.7 will be extensively used to explicit the dynamics of our system.

6.2 System Hamiltonians

We introduce in these sections the system Hamiltonians and the formal instruments used to define them.

6.2.1 Free Atomic Hamiltonian

The free atomic Hamiltonian H_A can be written as:

$$H_A = E_g P_g + E_e P_e,$$

where E_g and E_e are respectively ground and excited states energies. In the so called rotating wave approximation (see appendix C.1), the free Hamiltonian H_A is transformed in:

$$\tilde{H}_A = -\Delta E P_e = -\hbar\Delta P_e,$$

where $\Delta E = E_L - E_e$ and E_L is the laser energy level; Δ is usually called **laser detuning** being the difference between the laser and excited state angular frequency, i.e:

$$\Delta = (E_L - E_e)/\hbar.$$

The Hamiltonian $\tilde{H}_A$ corresponds to a system with 0 ground state energy and and excited state with energy $-\Delta E = -\hbar\Delta$.

6.2.2 Electric Field

The electric field will be fully modelled in the next chapter (see section 7.1.1) with the expression:

$$\vec{E}(t,z) = \mathrm{Re}\left\{\vec{E}_0 e^{i(\omega t - kz)}\right\}. \tag{6.8}$$

The electric field vector can be expressed in its two counter-rotating components, using the equality
$textRe(a) = \frac{1}{2}(a + a^*)$, as:

$$\vec{E}(t) = \frac{1}{2}\vec{E}_0 e^{i(\omega t - kz)} + \frac{1}{2}\vec{E}_0^* e^{-i(\omega t - kz)} = \vec{E}^+(t) + \vec{E}^-(t),$$

where we have defined:

$$\vec{E}^{\pm}(t) = \frac{1}{2}\vec{E}_0^{\pm} e^{\pm i(\omega t - kz)}, \tag{6.9}$$

$$\vec{E}_0^{+} = \vec{E}_0, \tag{6.10}$$

$$\vec{E}_0^{-} = \vec{E}_0^*. \tag{6.11}$$

In the following pages, it will be necessary to use the spherical basis [80] defined by the versors $\hat{e}_q$, with $-1 \leq q \leq 1$ (see appendix C.2). In this basis the electric field can be decomposed as:

$$E_q^{\pm}(t) := \vec{E}^{\pm}(t) \cdot \hat{e}_q = \frac{1}{2}E_q^{\pm} e^{\pm i(\omega t - kz)}. \tag{6.12}$$

$$E_q^{\pm} := \vec{E}_0^{\pm} \cdot \hat{e}_q, \tag{6.13}$$

6.2.3 Electric Dipole

The dipole $\vec{d}$ is the operator corresponding to the electric dipole moment associated with the transition. In general the transition dipole moment is a complex vector describing the interaction between the distribution of charge within the system and the electromagnetic wave.

The dipole operator will be very significant in our discussion because it is connected to the polarization vector (discussed in section 7.1.2) by the equation $\vec{P} = n\underline{\vec{d}}$ where n is the density number of the medium and $\underline{\vec{d}}$ is the dipole operator averaged value.

Using the identity in equation 6.4, one can expand the dipole operator as follows:

$$\vec{d} = (P_g + P_e)\vec{d}(P_g + P_e) = \vec{d}^- + \vec{d}^+.$$

In this equation we have assumed that $P_g\vec{d}P_g = P_e\vec{d}P_e = 0$: this is justified by the fact that the electric field doesn't cause ground to ground and excited to excited states excitations/transitions. We have also defined:

$$\begin{aligned}\vec{d}^- :=& P_g\vec{d}P_e,\\ \vec{d}^+ :=& P_e\vec{d}P_g.\end{aligned}$$

As detailed in appendix C.3 the dipole moments components, in the spherical basis, can be written as a function of the **lowering operator** $\vec{L}$, defined in equation C.1 of the appendix, as:

$$d_q^+ =(-1)^q d_0 L_{-q}^\dagger, \tag{6.14}$$

$$d_q^- =d_0 L_q, \tag{6.15}$$

so that the total dipole moment can be written as:

$$d_q = d_0(L_q + (-1)^q L_{-q}^\dagger) \tag{6.16}$$

The symbol † refers to the Hermitian adjoint and the operator $\vec{L}$, called lowering operator.

6.2.4 Atom-Field Interaction

The Hamiltonian for the atom-field interaction is written as:

$$H_{\mathrm{AF}} = -\vec{d}\cdot\vec{E} = (\vec{d}^+ + \vec{d}^-)\cdot(\vec{E}^+(t) + \vec{E}^-(t)),$$

where $\cdot$ represents the scalar product defined in appendix C.2.2.
Since the electric field and dipoles oscillate in phase [81], in other words:

$$\begin{aligned}E^\pm(t) &\propto e^{\pm i\omega t},\\ d^\pm &\propto e^{\pm i\omega t},\end{aligned}$$

fast oscillating terms proportional to $e^{\pm 2i\omega t}$ in the electric Hamiltonian (i.e. terms like $\vec{d}^\pm\cdot\vec{E}^\mp(t)$) can be neglected, so that the electric Hamiltonian can be simplified to:

$$H_{\mathrm{AF}} = -\frac{1}{2}(\vec{d}^+\cdot\vec{E}_0^+ e^{i\omega t} + \vec{d}^-\cdot\vec{E}_0^- e^{i\omega t}),$$

Applying the rotating wave approximation the phase dependent terms can be eliminated, so that the previous expression can be simplified to:

$$H_{\mathrm{AF}} = -\frac{1}{2}(\vec{d}^+\cdot\vec{E}_0^+ + \vec{d}^-\cdot\vec{E}_0^-), \tag{6.17}$$

Using equations 6.14 and 6.15 together with the definition of scalar product, the interaction Hamiltonian H_{AF} can be alternativelly expressed as:

$$H_{\mathrm{AF}} = -\frac{d_0}{2}(L_q(E_q)^* + L_q^\dagger E_q). \tag{6.18}$$

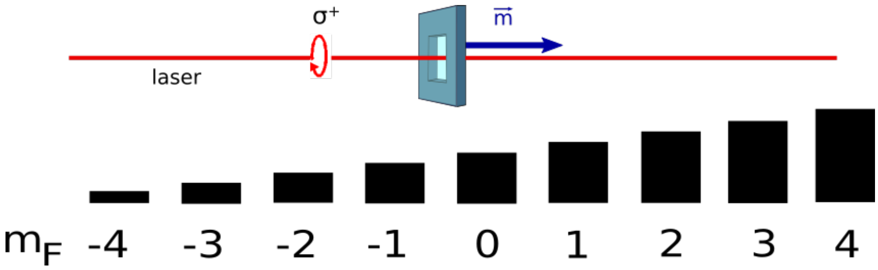

Figure 6.2: The circularly polarized light creates a population imbalance in the Zeeman sub-levels which corresponds to a macroscopic magnetization in the beam direction.

6.2.5 Angular Momentum Operator

We introduce here the angular momentum operator $\vec{F}$, which is necessary to define, in the next section, the magnetic Hamiltonian. We formally define the operator $\vec{F}$ in appendix C.4, given by the sum of the ground and excited state angular momentum operators $\vec{F}_g$ and $\vec{F}_e$.

As we will describe in section 6.4.1, the ground (excited) angular momentum operator is (proportional to) the ground (excited) **magnetization** vector created by the optical pumping phenomena.

The meaning of the magnetization vector can be appreciated by considering the (averaged) ground-state magnetization[3] component along the laser direction, i.e $(m_g)_z = (m_g)_0$; this component measures the linear population imbalance of the ground state magnetic sub-levels population. An example is depicted in the figure 6.2 for a ground state level of angular momentum $F_g = 4$. In the example, the σ^+ polarized light causes the population to be transferred to the sub-levels with higher magnetic quantum number m_F which creates a ground-state magnetization vector $\vec{m}$ along the laser direction; a σ^- polarized light would build the population to the sub-levels with lower magnetic quantum numbers and create a magnetization vector in the opposite direction. Formally $(m_g)_z = (m_g)_0$ measures the difference between the populations of levels 1, 2, 3, 4 and the populations of levels -1, -2, -3, -4, and the other two components of $\vec{m}_g$ measure the ground state sub-levels coherences excited by the magnetic field.

---

[3] The excited state magnetization $\vec{m}_e$ has a similar meaning.

6.2.6 Magnetic Field Operator

Similarly to the electric field case, the magnetic field Hamiltonian is defined by:

$$H_B = -\vec{\mu} \cdot \vec{B},$$

where $\vec{B}$ is the magnetic field vector and $\vec{\mu}$ is the magnetic dipole moment, which is connected to the total atomic angular momentum operator vector $\vec{F}$ by:

$$\vec{\mu} = g_F \mu_B \vec{F},$$

where μ_B is the Bohr magneton and g_F is the Landé g-factor of the caesium $6^2\mathrm{S}_{1/2}$ ground state. The calculation of the constant g_F can be found in [7] and its value is reported in table 2; note that the absolute value of γ_ν (reported in the same table) is independent on the quantum number F_l of the level l considered, but its sign is negative for $F = 3$ and positive for $F = 4$.
Defining the caesium gyromagnetic ratio γ as:

$$\gamma = 2\pi\gamma_\nu = 2\pi\frac{g_F \mu_B}{h} \approx 2\pi \cdot 350 \text{ Hz/mG} = 2\pi \cdot 3.5 \text{ kHz/}\mu\text{T}. \tag{6.19}$$

and the **Larmor** angular **frequency** vector $\vec{\omega}$ as:

$$\vec{\omega} := \gamma\vec{B}, \tag{6.20}$$

then the magnetic Hamiltonian can be more simply written as:

$$H_B = \hbar\vec{\omega} \cdot \vec{F}.$$

As we will show, $\vec{\omega}$ actually dictates the rotation of the angular momentum $\vec{F}$ around the magnetic field vector $\vec{B}$; in other words $\vec{F}$ rotates in the plane perpendicular to the magnetic field, at the so called **Larmor** angular frequency given by $\omega = \gamma B$, where $\omega = |\vec{\omega}|$ and $B = |\vec{B}|$.

6.2.7 Decay Operator

The last term in the master equation 6.5 is the decay operator V_D that describes the spontaneous decay of the excited population to the ground state and the decay of the state coherences; this operator can be expressed by [81, 82, 83]:

$$V_D = \Gamma\frac{2F_e + 1}{2F_g + 1}\sum_q \mathcal{D}(L_q)\rho,$$

where the Lindblad super-operator $\mathcal{D}$ is defined by:

$$\mathcal{D}(A)\rho = A\rho A^{+} - \frac{1}{2}(A^{+}A\rho + \rho A^{+}A),$$

and Γ is the natural line-width of the caesium D_1 spectrum, reported in table 2.

6.3 Irreducible Multipoles

For our theoretical analysis we make extensive use of the the density matrix expansion in its irreducible multipole operators [84, 85, 86, 87, 88]. As fully explained in appendix C.6, using this expansion, the density matrix can be written as:

$$\rho = \sum_{l_1 l_2 kq} m^{kq}_{l_1 l_2} T^{kq}_{l_1 l_2}, \tag{6.21}$$

with l_1 and l_2 both taking the two values g and e, $0 < k < F_1 + F_2$ and $-k < q < k$.
$T^{kq}_{l_1 l_2}$ and $m^{kq}_{l_1 l_2}$ are respectively called the irreducible multipole moments operators and multipole coefficients of the density matrix; we explain their meaning and significance in the next sections.

6.3.1 Multipole Operators

In this section we clarify the meaning of the multipole operators, up to the first order (i.e. $k = 0, 1$), by connecting them to the common operators we introduced in the previous pages to define the system.
The zero order operators $T^{00}_{l_1 l_2}$ are:

- T^{00}_{gg} proportional to the **ground state projection operator** P_g;
- T^{00}_{ee} proportional to the **excited state projection operator** P_e;

When $k = 1$ then $q \in [-1, 1]$ and the multipoles operators $T^{1q}_{l_1 l_2}$ (with varying q) are the components, in the spherical basis, of the operator vectors:

$$\vec{T}_{l_1 l_2} \equiv (T^{1,-1}_{l_1 l_2}, T^{1,0}_{l_1 l_2}, T^{1,1}_{l_1 l_2}).$$

With varying l_1 and l_2 these vectors are:

- The operator $\vec{T}_{gg}$ is proportional to the ground state angular momentum operator $\vec{F}_g$ and so to the ground state **magnetization** operator $\vec{m}_g$;

- similarly, the operator $\vec{T}_{ee}$ is proportional to the excited state angular momentum operator $\vec{F}_e$ and so to the ground state **magnetization** operator $\vec{m}_e$;
- the operator $\vec{T}_{ge}$ is proportional to the **dipole** $\vec{d}^-$, or alternativelly to the lowering operator $\vec{L}$; similarly, the vector $\vec{T}_{eg}$ is proportional to the **dipole** operator $\vec{d}^+$, or alternatively to the operator $\vec{L}^\dagger$.

These section proves that all the operators we previously introduced to define our system (to the exception of the decay operator V_D) can be written as multipole operators up to order 1. The exact relationships and proportionality coefficients are presented in appendix C.6.1.

6.3.2 Multipole Coefficents

We present the significance and meaning of the multipole coefficients up to the first order. As we will see, they are connected to the corresponding averaged values of the multipole operators explored in the previous section.
In first approximation, i.e. considering the magnetic sub-levels degenerate, the complex structure of levels can be approximated by a much simpler two levels system, which is described only by the ground and excited state populations and zero order coherences. The zero order multipole coefficients basically describes the system in this approximation.
When $k = 0$, q has to be 0 and the multipoles coefficients $m^{00}_{l_1 l_2}$ are:

- the coefficient m^{00}_{gg} is proportional to the **ground state overall population** p_g;
- the coefficient m^{00}_{ee} is proportional to the **excited state overall population** p_e;
- the coefficient m^{00}_{ge} (and the analogous m^{00}_{eg}) measures the 0 order **coherence** between the ground and excited state.

The first order multipole coefficients describe the system with more accuracy by considering a simplified Zeeman structure; the description is enriched with the inclusion of the ground and excited state populations imbalance, ground state coherences, excited state coherences and ground-excited states first order coherences.
When $k = 1$ then $q \in [-1, 1]$ and the multipoles $m^{1q}_{l_1 l_2}$ (with varying q) are the components, in the spherical basis, of the vectors:

$$\vec{m}_{l_1 l_2} \equiv (m^{1,-1}_{l_1 l_2}, m^{1,0}_{l_1 l_2}, m^{1,1}_{l_1 l_2}).$$

With varying l_1 and l_2 these vectors are:

- The vector $\vec{m}_{gg}$ is proportional to the (averaged) ground state angular momentum $\underline{\vec{\mathrm{F}}}_g$, and so to the (averaged) ground state **magnetization** $\vec{m}_g$;
- similarly, the vector $\vec{m}_{ee}$ is proportional to the (averaged) excited state angular momentum $\underline{\mathrm{F}}_e$, and so to the (averaged) excited state **magnetization** $\underline{\vec{\mathrm{m}}}_e$;
- the vector $\vec{m}_{ge}$ is proportional to the (averaged) **dipole** $\underline{\vec{\mathrm{d}}}^-$; similarly, the vector $\vec{m}_{eg}$ is proportional to the (averaged) **dipole** $\underline{\vec{\mathrm{d}}}^+$. Both $\underline{\vec{\mathrm{d}}}^+$ and $\underline{\vec{\mathrm{d}}}^-$ measures the first order coherences of the system.

The exact relationships and proportionality coefficients are presented in appendix C.6.1.

6.3.3 Multipoles Commutators

We are mostly interested in the evolution of the dipole operator $\vec{d}$, i.e. to the derivative $\dot{\underline{\vec{\mathrm{d}}}}$; as it can be seen from equation 6.7 the calculation of $\dot{\underline{\vec{\mathrm{d}}}}$ requires the evaluation of the commutators $|[H, \vec{d}]|$.
As already explained in section 6.3.1, both H and $\vec{d}$ can be written as a combination of multipole operators; so in order to find the dipole evolution, we had to first solve the problem of evaluating the commutator of two generic multipole operators, or formally, of:

$$[T^{k_1q_1}_{l_1l_2}, T^{k_2q_2}_{l_3l_4}].$$

We find that this operator can be still written as a linear combinations of multipole operators $T^{k_3q_3}_{l_5l_6}$ and the coefficients of the summation can be obtained from the following trace:

$$|[T^{k_1q_1}_{l_1l_2}, T^{k_2q_2}_{l_3l_4}](T^{k_3q_3}_{l_5l_6})^\dagger|. \tag{6.22}$$

We found an elegant expression for these coefficients which is reported appendix C.6.2.

6.4 Vectorial Representation

The method mostly used for solving this complex system is to numerically calculate the evolution, or the stationary values, of all populations and coherences. This method, although very effective, doesn't allow for a qualitative

reading of the system which is more immediate for an analytical solution.
The purpose of this section is to demonstrate that an approximate analytical solution is possible, and that it can be written in a easily readable vectorial form; in the next chapter we will use this system of vectorial equations to qualitative describe and confirm most of the experimental observations outlined in chapter 4.
The formal derivation of these equations would requires the extensive calculation of many traces like the one in equation 6.22; that's why we won't report the formal demonstration which would otherwise require too many pages. Nevertheless, as a starting point and for initial clarifications, we explicit the time evolution of the dipole operator $\vec{d}^-$ and then present the complete set of vectorial equations.

6.4.1 Dipole Evolution

We report here the the evolution of the dipole $\vec{d}^-$, where we explicitly label the contribution coming from each Hamiltonian:

$$\begin{array}{ccccc} \overset{\text{Dipole Evolution}}{\dot{\vec{d}}^+} & = & \overset{\text{Free Evolution}}{-i\Delta\vec{d}^+} & + & \overset{\text{Atom-Field Interaction}}{\frac{1}{\hbar}(-ip_d\vec{E}_0+\vec{m}\times\vec{E}_0)} \\ & & \overset{\text{Decay Rate}}{-\gamma\vec{d}^+} & - & \overset{\text{Magnetic Field}}{\vec{d}^+\times\vec{\omega}.} \end{array} \tag{6.23}$$

Each operator appearing in equation 6.23 is intended averaged, but the subscript notation is avoided to make the reading easier (see the definitions of averaged operators in equations 6.2 and 6.7).
Each Hamiltonian gives a different contribution to the dipole evolution; in particular all Hamiltonian operators give contribution up to order 1, except for the atom-field Hamiltonian $\mathrm{H_{AF}}$ which gives also higher multipoles contributions; in order to write the equations in a simple vectorial form, we adopted the **simplification** of ignoring contributions of orders higher than the first; in other words, we average all operators with a truncated summation of the density matrix, ρ_1, obtained from equation 6.21 limiting k to 1.
For the transition $F_g = 1 \to F_e = 1$ this is equivalent to solving the corresponding exact system without approximations. For a generic transition $F_g \to F_e$ instead the first order approximation allows to investigate the system dynamics with a level of accuracy higher than that provided by a simple two level approximation. Furthermore all the constants that define the system under the first order approximation (see page 128) depend on F_g and F_e, so the their information is not lost in the simplification.
The first term, in the right hand side of the equation 6.23, is the contribution coming from the free atomic Hamiltonian H_A and it is the same term

appearing in the analogous equations for the simpler two level system (see for example [81]).
The electric field Hamiltonian gives a contribution coming from the comutator trace $[\vec{d}^-, H_{\mathrm{AF}}]$; remembering the expression of the electric Hamiltonian in equation 6.17 and using the symbols in appendix C.6.2, it can be proven that:

$$\frac{1}{i\hbar}[\vec{d}^+, H_{\mathrm{AF}}] = \frac{1}{2i\hbar}[\vec{d}^+, \vec{d}^- \cdot \vec{E}^-] = \frac{1}{\hbar}(-ip_d\vec{E}_0 + \vec{m} \times \vec{E}_0), \tag{6.24}$$

where we have defined the **magnetization** operator vector $\vec{m}$ directly from the dipole commutators; its spherical components are given by:

$$\begin{aligned} m_{-1} &:= \tfrac{1}{4}[d_{-1}, d_0], \\ m_0 &:= \tfrac{1}{4}[d_{-1}, d_1], \\ m_1 &:= \tfrac{1}{4}[d_0, d_1], \end{aligned} \tag{6.25}$$

and the ground and excited state magnetization operator vectors $\vec{m}_g$ and $\vec{m}_e$ are defined by:

$$\begin{aligned} \vec{m}_g &= P_g\vec{m}, \\ \vec{m}_e &= P_e\vec{m}, \end{aligned}$$

where obviously $\vec{m} = \vec{m}_g + \vec{m}_e$. The ground-state magnetization $\vec{m}_g$, as it has been just defined, is proportional to the ground-state angular momentum $\vec{F}_g$ and so to the first order multipole vector $\vec{T}_{gg}$, defined in section 6.3.1; the same could be said for the excited state magnetization m_e; in other words:

$$\begin{aligned} \vec{m}_g &\propto \vec{F}_g \propto \vec{T}_{gg}, \\ \vec{m}_e &\propto \vec{F}_e \propto \vec{T}_{ee}. \end{aligned}$$

We don't use $\vec{F}_g$ and $\vec{F}_e$ or $\vec{T}_{gg}$ and $\vec{T}_{ee}$ to define the magnetization because it will require several additional coefficients that would make the equations much heavier and less immediate.
Note also the the magnetization operator $\vec{m}$, as it is defined in the equations 6.25, contains multipole higher than the first which, as previously mentioned, will be discarded. Those contributions cannot be put in a simple vectorial form but will require a more complex tensor notation; furthermore we expect the higher orders multipoles to describe finer experimental observations which we either don't detect or we are not interested in.
The operator p_d, in equation 6.24, is defined by:

$$p_d := \tfrac{1}{2}[d_0, d_0^+],$$

which, ignoring multipoles of order higher than the first, can be written as:

$$\begin{aligned} p_d &= \tfrac{1}{6} d_0^2 (p_g - f_{ge} p_e), \\ f_{ge} &= \frac{2F_g + 1}{2F_e + 1}, \end{aligned} \tag{6.26}$$

where p_g and p_e are respectively the overall ground and excited state populations (operators or corresponding averaged values). Formula 6.26 proves that p_d measures the overall **population difference** between the ground and excited states; the coefficent f_{ge} accounts for a possible difference in the number of magnetic sub-levels of the ground and excited state. We will show in section 7.2.2 that, as expected, p_d is a function of the laser intensity, thus becoming related to the pump level.

The decay operator V_D gives the result expected[4], i.e a decaying contribution; the dipole $\vec{d}^-$ measures in fact the first order ground-excited state coherences which decay at a rate proportional to $\Gamma/2$. The term γ is a sum of two terms:

$$\gamma = \frac{\Gamma}{2} + \gamma_c, \tag{6.27}$$

where γ_c is the **pressure broadening** contribution, due to the buffer gas presence, which increases the coherences decay rate[5];

Finally, the contribution coming from the magnetic Hamiltonian H_B describes the rotation of the dipole $\vec{d}^-$ around the magnetic field $\vec{B}$.

6.4.2 Complete Set of Equations

In order to complete the description of the system evolution, equation 6.23 for the dipole $\vec{d}^-$ is not enough, and it has to be coupled with the time evolution of all other (averaged) operators with which we define the system, i.e. the dipole $\vec{d}^+$, the magnetization vector $\vec{m}$, the zero order coherences and the population imbalance p_d. In the following section we present the final time dependent equations, without providing the analytical demonstration, which would require too many pages.

The complete set of time dependent equations describing the single general transition $F_g \to F_e$, up to the first multipole order, is reported on page 128. The operator c^- together with c^+ describe the **zero order ground-excited**

---

[4] We don't provide an analytical proof of this contribution cause it require the evaluation of the trace of four multipole moments; the result can still be proven computationally.

[5] As it is usually done (see for example [81]), the contribution proportional to γ_c has been added artificially to describe the buffer gas effect, i.e. it does not come directly from the decay operator V_D.

Vectorial Representation

Dipoles

$$\dot{\vec{d}}^{+} = - i\Delta\vec{d}^{+} + \frac{1}{\hbar}(-ip_d\vec{E}_0 + \vec{m}\times\vec{E}_0) - \gamma\vec{d}^{+} - \vec{d}^{+}\times\vec{\omega} \tag{6.28a}$$

$$\dot{\vec{d}}^{-} = (\vec{d}^{+})^{*} \tag{6.28b}$$

Magnetizations

$$\begin{aligned}\dot{\vec{m}}_g =& \frac{l_g}{\hbar}(\vec{d}^{+}\times\vec{E}_0^{*} + \vec{d}^{-}\times\vec{E}_0) - \frac{1}{i\hbar}(c^{+}\vec{E}_0^{*} + c^{-}\vec{E}_0) + \\ & - \vec{m}_g\times\vec{\omega} + k_g\Gamma\vec{m}_e\end{aligned} \tag{6.28c}$$

$$\begin{aligned}\dot{\vec{m}}_e =& \frac{l_e}{\hbar}(\vec{d}^{+}\times\vec{E}_0^{*} + \vec{d}^{-}\times\vec{E}_0) + \frac{1}{i\hbar}(c^{+}\vec{E}_0^{*} + c^{-}\vec{E}_0) + \\ & - \vec{m}_e\times\vec{\omega} + \Gamma\vec{m}_e\end{aligned} \tag{6.28d}$$

$$\vec{m} = \vec{m}_g + \vec{m}_e$$

Populations

$$\dot{p}_g = \frac{1}{2i\hbar}(\vec{d}^{+}\cdot\vec{E}_0 - \vec{d}^{-}\cdot\vec{E}_0^{*}) + \Gamma p_e \tag{6.28e}$$

$$\dot{p}_e = - \frac{1}{2i\hbar}(\vec{d}^{+}\cdot\vec{E}_0 - \vec{d}^{-}\cdot\vec{E}_0^{*}) - \Gamma p_e$$

$$1 = p_g + p_e, \quad f_{eg} = \tfrac{2F_e+1}{2F_g+1}$$

$$p_d = \tfrac{d_0^2}{6}(p_g - f_{ge}p_e) = \tfrac{d_0^2}{6}(1 - p_e(f_{ge}+1)) \tag{6.28f}$$

Coherences

$$\dot{c}^{+} = \delta(-i\Delta c^{+} + \frac{l_c}{i\hbar}(\vec{m}_e - \vec{m}_g)\cdot\vec{E}_0^{*} - \gamma c^{+}) \tag{6.28g}$$

$$c^{-} = - (c^{+})^{*}$$

state coherences of the system; they are defined by:

$$\begin{aligned} c^- &:= \tfrac{1}{2}[(m_g)_0, d_0^-], \\ c^+ &:= \tfrac{1}{2}[(m_g)_0, d_0^+], \end{aligned} \tag{6.29}$$

and are proportional to the multipole vectors $\vec{T}_{ge}$ and $\vec{T}_{eg}$. As for the magnetization operator the operators c^+ and c^- are used instead of $\vec{T}_{ge}$ and $\vec{T}_{eg}$ to make the equations more readable.

The constants l_g, k_g, l_e, l_c and δ depends on the particular transition considered and their expressions are reported in appendix C.8.

Note that it was necessary to explicit the time evolution of the ground and excited magnetizations $\vec{m}_g$ and $\vec{m}_e$ separately: in fact the magnetization of the excited state decays and contributes to the magnetization of the ground state[6]. Likewise we explicated the evolution of the ground and excited state overall populations p_g and p_e, because the excited state decays contributing to the ground state population. We note also that the electric field acts in opposite ways on the population levels; when it pumps the excited state it depletes the ground state. On the contrary, as expected, it acts in the same way on the magnetizations: if the laser creates a positive population imbalance in the ground state, it will create a positive population imbalance also in the excited state.

As it can be observed, the dipole and magnetization vectors oscillate around each other at a frequency proportional to the electric field amplitude; these are the well know **Rabi Oscillations** which are too fast to be detected.

Furthermore, as the equations prove, both the magnetization and dipole vectors independently oscillates around the magnetic field at the so called **Larmor** (angular) frequency ω: we have extensively observed and documented these oscillations in chapter 4.

Finally it can be noted that the the magnetizations and populations decay at the rate Γ given by the caesium D_1 natural line-width, while the zero order coherences, as the dipoles, decay at the faster rate γ, which is affected by the pressure broadening (see equation 6.27).

6.5 Concluding Remarks

As we will show in the next chapter, the model already gives a successful qualitative explanation of the main experimental observations, but it could

---

[6] More specifically, when $F_g = F_e$, $k_g > 0$ and m_g and m_e have the same sign; when $F_g \neq F_e$, $k_g < 0$ and m_g and m_e have opposite sign.

be expanded to describe the complete system composed of the 4 levels described in figure 6.1, in the assumption of pressure broadening γ much higher than the excited state frequency difference ω_e. One could include a second excited state by averaging the constants defining the vectorial representation over the excited state angular momentum F_e; a second ground state could be included artificially as a pathway for the spontaneous decay from the excited states.

We will apply the vectorial representation on page 128, in the next chapter where the response of the caesium vapour to the laser will be modelled with the polarization vector $\vec{P}$ connected to the laser electric field with the Maxwell equations. The bridge between this classical approach and the density matrix formalism, we developed in this chapter, is given by the equation:

$$\vec{P} = n\vec{d}, \tag{6.30}$$

where n is the caesium vapour number density and $\vec{d}$ the (averaged) dipole operator.

Chapter 7

Experiment Model

In this chapter we apply the vectorial representation of the density matrix evolution, developed in the previous chapter, to qualitatively describe and predict the main experimental observations described in chapter 4.
We present a general that describes both the pump and the probe stage of the experiment and, in particular, clarifies the effect of the following parameters on the observed Larmor signals:

- laser frequency;
- laser input polarization;
- laser intensity;
- pressure broadening broadening, i.e. nitrogen pressure in the cell;
- sensor head temperature;
- input laser intensity;
- magnetic field intensity and direction.

7.1 Light-Matter Interaction

In this section we provide the classical instruments to model the interaction between the laser and the caesium atoms in the sensor head. As usually done, the laser is modelled by an electric field vector $\vec{E}$, while the medium response with a polarization vector $\vec{P}$,and both field are simplified by plane waves with slowly varying envelopes. As we will show the envelopes are connected by a simple first-order equation that can be used to model the basics phenomena in the sensor head: the electric field absorption and the rotation of the elctric field plane of polarization.

7.1.1 Electric Field

The laser light can be modelled by an electric plane wave travelling in the z direction; since the electric field vector has to be orthogonal to the direction of propagation z, it has only x and y components and can be written as:

$$\vec{E}(t,z) = E_0^x \hat{e}_x \cos(\omega t - kz + \varphi) + E_0^y \hat{e}_y \cos(\omega t - kz + \varphi + \delta),$$

where $\hat{e}_x$ and $\hat{e}_y$ are respectively the versors in the x and y directions, E_0^x and E_0^y are the two electric field (real) amplitudes components along the x and y axis respectively, ω and k are the electric field angular frequency and wave number, φ an initial phase and δ is the phase difference between the x and y components of the electric field.
The expression above, as it is written, is not very suitable for analytical calculations and, as it is usually done, it is rewritten using the identity $\cos(\phi) \equiv \mathrm{Re}(e^{i\phi})$, as:

$$\begin{aligned}\vec{E}(t,z) &= \mathrm{Re}(E_0^x \hat{e}_x e^{i(\omega t - kz + \varphi)} + E_0^y \hat{e}_y e^{i(\omega t - kz + \varphi + \delta)}) && (7.1)\\ &= \mathrm{Re}\left(e^{i(\omega t - kz)} e^{i\varphi} (E_0^x \hat{e}_x + E_0^y \hat{e}_y e^{i\delta})\right). && (7.2)\end{aligned}$$

If we now introduce the **polarization angle** θ and overall electric field amplitude E_0 such that:

$$\begin{aligned}E_0^x &= E_0 \cos(\theta), && (7.3)\\ E_0^y &= E_0 \sin(\theta), && (7.4)\\ E_0 &= \sqrt{(E_0^x)^2 + (E_0^y)^2}, && (7.5)\end{aligned}$$

then the electric field can be written as:

$$\vec{E}(t,z) = \mathrm{Re}\left(E_0 e^{i\varphi} (\cos(\theta)\hat{e}_x + \sin(\theta)\hat{e}_y e^{i\delta}) e^{i(\omega t - kz)}\right).$$

Let's also introduce the **electric polarization** (complex) versor $\hat{e}$ defined as:

$$\hat{e} = (\cos(\theta)\hat{e}_x + \sin(\theta)\hat{e}_y e^{i\delta}), \tag{7.6}$$

and the **envelope** (complex) vector $\vec{E}_0$, defined by:

$$\vec{E}_0 = E_0 e^{i\varphi} \hat{e}. \tag{7.7}$$

In this way, the electric field can be written as:

$$\vec{E}(t,z) = \vec{E}_0 e^{i(\omega t - kz)}, \tag{7.8}$$

being aware that the physically meaningful counterpart is given by its real part.
The envelope $\vec{E}_0$ describes the part of the field oscillating (in time and space[1]) at a much slower rate compared to the fast wave plane part of the field: all the slow time and space dependencies in the envelope are included in E_0, φ and θ.

Laser Polarization Let's define the total laser power[2] I_T where:

$$I_T = \vec{E} \cdot \vec{E} = |E_{-1}|^2 + |E_1|^2 = I_1 + I_{-1},$$

where $I_q = |(E_0)_q|^2$ is the power of the electric field component q in the spherical basis (defined in appendix C.2), and we have assumed no electric power along the laser direction: in fact $(E_0)_0 = (E_0)_z = 0 \Rightarrow I_0 = I_z = 0$. Note that the powers I_{-1} and I_1 measure respectively the σ^+ and σ^- polarization competent of the laser.
Let's introduce the power difference I_D defined by:

$$I_D = I_1 - I_{-1},$$

which measures the power difference between the σ^+ and σ^- polarization components of the laser. It is useful to write I_D as:

$$I_D = aI_T. \tag{7.9}$$

From the spherical basis component of the electric field polarization versor $\hat{e}$ (introduced in equation 7.6) it is easy to demonstrate that:

$$a = \sin(2\theta)\sin(\delta). \tag{7.10}$$

From both equation 7.9 and 7.10 it follows that a actually measures the electric field polarization. In fact:

$$a = 0 \iff I_{-1} = I_1 \iff \begin{cases} \theta = 0 & \forall\, \delta \\ \theta = \frac{\pi}{2} & \forall\, \delta \\ \delta = 0 & \forall\, \theta \end{cases}$$

$$a = \pm 1 \iff I_T = I_{\mp 1} \iff \theta = \tfrac{\pi}{4} \text{ and } \delta = \pm\tfrac{\pi}{2}.$$

From which it follows that $a = 0$ refers to **linear** electric polarization, while $a = \pm 1$ to the two counter-rotating **circular** electric polarizations $\sigma^{\pm}$.

---

[1] The space variation is assumed only along the direction of propagation z.

[2] We will use the symbol I to indicate the laser power and not its intensity; the two however are connected by equation 7.21.

7.1.2 Polarization

The caesium vapour in the sensor head together with the buffer gas will respond to the electric field presence with a degree of polarization, proportional to the electric field itself, given by:

$$\vec{P} = \epsilon_0 \chi \vec{E}, \tag{7.11}$$

where ϵ_0 is the electric permittivity in vacuum and χ is the electric susceptibility.
As we will demonstrate, this formula doesn't allow the possibility of a rotation of the electric plane of polarization caused by the polarization (i.e. a change of the electric field direction $\hat{e}$), which is a possible physical phenomena we cannot exclude.
To formally include this possibility, we can define the electric field $\vec{E}_\perp = \vec{E} \times \hat{e}_z$ perpendicular to both $\vec{E}$ and $\hat{e}_z$ and extend equation 7.11 to:

$$\vec{P} = \epsilon_0 \chi \vec{E} + \epsilon_0 \chi_\perp \vec{E}_\perp. \tag{7.12}$$

This generalization is not physically unreasonable; a well known example that supports the validity of this extension is the *Faraday effect*, in which a rotation of the input electric polarization is caused by a magnetic field in the direction of propagation.
Since the polarization follows the electric field 7.8, it can be reasonably expressed in the same way as:

$$\vec{P}(t, z) = \vec{P}_0 e^{i(\omega t - kz)}. \tag{7.13}$$

where, as for the electric field, the physically meaningful counterpart of the polarization is given by its real part; $\vec{P}_0$ is a vector representing the slow polarization envelope, which using equation 7.12 can be written as:

$$\vec{P}_0 = \epsilon_0 \chi \vec{E}_0 + \epsilon_0 \chi_\perp (\vec{E}_0)_\perp = \epsilon_0 \chi E_0 e^{i\varphi} \hat{e} + \epsilon_0 \chi_\perp E_0 e^{i\varphi} \hat{e}_\perp, \tag{7.14}$$

where $\hat{e}_\perp = \hat{e} \times \hat{e}_z$.
Most of the physics would be described by the explicit or implicit expression of the susceptibilities; in other words we can expect χ and $\chi_\perp$ to be dependent on the laser frequency, polarization and intensity, the sensor head temperature and the pressure broadening due to the buffer gas.

7.1.3 Medium Response

As fully detailed in appendix C.7.1, the Maxwell equations (see equations C.5, C.6, C.7 and C.8) can be used to obtain the following first-order equation, that connects the electric field to the polarization vector in the case of transverse plane waves:

$$\boxed{(\partial_t + c\partial_z)\vec{E}_0 = \frac{i\omega_c}{2\epsilon_0}\vec{P}_0} \tag{7.15}$$

This equation can be used to calculate the electric field (envelope) gradient $\partial_z\vec{E}_0$, in the steady state case ($\partial_t\vec{E}_0 = 0$):

$$\partial_z\vec{E}_0 = \frac{i\omega_c}{2c\epsilon_0}\vec{P}_0, \tag{7.16}$$

Using equation 7.7 and 7.14, the previous result can be expanded in:

$$(\partial_z E_0)e^{i\varphi}\hat{e} + i(\partial_z\varphi)E_0e^{i\varphi}\hat{e} + E_0e^{i\varphi}(\partial_z\hat{e}) = \frac{i\omega}{2c}(\chi E_0e^{i\varphi}\hat{e} + \chi_\perp E_0e^{i\varphi}\hat{e}_\perp).$$

Simplifying $e^{i\varphi}$, separating the real and imaginary part of χ, and dividing the equation into its two orthogonal vectorial components ($\hat{e}$ and $\hat{e}_\perp$), the previous equation leads to:

$$\boxed{\begin{aligned} \partial_z E_0 &= -\frac{\omega}{2c}\mathrm{Im}(\chi)E_0, && (7.17)\\ \partial_z\varphi &= \frac{\omega}{2c}\mathrm{Re}(\chi), && (7.18)\\ \partial_z\hat{e} &= \frac{i\omega}{2c}\chi_\perp(\hat{e}\times\hat{e}_z), && (7.19) \end{aligned}}$$

which shows that the imaginary part of the susceptibility χ causes a drop in the electric field amplitude, while its real part causes a phase shift. As already mentioned, the electric field is rotated in the medium ($\partial_z\hat{e} \neq 0$) only when $\chi_\perp \neq 0$, i.e. only when the medium responds to the field also with an orthogonal polarization. As we will prove in section 7.2.1, $\chi_\perp$ is proportional to the magnetization component along the laser light, i.e. $\chi_\perp \propto m_z$.

Equation 7.19 together with the definition of the electric polarization versor in equation 7.6 can be used to explicitly evaluate the rotation $\partial_z\theta$ of polarization angle as:

$$\partial_z\theta = -\frac{\omega}{2c}\chi_\perp, \tag{7.20}$$

from which it follows that $\chi_\perp$ is real.

Beer-Lamert Law What is directly measured is not the electric field but its corresponding intensity I; in the case of an electromagnetic radiation described by a plane-wave, the intensity is given by:

$$I = c\epsilon_0 < |E(t,z)|^2 >,$$

where the angular brackets denote a time-averaged quantity, which can be found by integrating over an optical cycle ($2\pi/\omega$), the duration of which is sufficiently small that the magnitude and phase of the envelope are effectively constant. Using this idea, the intensity can be written as:

$$I = \frac{c\epsilon_0}{2}|E_0|^2. \tag{7.21}$$

Equation 7.17 can be used to evaluate the intensity gradient; in fact from:

$$\partial_z|E_0|^2 = \partial_z(E_0E_0^*) = ((\partial_z E_0)E_0^* + E_0\partial_z E_0^*)) = -\frac{\omega}{c}|E_0|^2,$$

we obtain:

$$\partial_z I = -\frac{\omega\epsilon_0}{2}\text{Im}(\chi)I, \tag{7.22}$$

which is the famous Beer-Lambert law.

Polarimeter The polarimeter detects the intensities of the two orthogonal components of the electric field; in other words it independently detects the signals:

$$I_x = \frac{c\epsilon_0}{2}|E_0^x|^2 = \frac{c\epsilon_0}{2}|E_0|^2\cos(\theta)^2 = I\cos(\theta)^2, \tag{7.23}$$

$$I_y = \frac{c\epsilon_0}{2}|E_0^y|^2 = \frac{c\epsilon_0}{2}|E_0|^2\sin(\theta)^2 = I\sin(\theta)^2, \tag{7.24}$$

Following the same reasoning used in the previous section, we can evaluate the signals variations in the z direction as:

$$\partial_z I_x = -\frac{\omega\epsilon_0}{2}\text{Im}(\chi)I_x + 2I\cos(\theta)\sin(\theta)d\theta, \tag{7.25}$$

$$\partial_z I_y = -\frac{\omega\epsilon_0}{2}\text{Im}(\chi)I_y - 2I\cos(\theta)\sin(\theta)d\theta. \tag{7.26}$$

Using equations 7.20 in equations 7.25 and 7.26 we obtain:

$$\partial_z I_x = -\frac{\omega\epsilon_0}{2}\text{Im}(\chi)I_x - \frac{\omega}{c}\text{Re}(\chi_\perp)I\cos(\theta)\sin(\theta), \tag{7.27}$$

$$\partial_z I_y = -\frac{\omega\epsilon_0}{2}\text{Im}(\chi)I_y + \frac{\omega}{c}\text{Re}(\chi_\perp)I\cos(\theta)\sin(\theta). \tag{7.28}$$

From this result it is obvious that any variations in phase in the polarimeter signals is due to $\text{Im}()\chi)$, i.e. to the component of the polarization parallel to electric field, while any change in phase opposition is due to $|\chi_\perp|$, i.e. to the component of the polarization perpendicular to the electric field. In other words the polarimeter actually detects variations in the polarization angle θ and these, as we know, are due the perpendicular component of the polarization.

7.2 Steady State

Since the polarization $\vec{P}$ is connected to the dipole $\vec{d}$ with equation 6.30, we use the vectorial representation described in page 128 to determine the steady state solution of the dipole evolution and so find its components parallel and perpendicular to the electric field.
This would be used also to find the steady state solution of the ground-excited states population imbalance as a function of the laser intensity, and to describe the magnetization evolution.

7.2.1 Dipoles

Since the dipoles decay usually much faster that the populations and magnetizations, we can apply the **adiabatic elimination** and find the dipoles steady state solutions. Imposing $\dot{\vec{d}} = 0$ in equations 6.28a one obtains:

$$\vec{d}^{+} = \frac{1}{\hbar(\gamma + i\Delta)}(-ip_d\vec{E}_0 + \vec{m} \times \vec{E}_0), \tag{7.29}$$

where $\vec{m}$ is the steady state magnetization vector. This solution is valid for negligible magnetic field contribution $\vec{\omega}$, and so it is legitimate during the pump stage of the experiment, where the the electric field is very high; nevertheless it can be extended also during the probe stage, as an approximate solution dependent on the intensity of the magnetic field.
Note that the dipole d^+ in equation 7.29 rotates synchronously with the electric field $\vec{E}_0$, while the dipole $d^- = (d^+)^*$ with the electric field $\vec{E}_0^*$. Since in equation 7.13 we modelled the polarization with its positively rotating complex counterpart, we can connect it to the dipole through the following equation:

$$\vec{P}_0 = n\vec{d}^{+}.$$

Using the expression of P_0 in equation 7.14 we can we can find a convenient expression for electric susceptibilities χ and $\chi_\perp$:

$$\begin{aligned} \chi =& \frac{n\vec{d} \cdot \hat{e}}{\epsilon_0 E_0 e^{i\phi}} = \frac{-inp_d}{\hbar\epsilon_0(\gamma + i\Delta)}, \\ \chi_\perp =& \frac{n\vec{d} \cdot \hat{e}_\perp}{\epsilon_0 E_0 e^{i\phi}} = \frac{nm_z}{\hbar\epsilon_0(\gamma + i\Delta)}, \end{aligned} \tag{7.30}$$

where the last result is obtained from the identity:

$$(\vec{m} \times \vec{E}_0) \cdot e_\perp = (\vec{E}_0 \times \hat{e}_\perp) \cdot \vec{m} = E_0 m_z.$$

Using the identity $\frac{1}{\gamma + i\Delta} = \frac{\gamma - i\Delta}{\gamma^2 + \Delta^2}$ we can evaluate $\mathrm{Im}(\chi)$ and $\mathrm{Re}(\chi_\perp)$ as:

$$\boxed{\begin{aligned} \mathrm{Im}(\chi) =& \frac{\Delta n p_d}{\hbar\epsilon_0(\gamma^2 + \Delta^2)}, && (7.31)\\ \mathrm{Re}(\chi_\perp) =& \frac{n m_z}{\hbar\epsilon_0(\gamma^2 + \Delta^2)}, && (7.32)\end{aligned}}$$

Firstly we note the resonant effect of the **detuning** Δ on both expressions of the susceptibilities, which results in a Lorentzian line shape.

The part of the dipole (and so of the polarization) parallel to the electric field is affected by the overall ground to excited states population imbalance p_d (defined in section 6.4.1); this part of the polarization affects the overall electric intensity drop along the sensor head (as described by the Beer-Labert law in equation 7.22) and p_d (as we will demonstrate in the next section) is a function of the Laser intensity itself. From these two observations, we can expect a dependency of $\mathrm{Im}\chi$ on the laser intensity, which is also predicted by a simpler two level model (see for example [81]).

Equation 7.32 together with the results in equations 7.27 and 7.28 demonstrates that the polarimeter detects only the component of the magnetization along the laser direction and that the two polarization components of the Larmor oscillations detected by the polarimeter are in **phase opposition**.

The effect of the detuning on the Larmor oscillations can be found from equation 7.30; writing

$$m_z(t) = \mathrm{Re}(m_0 e^{(i\omega_l t + \phi_0) - f_d t})$$

and remembering that since for small Δ:

$$\frac{1}{\gamma + i\Delta} \propto e^{-\frac{\Delta}{\gamma}},$$

the phase of the observed magnetic larmor oscillations is:

$$\phi(\Delta) \approx \phi_0 - \frac{\Delta}{\gamma}. \tag{7.33}$$

The observed amplitude of the Larmor oscillations $A \propto m_0$ (see equation 4.2) can be found combining equations 7.27 and 7.28 with the result in equation 7.32:

$$A(\Delta) \propto m_0 \mathrm{Re}(\chi_\perp) \propto \frac{m_0}{\gamma^2 + \Delta^2}, \tag{7.34}$$

which describes a Lorentzian profile as a function of the detuning Δ.

7.2.2 Populations

Using the dipole steady state solutions in equation 7.29 in the evolution of p_e (equation 6.28e) one finds:

$$\dot{p}_e = \mathrm{Im}\left(\frac{1}{i\hbar^2(\gamma + i\Delta)}(-ip_d\vec{E}_0 \cdot \vec{E}_0 + (\vec{m} \times \vec{E}_0) \cdot \vec{E}_0)\right) - \Gamma p_e. \tag{7.35}$$

Obviously $\vec{E}_0 \cdot \vec{E}_0 = I_T$ and it is not difficult to prove that:

$$(\vec{m} \times \vec{E}_0) \cdot \vec{E}_0 = -im_0 I_D = -iam_0 I_T,$$

where m_0 is the steady state component of the magnetization along the laser. We can rewrite the equation 7.35 in the steady state as:

$$\frac{I_T\gamma}{\hbar^2(\gamma^2 + \Delta^2)}(p_d + am_0) - \Gamma p_e = 0,$$

Since p_d and p_e are connected by the equation 6.28f, the last equation can be easily solved for p_d; the solution is:

$$\boxed{p_d = \frac{d_0^2 - am_0\bar{I}_T}{6 + \bar{I}_T}}, \tag{7.36}$$

where:

$$\bar{I}_T = I_T\frac{\gamma d_0^2(f_{ge} + 1)}{\Gamma\hbar^2(\gamma^2 + \Delta^2)}.$$

As expected the solution shows that, for very low laser intensity, all the population is in the ground state, where p_d reaches its maximum value ($p_d = \frac{d_0^2}{6}$). With no magnetization along the laser (i.e. $m_0 = 0$), and for very high laser intensity, p_d reaches its minimum value, zero, where the overall population of the ground and excited state are the same, which corresponds to **population balance**. We can define the **saturation intensity** I_T^s imposing that p_d reaches half its maximum level in equation 7.36, which implies $\bar{I}_T^s = 6$ or:

$$I_T^s = \frac{6\Gamma\hbar^2(\gamma^2 + \Delta^2)}{\gamma d_0^2(f_{ge} + 1)}.$$

With $m_0 \neq 0$ and very high intensity, the system doesn't reach complete population balance, i.e.:

$$p_d = -am_0.$$

In the simple case in which $F_g = F_e$ (i.e. $f_{eg} = 1$) and the solution for the overall ground and excited state populations is:

$$\begin{aligned} p_g =& \frac{1}{2} - 3am_0, \\ p_e =& \frac{1}{2} + 3am_0. \end{aligned}$$

This means that, for example, an ensemble with positive (steady state) Zeeman population imbalance (i.e. $m_0 \geq 0$) interacting with a positively polarized light (i.e. $a \geq 0$) will reach a lower level of population imbalance because not all the Zeeman sub-levels are equally pumped; this is a conclusion that could not be reached with a simple two level approximation. Figure 7.1 plots the ground and excited state populations as a function of the reduced light intensity $\bar{I}_T$ and shows that the population imbalance at high intensity is increased by the magnetization level am_0.

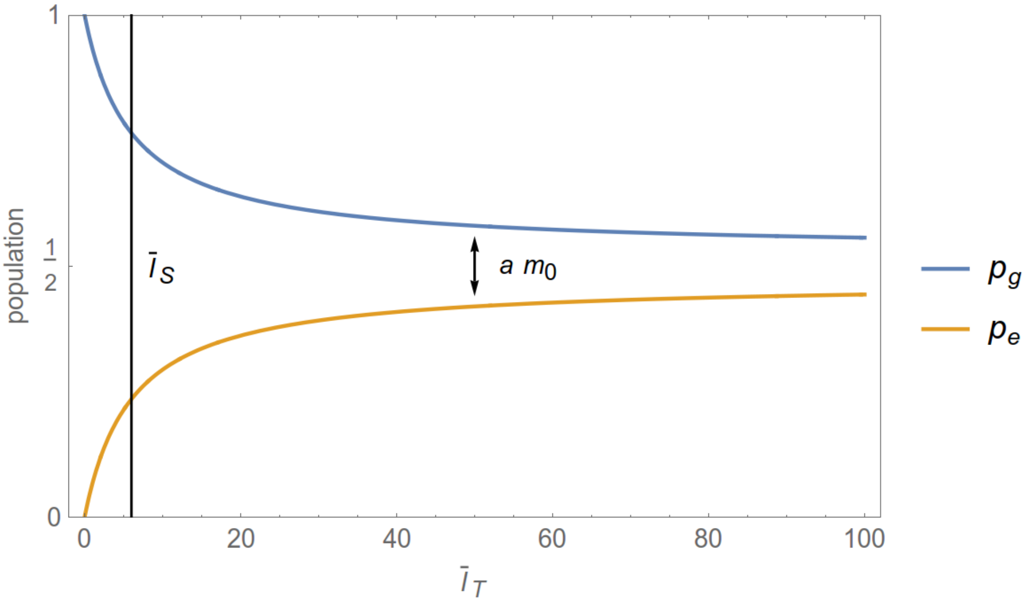

Figure 7.1: Ground and excited state population as a function of the reduced light intensity $\bar{I}_T$. The population imbalance at high intensity is increased by the magnetization level am_0.

7.3 Magnetization Evolution

The evolution of total magnetization $\vec{m}$ can be found summing the evolutions of $\vec{m}_e$ and $\vec{m}_g$ in equations 6.28d:

$$\dot{\vec{m}} = \frac{l_g + l_e}{\hbar}(\vec{d}^+ \times \vec{E}_0^* + \vec{d}^- \times \vec{E}_0) + (k_g - 1)\Gamma \vec{m}_e - \vec{m} \times \vec{\omega}. \tag{7.37}$$

The term proportional to m_e can be neglected because the constant k_g is almost 1 for all of the 4 possible transitions.
Using the adiabatic elimination, we can insert the steady state solution of the dipoles (equation 7.29) to explicit the first term in the evolution of $\vec{m}$:

$$\frac{l_g + l_e}{\hbar}(\vec{d}^+ \times \vec{E}_0^* + \vec{d}^- \times \vec{E}_0) = 2\frac{l_g + l_e}{\hbar}\mathrm{Re}(\vec{d}^+ \times \vec{E}_0^*)$$

$$= 2\frac{l_g + l_e}{\hbar^2}\mathrm{Re}\left(\frac{1}{\gamma + i\Delta}\left(-ip_d(\vec{E}_0^* \times \vec{E}_0) + (\vec{m} \times \vec{E}_0^*) \times \vec{E}_0\right)\right),$$

using the identities in appendix C.9:

$$= 2\frac{l_g + l_e}{\hbar^2}\mathrm{Re}\left(\frac{1}{\gamma + i\Delta}\left(iaI_T\hat{e}_z - iaI_T\hat{e}_z \times \vec{m} - I_T\vec{m} + (\vec{m} \cdot \vec{E}_0^*)\vec{E}_0^*\right)\right),$$

taking the real part of each term one can write the evolution of the magnetization as:

Magnetization Evolution

$$\boxed{\begin{array}{llll} \dot{\vec{m}} = \overset{\text{frequency}}{\frac{2(l_g+l_e)}{\hbar^2(\gamma^2+\Delta^2)}} & \overset{\text{pumping}}{\Big[ap_d\gamma I_T\hat{e}_z} & \overset{\text{laser-damping}}{-I_T\gamma\vec{m}} & \overset{\text{pseudo-precession}}{-(aI_T\Delta\hat{e}_z)\times\vec{m}\Big]} \\ & \overset{\text{transverse}}{+\frac{2(l_g+l_e)}{\hbar^2}\mathrm{Re}\left(\frac{(\vec{m}\cdot\vec{E}_0^*)\vec{E}_0^*}{\gamma+i\Delta}\right)} & \overset{\text{precession}}{-\vec{m}\times\vec{\omega}} & \overset{\text{natural-damping}}{-\gamma_0\vec{m}} \end{array}} \tag{7.38a}$$

Lets analyse each term in the equation separately:

- the term labelled *frequency* describes the dependency of the magnetization evolution on the laser detuning Δ and the pressure broadening γ;

- the term *pumping* is responsible for the pumping of the magnetization vector in the laser direction: this term is predominant during the pumping stage of the experiment and for circularly polarized light ($a = 1$). This term suggests the use of linear polarized light during the probe stage, i.e. $a = 0$, in order to minimize the effect of the *pumping* term.

- as it is usually done, the term *natural-damping* is added artificially to describe the natural decay of the magnetization;

- the term *laser-damping* shows that the magnetization decays in time with a decay rate proportional to the total laser intensity. This phenomena is observed in the probing stage, but affects the pumping stage as well.

- the term *precession* describes the precession of the magnetization vector $\vec{m}$ around the magnetic field at the Larmor angular frequency ω; this contribution is more relevant during the probing stage;

- the term *pseudo-precession* describes the precession of the magnetization vector around a pseudo-magnetic field pointing in the laser direction and proportional to the laser total intensity I_T and polarization a; this phenomena is observed in the probing stage;

- the last term labelled *transverse* points out that the component of the magnetization transverse to the laser direction is not damped by the laser intensity; in fact considering for the moment only the *damping* and *transverse* components:

  $$\dot{\vec{m}} \cdot \vec{E} \propto -I_T \vec{m} \cdot \vec{E} + (\vec{m} \cdot \vec{E})(\vec{E} \cdot \vec{E}) = 0.$$

  In other words the term *damping* applies only to the component of the magnetization perpendicular to the electric field. Since the pump produces only a magnetization along the z direction, the term *transverse* is redundant and can be neglected.

7.3.1 Pump Stage

During the pump stage, we assume that the magnetic field is negligible compared to the electric field; since the magnetization is pumped along the laser direction the pseudo magnetic field is zero. For this reasons, to describe the evolution of the magnetization during the pumping stage we use equation

7.38a discarding the *pseudo-precession*, *transverse* and *precession* terms:

$$\boxed{\dot{\vec{m}} = \frac{2\gamma(l_g + l_e)I_T}{\hbar^2(\gamma^2 + \Delta^2)}\left(ap_d\hat{e}_z - \vec{m}\right) - \gamma_0\vec{m}}.$$

Imposing $\dot{\vec{m}} = 0$ we find the steady state solution for the magnetization in the pumping stage:

$$\vec{m} = \frac{al\bar{I}_T p_d}{d_0^2\gamma_0 + l\bar{I}_T}\hat{e}_z, \tag{7.39}$$

where $l = l_g + l_e$ and $f_{ge} \approx 1$. The equation proves that the magnetization is pumped only in the z direction, and only when the polarization is not linear ($a \neq 0$): the highest pump is obtained for circularly polarized light (i.e $a = \pm 1$). Furthermore the magnetization amplitude saturates as function of the pump intensity to $m_s = ap_d$ as described in figure 7.2; the plot demonstrates that the highest pump available can be used to obtain the best magnetization in the direction of the laser beam.

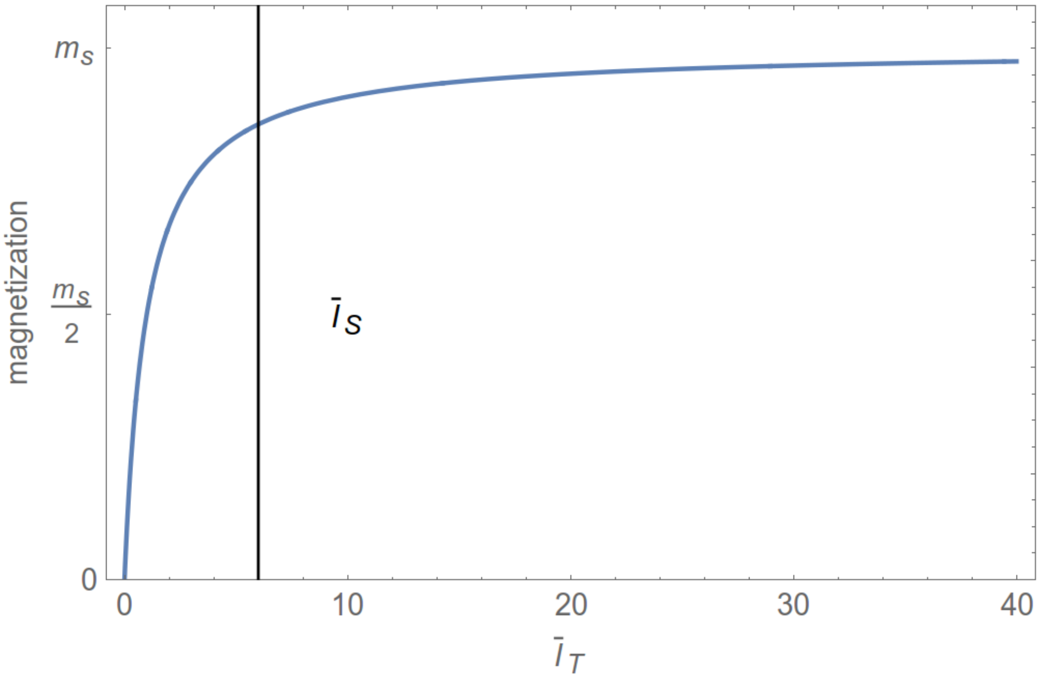

Figure 7.2: Ground and excited state population as a function of the reduced light intensity $\bar{I}_T$. The population imbalance at high intensity is increased by the magnetization level am_0.

More specifically, we assume that the pump will end when all population is transferred to the the $m_F = \pm F_g$ states, depending if the light polarization a is positive or negative, which corresponds to the highest Zeeman sub-level imbalance. With this assumption, we can evaluate the highest magnetization amplitude, that can be reached in correspondence of each of the four possible transitions. Using the definition of magnetization given in equation 6.25, we have calculated these values[3] for both ground and excited state magnetizations m_g and m_e; the values are printed in the following table:

i	$F_g \to F_e$	m_g	m_e	m
1	$4 \to 3$	0.25	-0.24	0.009
2	$4 \to 4$	0.05	0.05	0.1
3	$3 \to 3$	0.063	0.063	**0.12**
4	$3 \to 4$	-0.19	0.19	0.007

As it can be seen, transition 1 and 4 have the highest possible magnetization of the ground and excited states, but those sum destructively, resulting in a very poor overall magnetization m. From the table it is clear that the best transition is the third (i.e. the $3 \to 3$).
Another factor affecting the pump level is the constants $l_g + l_e$ which depend on the particular transition considered. We report here its values[4]:

i	$F_g \to F_e$	$l_g + l_e$
1	$4 \to 3$	0.138
2	$4 \to 4$	0.0063
3	$3 \to 3$	**0.0104**
4	$3 \to 4$	0.1076

Again the best values are reached for transition 1 and 4, but the low level of magnetization those transitions allow, makes again the third transition the optimum one.

7.4 Model Predictions

The model predicts the following:

---

[3] We calculate these values assuming all population pumped in the $m_F = F_g$ state, i.e. $a > 0$ and $m_0 > 0$. For opposite polarization the amplitude is the same but its sign is opposite. The table refers to the z component of the magnetizations and all values are assumed multiplied by d_0^2.

[4] All values are assumed multiplied by d_0^2.

- the laser best frequency is close to the 3 → 3 or **third transition** of the D_1 caesium spectrum; furthermore the model predicts a Lorentzian dependency of the resonance on the laser detuning Δ; these predictions are confirmed experimentally by the results in figure 5.1 and 5.2;
- the two Larmor signals detected by the polarimeter are predicted **out of phase**; this result has been extensively verified experimentally and described in chapter 5;
- the best predicted polarization for the pumping and probing stage is respectively circular and linear; since only one polarization is used for both pump and probe, the model suggests the use of **elliptical polarization**; this is confirmed by the result in figure 5.5;
- for high temperatures the polarization increases, because the caesium vapour density increases; this in turn improves the visibility of the Larmor oscillations. In order to explain the maximum sensitivity reached around 125° (see plot in figure 5.4), the transverse decay rate γ_0 should be proportional to the temperature.
- as described by figure 7.2, the best **pump level** is the highest available; furthermore the pumped magnetization should follow a saturation curve as a function of the pump intensity; this is confirmed by the experimental results in figure 5.7;
- the signal decay rate is proportional to the laser intensity (confirmed by the decay plot in figure 5.8);
- the **probe intensity** both enhances the Larmor oscillations (see equations 7.27 and 7.28) and destroy them, due to the *damping* term in equation 7.38a; this implies the existence of an optimum probe level which is confirmed by the amplitude plot in figure 5.8;
- the probe creates a **pseudo-magnetic field** in the direction of the laser, proportional to the probe intensity; the magnetization precess around both the magnetic and pseudo-magnetic field; this prediction is confirmed by the Larmor frequency plot in figure 5.8;
- a **parallel magnetic field** alone cannot be detected because the pumped magnetization points in the z direction; this result has been verified experimentally and described in section 5.5.2;

- the dipole precession around the magnetic field limits the validity of the adiabatic elimination hence determining a physical limit for the **highest magnetic field detectable**; section 5.5.1 confirms the prediction.

As it can be seen, we have developed a model that predicts the main observations discussed in chapter 5.
Equation 7.38a extends an analogous result found in the literature [3,4,5,31, 89,90], which describes the time evolution of the magnetization in the simpler transition $F_g = 1/2 \rightarrow F_e = 1/2$; more specifically describes the pumping of the magnetization in the laser direction, the presence of a pseudo-magnetic field and the increasing decay rate with laser intensity.
Unlike the previous models, ours is more general because it provides a more complete description of a generic transition $F_g \rightarrow F_e$, not only in term of the magnetization vector but also in terms of the dipoles, coherences and populations. Furthermore, the model developed in this chapter, unlike the one in literature, successfully predicts the use of linear polarization for the probing stage, successfully predicts the $3 \rightarrow 3$ transition as the best one, and the phase-opposition observed between the *parallel* and *perpendicular* signals detected by the polarimeter.

Chapter 8

Conclusions

In this thesis we presented the work done at Strathclyde University to realize a magnetometer in the Bell-Bloom scheme, which serves as the main experimental prototype for the corresponding chip-scale miniaturization. Moving in this direction, together with TI, we made considerable effort to reach a wafer based production of the sensor head cells and in parallel, develop a system based on caesium spectroscopy, to optically characterise a whole wafer in a short period of time. Before the last stage of anodic bonding in the production of the wafer, the small cells (≈ 20 mm^3) are dispensed with a caesium azide compound; the wafer is then UV exposed for several hours so that the azide liberates its constituents in the cell volume: caesium and nitrogen, the first in the vapour form, while the latter as a buffer gas used to increase the magnetometer performances. The spectroscopic analysis of the wafer, based on caesium D_1 line, is able to characterize the cells in term of caesium and nitrogen content and so to study the UV dissociation process; in this regard, we developed a specific software to make the analysis as accurate and quick as possible. The cells properties and spectroscopic characterization (extensively described respectively in chapter 2 and 3), has been the foundation work to implement and develop the amplitude modulated Bell-Bloom based magnetometer.

The basis idea behind it is to use the same light to both prepare the caesium atoms in a favourable polarization state, and detect how this state is perturbed by the presence of a magnetic field. This is experimentally achieved by cyclically modulate the input laser light so that a highly intensive but short impulse, called the pump, is followed by a longer and weaker beam, called the probe. From a semi-classical prospective, the pump is responsible for optically pumping the ensemble and creating a macroscopic magnetization in the direction of the laser beam, which then precess around the magnetic field at the so called Larmor frequency, proportional to the field itself; the

small probe finally detects those oscillations with little or no perturbation. We artificially applied an external magnetic field with a pair of orthogonal Helmholtz coils, which are used for their well known magnetic uniformity; The sensor head is heated with a non magnetic resistor to reach the proper caesium vapour density; its current is switched *on* and *off* and the signal is detects only during the *off* part to avoid undesired magnetic noise. The transmitted light is analysed by a polarimeter which splits the signal into its components of orthogonal polarization.
The signals so extracted have been extensively analysed with the following main conclusion:

- the Larmor oscillation display a typically relaxation rate of about 3 kHz which is increased by the probe intensity;
- the laser light produces a, so called, pseudo magnetic field in the direction of the laser beam which adds to the magnetic Larmor frequency;
- the best laser frequency of detection corresponds to the 3 → 3 transition of the caesium D_1 line;
- the two signals from the polarimeter are almost in phase opposition;
- the atoms can be pumped with the highest available laser intensity without perturbing the Larmor frequency; the best probing power is around 1.1 $\mathrm{mW/mm^2}$;
- the best sensor head temperature is around 125°C;
- the signal is optimized when the angle between the magnetic field and the laser direction is between 0 and 90° or, nominally 45°;
- the lowest and highest magnetic field amplitudes detectable are respectively around 4 and 100 mG.

In parallel we developed a satisfactory understanding and characterization of the magnetic noise level in the frequency domain in terms of the standard parameter used to measure a magnetometer performances: its sensitivity. For this purpose, we developed a specific software which transforms a sequence of Larmor oscillations into a proper magnetic signal used to measure the noise level at different frequencies; this had successfully helped to pinpoint and eliminate external as well as internal sources of magnetic noise. We are able to reach sensitivities as low as $\approx 4\ \mathrm{pT}/\sqrt{\mathrm{Hz}}$ at 850 Hz which, if reproduced on a miniaturized level, would allow the magnetometer to compete with the current chip-scale atomic magnetometers.

In the final part of the thesis we develop a theoretical framework which accurately predicts the main experimental findings. The theory is based on a first order multipole approximation of the density matrix which transforms the Shrödinger-von Neumann equation in 8 vectorial equations involving the evolution of the system dipoles, magnetizations and populations. These equations successfully describe the optical pumping stage of the experiment, the creation of a macroscopic magnetization, its precession around the magnetic field and finally the perturbation of the oscillations caused by the probe beam. The model extends the common representation already in literature [3, 4, 5] by particularly predicting the best laser frequency of detection, the phase opposition phenomena described before, the magnetic field direction and other observations which the common method fails to fully describe.

Appendices

Appendix A

Spectroscopy

A.1 Voigt Profile

Initial Definitions The Gaussian profile is defined as:

$$G(\nu, \sigma_g) = \frac{1}{\sigma_g \sqrt{2\pi}} \exp\left(-\frac{\nu^2}{2\sigma_g}\right),$$

where σ_g is the half width at $1/\sqrt{e}$ maximum.
The Lorentian profile is defined as:

$$L(\nu, \sigma_l) = \frac{\sigma_l}{\pi} \frac{1}{\nu^2 + \sigma_l^2},$$

where σ_l is the full width at half maximum. The Voigt profile is defined as the convolution of the Gaussian and Lorentian function:

$$\mathrm{Voigt}(\nu, \sigma_g, \sigma_l) = \int_{-\infty}^{\infty} G(\nu')L(\nu - \nu')d\nu'.$$

It can be shown that it can be expressed in a easier analytical form by:

$$\mathrm{Voigt}(\nu, \sigma_g, \sigma_l) = \frac{\mathrm{Re}(w(z))}{\sqrt{2\pi}\sigma_g},$$

where

$$z = \frac{x + i\sigma_l}{\sqrt{2}\sigma_g},$$

and:

$$w(z) = \exp(-z^2)\mathrm{erfc}(-iz),$$

in which erfc represents the complementary error function, defined by:

$$\mathrm{erfc}(z) = 1 + \frac{2i}{\sqrt{\pi}} \int_0^z e^{t^2} dt.$$

Numerical Approximation The Voigt function expressed in this form is still computationally very difficult to use, especially for fitting purposes. We have used a convenient approximation, labelled Voigt$_a$, composed by as a linear combination of the Lorentian and Gaussian functions [91]. In other words:

$$\mathrm{Voigt}_a(\nu, \sigma_g, \sigma_l) = c_l(d)L(\nu, \sigma_v) + c_g(d)G(\nu, \sigma_v),$$

where:

$$d = \frac{\sigma_l - \sigma_g}{\sigma_l + \sigma_g},$$

and the coefficents c_l and c_g are:

$$c_l(d) = 0.68188 + 0.61293d - 0.18384d^2 - 0.11568d^3,$$

$$c_g(d) = 0.32460 - 0.61825d + 0.17681d^2 + 0.12109d^3.$$

The width σ_v is:

$$\sigma_v = \frac{1}{2}\left(\sqrt{0.86639\sigma_l^2 + 4\sigma_g^2} + 1.0692\sigma_l\right).$$

The plot in figure A.1 shows the voigt profile and its approximation in a case representing our system; here the Gaussian width is due to the thermal Gaussian broadening at a temperature of 100°C and the Lorentzian width to the 100 Torr of nitrogen. The two curves appear basically undistinguishable. The percentage error is also shown, and as it can be seen, it is lower than 5% for the frequency range of interest.

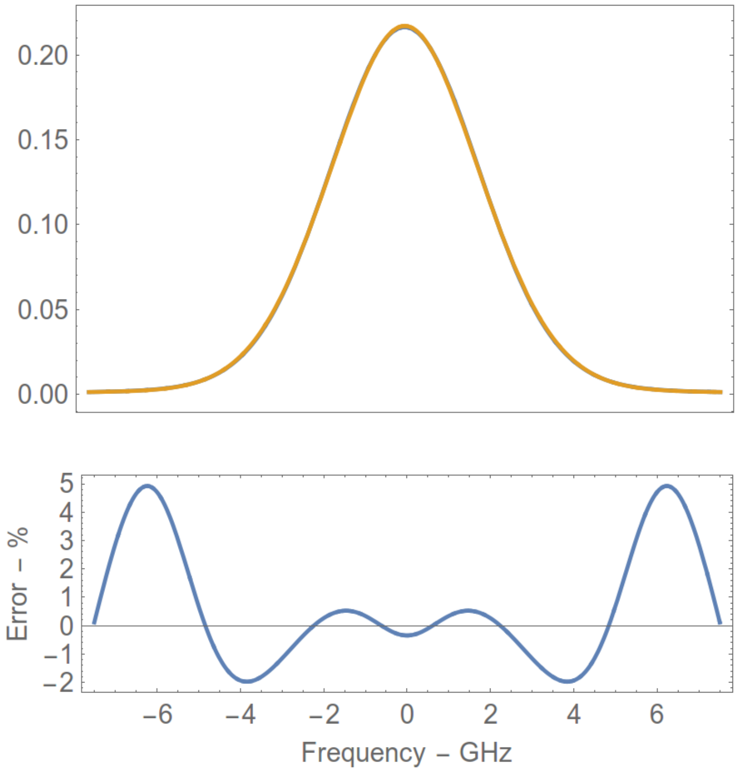

Figure A.1: The upper figure shows the plot of the voigt profile and its approximation. The percentage error is also shown in the lower plot.

Appendix B

Experiment

B.1 Circuits Schematics

In this appendix we presents the two main circuit schematics used for the experiment.

B.1.1 Coils Driver Circuitry

The circuit used for the coils driver is shown in figure B.1. The driver, supplied by a low-noise 12 V battery, consists of two independent sources of a very low noise current, up to 100 mA. The two orthogonal Helmholtz coils (one for the parallel and perpendicular magnetic fields), have a radius of 3.7 and 2.35 cm with 50 and 30 coils turns respectively; using equation B.1, we find that the maximum outputted parallel and perpendicular magnetic fields, are $\approx$1.1 and $\approx$1.2 G respectively.

B.1.2 Heater Driver Circuitry

The circuit used for the heater driver is shown in figure B.2. The driver, supplied by a low-noise 12V battery, transforms the RF voltage signal (coming from a RF pulse generator) in the correspondent current signal, supplied to the heater resistance; in this way the heater current can be switched *on* and *off* so that the signal can be analysed only in the *off* stage.

B.2 The Coils

The purpose of this section is to define and give an analytical expression for the magnetic uniformity and apply the results to give a numerical expression

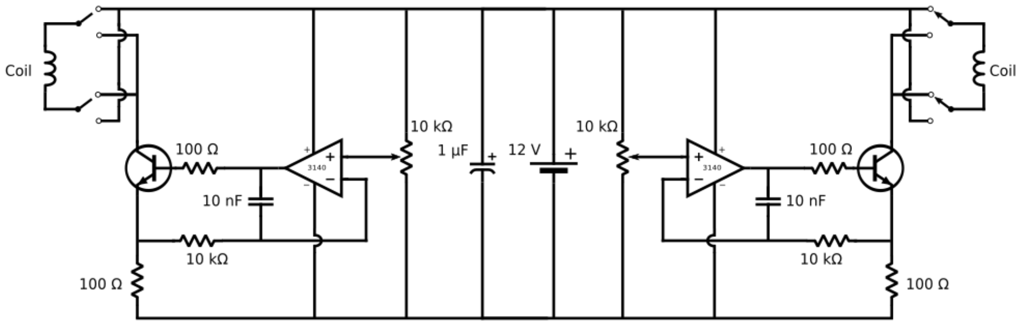

Figure B.1: Coils driver circuitry schematics.

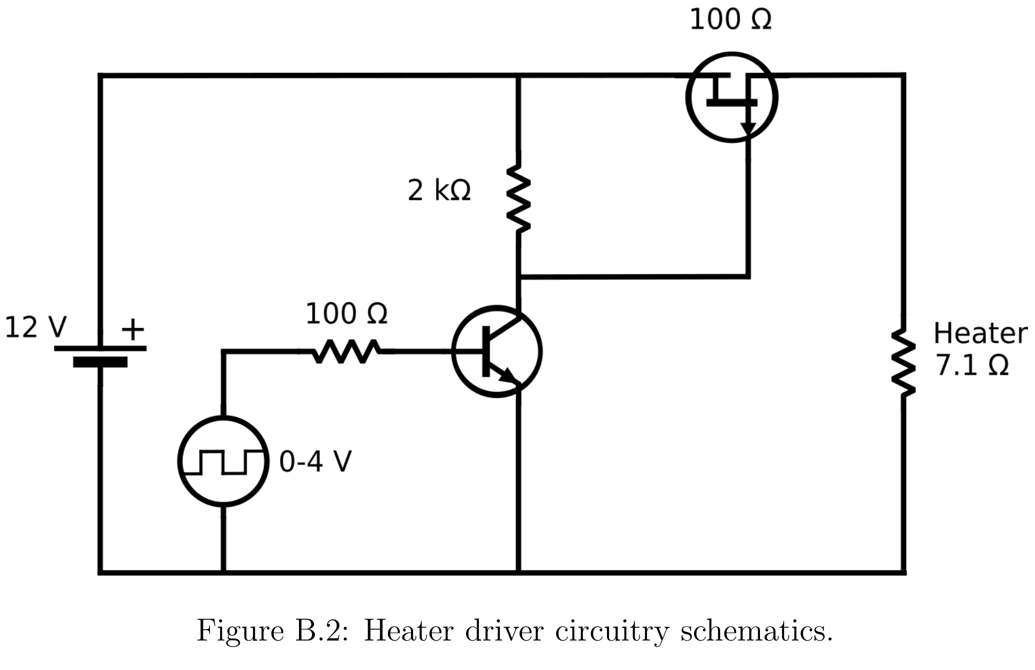

Figure B.2: Heater driver circuitry schematics.

for our experimental case.

B.2.1 Single coil

Let's consider an electric current I flowing in a coil of radius R, as shown in figure B.3.

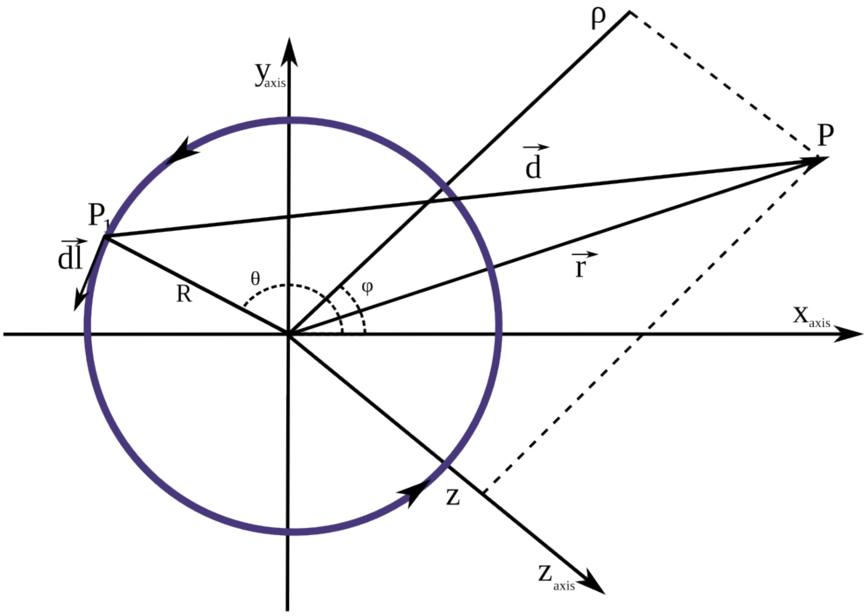

Figure B.3: The circumference in the xy place represent the single coil with current circulating clockwise. The magnetic field contribution from the infinitesimal part of the coil dl is calculated in the generic point P.

The contribution $d\vec{B}$ to the total magnetic field in the point P coming from an infinitesimal element of circuit $d\vec{l}$ located in the point $P_1 \equiv (R\cos(\theta), R\sin(\theta), 0)$ of the coil, is given by the Biot-Savart law:

$$d\vec{B} = \frac{\mu_0 I}{4\pi}\frac{\vec{dl} \times \vec{d}}{d^3},$$

where μ_0 is the magnetic permeability, $\vec{d} = \vec{r} - \vec{P_1}$ is the distance vector between the points P_1 and P and d is its norm.

The point P can be written as:

$$P \equiv (\rho\cos(\theta), \rho\sin(\theta), z),$$

where ρ is the distance of point P from the coil axis and z is the distance of point P from the coil plane. Using some trigonometry one can show that:

$$d^2 = R^2 + z^2 + \rho^2 - 2R\rho\cos(\theta - \phi),$$

where, θ is the azimuth angle of point P referring to the x axis, while ϕ is the angle distance of point P_1 to the x axis (see again figure B.3). The formula can be re-expressed as:

$$d = d_0 A,$$

where we have defined:

$$\begin{aligned} d_0 &= \sqrt{R^2 + \rho^2 + z^2}, \\ A &= \sqrt{1 - a\cos(\theta - \phi)}, \\ a &= \frac{2R\rho}{d_0^2}. \end{aligned}$$

If we take $\hat{u} \equiv (-R\sin(\theta), R\cos(\theta), 0)$ to be the unit vector along $\vec{dl}$, we can say:

$$\vec{dl} = Rd\theta\hat{u}.$$

so that the Biot-Savart law can be rewritten as:

$$d\vec{B} = c_I c_R \vec{s} d\theta,$$

where we have defined:

$$\begin{aligned} \vec{s} &:= \frac{\hat{u} \times \vec{d}}{d^3}, \\ c_I &:= \mu_0 I, \\ c_R &:= \frac{R}{4\pi}. \end{aligned}$$

It can be shown that:

$$\vec{s} \equiv \frac{1}{d^3}\left(z\cos(\theta), z\sin(\theta), R - \rho\cos(\theta - \phi)\right).$$

If we switch to cylindrical coordinates with unit vectors $\hat{\rho} \equiv (\cos(\phi), \sin(\phi), 0)$. $\hat{\phi} \equiv (-\sin(\phi), \cos(\phi), 0)$ and $\hat{z}$ then:

$$\vec{s} = \frac{1}{d^3}\Big(z\cos(\theta - \phi)\hat{\rho} + z\sin(\theta - \phi)\hat{\phi} + (R - \rho\cos(\theta - \phi))\hat{z}\Big).$$

The total magnetic field $\vec{B}$ in the point P is then:

$$\vec{B} = c_I c_R \vec{S},$$

where the dimensionless vector $\vec{S}$ is defined as:

$$\vec{S} = \int_0^{2\pi} \vec{s}(\theta)\ d\vec{\theta}.$$

which after integration gives:

$$\vec{S} = \frac{1}{d_0^3}\left(zI_c(a)\hat{\rho} + (RI_0(a) - \rho I_c(a))\hat{z}\right),$$

which has no component along $\hat{\phi}$ and where we have defined:

$$I_0(a) = \int_0^{2\pi} \frac{1}{(1-a\cos\theta)^{\frac{3}{2}}} d\theta,$$

$$I_c(b) = \int_0^{2\pi} \frac{\cos\theta}{(1-a\cos\theta)^{\frac{3}{2}}} d\theta.$$

We found the analytical solution of these two complex integrals and are reported in appendix B.2.4. It can be found though that:

$$\lim_{a\to 0} I_0 = 2\pi,$$
$$\lim_{a\to 0} I_c = 0,$$

which can be used to find the solution along the coil axis (where $\rho = a = 0$):

$$\vec{S}_{\text{axis}} = \frac{2\pi R}{d_0^3}\hat{z},$$

Since B_ϕ is always zero we can expressed the magnetic field in two cylindrical coordinates, in the form:

$$\vec{B} = [B_\rho, B_z].$$

B.2.2 Double Coils

Let's consider two coils facing each other at a distance z_0. The magnetic field in a generic point is:

$$\vec{B} = c_I c_R \vec{D},$$

where:

$$\vec{D}(\rho, z) = \vec{S}(\rho, z) + \vec{S}(\rho, z - z_0).$$

Helmholtz Coils If $z_0 = R$ the double coil structure is known as Helmholtz coils and, as it will be shown in the next section, it has very favourable uniformity properties. The magnetic field in the centre of the coils in this case is given by the well know expression:

$$\vec{B} = \left[0, \left(\frac{4}{5}\right)^{\frac{3}{2}} \frac{\mu_0 i}{R}\right]. \tag{B.1}$$

B.2.3 Magnetic Uniformity

We can define the magnetic field uniformity $\vec{U}$ of the double coil in a generic point as:

$$\vec{U} = \frac{d\vec{B}}{|\vec{B}|} = \frac{d\vec{D}}{|\vec{D}|} = \frac{\vec{D}(\rho + d\rho, z + dz) - \vec{D}(\rho, z)}{|\vec{D}(\rho, z)|}.$$

Given this definition it is possible to show that $\vec{U}$ has a minimum when $\rho = 0$ (i.e on the coils axis). Along the axis $\vec{U}$ has a maximum in the centre of the coils, where $z = z_0/2$, if $z_0 < \sqrt{3 - \sqrt{7}}R \cong 0.6R$ and a minimum for larger values of z_0. In the centre of the coils (i.e $\rho = 0$ and $z = z_0/2$), $\vec{U}$ has a minimum when $z_0 = R$ (i.e. in the Helmholtz configuration).
The uniformity in the centre of the Helmholtz coils is very high (numerically low) so that a series expansion of $\vec{D}$ up to order 4 was necessary. The uniformity in this point is:

$$\vec{U} = \frac{\vec{D}(d\rho, R/2 + dz) - \vec{D}(0, R/2)}{|\vec{D}(0, R/2)|} = \left[\frac{72\left(4\mathrm{d}\rho\mathrm{dz}^3 - 3\mathrm{d}\rho^3\mathrm{dz}\right)}{125R^4}, \frac{432\mathrm{d}\rho^2\mathrm{dz}^2}{125R^4}\right].$$

Given the dimensions of the sample, located in the centre of the coils, we can assume $dz = 0.1$ cm and $d\rho = 0.5$ cm. We use two Helmholtz coils perpendicular to each other with radii 2.35 and 3.7 cm respectively so that the respective uniformity vectors are:

$$\vec{U_1} = \cong [0.7, 0.3]\,‰, \tag{B.2}$$

$$\vec{U_2} = \cong [0.1, 0.05]\,‰. \tag{B.3}$$

Adding the two vector in the proper way one obtain the total magnetic uniformity in the centre of a double Helmholtz coils structure:

$$\vec{U_2} \cong [0.7, 0.3]\,‰,$$

so that the overall magnetic uniformity in the cell is around 0.7%.

B.2.4 Integrals

The analytical solution of the integrals presented in section B.2.2 is given by:

$$\int_0^{2\pi} \frac{1}{1-a\cos\theta}d\theta = \frac{4}{1+a}\sqrt{\frac{1}{1-a}}\text{EllipticE}\left(\frac{2a}{a-1}\right),$$
$$\int_0^{2\pi} \frac{\cos\theta}{1-a\cos\theta}d\theta = \frac{4}{1+a}\sqrt{\frac{1}{a(1-a)}}\left((1+a)\text{EllipticK}\left(\frac{2a}{a-1}\right) - \text{EllipticE}\left(\frac{2a}{a-1}\right)\right),$$

where:

$$\text{EllipticK}(m) = \int_0^{\frac{\pi}{2}} \frac{1}{\sqrt{1-m\sin(\theta)^2}}d\theta,$$
$$\text{EllipticE}(m) = \int_0^{\frac{\pi}{2}} \sqrt{1-m\sin(\theta)^2}d\theta,$$

are respectively the complete elliptical integrals of the first and second kind and are easily mapped by a computational system.

B.3 Noise Estimator

Let's consider the signal s_n given by:

$$s_n = f_n + \nu_n,$$

where a generic function f_n is embedded in the noise ν_n of variance σ^2. It is immediate to prove that the variance of the noise:

$$\nu_{n-1} + \nu_{n+1} - 2\nu_n,$$

is $6\sigma^2$.
Let's apply the Taylor series expansion to the function f_n around the data points $n+1$ and $n-1$:

$$f_{n+1} = \sum_{i=0}^{\infty} \frac{f_n^{(i)}}{i!},$$
$$f_{n-1} = \sum_{i=0}^{\infty} (-1)^n \frac{f_n^{(i)}}{i!},$$

where $f_n^{(i)}$ is the i-th derivative of f around n. From these expressions it follows that:

$$f_{n+1} + f_{n-1} - 2f_n = 2\sum_{i=1}^{\infty} \frac{f_n^{(2i)}}{(2i)!}.$$

We find that this quantity has a very low variance compared to f_n so that the variance of the signal:

$$s_{n+1} + s_{n-1} - 2s_n,$$

has variance $\approx 6\sigma^2$. This results can be used to estimate σ.

B.4 Cramér-Rao Lower Bounds

The Cramér-Rao lower bound (CRB) condition establishes the lowest possible values for the errors on the informations extracted from the signal 4.3 [79]. More specifically if we label with σ^2_A, $\sigma^2_{\bar{\omega}_l}$, σ^2_ϕ, $\sigma^2_{\bar{f}_d}$ the error (expressed as variance) on the information extracted on respectively the amplitude A, the angular frequency $\bar{\omega}_l$, the phase ϕ and the decay rate $\bar{f}_d$, the CRB conditions can be written as:

$$\begin{aligned}
\sigma^2_A &\geq A^2 \mathrm{CRB}_1(z, N)/R^2_{\mathrm{SN}}, \\
\sigma^2_{\bar{\omega}_l} &\geq \mathrm{CRB}_2(z, N)/R^2_{\mathrm{SN}}, \\
\sigma^2_\phi &\geq \mathrm{CRB}_1(z, N)/R^2_{\mathrm{SN}}, \\
\sigma^2_{\bar{f}_d} &\geq \mathrm{CRB}_2(z, N)/R^2_{\mathrm{SN}},
\end{aligned}$$

where $z = e^{-2\bar{f}_d}$ and the functions CRB_1 and CRB_2 are defined as:

$$\begin{aligned}
\mathrm{CRB}_1(z, N) &:= 2(1-z)\left(\frac{z\left(2N(z-1)z^N - \left(z^N - 1\right)\left(z^N + z\right)\right)}{z\left(z^N - 1\right)^2 - N^2(z-1)^2 z^N} + 1\right), \\
\mathrm{CRB}_2(z, N) &:= \frac{2(1-z)^3\left(1 - z^N\right)}{z\left(z^N - 1\right)^2 - N^2(z-1)^2 z^N}.
\end{aligned}$$

We have simplified these functions in the limit of very high sampling points ($M \to \infty$) and expressing everything as a function of the decay number $d = \bar{f}_d N$:

$$\begin{aligned}
\mathrm{CRB}_1(d, N \to \infty) &= \frac{8}{N} C_1(d), \\
\mathrm{CRB}_2(d, N \to \infty) &= \frac{24}{N^3} C_2(d).
\end{aligned}$$

where the functions C_1 and C_2 are:

$$\begin{aligned}
C_1(d) &= \frac{d e^{2d}\left(-2d^2 - 2d + e^{2d} - 1\right)}{-2e^{2d}\left(2d^2 + 1\right) + e^{4d} + 1}, \\
C_2(d) &= \frac{2d^3 e^{2d}\left(e^{2d} - 1\right)}{3\left(-2e^{2d}\left(2d^2 + 1\right) + e^{4d} + 1\right)},
\end{aligned}$$

and obviously $C_1(0) = C_2(0) = 1$.
In the limit of very high decay rate $d \gg 1$, these functions can be simplified to:

$$\begin{aligned} C_1(d \gg 1) &= d, \\ C_2(d \gg 1) &= \frac{2}{3} d^3, \end{aligned}$$

which shows how important is the decay rate in increasing the CRB noise levels.

Undamped Signal If we consider an *un-damped* signal (i.e $\bar{f}_d = d = 0$ or $z = 1$) in the presence of white Gaussian noise σ_ν, the CRB functions (in the limit of high N) are simply:

$$\begin{aligned} \mathrm{CRB}_1(0, N \to \infty) &= \frac{8}{N}, \\ \mathrm{CRB}_2(0, N \to \infty) &= \frac{24}{N^3}. \end{aligned}$$

Appendix C

Theory

C.1 Rotating Wave Approximation

Let's define the unitary operator U as:

$$U = e^{i\phi P_e},$$

which acts on the states as:

$$|\psi > \to |\widetilde{\psi} >= U|\psi >,$$

and on the density matrix as:

$$|\rho > \to |\widetilde{\rho} >= U|\psi > U^\dagger$$

where $U^\dagger = e^{-i\phi P_e}$.
It is not difficult to demonstrate these useful identities:

$$U = e^{i\phi} P_e + P_g$$
$$U^\dagger = e^{-i\phi} P_e + P_g$$

This operators defines the so called rotating wave approximation.

C.2 Spherical Basis

The versors $(\hat{e}_{-1}, \hat{e}_0, \hat{e}_1)$ in the spherical basis are defined from the Cartesian basis $(\hat{e}_x, \hat{e}_y, \hat{e}_z)$ as:

$$\hat{e}_{\pm 1} = \frac{1}{\sqrt{2}}(\mp \hat{e}_x - i\hat{e}_y),$$
$$e_0 = e_z.$$

These relationships can be inverted, resulting in:

$$\begin{aligned}\hat{e}_x &= \frac{1}{\sqrt{2}}(-\hat{e}_+ + i\hat{e}_-),\\ \hat{e}_y &= \frac{i}{\sqrt{2}}(+\hat{e}_+ + i\hat{e}_-),\\ \hat{e}_0 &= \hat{e}_z.\end{aligned}$$

A Cartesian vector $\vec{v}$ of coordinates (v_x, v_y, v_z) has coordinates (v_{-1}, v_0, v_1) in the spherical basis defined by:

$$\begin{aligned}v_{\pm 1} &= \mp\frac{1}{\sqrt{2}}(v_x \pm i v_y),\\ v_0 &= v_z.\end{aligned}$$

The inverted equations are:

$$\begin{aligned}v_x &= \frac{1}{\sqrt{2}}(s_- - s_+),\\ v_y &= \frac{i}{\sqrt{2}}(s_- + s_+).\end{aligned}$$

C.2.1 Spherical Conjugate

It is easy to demonstrate that, in the spherical basis, the complex conjugate of a vector $\vec{v}$ has coordinates defined by:

$$(\vec{v}^*)_q = (-1)^q v^*_{-q} \quad \text{for } -1 \leq q \leq 1,$$

where v_q are the spherical coordinates of the vector $\vec{v}$ and v^*_q their complex conjugate.

C.2.2 Scalar Product

The scalar product $\vec{a} \cdot \vec{b}$ between two complex vectors $\vec{a}$ and $\vec{b}$ in the Cartesian basis is defined as:

$$\vec{a} \cdot \vec{b} := a_i b^*_i \quad \text{for } i \in [x, y, z],$$

where a_i and b_i are respectively the Cartesian coordinates of vectors $\vec{a}$ and $\vec{b}$. It can be easily shown that, in order for this scalar product to be transposed in the spherical basis, it has to be written as:

$$\vec{a} \cdot \vec{b} := (-1)^q a_q b^*_{-q} \quad \text{for } -1 \leq q \leq 1,$$

where a_q and b_q are respectively the coordinates of vectors $\vec{a}$ and $\vec{b}$ in the spherical basis.

C.2.3 Vectorial Product

Following the same reasoning adopted in the previous section, we can define the cross or vectorial product $\vec{a} \times \vec{b}$ between two complex vectors $\vec{a}$ and $\vec{b}$, in the spherical basis, as:

$$(\vec{a} \times \vec{b})_q = i \sum_t \mathrm{Sign}(q - 2t) a_t b_{q-t},$$

where the sum over t is intended from $\max(q-1,-1)$ to $\min(q+1,1)$, and *Sign* is the sign function.

C.3 Dipole Operator

Using the spherical base decomposition (see appendix C.2) we can define the dipole components in the spherical basis as:

$$\begin{aligned} d_q &:= \vec{d} \cdot \hat{e}_q, \\ d_q^- &:= \vec{d}^- \cdot \hat{e}_q = P_g d_q P_e, \\ d_q^+ &:= \vec{d}^+ \cdot \hat{e}_q = P_e d_q P_g. \end{aligned}$$

These equations can be expanded using the definitions of the projection operators in equations 6.3:

$$\begin{aligned} \vec{d}_q^- &= \sum_{m_g, m_e} \langle m_g | d_q | m_e \rangle \left| m_g \right\rangle \left\langle m_e \right| , \\ \vec{d}_q^+ &= \sum_{m_g, m_e} \langle m_e | d_q | m_g \rangle \left| m_e \right\rangle \left\langle m_g \right| . \end{aligned}$$

At this point it is useful to remember the **Wigner-Eckart theorem** [61] which, when applied to our case, can be written as:

$$\begin{aligned} \langle m_g | d_q | m_e \rangle \quad &= \langle F_g || \vec{d} || F_e \rangle \langle F_g, m_g | F_e, m_e; 1, q \rangle , \\ \langle m_e | d_q | m_g \rangle \quad &= \langle F_e || \vec{d} || F_g \rangle \langle F_e, m_e | F_g, m_g; 1, q \rangle , \end{aligned}$$

where $\langle F_g, m_g | F_e, m_e; 1, q \rangle$ are the ClebschGordan coefficients, defined in appendix C.5. Defying for simplicity:

$$d_0 := \langle F_g || \vec{d} || F_e \rangle \equiv \langle F_e || \vec{d} || F_g \rangle ,$$

and the lowering and rising operators $\vec{L}$ and $\vec{R}$ respectively by:

$$\begin{aligned} L_q \quad &:= \textstyle\sum_{m_g, m_e} \langle F_g m_g | F_e m_e; 1q \rangle \left| m_g \right\rangle \left\langle m_e \right| \text{ for } m_g = m_e + q, \\ R_q \quad &:= \textstyle\sum_{m_g, m_e} \langle F_e m_e | F_g m_g; 1q \rangle \left| m_e \right\rangle \left\langle m_g \right| \text{ for } m_e = m_g + q, \end{aligned} \tag{C.1}$$

then the dipole components can be written as:

$$\vec{d}_q^- = d_0 L_q,$$

$$\vec{d}_q^+ = d_0 R_q.$$

Note that we adopt in this context the same symbol d_0 used in equation 3.10 of chapter 3 to define the dipole matrix element $\langle L_g||\vec{d}||L_e\rangle$, even tough we obviously refer to different dipole matrices; the connection between the two definitions is clarified however by equations 3.8 and 3.9.

Dipole Hermitian Using the following identities:

$$\langle F_2 m_2 | F_1 m_1 1 q\rangle = (-1)^{F_1-F_2+m_1-m_2}\sqrt{\frac{2F_2+1}{2F_1+1}}\left\langle F_1 m_1 | F_2 m_2 1 -q\right\rangle,$$
$$\langle F_1||\vec{d}||F_2\rangle = (-1)^{F_1-F_2}\sqrt{\frac{2F_1+1}{2F_2+1}}\left\langle F_2||\vec{d}||F_1\right\rangle,$$

one can prove that:

$$\begin{aligned} d_q^+ =&(-1)^q(d_{-q}^-)^\dagger,\\ d_q^- =&(-1)^q(d_{-q}^+)^\dagger, \end{aligned}$$

where † denotes the Hermitian adjoint; the last equations can be used to re-write the dipoles as a function of the lowering operator $\vec{L}$ alone; in fact:

$$\begin{aligned} d_q^+ =&(-1)^q d_0 L_{-q}^\dagger,\\ d_q^- =&d_0 L_q, \end{aligned}$$

and the spherical basis component of the total dipole $\vec{d}$ can written as:

$$d_q = d_0(L_q + (-1)^q L_{-q}^\dagger).$$

C.4 Angular Momentum Operator

The ground state angular momentum operator $\vec{F}_g$ is defined, in the spherical basis, by:

$$(F_g)_q = \sum_{m_g}^{-F_g,F_g} |m_g+q\rangle\langle m_g|\, c_q(m_g,F_g),$$

where:

$$c_q(m_g, F_g) = \begin{cases} m_g & \text{if } q = 0, \\ -\frac{q}{\sqrt{2}}\sqrt{F_g(F_g+1) - m_g(m_g+q)} & \text{otherwise.} \end{cases}$$

Analogously, the excited state angular momentum operator $\vec{F_e}$ is defined by:

$$(F_e)_q = \sum_{m_e}^{-F_e,F_e} |m_e + q\rangle \langle m_e| \, c_q(m_e, F_e),$$

so that the total magnetization operator $\vec{m}$ is defined by:

$$\vec{F} = \vec{F_g} + \vec{F_e}.$$

C.5 Clebsch-Gordan coefficients

Two angular momentum states $|l_1, m_1\rangle$, $|l_2, m_2\rangle$ can be combined in a single state trough the tensor product:

$$|l_1, m_1; l_2, m_2\rangle = |l_1, m_1\rangle \otimes |l_2, m_2\rangle \,,$$

which is still an angular momentum state that can be written as $|k, q\rangle$, where $0 \leq k \leq F_1 + F_2$ and $-k \leq q \leq k$.
The states $|l_1, m_1; l_2, m_2\rangle$ and $|k, q\rangle$ are connected by the Clebsh-Gordon coefficients defined by:

$$\langle kq|l_1, m_1; l_2, m_2\rangle = (-1)^q \sqrt{2k+1} \begin{pmatrix} F_1 & F_2 & k \\ m_1 & m_2 & -q \end{pmatrix},$$

where the term in parenthesis is 3-j Wigner symbol.

C.6 Irreducible Tensors

The irriducible tensor operators T^{kq} are defined by:

$$T^{kq}_{l_1 l_2} := \sum_{m_1}^{-F_1,F_1} \sum_{m_2}^{-F_2,F_2} (-1)^{F_2 - m_2} \langle kq|F_1, m_1; F_2, -m_2\rangle \, |F_1 m_1\rangle \langle F_2 m_2| \,,$$

This formula can be inverted resulting in:

$$|l_1 m_1\rangle \langle l_2 m_2| = \sum_{kq} (-1)^{F^{'}-m^{'}} \langle kq|l_1, m_1; l_2, -m_2\rangle \, T^{kq}_{l_1 l_2}, \tag{C.2}$$

from which one can find the matrix element of the multipole operator:

$$\langle lm|T^{kq}_{l_1 l_2}|l^{'} m^{'}\rangle = (-1)^{F^{'}-m^{'}} \langle kq|F, m; F^{'}, -m^{'}\rangle \, .$$

Using equation C.2 together with the usual expansion of the density matrix in eigenvectors (see equation 6.1), one can easily prove that the density matrix can be equivalently written as:

$$\rho = \sum_{kq} m^{kq}_{l_1, l_2} T^{kq}_{l_1, l_2}, \tag{C.3}$$

where the multi-pole components $m^{kq}_{l_1 l_2}$ are defined by:

$$m^{kq}_{l_1 l_2} := \sum_{m_1}^{-F_1, F_1} \sum_{m_2}^{-F_2, F_2} \langle kq|F_1, m_1; F_2, -m_2\rangle \langle F_2 m_2|\rho|F_1 m_1\rangle \, .$$

Given the definitions it is easy to prove that:

$$m^{kq}_{l_1 l_2} = \mathrm{Tr}(\rho T^{kq}_{l_1 l_2}{}^{\dagger}).$$

Furthermore the hermitian conjugate of the multipole operators can be obtained from the following identity:

$$(T^{kq}_{l_2 l_1})^{\dagger} = (-1)^{F_2 - F_1 + q} T^{k-q}_{l_1 l_2},$$

and analogously the complex conjugate of the multipole components can be found from:

$$m^{kq}_{l_2 l_1} = (-1)^{F_2 - F_1 + q} (m^{k-q}_{l_1 l_2})^{*}.$$

C.6.1 Zero and First Order Multipoles

We relate the multipole operators and coefficients (up to the first order) to known operators and correspondent averaged values.

- When $k = 0$, q is always zero. In this case the operators $m^{00}_{l_1 l_2}$ and coefficients $m^{1q}_{l_1 l_2}$ are:

- the multipole operator T^{00}_{gg} is proportional to the ground state projection operator P_g:

  $$T^0_g = \frac{P_g}{\sqrt{2F_g+1}};$$

  so the multipole coefficient m^{00}_{gg} is proportional to the ground state overall population $p_g = |P_g\rho|$:

  $$m^{00}_{gg} = \frac{p_g}{\sqrt{2F_g+1}};$$

- the multipole operator T^{00}_{ee} is proportional to the excited state projection operator P_e:

  $$T^0_e = \frac{P_e}{\sqrt{2F_e+1}};$$

  so the multipole coefficient m^{00}_{ee} is proportional to the excited state overall population $p_e = |P_e\rho|$

  $$m^{00}_{ee} = \frac{p_e}{\sqrt{2F_e+1}};$$

- the multipole operator T^{00}_{ge} is proportional to the ground/excited state coherence operator P_{ge}:

  $$T^{00}_{ge} = \frac{P_{ge}}{\sqrt{2F_g+1}}$$

  so the multipole coefficient m^{00}_{ge} is proportional to the excited/ground state zero order coherence $c = |P_{eg}\rho|$:

  $$m^{00}_{ge} = \frac{c}{\sqrt{2F_g+1}};$$

- When $k = 1$, then $-1 < q < 1$. In this case the operators $m^{1q}_{l_1 l_2}$ and coefficients $m^{1q}_{l_1 l_2}$ are:

  - the multipole operators T^{1q}_{gg} is proportional to the ground state magnetization component m_{g_q}:

    $$T^{1q}_{gg} = \sqrt{\frac{3}{(2F_g+1)(F_g+1)F_g}}(m_g)_q;$$

so the multipole coefficient m_{gg}^{1q} is proportional to the ground state angular momentum operator component $\underline{\mathrm{m}}_{g\,-q}$ averaged value:

$$m_{gg}^{1q} = \sqrt{\frac{3}{(2F_g+1)(F_g+1)F_g}}(-1)^q(\underline{\mathrm{m}}_g)_{-q};$$

– the multipole operators T_{ee}^{1q} is proportional to the excited state angular momentum operator component m_{eq}:

$$T_{ee}^{1q} = \sqrt{\frac{3}{(2F_e+1)(F_e+1)F_e}}(F_q)^e;$$

so the multipole coefficient m_{ee}^{1q} is proportional to the ground state angular momentum operator component $\underline{\mathrm{m}}_{e\,-q}$ averaged value:

$$m_{ee}^{1q} = \sqrt{\frac{3}{(2F_e+1)(F_e+1)F_e}}(-1)^q(\underline{\mathrm{m}}_e)_{-q};$$

– the multipole operators T_{ge}^{1q} is proportional to the dipole operator component d_q^-:

$$T_{ge}^{1q} = \sqrt{\frac{3}{2F_g+1}}\frac{d_q^-}{d_0}$$

so the multipole coefficient m_{ge}^{1q} is proportional to the dipole operator component $\underline{\mathrm{d}}_{-q}^-$ average value;

$$m_{ge}^{1q} = \sqrt{\frac{3}{2F_g+1}}\frac{(-1)^q\underline{\mathrm{d}}_{-q}^-}{d_0}$$

– the multipole operators T_{eg}^{1q} is proportional to the dipole operator component d_q^+:

$$T_{eg}^{1q} = \sqrt{\frac{3}{2F_g+1}}\frac{(-1)^{F_g+F_e}d_q^+}{d(F_g,F_e)}$$

so the multipole coefficient m_{eg}^{1q} is proportional to the dipole operator component $\underline{\mathrm{d}}_{-q}^+$ average value;

$$m_{eg}^{1q} = \sqrt{\frac{3}{2F_g+1}}\frac{(-1)^{F_g+F_e+q}\underline{\mathrm{d}}_{-q}^+}{d(F_g,F_e)}.$$

C.6.2 Multipoles Commutators

In order to solve the problem of evaluation the commutator of two generic multipole operators, we first define the symbol:

$$|T^{k_1q_1}_{l_1l_2}T^{k_2q_2}_{l_2l_3}(T^{k_3q_3}_{l_1l_3})^\dagger| = \begin{bmatrix} k_1 & k_2 & k_3 \\ q_1 & q_2 & q_3 \\ l_1 & l_2 & l_3 \end{bmatrix}. \tag{C.4}$$

We find that using the summation rules of three Clebsch-Gordan coefficients the previous symbol can be explicatively written as:

$$\begin{aligned}\begin{bmatrix} k_1 & k_2 & k_3 \\ q_1 & q_2 & q_3 \\ l_1 & l_2 & l_3 \end{bmatrix} =& (-1)^{F_3+F_1+q_3}\sqrt{2k_1+1}\sqrt{2k_2+1}\sqrt{2k_3+1} \\ & \begin{pmatrix} k_3 & k_2 & k_1 \\ -q_3 & q_2 & q_1 \end{pmatrix}\begin{Bmatrix} k_3 & k_2 & k_1 \\ F_2 & F_1 & F_3 \end{Bmatrix}.\end{aligned}$$

The operator $[T^{k_1q_1}_{l_1l_2}, T^{k_2q_2}_{l_3l_4}]$ is a linear combination of multipole operators $T^{k_3q_3}_{l_5l_6}$ and the coefficients of the summation can be obtained from the trace:

$$\begin{aligned}|[T^{k_1q_1}_{l_1l_2}, T^{k_2q_2}_{l_3l_4}](T^{k_3q_3}_{l_5l_6})^\dagger| = & \delta_{l_1l_5}\delta_{l_2l_3}\delta_{l_4l_6}\begin{bmatrix} k_1 & k_2 & k_3 \\ q_1 & q_2 & q_3 \\ l_1 & l_2 & l_4 \end{bmatrix} \\ & - \delta_{l_3l_5}\delta_{l_4l_1}\delta_{l_2l_6}\begin{bmatrix} k_2 & k_1 & k_3 \\ q_2 & q_1 & q_3 \\ l_3 & l_4 & l_2 \end{bmatrix},\end{aligned}$$

which is obtained extending the result in equation C.4.

C.7 Maxwell Wave Equation

The four well known Maxwell equations [92] for the propagation and creation of electromagnetic fields are in a non magnetic medium with no charges:

$$\nabla \cdot \vec{E} = \frac{\nabla \cdot \vec{P}}{\epsilon_0}, \tag{C.5}$$

$$\nabla \cdot \vec{B} = 0, \tag{C.6}$$

$$\nabla \times \vec{E} = -\partial_t \vec{B}, \tag{C.7}$$

$$\nabla \times \vec{B} = \mu_0 \partial_t (\vec{P} + \epsilon_0 \vec{E}), \tag{C.8}$$

where ϵ_0 and μ_0 are, respectively, the permittivity and permeability of free space and the polarization vector $\vec{P}$ provides the coupling between the electromagnetic field and the atomic ensemble.
Taking the curl of C.7 and inserting the partial time derivative in C.8 using the identity we obtain:

$$\nabla(\nabla \cdot \vec{E}) - \nabla^2 \vec{E} = -\mu_0 \partial_t^2 (\vec{P} + \epsilon_0 \vec{E}),$$

where we have used the identity $\nabla \times (\nabla \times \vec{E}) \equiv \nabla(\nabla \cdot \vec{E}) - \nabla^2 \vec{E}$. The last equation can be rearranged in:

$$\nabla^2 \vec{E} - \epsilon_0 \mu_0 \partial_t^2 \vec{E} = \mu_0 \partial_t^2 \vec{P} + \nabla(\nabla \cdot \vec{E}).$$

Using the identity $\epsilon_0 \mu_0 = 1/c^2$ and the definition the d'Alembert operator $\Box \equiv \nabla^2 - c^{-2} \partial_t^2$ we obtain:

$$c^2 \Box \vec{E} = \frac{1}{\epsilon_0} (\partial_t^2 \vec{P} + \nabla(\nabla \cdot \vec{E})).$$

For the purpose of this discussion, we consider only plane waves propagating in the z direction; for this waves $E_z = 0$, $\partial_x \vec{E} = \partial_y \vec{E} = 0$ and so $\nabla(\nabla \cdot \vec{E}) = 0$. In this simplified scenario we arrive to the Maxwell Wave Equation:

$$c^2 \Box \vec{E} = \frac{1}{\epsilon_0} \partial_t^2 \vec{P}. \tag{C.9}$$

C.7.1 SVEA

As already been clarified in sections 7.1.1 and 7.1.2 the electric field and polarization vectors can be written in this form:

$$\vec{E} = \vec{E}_0 e^{i(\omega t - kz)},$$

$$\vec{P} = \vec{P}_0 e^{i(\omega t - kz)}.$$

where $\vec{E}_0$ and $\vec{P}_0$ are the slow varying envelopes of respectively the electric field and polarization fields. These expression can be used to arrive to a simplified version of the Maxwell Wave Equation C.9; in fact, with these assumptions the second order derivatives can be written as:

$$\begin{aligned}
\partial_z^2 \vec{E} &= (\partial_z^2 \vec{E}_0 - 2ik\partial_z \vec{E}_0 - k^2 \vec{E}_0) e^{i\phi}, \\
\partial_t^2 \vec{E} &= (\partial_t^2 \vec{E}_0 + 2i\omega \partial_t \vec{E}_0 - \omega^2 \vec{E}_0) e^{i\phi}, \\
\partial_t^2 \vec{P} &= (\partial_t^2 \vec{P}_0 + 2i\omega \partial_t \vec{P}_0 - \omega^2 \vec{P}_0) e^{i\phi}.
\end{aligned}$$

so that the left hand side of equation C.9 can be written as:

$$c^2\Box\vec{E} = (c^2\partial_z^2 - \partial_t^2)\vec{E} = (c^2\Box\vec{E}_0 - 2i\omega(c\partial_z + \partial_t)\vec{E}_0)e^{i\phi},$$

where we have used the dispersion relationship $\omega = kc$.
Assuming that the electric envelope change is small over a distance of the order of the wavelength:

$$|\partial_z^2\vec{E}_0| \ll |k\partial_z\vec{E}_0|,$$

and that the change of the electric field and polarization envelopes are small in an optical cycle:

$$|\partial_t^2\vec{E}_0| \ll |\omega\partial_t\vec{E}_0|,$$
$$|\partial_t^2\vec{P}_0| \ll |\omega\partial_t\vec{P}_0|,$$
$$|\partial_t\vec{P}_0| \ll |\omega\vec{P}_0|,$$

which are known as the slowly-varying envelope (SVEA) then we can assume $\Box\vec{E}_0 \cong 0$, and $\partial_t^2\vec{P}_0 \cong 0$, $\partial_t\vec{P}_0 \cong 0$ and rewrite equation C.9 as:

$$-2i\omega(c\partial_z + \partial_t)\vec{E}_0 e^{i\phi} = (-\omega^2\vec{P}_0)e^{i\phi},$$

dividing each member by $e^{i\phi}$, we finally obtain the first order equation:

$$\boxed{(\partial_t + c\partial_z)\vec{E}_0 = i\frac{\omega_c}{2\epsilon_0}\vec{P}_0} \tag{C.10}$$

which is known as the slowly-varying envelope approximation (SVEA) of equation C.9.

C.8 Vectorial Representation Constants

In the following table we report the formulas used to evaluate the constants in the vectorial representations described in section 6.4. All the traces are evaluated using the density matrix ρ_1 truncated to the first order and described in section 6.4.1.

$$\boxed{\begin{aligned}
l_g &= -\frac{|[m_0^g, d_{-1}^+]\rho_1|}{2|d_{-1}^+\rho_1|},\\
l_e &= -\frac{|[m_0^e, d_{-1}^+]\rho_1|}{2|d_{-1}^+\rho_1|},\\
k_g &= \frac{|m_0^g V_D|}{\Gamma|m_0^e\rho_1|},\\
l_c &= \frac{|P_g[c_0^-, d_1^+]\rho_1|}{2|d_1^+\rho_1|}\\
\delta &= \delta_{F_gF_e}.
\end{aligned}}$$

Here the operator $\vec{t}$ and c are defined as:

$$\begin{aligned}\vec{t} =& \vec{d}^{+} - \vec{d}^{-},\\ c =& c^{+} + c^{-}.\end{aligned}$$

The parameters l_g, l_e, v_g and v_e in the table above have dimension d_0^2; all other are dimensionless.

C.9 Vectorial Products

These are the the most important identities, involving different vectorial products, used to demonstrate the results in section 7.3.

$$(\vec{a} \times \vec{b}) \times \vec{c} + (\vec{b} \times \vec{c}) \times \vec{a} =(\vec{c} \times \vec{a}) \times \vec{b} = 0 \tag{C.12}$$

$$\vec{E}_0 \times \vec{E}_0^* = - iI_D \hat{e}_z = iaI_T \hat{e}_z, \tag{C.13}$$

$$(\vec{a} \times \vec{b}) \times \vec{c} = - (\vec{c} \cdot \vec{b}^*)\vec{a} + (\vec{c} \cdot \vec{a}^*)\vec{b}, \tag{C.14}$$

$$a \cdot b^* = b \cdot a^*, \tag{C.15}$$

Bibliography

[1] W. E. Bell and A. L. Bloom, "Optically driven spin precession," *Phys. Rev. Lett.*, vol. 6, pp. 280–281, Mar 1961.

[2] Z. D. Grujić and A. Weis, "Atomic magnetic resonance induced by amplitude-, frequency-, or polarization-modulated light," *Phys. Rev. A*, vol. 88, p. 012508, Jul 2013.

[3] D. Suter, M. Rosatzin, and J. Mlynek, "Optically driven spin nutations in the ground state of atomic sodium," *Physical Review A*, vol. 41, no. 3, p. 1634, 1990.

[4] M. Möller and W. Lange, "Radiation trapping: An alternative mechanism for chaos in a nonlinear optical resonator," *Phys. Rev. A*, vol. 49, pp. 4161–4169, May 1994.

[5] F. Mitschke, R. Deserno, W. Lange, and J. Mlynek, "Magnetically induced optical self-pulsing in a nonlinear resonator," *Phys. Rev. A*, vol. 33, pp. 3219–3231, May 1986.

[6] P. J. Mohr, B. N. Taylor, and D. B. Newell, "Codata recommended values of the fundamental physical constants: 2010a)," *Journal of Physical and Chemical Reference Data*, vol. 41, no. 4, p. 043109, 2012.

[7] D. A. Steck, "Cesium D Line Data," *Theoretical Division (T-8)*, vol. MS B285, 1998.

[8] M. P. Bradley, J. V. Porto, S. Rainville, J. K. Thompson, and D. E. Pritchard, "Penning trap measurements of the masses of c 133 s, r 8 7, 8 5 b, and n 23 a with uncertainties 0.2 ppb," *Physical Review Letters*, vol. 83, no. 22, p. 4510, 1999.

[9] E. Arimondo, M. Inguscio, and P. Violino, "Experimental determinations of the hyperfine structure in the alkali atoms," *Reviews of Modern Physics*, vol. 49, no. 1, p. 31, 1977.

[10] P. Schwindt, S. Knappe, V. Shah, L. Hollberg, and J. Kitching, "Chip-scale atomic magnetometer," *Applied Physics Letters*, vol. 85, no. 26, 2004.

[11] V. Shah, S. Knappe, P. D. D. Shwindt, and J. Kitching, "Subpicotesla atomic magnetometry with a microfabricated vapour cell," *Nature Photonics*, vol. 1, no. 10.1038, 2007.

[12] S. Knappe, P. Schwindt, V. Gerginov, V. Shah, L. Liew, J. Moreland, H. G. Rinson, L. Hollberg, and J. Kitching, "Microfabricated atomic clocks and magnetometers," *Journal of Optics A: Pure and Applied Optics*, vol. 8, no. S318-S322, 2006.

[13] J. Preusser, S. Knappe, V. Shan, P. Schwindt, C. Griffth, R. Jimenez, and J. Preusser, "Microfabricated atomic magnetometers and applications," *Proc. 2007 IEEE Intl. Freq. Cont. Symp.*, pp. 789–794, 2008 BC.

[14] P. D. D. Schwindt, S. Knappe, V. Shah, L.-A. Liew, and J. Moreland, "Microfabricated atomic magnetometers," in *Sensors, 2005 IEEE*, p. 4 pp., Oct 2005.

[15] P. Schwindt, B. Lindseth, S. Knappe, V. Shah, and J. Kitching, "Chip-scale atomic magnetometers with improved sensitivity by use of the M_x technique," *A*, vol. 90, no. 081102, Applied Physics Letters.

[16] J. Moreland, J. Kitching, P. Schwindt, S. Knappe, V. Shah, L. Liew, V. Gerginov, Y. Wang, and L. Hollberg, "Chip-scale atomic magnetometers," *Meeting of the Military Sensing Synposia (MSS) Speciality Group on Battlefield Acoustic and Seismic Sensing, Magnetic and Electric Field Sensors (BAMS)*, vol. MD, 2005.

[17] S. Knappe, T. H. Sander, O. Kosch, F. Wiekhorst, J. Kitching, and L. Trahms, "Cross-validation of microfabricated atomic magnetometers with superconducting quantum interference devices for biomagnetic applications," *Applied Physics Letters*, vol. 97, no. 13, 2010.

[18] T. Sander, J. Preusser, R. Mhaskar, J. Kitching, L. Trahms, and S. Knappe, "Magnetoencephalography with a chip-scale atomic magnetometer," *Biomedical optics express*, vol. 3, no. 5, pp. 981–990, 2012.

[19] S. Groeger, G. Bison, P. E. Knowles, R. Wynands, and A. Weis, "Laser-pumped cesium magnetometers for high-resolution medical and fundamental research," *Sensors and Actuators A: Physical*, vol. 129, no. 1, pp. 1–5, 2006.

[20] J. Preusser, V. Gerginov, S. Knappe, and J. Kitching, "A microfabricated photonic magnetometer," *Proc. 2008 IEEE Sensors*, 2009.

[21] W. Gawlik, L. Krzemień, S. Pustelny, D. Sangla, J. Zachorowski, M. Graf, A. Sushkov, and D. Budker, "Nonlinear magneto-optical rotation with amplitude modulated light," *Applied physics letters*, vol. 88, no. 13, p. 131108, 2006.

[22] D. Budker, D. F. Kimball, S. M. Rochester, V. V. Yashchuk, and M. Zolotorev, "Sensitive magnetometry based on nonlinear magneto-optical rotation," *Phys. Rev. A*, vol. 62, p. 043403, Sep 2000.

[23] J. A. Kusters and C. A. Adams, "Performance requirements of communication base station time standards," *AGING*, vol. 1, p. 11, 1999.

[24] R. Jimenez-Martinez, W. C. Griffith, Y. J. Wang, S. Knappe, J. Kitching, K. Smith, and M. D. Prouty, "Sensitivity comparison of mx and frequency-modulated bell-bloom Cs magnetometers in a microfabricated cell," *IEEE Transactions on Instrumentation and Measurement*, vol. 59, pp. 372–378, Feb 2010.

[25] T. Scholtes, V. Schultze, R. IJsselsteijn, S. Woetzel, and H.-G. Meyer, "Light-narrowed optically pumped m x magnetometer with a miniaturized Cs cell," *Physical Review A*, vol. 84, no. 4, p. 043416, 2011.

[26] N. Beverini, O. Faggioni, C. Carmisciano, E. Alzetta, E. Maccioni, M. Francesconi, A. Donati, E. Simeone, and F. Strumia, "A project for a new alkali vapour magnetometer, optically pumped by a diode laser," *Annals of Geophysics*, vol. 41, no. 3, 1998.

[27] W. C. Griffth, R. Jimenez-Martinez, V. Shan, S. Knappe, and J. Kitching, "Miniature atomic magnetometer integrated with flux concentrators," *Applied Physics Letters*, vol. 94, no. 023502, 2009.

[28] M. Ledbetter, I. Savukov, D. Budker, V. Shah, S. Knappe, J. Kitching, D. Michalak, S. Xu, and A. Pines, "Zero-field remote detection of nmr with a microfabricated atomic magnetometer," *Proceedings of the National Academy of Sciences*, vol. 105, no. 7, pp. 2286–2290, 2008.

[29] J. Mlynek, M. Rosatzin, and D. Suter, "Optically induced coherent spin transients in an atomic ground state," in *Coherence and Quantum Optics VI* (J. Eberly, L. Mandel, and E. Wolf, eds.), pp. 763–767, Springer US, 1989.

[30] D. Suter, "Polarization oscillations of coupled laser beams in an optically pumped atomic vapour," *Optics Communications*, vol. 95, no. 4, pp. 255 – 259, 1993.

[31] T. Ackemann, Y. A. Logvin, A. Heuer, and W. Lange, "Transition between positive and negative hexagons in optical pattern formation," *Phys. Rev. Lett.*, vol. 75, pp. 3450–3453, Nov 1995.

[32] P. Siddons, C. S. Adams, C. G.e., and I. G. Hughes, "Absolute absorption on rubidium D lines: comparison between theory and experiment," *Journal Of Physics B: Atomic, Molecular and Optical Physics*, vol. 41, no. 155004, 2008.

[33] D. A. Steck, "Rubidium 87 D Line Data," 2001.

[34] V. Shah and J. Kitching, "Advances in coherent population trapping for atomic clocks," *Advances in Atomic, Molecular, and Optical Physics*, vol. 59, 2010.

[35] A. Bauch, "Caesium atomic clocks: function, performance and applications," *Measurement Science and Technology*, vol. 14, no. 8, p. 1159, 2003.

[36] S. Rosin and I. I. Rabi, "Effective collision cross sections of the alkali atoms in various gases," *Phys. Rev.*, vol. 48, pp. 373–379, Aug 1935.

[37] H. Seidel, L. Csepregi, A. Heuberger, and H. Baumgärtel, "Anisotropic etching of crystalline silicon in alkaline solutions i. orientation dependence and behavior of passivation layers," *Journal of the electrochemical society*, vol. 137, no. 11, pp. 3612–3626, 1990.

[38] L.-A. Liew, S. Knappe, J. Moreland, H. Robinson, L. Hollberg, and J. Kitching, "Micromachined alkali atom vapor cells for chip-scale atomic clocks," in *Micro Electro Mechanical Systems, 2004. 17th IEEE International Conference on.(MEMS)*, pp. 113–116, IEEE, 2004.

[39] M. Hasegawa, R. Chutani, C. Gorecki, R. Boudot, P. Dziuban, V. Giordano, S. Clatot, and L. Mauri, "Microfabrication of cesium vapor cells with buffer gas for mems atomic clocks," *Sensors and Actuators A: Physical*, vol. 167, no. 2, pp. 594–601, 2011.

[40] L.-A. Liew, J. Moreland, and V. Gerginov, "Microfabricated alkali atom vapor cells," *Applied Physics Letters*, vol. 84, 2004.

[41] A. Cozma and B. Puers, “Characterization of the electrostatic bonding of silicon and pyrex glass,” *Journal of Micromechanics and Microengineering*, vol. 5, no. 2, p. 98, 1995.

[42] T. M. Lee, D. H. Lee, C. Y. Liaw, A. I. Lao, and I.-M. Hsing, “Detailed characterization of anodic bonding process between glass and thin-film coated silicon substrates,” *Sensors and Actuators A: Physical*, vol. 86, no. 12, pp. 103 – 107, 2000.

[43] S. Woetzel, V. Schultze, R. IJsselsteijn, T. Shulz, S. Anders, R. Stolz, and H. G. Meyer, “Microfabricated atomic vapor cell arrays for magnetic field measurements,” *Applied Physics Letters*, vol. 84, 2004.

[44] L.-A. Liew, J. Moreland, and V. Gerginov, “Wafer-level filling of microfabricated atomic vapor cells based on thin-film deposition and photolysis of cesium azide,” *Applied Physics Letters*, vol. 90, 2007.

[45] B. Woratschek, W. Sesselmann, J. Küppers, G. Ertl, and H. Haberland, “The interaction of cesium with oxygen,” *The Journal of chemical physics*, vol. 86, no. 4, pp. 2411–2422, 1987.

[46] P. Bicchi, L. Moi, P. Savino, and B. Zambon, “Measurement of the diffusion coefficient of oriented na atoms in different buffer gases,” *Il Nuovo Cimento B (1971-1996)*, vol. 55, no. 1, pp. 1–14, 2007.

[47] D. Giel, G. Hinz, D. Nettels, and A. Weis, “Diffusion of Cs atoms in ne buffer gas measured by optical magnetic resonance tomography,” *Opt. Express*, vol. 6, pp. 251–256, Jun 2000.

[48] S. Manz, T. Fernholz, J. Schmiedmayer, and J.-W. Pan, “Collisional decoherence during writing and reading quantum states,” *Phys. Rev. A*, vol. 75, p. 040101, Apr 2007.

[49] J. C. Allred, R. N. Lyman, T. W. Kornack, and M. V. Romalis, “High-sensitivity atomic magnetometer unaffected by spin-exchange relaxation,” *Phys. Rev. Lett.*, vol. 89, p. 130801, Sep 2002.

[50] M. Baranger, “General impact theory of pressure broadening,” *Phys. Rev.*, vol. 112, pp. 855–865, Nov 1958.

[51] D. S. Glassner, “Influences of quenching and inert buffer gases in degenerate four-wave mixing in alkali vapors,” *Phys. Rev. Lett.*, 1994.

[52] E. Speller, B. Staudenmayer, and V. Kempter, "Quenching cross sections for alkali-inert gas collisions," *Zeitschrift für Physik A Atoms and Nuclei*, vol. 291, no. 4, pp. 311–318, 1979.

[53] A. Nesmeyanov, "Vapor pressure of the chemical elements," *Elsevier*, vol. Amsterdam, 1963.

[54] A. Fick, "Ueber diffusion," *Annalen der Physik*, vol. 170, no. 1, pp. 59–86, 1855.

[55] R. P. Feynman, R. B. Leighton, and M. Sands, *The Feynman Lectures on Physics, Desktop Edition Volume I*, vol. 1. Basic books, 2013.

[56] R. Serway, C. Moses, and C. Moyer, *Modern physics.* Cengage Learning, 2004.

[57] G. A. Pitz, "Collisional dynamics of the cesium D1 and D2 transitions," *Air Force Institute of Technology*, vol. 71-10-B, 2010.

[58] D. T. HAAR, "Molecular theory of gases and liquids. joseph o. hirschfelder, charles f. curtiss, and r. byron bird. wiley, new york; chapman & hall, london, 1954. xxvi + 1219 pp. illus. 20," *Science*, vol. 120, no. 3131, pp. 1097–1097, 1954.

[59] T. G. Walker, "Estimates of spin-exchange parameters for alkali-metal–noble-gas pairs," *Physical Review A*, vol. 40, no. 9, p. 4959, 1989.

[60] T. Rosenband, D. B. Hume, P. O. Schmidt, C. W. Chou, A. Brusch, L. Lorini, W. H. Oskay, R. E. Drullinger, T. M. Fortier, J. E. Stalnaker, S. A. Diddams, W. C. Swann, N. R. Newbury, W. M. Itano, D. J. Wineland, and J. C. Bergquist, "Frequency ratio of Al+ and Hg+ single-ion optical clocks; metrology at the 17th decimal place," *Science*, vol. 319, no. 5871, pp. 1808–1812, 2008.

[61] D. A. Steck, "The Angular Distribution of Resonance Fluorescence from a Zeeman-Degenerate Atom: Formalism,"

[62] J. Sagle, R. Namiotka, and J. Huennekens, "Measurement and modelling of intensity dependent absorption and transit relaxation on the cesium line," *Journal of Physics B: Atomic, Molecular and Optical Physics*, vol. 29, no. 12, p. 2629, 1996.

[63] R. Loudon, *The quantum theory of light.* OUP Oxford, 2000.

[64] G. A. Pitz, D. E. Wertepny, and G. P. Perram, "Pressure broadening and shift of the cesium D_1 transition by noble gases N_2, H_2, HD, D_2, CH_4, C_2H_6, CF_4 and ^{3}He," *Physical Review A*, vol. 80, no. 062718, 2009.

[65] G. A. Pitz, C. D. Fox, and G. P. Perram, "Pressure broadening and shift of the cesium D_2 transition by noble gases N_2, H_2, HD, D_2, CH_4, C_2H_6, CF_4 and ^{3}He with comparison to the D_1 transition," *Physical Review A*, vol. 82, no. 042502, 2010.

[66] A. H. Couture, T. B. Clegg, and B. Driehuys, "Pressure shifts and broadening of the Cs D_1 and D_2 lines by He, N_2, and Xe at densities used for optical pumping and spin exchange polarization," *Journal of applied Physics*, vol. 104, no. 094912, 2008.

[67] O. Kozlova, J.-M. Danet, S. Guérandel, and E. De Clercq, "Temperature dependence of a Cs vapor cell clock: Pressure shift, signal amplitude, light shift," in *Frequency Control and the European Frequency and Time Forum (FCS), 2011 Joint Conference of the IEEE International*, pp. 1–5, IEEE, 2011.

[68] O. Kozlova, S. Guerandel, and E. de Clercq, "Temperature and pressure shift of the Cs clock transition in the presence of buffer gases: Ne, N_2, Ar," *Physical Review A*, vol. 83, no. 062714, 20011.

[69] A. Andalkar and R. B. Warrington, "High-resolution measurement of the pressure broadening and shift of the Cs D_1 and D_2 lines by N_2 and he buffer gases," *Physical Review A*, vol. 65, no. 032708, 2002.

[70] A. Andalkar and R. Warrington, "High-resolution measurement of the pressure broadening and shift of the Cs D 1 and D 2 lines by N 2 and He buffer gases," *Physical review A*, vol. 65, no. 3, p. 032708, 2002.

[71] E. Bernabeu and J. Alvarez, "Shift and broadening of hyperfine components of the first doublet of cesium perturbed by foreign gases," *Physical Review A*, vol. 22, no. 6, p. 2690, 1980.

[72] A. Couture, T. Clegg, and B. Driehuys, "Pressure shifts and broadening of the Cs D_1 and D_2 lines by He, N_2, and Xe at densities used for optical pumping and spin exchange polarization," *Journal of Applied Physics*, vol. 104, no. 9, 2008.

[73] A. Lipson, S. G. Lipson, and H. Lipson, *Optical physics*. Cambridge University Press, 2010.

[74] S. Pustelny, A. Wojciechowski, M. Gring, M. Kotyrba, J. Zachorowski, and W. Gawlik, "Magnetometry based on nonlinear magneto-optical rotation with amplitude-modulated light," *Journal of Applied Physics*, vol. 103, no. 6, 2008.

[75] V. Schultze, R. IJsselsteijn, T. Scholtes, S. Woetzel, and H.-G. Meyer, "Characteristics and performance of an intensity-modulated optically pumped magnetometer in comparison to the classical mx magnetometer," *Opt. Express*, vol. 20, pp. 14201–14212, Jun 2012.

[76] P. D. Schwindt, B. J. Lindseth, V. Shah, S. Knappe, and J. Kitching, "Chip-scale atomic magnetometer," in *Conference on Lasers and Electro-Optics/Quantum Electronics and Laser Science Conference and Photonic Applications Systems Technologies*, p. QWG7, Optical Society of America, 2006.

[77] D. Edmonds, "Larmor precession as a mechanism for the detection of static and alternating magnetic fields," *Bioelectrochemistry and Bioenergetics*, vol. 30, pp. 3 – 12, 1993.

[78] M. Ledbetter, I. Savukov, D. Budker, V. Shah, S. Knappe, J. Kitching, D. Michalak, S. X.u., and A. Pines, "Zero-field remote detection of nmr with a microfabricated atomic magnetometer," *Proceedings of the National Academy of Sciences*, vol. 105, no. 7, pp. 2286–2290, 2008.

[79] Y.-X. Yao and S. Pandit, "Cramer-rao lower bounds for a damped sinusoidal process," *Signal Processing, IEEE Transactions on*, vol. 43, pp. 878–885, Apr 1995.

[80] D. M. Brink and G. R. Satchler, *Angular momentum.* Oxford, 1962.

[81] D. A. Steck, *Quantum and Atom Optics Notes.* 2007.

[82] H.-P. Breuer and F. Petruccione, *The theory of open quantum systems.* Oxford University Press on Demand, 2002.

[83] H. J. Carmichael and M. O. Scully, "Statistical methods in quantum optics 1: Master equations and fokker-planck equations," *Physics Today*, vol. 53, no. 3, p. 78, 2000.

[84] K. Blum, *Density matrix theory and applications; 3rd ed.* Springer Series on Atomic Optical and Plasma Physics, Berlin: Springer, 2012.

[85] H.-J. Stckmann and D. Dubbers, "Generalized spin precession equations," *New Journal of Physics*, vol. 16, no. 5, p. 053050, 2014.

[86] A. Weis, G. Bison, and A. S. Pazgalev, “Theory of double resonance magnetometers based on atomic alignment,” *Phys. Rev. A*, vol. 74, p. 033401, Sep 2006.

[87] P. Hammerling, “Generalized bloch equations for any multipole,” *Journal of Physics B: Atomic and Molecular Physics*, vol. 1, no. 5, p. 759, 1968.

[88] G. Bevilacqua, E. Breschi, and A. Weis, “Steady-state solutions for atomic multipole moments in an arbitrarily oriented static magnetic field,” *Phys. Rev. A*, vol. 89, p. 033406, Mar 2014.

[89] D. Suter, “Optically excited zeeman coherences in atomic ground states: Nuclear-spin effects,” *Phys. Rev. A*, vol. 46, pp. 344–350, Jul 1992.

[90] D. Suter and J. Mlynek, “Dynamics of atomic sublevel coherences during modulated optical pumping,” *Phys. Rev. A*, vol. 43, pp. 6124–6134, Jun 1991.

[91] Y. Liu, J. Lin, and G. Huang, “Simple empirical analytical approximation to the Voigt profile,” *J. Opt. Soc. Am. B*, vol. 18, 2001.

[92] J. D. Jackson, *Classical electrodynamics.* Wiley, 1999.